MRI-based Morphometry during Neurodevelopment

Alonso Cárdenas de la Parra

Department of Biological and Biomedical Engineering

McGill University

Montréal, Canada

April 2020

A thesis submitted to McGill University in partial fulfillment of the requirements for the degree of Doctor of Biological and Biomedical Engineering

Abstract

Magnetic resonance imaging (MRI) is a non-invasive imaging technique commonly used to study neurological changes associated with disease. Morphometric analysis of MRI focuses on the quantitative analysis of size and shape of regions within the brain, thus providing a powerful tool for observing neurological changes. While many image processing tools have been developed for morphometric analyses, most have been designed with the adult population in mind. However, numerous diseases and disorders present themselves during childhood, and pediatric neuroimaging studies can help us better characterize them, aiding in understanding their etiology and progression, and providing information for better diagnostic tools. Pediatric neuroimaging studies present a series of unique challenges due to the normal neurodevelopment occurring during childhood and adolescence, with the brain undergoing substantial changes in size, shape, and maturation. The primary objective of this thesis is to design, test and validate morphometric techniques for pediatric neuroimaging studies. The first proposed technique focuses on early childhood (6-24 months of age), and consists of the application of tensor-based morphometry (TBM) by using T1 and T2-weighted scans simultaneously for the non-linear registration of scans to better account for the normal contrast changes that occur in this age range, as well as using age-appropriate templates as the target for this registration. This technique was applied to the study of autism spectrum disorder (ASD), with the results showing distinct differences in the growth trajectories of children with ASD when compared to controls in several regions across the brain. The second proposed technique focuses on later childhood and adolescence (4-23 years of age) and consists of a morphometric normalization technique that uses a large longitudinal normative database to establish normal growth trajectories for the volume of several regions in the brain, as well as at the voxel level. This technique was applied to study 16p11.2 copy number variants, with the results showing significant differences for the duplication and deletion cohorts already present at 4.5 years of age and remaining stable throughout childhood and adolescence. Finally, we propose an extension of this normalization technique that includes the addition of a second normative dataset and improved preprocessing, enabling normalization in studies with data acquired at both 1.5 and 3 T. This technique was applied to study pediatric onset multiple sclerosis (MS), with the results showing a lack of age expected growth in the MS patients in overall brain volume, and specifically in the thalamus, putamen, and globus pallidus.

Résumé

L'imagerie par résonance magnétique (IRM) est une technique d'imagerie non-invasive utilisée pour étudier les changements neurologiques associés aux maladies. L'analyse morphométrique d'IRM se concentre sur l'analyse de la taille et forme de régions du cerveau, constituant ainsi un outil pour observer les changements du cerveau. Bien que de nombreux outils de traitement des images aient été développés, la plupart ont été conçues pour les adultes. Cependant, de nombreuses maladies apparaissant pendant l'enfance, les études de neuroimagerie pédiatrique peuvent donc permettre de mieux caractériser l'étiologie et progression de ces maladies et fournissant de l'information pour l'amélioration des outils de diagnostic. Ces études comportent une série d'enjeux liés au neurodéveloppement pendant l'enfance, avec d'importants changements de taille, forme et maturation du cerveau. L'objectif principal de cette thèse est de développer, tester et valider des techniques morphométriques pour les études de neuroimagerie pédiatrique. La première technique proposée se concentre sur la petite enfance (6-24 mois d'âge) et consiste à l'application de morphométrie basée sur les tenseurs (TBM) en utilisant simultanément des scans T1 et T2 pour l'enregistrement non-linéaire afin de mieux prendre en compte les changements de contrastes qui apparaissent à cette tranche d'âge, ainsi que d'utiliser des patrons adaptés à l'âge comme cible. Cette technique a été appliquée à l'étude des troubles du spectre autistique (TSA), les résultats ont montré des différences distinctes dans les trajectoires de croissances des enfants ayant un TSA en comparaison avec des contrôles dans plusieurs régions à travers du cerveau. La deuxième technique proposée se concentre sur l'enfance plus avancée et l'adolescence (4-23 ans d'âge) et consiste à une technique de normalisation morphométrique utilisant une large base de données normatives longitudinales pour établir des trajectoires de croissance normale pour le volume du cerveau, ainsi qu'au niveau du voxel. Cette technique a été appliquée à l'étude des variations du nombre de copie 16p11.2, les résultats ont montré des différences significatives pour les cohortes de duplication et de suppression déjà présentes à l'âge de 4.5 ans et restant stables durant l'enfance et l'adolescence. Enfin nous proposons une extension de cette technique de normalisation incluant l'ajout d'une deuxième base de données normatives et une amélioration du pré-traitement, permettant la normalisation d'études avec des données acquise à 1.5 et 3 T. Cette technique a été appliquée à l'étude de l'apparition pédiatrique de la sclérose en plaques (SP), les résultats ont montré un manque de croissance attendue pour l'âge chez les patients SP au niveau du volume total du cerveau, en particulier pour le thalamus, putamen, et globus pallidus.

Acknowledgements

First and foremost, I would like to express my gratitude to my supervisor, Dr. Louis Collins, without his guidance, encouragement and support, none of this work would have been possible. His dedication and mentorship to his students is outstanding and deserving of praise.

I am grateful to Vladimir Fonov, whose guidance in all the technical knowledge required throughout these years of work has been invaluable.

I would like to thank my committee members, John Lewis, Simon Ducharme, and Georgios Mitsis, for their support and guidance. I would also like to thank my co-authors and colleagues, in particular Sandra Martin-Brevet, Brenda Banwell, Mahsa Dadar, and Azar Zandifar.

No work like this could be completed without the support of friends, particularly those that have been along for the ride, including Jason Vinck, Johann Vargas, Mathilde Salamon, and Ahmed Soroko, among others.

Last but not least, a special thanks to my parents, Sergio and Phoebe, my brother Sergio, and specially my wife María, for their unconditional love and support.

Contents

List of Figures

Supplementary Figures

List of tables

Supplementary Tables

Chapter 1
Introduction and motivation

1 Introduction

The main purpose of this thesis is to describe the motivation, development and application of morphometric image analysis techniques of magnetic resonance imaging (MRI) for pediatric studies. The following sections provide the motivation for the thesis, as well as an overview of its contents and a summary of its scientific contributions.

2 Motivation

Neuroimaging is often useful to quantitively assess the size and shape of regions in the brain. This analysis is known as morphometry, from the Greek μορφώ (morpho) meaning form or shape, and μετρία (metria) meaning measurement. MRI is a non-invasive, non-ionizing imaging technique, that in addition provides high resolution and strong tissue contrast. Morphometric analysis of MRI data can be used to observe potential changes in the brain both within a single subject as well as across populations. If we couple these morphometric analyses with clinical data, many scientific questions regarding the identification and progression of neurological diseases and disorders can be addressed. Among these questions, MRI morphometry can help to find biomarkers that can potentially aid diagnosis. It can help in understanding the etiology and progression of a disease. It can even be used as a tool for measuring potential changes during a clinical trial for a new drug.

In particular, MRI morphometry can be used to understand the changes that occur in the brain during childhood as part of normal neurodevelopment, as well as to identify potential abnormalities in neurodevelopment associated with a wide array of diseases and disorders. However, most of the imaging processing tools commonly used in MRI morphometry have been developed for use in adult populations. Performing MRI morphometry in pediatric studies presents several complications, mainly due to a wide array of changes that occur during the different stages of neurodevelopment.

Some of the underlying changes that affect MRI morphometry in pediatric studies include the reversal of contrast between white matter and grey matter in the first months of life, myelination throughout childhood, increasing cortical gyrification, changes in the shape and size of the skull, and overall brain growth, among others. Thus, when performing MRI

morphometry during childhood, it is very important to fine-tune neuroimaging techniques to the age range to be studied, as well as to have a firm framework that accounts for normal neurodevelopment.

In addition to the technical difficulties caused by normal neurodevelopment, it is usually difficult to recruit normally developing controls for pediatric studies, particularly when they involve numerous visits. As such, the ability to use established databases of normal development during childhood to model the underlying changes presents itself as an opportunity to better discriminate abnormal changes due to disease. The present thesis aims to design, test and validate techniques that can account for the changes that occur during normal neurodevelopment while also dealing with the possibility of a small number of normal controls within a study.

3 Thesis Overview

The present thesis is organized as follows. Chapter 2 provides a background on magnetic resonance imaging, image pre-processing techniques, morphometric techniques and statistical analyses, as well as a review of normal neurodevelopment during childhood and how this affects image processing and morphometry. Chapter 3 presents a longitudinal tensor-based morphometry approach to understand potential growth abnormalities during the first 2 years of life. It uses age-appropriate templates to deal with contrast differences between 6 months and 2 years of age and provides a voxel-wise assessment of growth trajectories. The technique is applied to a dataset of children at high risk of autism spectrum disorder (ASD), showing differences in the growth trajectories of children diagnosed with ASD when compared to normally developing controls. Chapter 4 presents a morphometric normalization technique for pediatric studies. In general, it uses a large longitudinal normative database to establish normal growth trajectories from 4 to 23 years of age for the volume of several regions in the brain. A variant of this method enables voxel-wise growth trajectory analysis. These growth trajectories are used to normalize a small set of study-specific controls, as well as subjects with 16p11.2 copy number variants, thus providing information on the brain abnormalities present in this genetic disorder. Chapter 5 presents an extension of the normalization technique presented in Chapter 4. This extension includes the addition of a second normative dataset, this one acquired at 3 Tesla, as well as improvements in pre-processing in order to account for the use of data acquired at both 1.5 and 3 T. This normalization is applied to a multi-centre database, acquired at both 1.5 and 3 T, of children with multiple sclerosis (MS). Finally, Chapter 6 provides the discussion and conclusion of the thesis.

4 Scientific Contributions

The main original contributions of this thesis are described below:

- Implementation of Tensor Based Morphometry (TBM) in early childhood (6-24 months of age) and its application to Autism Spectrum Disorder (ASD). The application of TBM within this age range poses several unique challenges, primarily due to the fast and important changes in brain size that occur during this period as well as changes in intensity due to the reversal of contrast in T1 and T2-weighted images caused by myelination as the brain matures. In order to get better results given these challenges, the subjects' MRI scans were registered to age appropriate templates created from the same database and inter-template registrations were used to bring all the subjects to a common space. This analysis has provided information regarding morphological abnormalities at the voxel level occurring during the first 2 years of life in children with ASD when compared to normally developing children. These abnormalities include regions with increased growth rate (posterior cingulate gyrus, left temporal pole, among others) as well as reduced growth rate in other regions (left precuneus, subgenual anterior cingulate cortex, among others).
- The development and implementation of a method to use a large normative dataset (NIHPD) to obtain voxel-wise trajectories of normal development using mixed effects modelling. These trajectories were used to obtain voxel-wise z-scores of children with 16p11.2 Copy Number Variants (CNVs). This method is a valuable alternative since many databases lack a sufficient amount of normal controls with which to compare the population of interest. The results provided valuable information, particularly showing that all the growth abnormalities were already present at 4 years of age and were stable throughout childhood and adolescence until 23 years of age in both deletion and duplication carriers. Some of the results worth highlighting include increased volume in the calcarine cortex and insula in deletions, compared to controls, with an inverse effect in duplication carriers.
- The refinement and validation of a 4-dimensional model of voxel-wise growth trajectories from normally developing subjects that enables application of the previously mentioned z-scoring to a wider variety of studies. This model is constructed using an improved longitudinal processing pipeline that incorporates better pre-processing and registration algorithms. It includes data acquired at both 1.5 and 3 T to better account for field strength differences and allows for z-scoring

of databases at either field strength without the need for further corrections. Its application to a large, multi-centre, multiple sclerosis (MS) database showed a lack of age-expected growth in the MS cohort compared to controls in the overall brain volume, thalamus, globus pallidus, and putamen.

5 Contribution of Authors

Chapter 3. A Voxel-wise Assessment of Growth Abnormalities in Infants with Autism Spectrum Disorder

- Authors.- Cárdenas de la Parra, A., Lewis, J.D., Fonov, V.S., Botteron, K., McKinstry, R., Gerig, G, Pruett Jr., J.R., Evans, A.C., Collins, D.L
- Contributions.- Original concept and design: ACP and DLC. Method implementation: ACP. Data preparation and preprocessing: ACP, VSF. Manuscript preparation: ACP. Results interpretation: ACP, DLC, JDL, KB, RM, JP. Manuscript revision: All authors.

Chapter 4. Developmental Trajectories of Neuroanatomical Alterations Associated with the 16p11.2 Copy Number Variants

- Shared 1st authorship.- Cárdenas de la Parra, A., Martin-Brevet, S.
- Shared senior authorship.- Collins, D.L., Jacquemont, S.
- Co-authors.- Moreau,C., Rodriguez Herreros, B., Fonov, V.S., Maillard, A.M., Zürcher, N.R., Hadjikhani, N., Beckmann, J.S., Reymond, A., Dragansky, B.
- Contributions.- Original concept and design: ACP, DLC, JS. Data acquisition: AMM, NRZ, NH, JSB. Data quality control: SMB, CM, BRH, BD. Method implementation: ACP. Data preparation and preprocessing: ACP. Volumetric statistical analysis: SMB. Voxelwise statistical analysis: ACP. Manuscript preparation: ACP, SMB. Results interpretation: ACP, DLC, SMB, SJ. Manuscript revision: All authors. Editing and final version: ACP, DLC, SMB, SJ.

Chapter 5. Methodology for Normalization of Serial 1.5 and 3 Tesla Magnetic Resonance Imaging Scans and its Application in Pediatric Multiple Sclerosis

- Authors.- Cárdenas de la Parra, A., Fonov, V.S., Yeh, E.A., Bar-Or, A., Marrie, R.A., Arnold, D.L., O'Mahony, J., Banwell, B., Collins, D.L.
- Contributions.- Original concept and design: ACP, DLC. Data acquisition: AEY, ABO, RAM, DA, BB. Method implementation: ACP. Data preparation and preprocessing: ACP, VSF. Manuscript preparation: ACP. Results interpretation: ACP, DLC, BB, JO. Manuscript revision: All authors.

Chapter 2

Background

1 Magnetic Resonance Imaging

1.1 Overview

Magnetic Resonance Imaging (MRI) is a non-invasive medical imaging technique that is widely used to investigate the internal human anatomy. It is commonly used both in the clinic and in research studies due to its lack of ionizing radiation, making it a safe technique to be used in longitudinal and pediatric applications.

MRI relies on the behaviour of nuclei when exposed to a strong external magnetic field. Nuclei composed of an odd number of protons and/or neutrons possess an angular momentum S that represents the intensity of their spinning motion. This spin leads to protons and neutrons having a proportional magnetic dipole moment μ perpendicular to the direction of the spin. The most common signal source for MRI in the human body are the hydrogen nuclei. Hydrogen nuclei are composed of a single proton, are found in all the water and fat molecules of the human body and have a high magnetic moment relative to the spin, known as the gyromagnetic ratio γ.

Without the application of an external magnetic field, the magnetic moments of hydrogen nuclei are randomly oriented. When these nuclei are exposed to an external field B_0, their magnetic moment vectors are aligned either in the direction of B_0 (known as a low energy state), or in the opposite direction of B_0 (known as a high energy state). Conventionally, the direction of B_0 is known as the longitudinal or z direction. Since the number of nuclei in a low energy state is slightly larger than those in a high energy state, we end up with a net magnetic moment M_0. The spins will also exhibit a precession around B_0 at an angular frequency ω_0, known as the Larmor frequency. The Larmor frequency is related to the gyromagnetic moment and to the external magnetic field by $\omega_0 = \gamma B_0$.

After the magnetization reaches the equilibrium state, a short RF magnetic pulse B_1 of frequency $\omega=\omega_0$ is applied in the transversal plane (i.e. the xy plane), breaking the equilibrium and leading to a precession in the transversal plane. After an RF pulse excitation, the longitudinal magnetization (i.e. parallel to B_0) will undergo a relaxation back to its equilibrium state, while the transverse component (i.e. perpendicular to B_0) decays.

The varying magnetization caused by the precession in the transversal plane induces an electric current in an RF receiver coil following Faraday's law of induction. The corresponding signal is called Free Induction Decay (FID), and it oscillates sinusoidally at the Larmor frequency while gradually decaying. Before using the FID in further processing, the oscillating component is removed by demodulation, leaving only a decaying signal known as the envelope of the FID.

1.2 Spatial localization and k-space

So far, the induced signal in the RF receiver coil will provide us with information in time, but since all the induced signals are received at the same frequency it does not provide spatial information. In MRI, the spatial information comes from the application of an additional linear gradient field G. This gradient field is superimposed on B_0 and varies linearly in each direction, yielding 3 perpendicular components of G (G_x, G_y, G_z).

One common method of spatial localization is using one component of G (typically referred to as G_S or slice-select gradient) to vary the frequency of precession of spins along the longitudinal axis, so that the frequencies contained in the RF pulse can be adjusted to excite spins only within a thin slice. The remaining components of G are used to incorporate additional spatial information within the slice defined by G_S. The frequency encoding or readout gradient (G_f) causes the frequency of precession of spins to vary from one end of the slice to the other. The phase encoding gradient G_p causes spins at one end of the slice to briefly spin faster than the spins at the other end, causing a phase shift parallel to G_p. As a result of this process, we can now tell individual spins within the slice apart by their frequency and phase.

The acquired signal is digitized and stored in k-space. K-space is an abstract spatial frequency domain, with a horizontal frequency axis and vertical phase axis. While k-space does not correspond spatially to the acquired image, it contains all the information required to reconstruct the MR image. This reconstruction is done by applying the inverse Fourier transform to the raw k-space data. Figure 1 shows an example of data represented in k-space and the corresponding reconstructed MR slice.

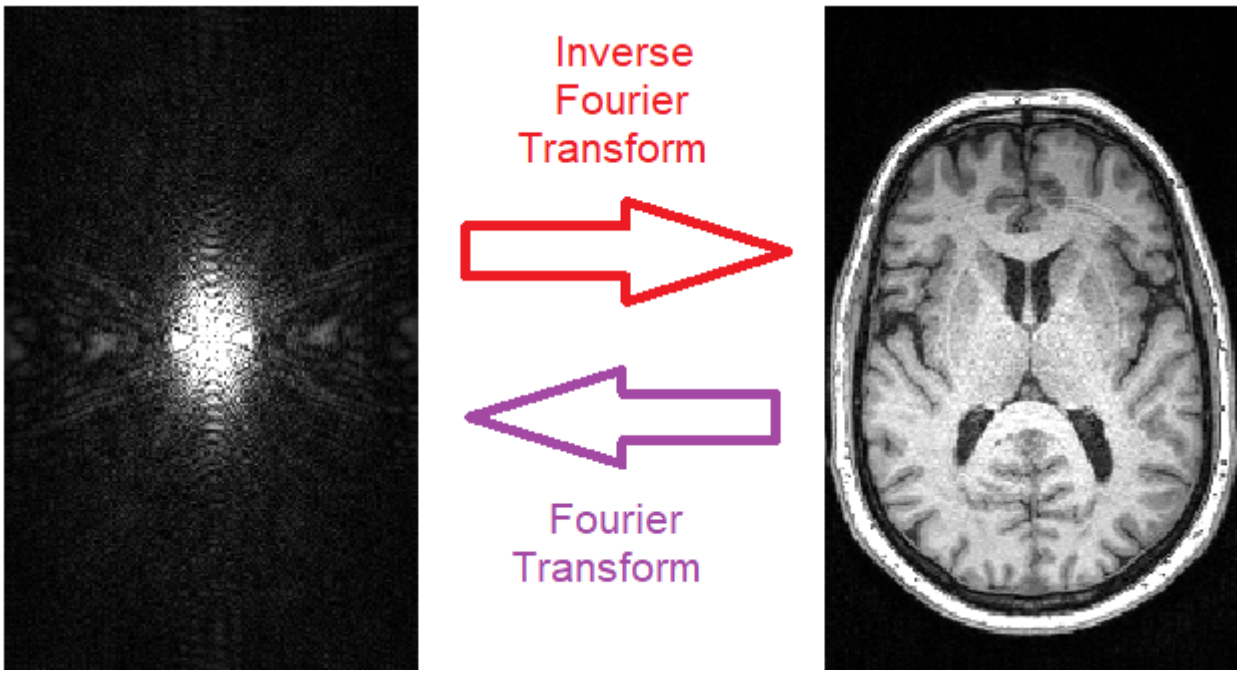

Figure 1. Data in k-space (left) where pixel intensity corresponds to amplitude of frequency component. The center of the k-space image corresponds to low frequency components, while the periphery corresponds to higher frequency components. Reconstructed MR slice after application of the Inverse Fourier Transform (right).

1.3 T1 and T2 weighted modalities

As mentioned in section 1.2, after an RF pulse is applied, the longitudinal component of the net magnetization returns to equilibrium as the spins dissipate their energy, while the perpendicular component decays due to the interaction between the magnetic field of neighbouring spins. The time constants that characterize these events are known as the spin-lattice relaxation time (T_1), and the spin-spin relaxation time (T_2), respectively. The equation relating T_1 to the longitudinal magnetization is:

$$M_z(t) = M_0\left(1 - e^{-\frac{t}{T_1}}\right) \quad (1)$$

where $M_z(t)$ is the longitudinal magnetization at time t, M_0 is the longitudinal magnetization in equilibrium, and T_1 is the spin-lattice relaxation time. The equation relating T_2 to transverse magnetization is:

$$M_{xy}(t) = M_{xy}\, e^{-\frac{t}{T_2}} \quad (2)$$

where $M_{xy}(t)$ is the transverse magnetization at time t, M_{xy} is full transverse magnetization, and T_2 is the spin-spin relaxation time.

The T_1 and T_2 relaxation times are inherent to the tissue being imaged. T_1 largely depends on the ability of the tissue to absorb the energy dissipated by the spins, how well the molecular motion of the molecules matches the Larmor frequency, as well as the strength of B_0. For example, fat can absorb energy more efficiently than water, leading to the T_1 of fat being much shorter than the one of water. Since T_2 depends on the energy transfer between neighbouring spins, it depends on how closely molecules are found in a given context. For example, the molecules in fat are tightly packed while the molecules in water tend to be spaced, leading to the T_2 of fat being very short while the one for water is very long.

During an MRI acquisition, we apply a collection of RF and gradient pulses, known as the MR pulse sequence. The parameters of this pulse sequence can be selected to give different weight to the tissue properties and control the contrast of the resulting image. A common equation to show this is:

$$I = PD * e^{-\frac{TE}{T_2}}\left(1 - e^{-\frac{TR}{T_1}}\right) \quad (3)$$

where:

- I is the resulting signal intensity.
- PD is proton density in the tissue.
- TE, or time to echo, is the time between the application of an RF pulse and the collection of the signal.
- TR, or repetition time, is the time between the application of 2 subsequent RF pulses for a particular slice.
- T_2 is the spin-spin relaxation time.
- T_1 is the spin-lattice relaxation time.

From equation 3 we can deduce that we can produce an image that mainly depends on the differences in T_1 between tissues (known as a T1-weighted image) by choosing a relatively short TR and a short TE, while a T2-weighted image can be obtained by using a relatively long TR and a long TE. Figure 2 shows an example of T1 and T2-weighted images.

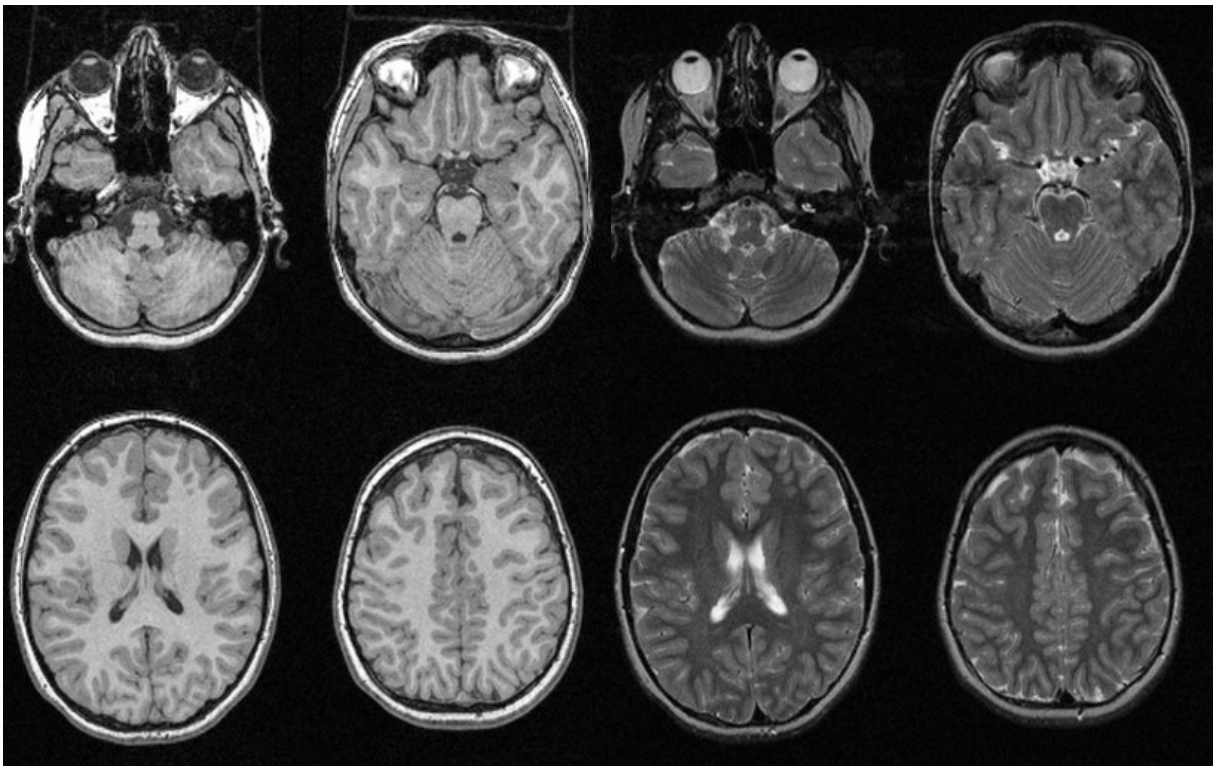

Figure 2. Comparison between T1 and T2-weighted axial images of the same subject. T1-weighted is shown in the 2 left columns, with T2-weighted shown in the right 2 columns.

The ability to obtain both T1 and T2-weighted images, and other contrasts, is one of the main advantages of MRI in brain imaging, since it provides images where the main tissue classes of the brain can be discriminated. In general, a T1-weighted scan of an adult brain will show contrast between white matter (WM), grey matter (GM), and cerebrospinal fluid (CSF) by having higher intensities for WM, medium for GM and darker for CSF. On the other hand, a T2-weighted image shows the opposite contrast between tissues, with CSF being brightest, followed by GM, and finally by WM.

1.4 Image artifacts

Image artifacts can be thought of as an undesirable set of features that appear in an image but are not present in the imaged object. Several artifacts are commonly present in reconstructed MR images, affecting our ability to interpret and process them. We will describe some of the most common artifacts found in MRI.

One of the main causes of artifacts in MRI are magnetic field inhomogeneities. Local inhomogeneity in the magnetic field B_0 can cause non-uniformity in the image intensity due to signal loss, while long-range inhomogeneities can cause geometric distortion of the image. Even though modern MRI equipment is designed to minimize inhomogeneities in B_0 and techniques like shimming are used in reducing them, the spatial changes in the magnetic susceptibility of the imaged object and objects outside the scanner will always lead to some amount of inhomogeneity. Furthermore, inhomogeneity in the RF pulses due to noise or technical limitations of the equipment, as well gradient non-linearity, can also lead to intensity non-uniformity and geometric distortion.

Another common source of artifacts is motion. When motion is present during acquisition, the resulting image is blurred or the object is extended or repeated along the direction of motion, known as ghosting. Motion artifacts cannot be fully controlled, since the acquisition time of MRI is relatively long, and are caused by voluntary motion from the patient, and can also occur due to involuntary movements like respiration and blood flow.

The Larmor frequency of a hydrogen proton is affected by the electrons that surround it within its local environment. This causes chemical shift artifact where tissue (usually fat) appears slightly shifted along the frequency encoding direction. This artifact increases with the strength of B_0.

Other common artifacts in MRI include wrap-around, where the imaged object is larger than the field of view. It can be seen as a folding over of anatomical parts into the area of interest and it is usually common along the phase encoding direction. Finally, Gibb's ringing is caused by the behaviour of the Fourier series used in reconstruction when presented with jump discontinuities, and they typically appear as parallel lines next to high-contrast regions (e.g. the boundary between WM and GM).

2 Image Pre-processing

2.1 Overview

Due to the variability in the acquisition parameters as well as with inherent differences that depend on individual scanner hardware, MR images typically undergo a series of pre-processing techniques in order to improve the quality of the image and provide a certain amount of standardization. These pre-processing tools provide a better starting point for any subsequent analysis or processing. Some of the most common steps in pre-processing include the correction of image artifacts, like intensity inhomogeneity and denoising, as well as image registration,

intensity normalization and brain extraction. In this section we will briefly describe some of the most common pre-processing steps, however image registration, due to its overall importance in the present work, will be described separately in Section 3.

2.2 Intensity Inhomogeneity Correction

After reconstruction, the MRI signal intensities from homogeneous tissue are not usually uniform, but rather present a low-frequency gradient across the image. This intensity non-uniformity can cause problems and affect the performance of several processing techniques such as registration and tissue classification, where an assumption of tissue intensity homogeneity is typically made. Some of the factors that cause this intensity inhomogeneity include poor uniformity receptivity in the RF coil, inhomogeneity in the magnetic field used in acquisition, eddy currents induced by the applied gradients, as well as heterogeneity in the anatomy of the patient. Additionally, the strength of the magnetic field B_0 affects the frequency characteristics of the inhomogeneity, with stronger fields resulting in higher frequency gradients.

A well-known, robust, automatic technique for intensity inhomogeneity correction called the nonparametric nonuniform intensity normalization (N3) was proposed by Sled et al. (1998). Like most of the state-of-the-art techniques, it is based on modelling the inhomogeneity as a multiplicative nonuniform field as follows:

$$v(x) = u(x)f(x) + n(x) \tag{4}$$

where *v(x)* is the corrupted signal at location *x*, *u(x)* is the corresponding true signal, *f(x)* is the bias field causing the inhomogeneity, and *n(x)* is white Gaussian noise. We further simplify the model by looking at the noise free case and taking the logarithm of both sides as follows:

$$\hat{v}(x) = \hat{u}(x) + \hat{f}(x) \;\; where\; \hat{v}(x) = \log\big(v(x)\big) \tag{5}$$

using the probability densities of $\hat{v}$, $\hat{u}$, and $\hat{f}$, and assuming that $\hat{u}$ and $\hat{f}$ are uncorrelated random variables, we can describe the distribution of their sum as a convolution:

$$V(\hat{v}) = F(\hat{v}) * U(\hat{v}) = \int F\big(\hat{v} - \hat{f}\big)U\big(\hat{f}\big)d\hat{f} \tag{6}$$

If we look at *F* as a low-pass filter applied to *U*, the correction of the intensity inhomogeneity will then consist in restoring the frequency content of *U*. In N3 this is achieved by searching for the multiplicative bias field that maximizes the frequency content in *U*. This is done

iteratively by obtaining an estimate of *U*, from the deconvolution of a proposed Gaussian distribution *F* from *V*. The formula describing the iterative solution being:

$$\hat{u}^n = \hat{v} - \hat{f}_e^n = \hat{v} - S\{\hat{v} - E[\hat{u}|\hat{u}^{n-1}]\} \quad (7)$$

where $\hat{f}_e^n$ is the estimated total bias field at the nth iteration, $S\{\cdot\}$ is a B-spline least squares approximator used to smooth the estimated bias field and $E[\hat{u}|\hat{u}^{n-1}]$ is the expected value of $\hat{u}$ given a measurement of $\hat{u}$ estimated in the previous iteration. The iterations are terminated when the variation between subsequent field estimates is smaller than a given parameter *e.* The final estimated bias field is extrapolated to the whole volume and is removed from the uncorrected image by a simple voxelwise division.

An improved version of N3 known as N4 was proposed by Tustison et al. (2010a). N4 uses the following iterative solution:

$$\hat{u}^n = \hat{u}^{n-1} - \hat{f}_r^n = \hat{u}^{n-1} - S^*\{\hat{u}^{n-1} - E[\hat{u}|\hat{u}^{n-1}]\} \quad (8)$$

with $S^*\{\cdot\}$ being a generalized n-dimensional C^k B-spline approximation used to smooth the bias field and $\hat{f}_r^n$ is the estimated *residual* bias field at the nth iteration. The main advantages of N4 over N3 being the better behaviour of $S^*\{\cdot\}$ when compared to $S\{\cdot\}$, and improved convergence in higher magnetic fields (i.e. 3T or 7T). Figure 3 shows an example of an MR image with intensity inhomogeneity, as well as the estimated bias field and a corrected image.

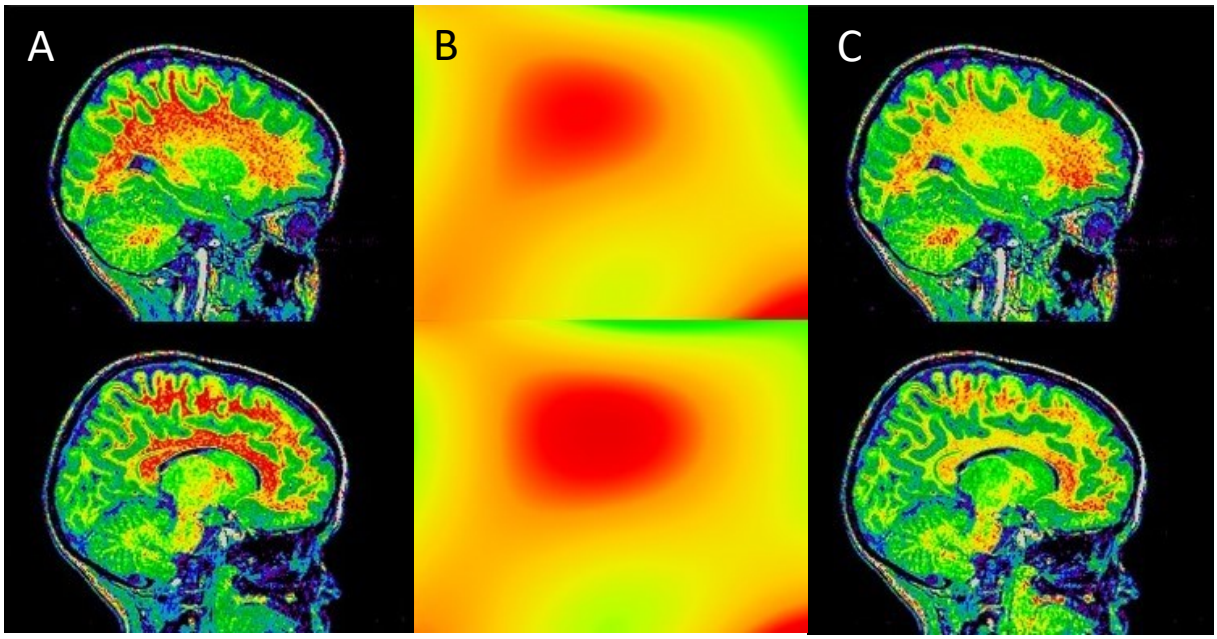

Figure 3. Example of two MR images with intensity non-uniformity (A), the estimated underlying bias field (B), and the corrected image (C).

2.3 Denoising

During MR image reconstruction, the Gaussian noise present in the acquisition undergoes a non-linear mapping, causing the noise present in the reconstructed image to be non-Gaussian. Gudbjartsson and Patz (1995) showed that the probability distribution of the measured pixel intensities in a reconstructed MR image follows the Rician distribution, which, for small signal-to-noise ratios deviates considerably from a Gaussian distribution.

A wealth of different approaches to denoising MR images have been used throughout the years, including simple low-pass filtering, wavelet-based filtering (Healy and Weaver, 1992; Yang and Fei, 2011), anisotropic diffusion filtering (Gerig et al., 1992; Samsonov and Johnson, 2004), spectral subtraction (Erturk et al., 2013) and non-local means (Coupe et al., 2008; Manjon et al., 2008).

In general, the choice of a denoising algorithm will depend on the signal-to-noise ratio of the images, as well as the subsequent analyses to be performed, since different methods can impact the data by blurring edges, erasing small features, modification of the image statistics, amongst others. Some of the modern non-local means methods (Coupe et al., 2008; Manjon et al., 2008) seem to overcome most of these limitations and appear to be well-suited for MR images with higher levels of noise, but may be more computationally expensive to apply.

2.4 Intensity Normalization

The image intensity values in a reconstructed MR image do not have an inherent meaning nor do they relate directly to any physical quantity, but rather depend on the selection of acquisition and calibration parameters, the scanner hardware, and even slight differences in the position of the subject. Typically, the absolute values of the intensities do not severely impact visual interpretation by a specialist, as they depend more on the simple contrast between tissue types and structures. However, these differences in intensity values can hinder the functionality of automatic image processing tools that require quantitative comparisons of intensities, like image registration or tissue classification.

The goal of any intensity normalization technique is to transform the acquired images in such a way that the intensities of similar anatomical regions between different scans have smaller variations. Several methods have been used to achieve intensity normalization, ranging from simple normalization of the intensities to have zero mean, to more complex intensity mappings derived from specific mean tissue intensities.

Perhaps the most commonly used methods rely on histogram matching. In general, histogram matching techniques estimate a set of intensity landmarks and maps those landmarks to those of a previously chosen reference histogram. The main difference amongst histogram matching methods is the choice of mathematical mapping between the histograms with 1-dimensional linear (Wang et al., 1998), 1-dimensional piecewise linear (Nyul et al., 2000; Nyúl and Udupa, 1999), Gaussian mixture fit (Hellier, 2003), and multi-dimensional joint histogram non-linear mapping (Jager and Hornegger, 2009) as examples.

Other methods have been proposed, that include additional information for the normalization procedure. These methods include combined intensity normalization and inhomogeneity correction by minimizing the Kullback-Leibler divergence between a reference MR image and the uncorrected image (Weisenfeld and Warfield, 2004) and the incorporation of expected tissue intensities to inform the intensity mapping (Manjón and Coupé, 2016; Robitaille et al., 2012).

2.5 Brain extraction

In several applications of MRI, it is desirable to isolate the brain tissue from its surrounding environment (i.e. skull, dura, eyes, etc.). As such, brain extraction (also known as skull-stripping) is a common preprocessing step. Its accuracy can affect the results of non-linear registration algorithms, volume estimations, and cortical thickness, among others (Novosad et al., 2018). Some common approaches to brain extraction include the use of deformable models made to fit the brain's surface (Smith, 2002), hybrid approaches that combine watershed algorithms, deformable surface models and correction from a statistical atlas (Ségonne et al., 2004), as well as more complex, learning-based methods that use a template or a set of atlases to drive the segmentation to a target image (Avants et al., 2011; Lutkenhoff et al., 2014). One example of brain extraction can be seen in Figure 4.

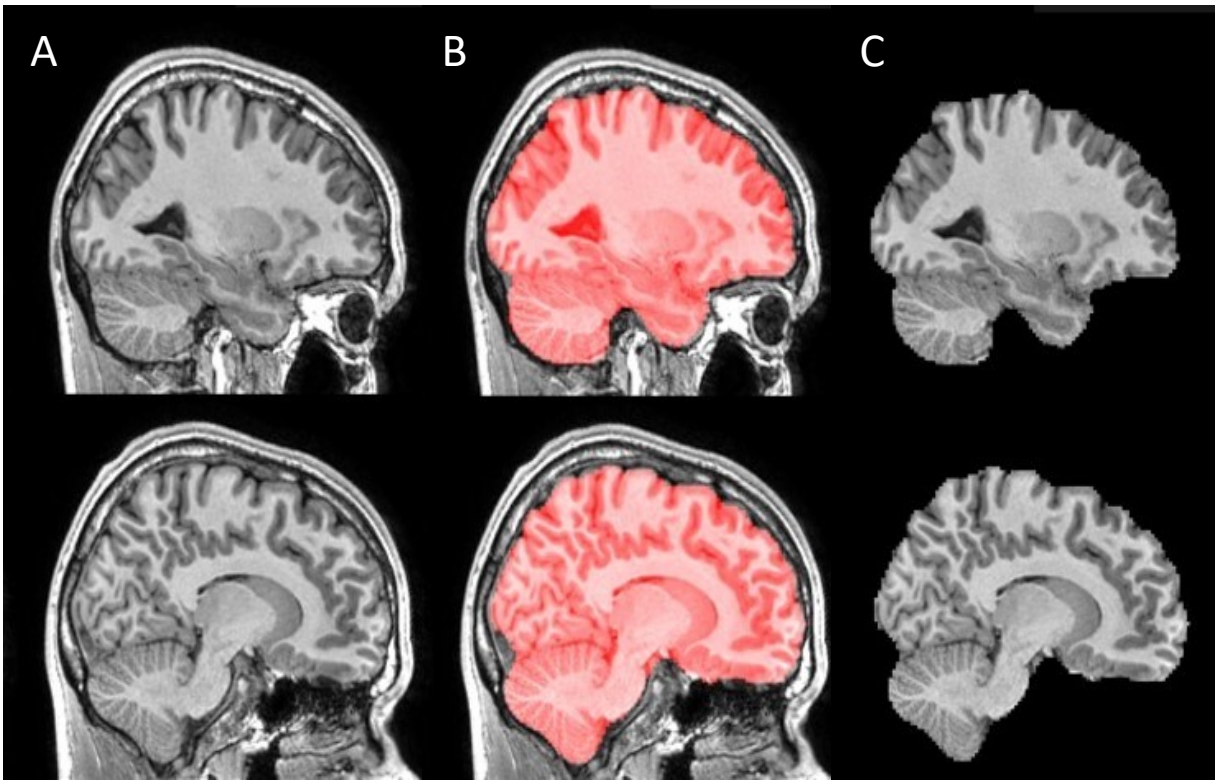

Figure 4. Example of brain extraction. Column A shows a regular MR image, column B shows the same image with the estimated brain mask overlayed in red, and column C shows the final extracted brain.

One common technique, and the one used in this work, is the brain extraction based on nonlocal patches segmentation technique (BEaST) developed by Eskildsen et al. (2012). BEaST relies on a library of segmentation priors, and it applies a label to a given voxel in the target image based on the similarity of its surrounding patch to all the patches found in the library. BEaST performs this in a multi-resolution framework, beginning with lower resolution images

and refining the results. The library of segmentation priors can be enriched by adding examples of good brain segmentations of a particular dataset, which increases the accuracy of BEaST by providing priors with patches that are likely to have more similar contrast profiles.

3 Image Registration and Brain Templates

3.1 Overview

Image registration consists of the spatial alignment of two or more images by applying a transformation, so that corresponding points of features assume the same coordinates, thus maximizing their similarity and facilitating spatial comparison. Registration is a particularly important step in neuroimaging, since it allows the analysis of shape, structure, and size of anatomical structures, as well as providing a way of performing longitudinal analyses or comparisons amongst subjects.

The origins of medical imaging registration started with the use of markers and immobilization tools so that the position of the patient could be reproducible. Unfortunately, these strategies are not useful for the registration of scans from different subjects, and are time consuming, uncomfortable, and unreliable.

Currently, image registration is achieved post-acquisition by using algorithms that estimate the optimal spatial transformation from one image (known as the “moving” image) and another image (known as the “fixed” or “target” image). We can broadly separate MRI registration algorithms into linear registration and non-linear (or non-rigid) registration. In order to facilitate processing, provide prior information, and define a common coordinate system for a set of images, it is common to perform image registration of the MR images of interest into a common template, making the creation of these templates an important area of research within the MR imaging processing community.

3.2 Linear Registration

Linear registration consists in finding a global set of parameters that maps the moving image to the fixed image. In MRI, the set of parameters typically used are rotation, translation, scaling and shear. The uses of linear transformations are numerous, ranging from multi-modality alignment, pre-processing for brain extraction, initialization for non-linear registration algorithms, and even simply to work within a standardized reference frame.

Several methods have been developed for linear registration, which can be grouped according to the feature type used, and the similarity metric used to assess the alignment. We will briefly review some of the features commonly used in linear registration:

- Point-based. They rely on the identification of a set of corresponding points in both images and minimizing the distance between them. The registration error in when using this type of feature is highly dependent on the number of points selected, n, decreasing by $1/\sqrt{n}$, as well as on the accuracy of the correspondence of the points between the two images. Point-based registration found a particular use in image-guided surgery (Hong and Hashizume, 2010; Maurer et al., 1998).
- Line-based. They rely on the identification of a set of corresponding curves in both images and minimizing the distance between them. In neuroimaging, contours of the whole brain, skull-based contours, as well as boundaries in the ventricles or other brain structures have been used as curves. Due to normal inter-subject variability in anatomy, this method can be reasonably reliable in intra-subject registration, but not in inter-subject registration. The work of Habib and Alruzouq (2004) is a general example of line-based registration for images from coming from multiple sources.
- Surface-based. Essentially a 2-dimensional version of line-based registration, where instead of curves the distance between surfaces is reduced. One famous example of this method is known as the "head and hat", proposed by Pelizzari et al. (1989), where the contours of the surface are selected on a series of slices from one image and identified as the "head", and a set of points in the other image that correspond to the same surface are identified as the "hat". The algorithm then proceeds to minimize the head-to-hat distance.
- Voxel-based. These methods operate directly on the intensity values of the images. Their biggest advantage is that they do not depend on prior data obtained by the user (such as manual point-selection) and can therefore be fully automatic.

Within voxel-based methods, the choice of similarity metric, a mathematical function that determine the distance between the transformed moving image and the target image, is very important. The mathematical definitions of some of the most common similarity metrics as described by Jenkinson et al. (2002) with the addition of cross-correlation are shown in Table 1.

Table 1. Mathematical definition of similarity metrics (Jenkinson et al., 2002). Notation: X and Y are the moving and target images as a set of intensities; μ(A) is the mean of set A; Var(A) is the variance of set A; Y_k is the intensity of image Y at voxels where the intensity of X is in the k^{th} intensity bin; n_k is the number of elements in Y_k such that $N = \sum_k n_k$; $H(X,Y) = -\sum_{ij} p_{ij} \log p_{ij}$ is the entropy function where p_{ij} is the joint probability estimated using the joint intensity histogram; H(X) and H(Y) are the marginal entropy functions.

Similarity Metric	*Formula*
Least Squares	$\sum (Y - X)^2$
Normalized Correlation	$\frac{\sum (X * Y)}{\sqrt{\sum X^2}\sqrt{\sum Y^2}}$
Woods	$\sum_k \frac{n_k}{N} \frac{\sqrt{Var(Y_k)}}{\mu(Y_k)}$
Correlation Ratio	$\frac{1}{Var(Y)} \sum_k \frac{n_k}{N} Var(Y_k)$
Mutual Information	$H(X,Y) - H(X) - H(Y)$
Normalized Mutual Information	$\frac{H(X,Y)}{H(X) + H(Y)}$
Cross-correlation	$\frac{\sum_{x=1}^{N} (Y - \mu(Y))(X - \mu(X)}{\sqrt{\sum_{x=1}^{N} Y - \mu(Y)}\sqrt{\sum_{x=1}^{N} X - \mu(X)}}$

One common feature in several linear registration is the use of a hierarchical approach. This can be done by using blurred versions of the image intensity volumes, starting by optimizing the registration the most blurred image and, once the optimal solution is found, it is used as the starting point for the next step using a less blurred volume. One example of a voxel-based technique with a hierarchical approach was proposed by Collins et al. (1994).

3.3 Non-linear Registration

As opposed to linear registration, non-linear registration is not global in nature, allowing it to model local geometric differences between images. As such, instead of estimating global parameters that align the images, non-linear registration consists in estimating a deformation field, where each voxel of the moving image undergoes a displacement that aligns it with a corresponding voxel in the target image. Non-linear registration is typically used for inter-subject registration as well as registration to a common template, where the deformations handle inherent biological variation while conserving correspondence between structures. Figure 5 shows an example of an MR image after being registered to a common template.

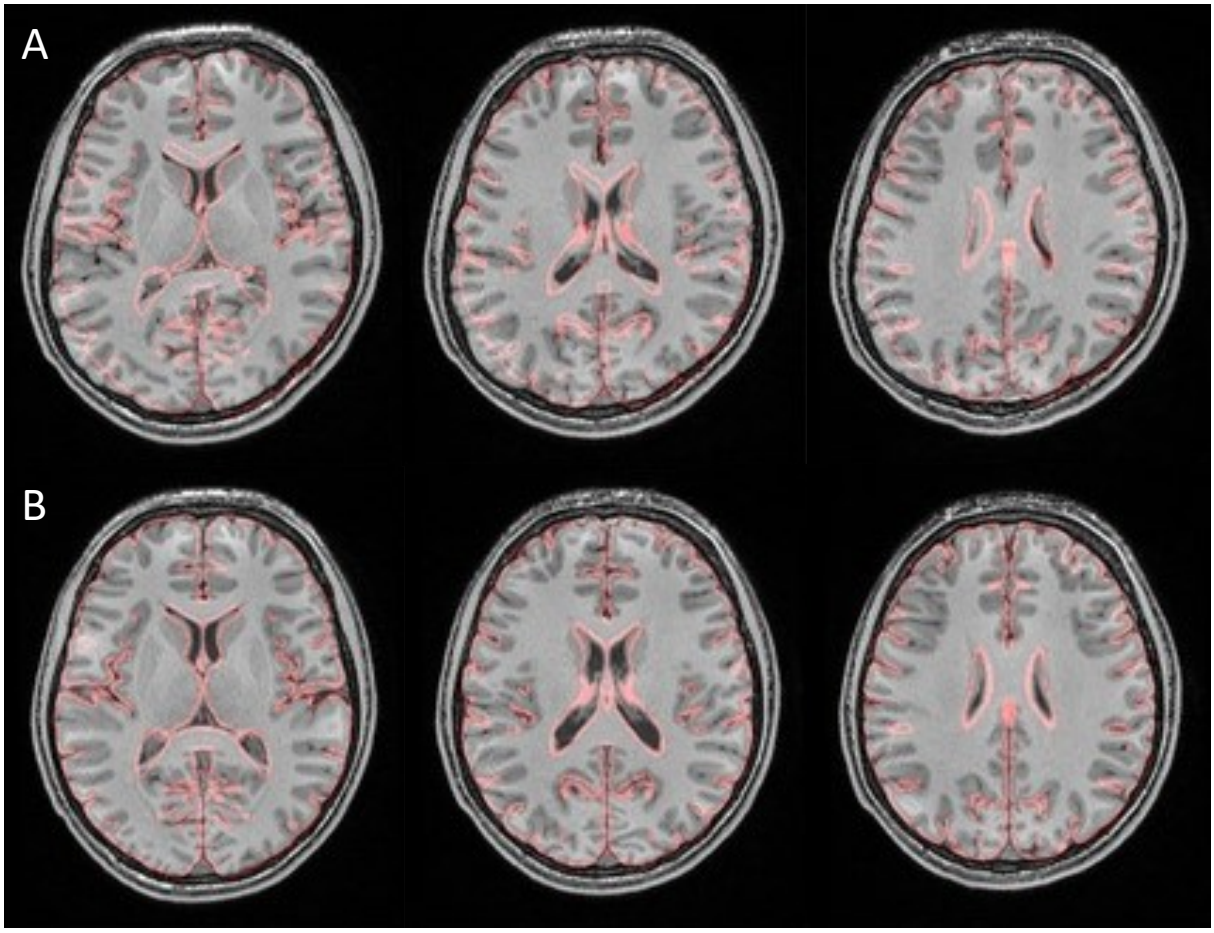

Figure 5. Example of registration to a template (ICBM152). The first row (A) shows the result of a linear registration of an MR image, with the template outline shown in red. The second row (B) shows the results after non-linear registration, again with the template outline shown in red.

In most current non-linear registration algorithms, we can find two different ways of modelling the deformation field. On one hand there are non-parametric models where the deformation at each voxel is estimated while modeling physical constraints to ensure smoothness, and on the other hand there parametrize the whole deformation field by using a set of basis functions (e.g. polynomials or B-splines).

In general, we can look at non-linear registration as an optimization problem where we optimize the transformation parameters by maximizing a similarity metric. Mathematical definitions of common similarity metrics were presented in Table 1 in the previous section. Some of the most common similarity metrics used in non-linear registration are cross-correlation and mutual information, with the latter being particularly useful in inter-modality registration due to it working with the probability distribution of intensities as opposed to the intensity values directly.

In the present thesis, two main non-linear registration algorithms, or slight modifications of them, were used: Automated Non-linear Image Matching and Anatomical Labelling (ANIMAL) (Collins et al., 1995) and the Symmetric Diffeomorphic non-linear registration (SyN) (Avants et al., 2008). Thus, these methods will now be described with more depth.

ANIMAL focuses on small neighbourhoods of the image that are selected by stepping in a 3D grid over the entire volume, where the deformation field is formed by a series of local linear deformations for each position in the grid. ANIMAL uses a hierarchical multi-scale approach, starting with a very blurred version of the volumes and subsequently reducing the blurring on each step. At each step, the deformation is recovered with a voxel spacing no greater than the Nyquist sampling limit, in this case denoted by half of the Full Width at Half Maximum (FWHM) of the blurring kernel. ANIMAL uses a similarity metric for each local neighbourhood, yielding a normalized similarity metric between the moving image and the target image as follows:

$$S(V_m, V_s; N) = \frac{1}{n}\sum_{\vec{x}\in V} R(V_m, V_s; N, \vec{x})$$

where n is the number of elements in the 3-dimensional cubic lattice that defines the deformation field, V_m is the target or model image, V_s is the moving or subject image, N is the current estimated transformation, and $R(V_m, V_s; N, \vec{x})$ is the similarity metric used for each local neighborhood of $\vec{x}$. The optimization problem is now to find the local deformation vector $\overrightarrow{d_i}$ that maximizes $R(V_m, V_s; (N + \overrightarrow{d_i}), \overrightarrow{x_i})$, but in order to ensure that the deformation field is continuous, a smoothing constraint is added as such:

$$\overrightarrow{d'} = \alpha\vec{d} + (1-\alpha)M(\vec{x})$$

where $0<\alpha<1$, allowing the user to control the level of smoothing, with values close to 0 ensuring a very smooth deformation and larger values increasing the weight of the estimated deformation vector.

The main idea behind SyN is that the use of differentiable maps with differentiable inverses, called diffeomorphisms, are able to deal with both small and large deformation problems. Additionally, SyN is a symmetric algorithm, which ensures that the end result is identical regardless of the choice of moving and target images, and provides exact inverse transformations, allowing for back and forth mapping between moving and target image. SyN allows the user to choose the preferred similarity metric, amongst them cross-correlation and mutual information. In general, this method defines a diffeomorphism ϕ which is used to transform an image V_s into the coordinate system from image V_m, and depends on parameters time t, spatial coordinate x, and velocity field v. After this, ϕ is decomposed into two parts, ϕ_1 and ϕ_2, of equivalent length that map V_s and V_m , respectively, to a mean shape between the images. The chosen similarity metric is calculated over local windows and maximized. A summary of the algorithm is given by Avants et al. (2008), as follows:

- Initialize ϕ_1 and ϕ_2 being the identity matrix.
- Compute the similarity metric.
- Compute the velocities by smoothing the result of the cross-correlation.
- Update the values of ϕ_1 and ϕ_2 by the corresponding velocity at every location.
- Calculate the inverses of ϕ_1 and ϕ_2.
- Calculate the solutions at time 1 using:

  $$\phi_1(1) = \phi_2^{-1}(\phi_1(x, 0.5), 0.5) \ \ and \ \phi_1^{-1}(1) = \phi_2(1) = \phi_1^{-1}(\phi_2(x, 0.5), 0.5)$$
- Repeat until convergence.

3.4 Brain Templates

Perhaps the first brain template to find application in neuroimaging was used by Fox et al. (1985) to register positron emission tomography images to a stereotactic atlas from a post-mortem brain image that included anatomical landmarks and labels for anatomical structures, previously devised by Talairach et al. (1967). One historically important atlas was proposed in 1988 by Talairach and Tournoux (1988). This atlas was built using photographs and drawings of a dissected brain and included labels for the Brodmann areas (Brodmann, 1909).

In order to better capture the variability of normal population anatomy, new templates have been constructed by averaging MR images. In particular, the ICBM152 template was created using the average of 152 images of healthy, young adults. The creation of the ICBM152 template involved an iterative registration procedure of the images into Talairach space, using both linear and non-linear registration.

Depending on the particular application, the use of templates created from healthy, young adults might not be ideal. One example of this is the use of templates for analyses during early childhood. Wilke et al. (2002) compared the performance of image registration of pediatric data to an adult template and a custom pediatric template. Their results show that the use of adult templates increase registration variability, so the use of age-appropriate templates is highly recommended. A comparison between different templates is shown in Figure 6.

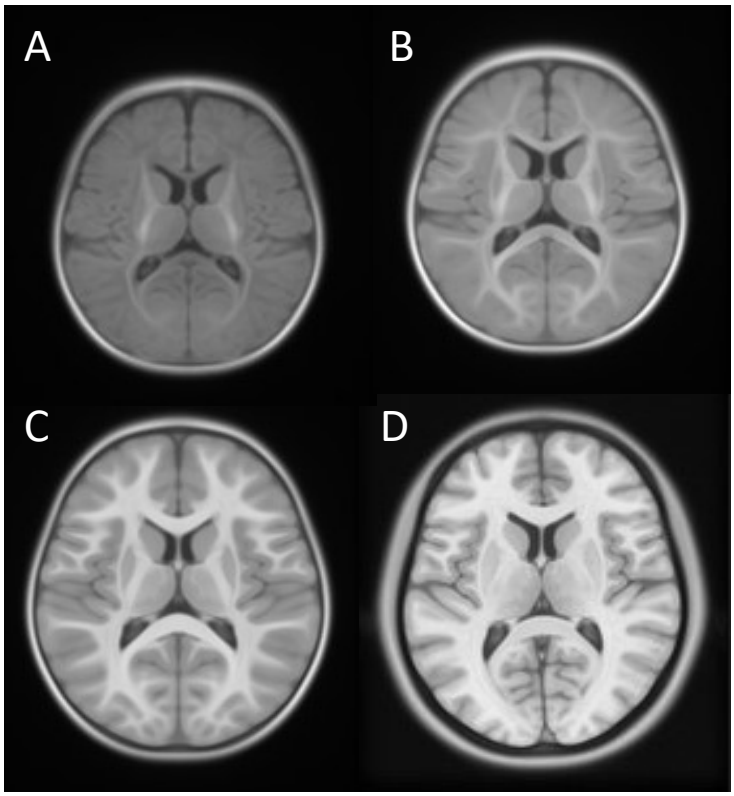

Figure 6. Comparison between different T1-weighted templates. A) Custom 3 months template, B) custom 6 months template, C) custom 2 years template, D) ICBM152 (adult) template.

One technique for the construction of age-appropriate templates was proposed by Fonov et al. (2011). In this method, all the MR images used for template construction are iteratively non-linearly registered, using the current estimation of the average template as the target image (in the first iteration, the ICBM152 template is used as the target image). Essentially, this method attempts to find a template Φ that simultaneously minimizes the intensity difference between the template and each subject's transformed image I_i, and the magnitude of the deformations $\Psi_{i,\Phi}$ that result from the non-linear registration of the template to each volume. The optimization problem is then posed as follows:

$$\Phi^* = arg\min_{\Phi}\left[\sum_{i=1}^{n}\int_{volume}\left(\Phi(v) - I_i\left(\Psi_{i,\Phi}(v)\right)\right)^2 dv\right] \quad (9)$$

$$\Phi^* = arg\min_{\Phi}\left[\sum_{i=1}^{n}\int_{volume}\left|\Psi_{i,\Phi}(v) - v\right|^2 dv\right] \quad (10)$$

Where v is a volume coordinate, $I_i(\Psi_{i,\Phi}(v))$ is the intensity in the individual images after application of the transformation $\Psi_{i,\Phi}$, and $\Phi(v)$ is the intensity of the template at location v. In practice, the algorithm interleaves the minimization of both equations for each iteration, and the algorithm stops when the root mean square magnitude of the average residual deformation vector field falls below a certain threshold.

The applications of template construction are not limited to age-appropriate or population specific templates. Average brain template construction has proven useful in the processing and analysis of longitudinal data, where a subject specific template can be created, allowing for consistency between timepoints and making the final transformations from each timepoint to the population template more consistent (Aubert-Broche et al., 2013).

4 Morphometry

4.1 Overview

Brain morphometry can be defined as the analysis of the size and shape of brain structures. The history of brain morphometry can be traced back to the late 1800s, where the study of the weight of the human brain showed differences between males and females, as well as a decrease associated with aging, and continued through the 1900s with the introduction of quantitative measures of area and volume (Haug, 1986).

With the advent of neuroimaging, we can now obtain quantitative measures of size and shape *in vivo,* allowing a large array of studies to be performed. A common morphometric approach in neuroimaging is to use measures of volume of specific brain structures or regions of interest (ROI) and compare them between subjects or groups of subjects. Some of the earliest efforts included the estimation of ventricle volume in healthy subjects (Condon et al., 1988, 1986) and comparing ventricle volumes in multiple sclerosis (Young et al., 1981). Many different tools exist to perform tissue classification and to estimate brain structure volumes. Studies designed under this paradigm typically require *a priori* hypotheses regarding which structures or ROIs are of interest. However, alternative approaches exist that are not limited to specific structures or ROIs, instead providing an assessment of morphometry on the whole brain in an exploratory voxelwise fashion. One of the first such techniques was proposed by Wright et al. (1995) by looking at the voxel-wise density of GM and WM in patients with schizophrenia.

Most of these alternative techniques rely on the deformation fields obtained from non-linear registration and include Voxel-Based Morphometry (VBM), Deformation Based Morphometry (DBM), and Tensor Based Morphometry (TBM). These three techniques rose to prominence mainly following the work of Ashburner and Friston (2000, 2004), and since then have been applied to a wide variety of studies.

4.2 Tissue Classification and Structure Segmentation

Image segmentation can be defined as the process of dividing an image into a set of semantically meaningful, homogeneous, and nonoverlapping regions with similar features (i.e. intensity, depth, color or texture) (Despotović et al., 2015). Image classification and segmentation are intrinsically connected, since segmentation implies a classification into regions, while classification will implicitly yield the segmentation of an image by labeling voxels into different groups (albeit without regard for connectivity).

In neuroimaging, the classification of MR images into white matter (WM), grey matter (GM) and cerebrospinal fluid (CSF) is a very common and useful tool for analyzing changes in the overall volumes of these tissues, allowing us to identify abnormal changes such as atrophy and overgrowth from a global brain perspective. The resulting tissue classification can also be used to perform further analyses, such as VBM, tissue density, and cortical thickness.

Besides tissue classification, the brain can also be segmented into specific anatomical structures, ranging from segmentation into lobes (i.e. frontal, parietal, occipital and temporal) to segmentation of smaller structures (e.g. hippocampus, putamen, etc.). Changes in volume and shape of some of these regions can be associated with different diseases, and if studied over time, with disease progression. An example of an MR image after tissue classification and lobe segmentation is shown in Figure 7.

Typically, manual segmentations provided by trained experts in neuroanatomy are considered the gold standard. However, manual segmentation is subject to inter-rater and intra-rater variability. One common approach to reduce inter-rater variability is to enforce a carefully defined protocol of segmentation. Additionally, inter-rater and intra-rater variability can be reduced by producing an ensemble segmentation, essentially averaging the segmentations produced by multiple experts. Unfortunately, manual segmentation is very time consuming and is usually used only in small-scale studies or as priors in fully automatic methods applied to large-scale studies.

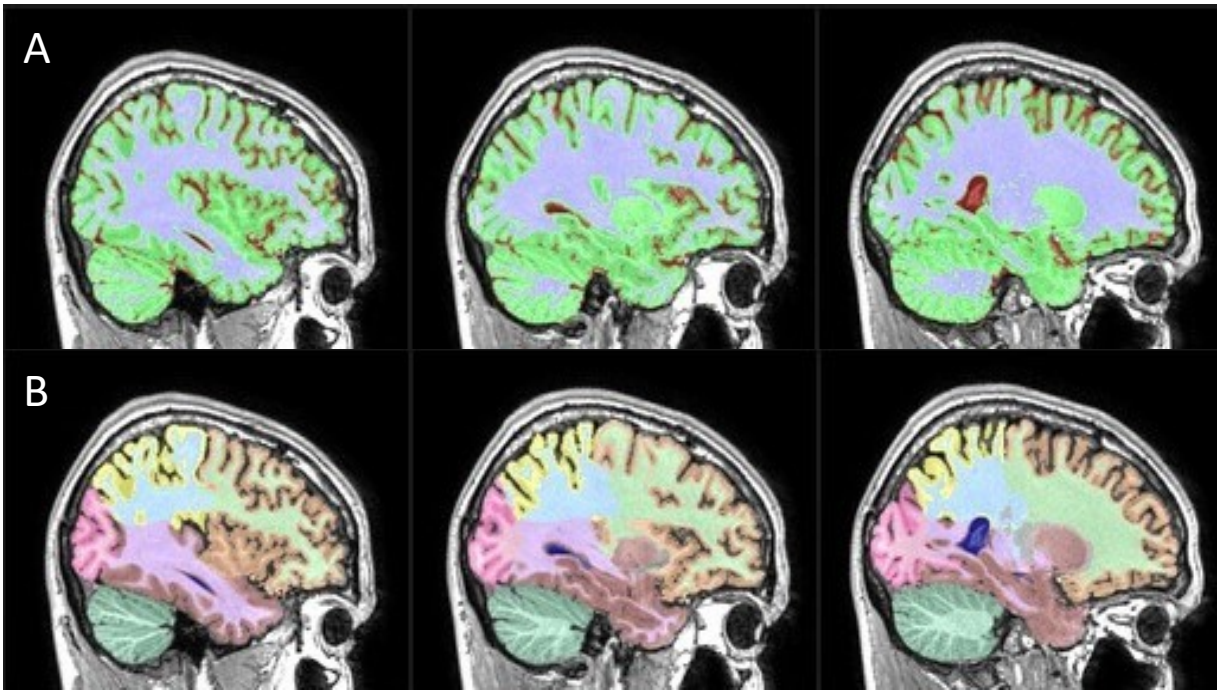

Figure 7. Examples of tissue classification (A) and lobe segmentation (B). In A, GM is shown in green, CSF in red, and WM in white. In B, the tissue classes are further segmented according to lobes (Frontal, parietal, temporal, and occipital) as well as cerebellum.

Automated image segmentation methods can be grouped in different ways. They can be categorized by whether the method requires annotated training data (supervised methods), or if they do not require annotated training data but rather are driven by directly by the data itself (unsupervised methods). An alternative categorization, and the one preferred in the present work, is the following:

- Based on the intensity value of voxels or intensity histograms (intensity-based methods).
- Based on the use of deformable models (surface-based methods).
- Based on previously segmented brain atlases (atlas-based methods).

4.2.1 Intensity-based methods

One of the simplest intensity-based methods for segmentation is thresholding. Thresholding consists on choosing an appropriate cut-off value in the image histogram that properly separates between classes (Hanson and Riseman, 1978; Lim and Pfefferbaum, 1989). An alternative method to thresholding is region growing, where a manually or automatically selected seed point is used to initialize a search of all neighbouring voxels, and if their intensities are similar enough, they are added into the growing region (del Fresno et al., 2009; Zucker, 1976).

Several classification methods, both supervised and unsupervised, can be used for intensity-based segmentation of MR-images. Some of the most common classifiers used in neuroimaging

include the k-nearest-neighbour classifier (Cocosco et al., 2003; Cover and Hart, 1967; Hellman, 1970; Warfield et al., 2000) and Bayesian classifiers, typically using the expectation-maximization algorithm (Ashburner and Friston, 2005; Fischl et al., 2002). Bayesian classifiers can also incorporate additional spatial context, particularly with the use of Markov random fields (Van Leemput et al., 1999; Zhang et al., 2001).

Additionally, clustering methods can be used as an unsupervised approach to segment images. The two most common clustering methods used in neuroimaging segmentation are the fuzzy C-means clustering (Ahmed et al., 2002; Chen and Zhang, 2004), and the expectation-maximization method (Liang et al., 1994).

4.2.2 Surface-based methods

Within the field of image segmentation, surface-based methods refer to the use of deformable models that are shaped in order to fit the desired object. These methods define a deformable model by parametric curves (2-dimensional case) or surfaces (3-dimensional case) which are deformed by the application of external "forces" derived from the image features and internal "forces" that enforce surface regularity. The external "forces" can be related to gradient-based edge information, region based information, or a combination of both (Despotović et al., 2015; Kass et al., 1988).

Although surface-based methods have been successfully applied to MR imaging segmentation (Albert Huang et al., 2009; Chunming Li et al., 2011; Mesejo et al., 2015), they have not garnered the same popularity as intensity-based and atlas-based methods.

4.2.3 Atlas-based methods

In atlas-based segmentation, the information contained in a previously segmented brain atlas or set of atlases is used to inform the segmentation of a new MR image. The actual segmentation is achieved by propagating the labels of the atlas(es) to the new image, assuming the correspondence across the brain structures (Bajcsy, 2003; Cabezas et al., 2011; Christensen et al., 1994; Gee et al., 1993).

The simplest case of atlas-based segmentation consists in using the transformation obtained from non-linear registration of the new image to an atlas. Subsequently, the inverse of this transformation is used to warp and resample the labels from the atlas, effectively mapping the labels onto the new image (Collins et al., 1995). The same idea can be applied when using a set of atlases instead of a single atlas, in which case the resampled labels from each atlas need to be combined in order to obtain a single, final label. This can be done by simple majority vote, or by assigning a voting weight to each atlas. The voting weights can be assigned from

similarity between the registered image and atlas, either globally (Heckemann et al., 2006), or locally (Artaechevarria et al., 2009; Hongzhi Wang et al., 2013).

Since non-linear registration is computationally expensive, non-local patch-based techniques have been proposed for multi-atlas segmentations. These techniques essentially consider multiple candidate patches from each atlas, making the final segmentation less sensitive to image misregistration, and allowing the use of less computationally expensive linear registrations to be used (Coupé et al., 2011; Rousseau et al., 2011).

4.3 Voxel Based Morphometry

In general, VBM is a technique that focuses on finding differences in the local concentration of brain tissue (GM or WM) while accounting for structure and shape differences. VBM performs this comparison voxelwise and results in a statistical parametric map of volume differences. The first step when performing VBM involves the non-linear registration of MR images to a common template. The next step consists in tissue classification, labeling each voxel as WM, GM or CSF. Afterwards, the segmented tissue maps are smoothed by convolving them with an isotropic Gaussian filter. Smoothing with the Gaussian filter helps to compensate for inexactitudes that arise from the spatial normalization step as well as making the data more normally distributed.

One optional step can be incorporated after the tissue classification, modulating the segmented images with the Jacobian determinants of the deformation field. This can be useful since, by multiplying the segmented tissue maps by the relative voxel volumes, VBM goes from comparing relative local concentration of tissue to comparing the absolute amounts of tissue density in the different regions.

Finally, a set of voxelwise statistical tests are done on the smoothed tissue maps. A variety of statistical tests can be used in VBM, including general linear models, general linear mixed-effects models, and ANOVA, among others. These tests will result in statistical parametric maps that provide values at each tested voxel. An example of a parametric map resulting from TBM can be seen in Figure 8, where the t-values resulting of a voxel-wise group comparison are shown. As such, these maps encompass the results of numerous statistical tests, and a correction for multiple comparisons is required for interpretation. Some of the commonly used multiple comparisons corrections in VBM include Gaussian random fields (Worsley et al., 1996), Bonferroni corrections (Holland and Copenhaver, 1987; Holm, 1979), and False Discovery Rate controls (Benjamini and Hochberg, 1995).

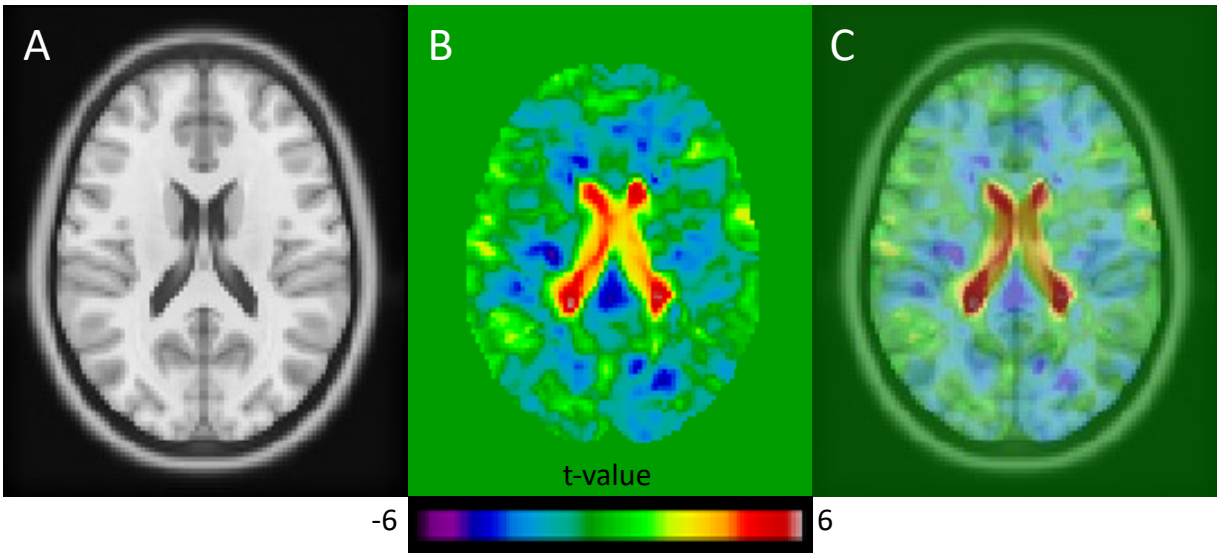

Figure 8. Example of a statistical parametric map. A) The ICBM152 template, B) is a map showing the t-values at each voxel for a linear regression test, C) is the overlay of both images, showing the highest t-values in the lateral ventricles.

The accuracy of VBM relies heavily on the performance of the non-linear registration and of the tissue classification. In addition, the choice of reference template is very important to avoid the introduction of bias to the VBM results, and it is recommended to use templates created with a large number of MR images, that are age-appropriate and, if possible, that come from the same cohort to be studied, this is known as "optimized" VBM (Good et al., 2001). In the case of tissue classification performance, VBM can become unreliable when applied to populations where tissue classification is not ideal. This is the case for example of MR images acquired during early childhood, where the contrast between GM and WM is not enough to reliably perform tissue classification with most automatic methods.

4.4 Deformation Based Morphometry

As opposed to VBM, DBM does not use the information of tissue classification, but rather depends only on the deformation fields of the non-linear registration to the reference template. One way to interpret these deformation fields is as vectors pointing from the coordinates of the reference template to the corresponding coordinates in the native image. This vector representation can be seen in Figure 9. Therefore, the parameters at each voxel of the deformation field contain the coordinates of the corresponding structure in the native image. DBM consists in taking these coordinates and comparing the relative position of structures in the images of different subjects or groups. This is possible because, in essence, the shape of an object is defined by the relative positions of each of its components.

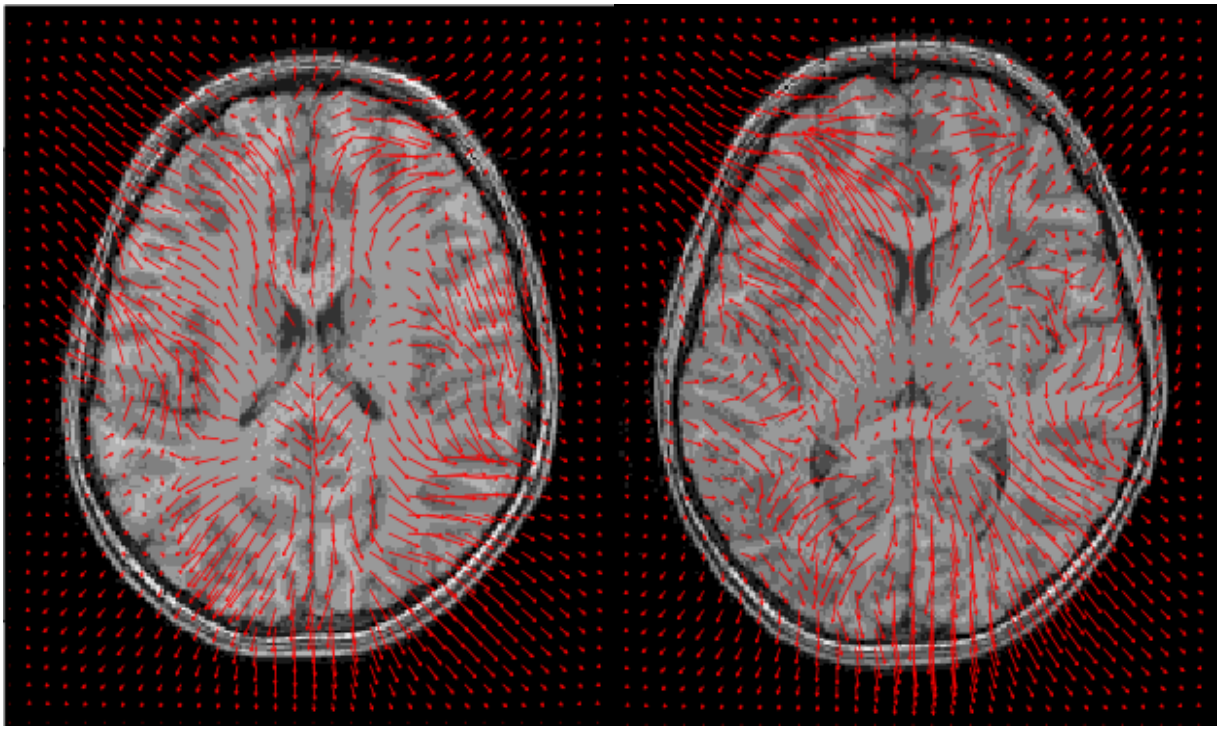

Figure 9. Visual representation of a deformation field as a set of vectors. Each vector essentially points to the corresponding point in the template. The size of the vectors is enlarged for visualization purposes.

In DBM, singular value decomposition is applied to the deformation fields, yielding different components related to global position, orientation and size, as well as a shape component (i.e. the component describing relative position of structures). Once we have decomposed the deformation fields, we can apply a multi-variate statistical test, usually multi-variate analysis of variance (MANCOVA). When DBM is applied globally, it does not provide a statistical parametric map, but rather a single p value for each of the explanatory variables (e.g. age, diagnosis, etc.).

As previously mentioned, the deformation fields contain more information than just the relative position of structures. The position, orientation and size information encoded in the deformation fields can be incorporated into a more complex analysis known as TBM, where information on local shape can be extracted and analyzed on a voxel-by-voxel basis. It is important to note that the definition of DBM presented in this subsection follows the definition given by Ashburner and Friston (2004), however, the term DBM is commonly used in the literature when referring to TBM, as described in the following subsection.

4.5 Tensor Based Morphometry

Briefly, TBM consists on using the information contained in the deformation fields from a non-linear registration to perform a voxelwise comparison of the relative volumes of different subjects or groups. The first step in TBM is to non-linearly register all the MR images of interest

to a common reference template. The second step consists in the extraction of the information contained in the deformation fields obtained from the first step. By far the most common way to obtain a metric that reliably describes local brain shape is the calculation of the Jacobian matrix of the deformation field (i.e. the matrix of all the first-order partial derivatives of the deformation field).

These Jacobian matrices contain information describing the local stretching, rotation, and shearing caused by the non-linear deformation. One possible approach is to use the full information of the Jacobian matrix to perform statistical comparisons. In order to do this, it is necessary to remove the information related to orientation encoded in the Jacobian matrix so that inferences are based only on changes in local stretching and shearing. This can be achieved by using the polar decomposition theorem to decompose the Jacobian matrix into a rotation matrix and a Lagrangian strain tensor. In the next step, a desirable metric that can be used to compare between tensors is required. This poses a complicated mathematical challenge, with different methods including Log-Euclidian metrics (Lepore et al., 2008) and eigen decomposition (Rajagopalan et al., 2015). Finally, we can apply a multi-variate test, typically Hotelling's T^2 test, to obtain a statistical parametric map.

A simpler, more common TBM technique, consists in calculating the determinant of the Jacobian matrix. By doing this, we obtain a single, meaningful metric that describes the local volume change of each voxel in the template when compared to the corresponding voxel in the native image. The Jacobian determinant metric is typically log-transformed in order to better prepare the data for subsequent parametric tests that have assumptions about data normality, as well as providing symmetry in the interpretation of the results. A value of 0 in the log-transformed Jacobian determinant indicates no difference in local volume, a value larger than 0 indicates expansion, and a value smaller than 0 indicates contraction. Figure 10 shows an example of a log-transformed Jacobian map, where each voxel represents the local contraction or expansion of a template to an individual subject's brain, according to their non-linear registration. Finally, voxelwise statistical tests are applied to the log-transformed Jacobian

determinants. Examples of these tests include the use of generalized linear models or linear mixed-effects models.

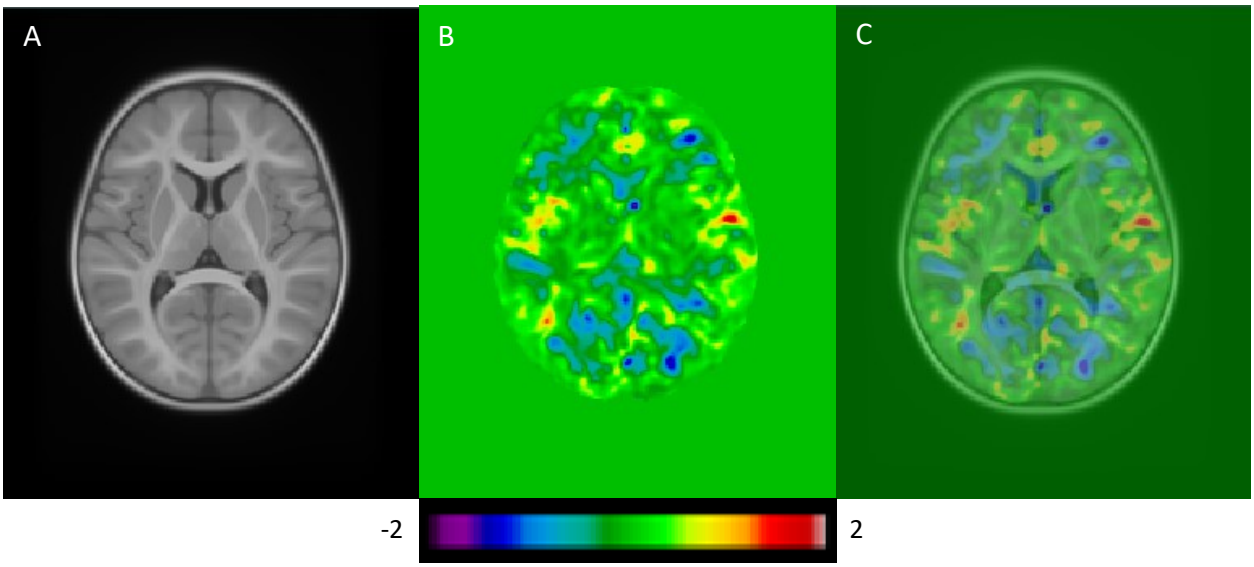

Figure 10. An example of a log-transformed Jacobian Determinant map. A) Custom 12 month old pediatric template, B) log-transformed Jacobian of single subject mapped to template, where values above 0 denote larger volume expansion, while values below 0 denote volume reduction when compared to the template, C) overlay of both images.

5 Statistical Tools

5.1 Linear Regression Models

Linear Regression is a common statistical method used to analyze the relationship between a response variable and a set of one or more factors (or explanatory variables). The inherent assumptions behind linear regression are simple:

- There is a linear relationship between the response variable and the explanatory variable(s).
- The errors of the response variable are uncorrelated.
- The response variable follows the normal distribution.

Formally, linear models are described as follows:

$$y = \beta X + \varepsilon \tag{11}$$

where y represents the vector of measurements of the response variable, β represents the vector of unknown regression coefficients, X is the matrix of explanatory variables, and ε is the vector of errors. Perhaps the most common way of obtaining estimates of the regression coefficients is the least-squares approach, which consists in finding a line that minimizes the sum of squared

residuals (i.e. the differences between the measured values and the predicted values of the response variable).

In cases where the assumption of the normal distribution of the response variable is not valid, or when the data is discrete, a simple linear regression cannot be used. For those cases, Generalized Linear Models were first proposed by Nelder and Wedderburn (1972), with some further extensions developed by McCullagh and Nelder (1989). Generalized Linear Models differ from traditional regression by assuming that the response variable follows an exponential family distribution.

Linear Regression and Generalized Linear Models are well suited for many cross-sectional studies, longitudinal studies that involve repeated measures over time of the same subject often require a way of accounting for within-subject correlations. As such, a different class of models, known as Linear Mixed-effects Models (Laird and Ware, 1982), are better suited for longitudinal applications.

5.2 Linear Mixed-effects Models

Linear Mixed Effects Models (LMEM) are class of statistical parametric regression models obtained by the introduction of random effects into a Linear Regression model. These random effects are parameters that are themselves random variables and can be used to account for intra-subject variability, as well as different situations that arise from a hierarchical structure.

Formally, the LMEM is described as follows:

$$y = \beta X + bZ + \varepsilon \tag{12}$$

where y represents the vector of measurements of the response variable, β represents the vector of unknown regression coefficients, X is the matrix of explanatory variables, Z is the matrix of random effects, b is the vector of random effects, and ε is the vector of errors.

In general, LMEM techniques estimate the unknown parameters β using a maximum likelihood approach, typically based on the maximum likelihood method or the restricted maximum likelihood method. The most common algorithm used in LMEM is the expectation-maximization (EM) algorithm, an iterative process that alternates between the E-step, a computation of the conditional expectation of the data given the current estimated parameters, and the M-step, the estimation of the parameters given the current estimated incomplete data by maximizing the conditional expectation. The use of maximum likelihood methods in LMEM allow the use of unbalanced data. Unbalanced data is a common problem in neuroimaging

studies, since missing data for a given timepoint can happen due to acquisition problems, imperfect timing or subject dropout. LMEM deals with this problem by weighting the parameter estimations based on the number of observations.

In 2013, Bernal-Rusiel et al. (Bernal-Rusiel et al., 2013) performed an objective comparison between LMEM, repeated measures ANOVA, and cross-sectional analysis of the slope in the context of neuroimaging studies. Their results suggest that LMEM provides better statistical power for detecting longitudinal group differences and provides a better overall framework for studies where inter-subject variability is important.

5.3 Multiple Comparisons Correction

Once a particular statistical model is chosen, we need to establish a way to determine if there is a significant difference between subjects or groups, as well as if the relationship between variables is statistically significant. This is done by defining a null hypothesis H_0 stating no difference between groups exists (or here is no relationship between variables), and an alternative hypothesis H_1 stating that the difference exists (or there is a relationship between variables). We can now calculate the probability of observing a result at least as extreme as the observed test statistic assuming H_0 is true, known as the p-value, and define a significance level α, which is the probability of incorrectly rejecting H_0. If the p-value is less than or equal to α, we reject H_0 in favor of H_1. Typical values for α include 0.1, 0.05 and 0.01. The selection of α largely depends on the field of study, study design, and specific question, and essentially represents the maximum tolerable exposure to erroneously rejecting H_0 for a given study. In neuroscience, α often is set at 0.05.

In the field of neuroimaging, it is unlikely that a study makes a single hypothesis comparison as described above, but rather a family of simultaneous tests are performed. For example, when using morphometric techniques such as VBM and TBM, hypothesis testing occurs at each voxel, which leads to a large susceptibility to false-positive results due to random chance, making classic theoretical thresholds for the individual tests unreliable. Dealing with this problem is known as multiple comparison correction.

Numerous methods of multiple comparison correction have been developed. A well-known, popular approach for multiple comparison correction is the Bonferroni correction (Bonferroni, 1936), where the nominal significance level α is replaced by the level α/k, where k is the number of tests being performed. The Bonferroni correction is known to be very effective in controlling for false discoveries, however, it is generally considered very

conservative, and in cases where hundreds of thousands of comparisons are involved it can lead to true positives not surviving the resulting threshold.

One alternative for the Bonferroni correction for use in neuroimaging was proposed by Worsley et al. (1999). The method, known as Gaussian Random Field Theory, is based on the Bonferroni correction, but instead of assuming independence of all voxels within a volume, only resels (resolution elements, essentially a group of voxels) are independent. This approach essentially reduces the value of *k* and works well in data where spatial correlation of neighbours is a fair assumption. The use of this method provides corrected p-values for local maxima as well as for cluster size, commonly known as peak and cluster threshold respectively.

Another alternative was proposed by Benjamini and Hochberg (1995), where instead of controlling the false positives for all tests regardless of rejection, the idea is to control the expected proportion of errors in the accepted hypotheses, the False Discovery Rate (FDR). One way of applying FDR control in neuroimaging studies was proposed by Genovese et al. (2002), it is based on the procedures previously described by Benjamini and Hochberg (1995), and Benajmini and Yekutieli (2001). This method is used as the basis for the mathematics presented in this sub-section.

In a voxelwise neuroimaging analysis, let V denote the total number of voxels, and each voxel will be classified as a true positive, a true negative, a false positive, or a false negative. If we let V_{TP} be the number of true positives, V_{TN} the number of true negatives, V_{FP} the number of false positives, and V_{FN} the number of false negatives, the FDR is defined as:

$$FDR = \frac{V_{FP}}{V_{TP} + V_{FP}} \tag{13}$$

The FDR is controlled by specifying a rate q between 0 and 1 and ensuring that, on average, the FDR is equal to or smaller than q. We can then express the control of the FDR as follows:

$$E(FDR) \leq \frac{V_{TN} + V_{FP}}{V} q \leq q \tag{14}$$

where E(FDR) is the expected value of the FDR.

Therefore, we can summarize the FDR controlling procedure as follows:

- Selection of q.
- Ordering from smallest to largest of the P values resulting from the hypothesis testing, letting i represent the index in the ordered P values.

- Choose an appropriate value for the constant c(V). The options are c(V)= 1 in the case of the P values being independent or positive dependent, or c(V)=$\sum_{i=1}^{V} 1/i$ for any joint distribution of the P values.
- Let r be the largest i that fulfills:

$$P_{(i)} \leq \frac{i}{V}\frac{q}{c(V)} \tag{15}$$

- The value corresponding to the P value $P_{(r)}$ denotes the desired threshold.

FDR control is popular amongst neuroimaging studies, and it has been applied to a variety of data, including fMRI (Fransson, 2005), cortical thickness (Shaw et al., 2006) and longitudinal TBM (Lau et al., 2008).

6 Childhood and Adolescence Neurodevelopment

6.1 Overview

During the course of life, the human brain undergoes a constant change and adaptation process. However, it is during the pre-natal, peri-natal and childhood developmental phases that it experiences the most dramatic and significant changes, perhaps shaping the majority of the potential and vulnerabilities inherent to a person. Therefore, understanding the process of neurodevelopment is a very important step in our overall comprehension of the human brain. Additionally, many diseases and disorders that affect the brain can be traced back to this critical neurodevelopmental period.

The study of brain development is a complex, multidisciplinary affair, since the processes that are involved are varied, including gene expression, environmental factors, and the interaction between them (Stiles and Jernigan, 2010). Before the advent of MR imaging in neuroscience, early histological studies like the ones performed by Yakovlev and Lecours (1967), and Huttenlocher (1979), showed the progression of myelination as well as synaptic proliferation and pruning in different areas of the brain. Perhaps some of the first studies of brain development using MR imaging were performed by Jernigan et al. (1991; 1990), using simple morphometric techniques to observe *in vivo* the changes in GM and WM volumes in the different cerebral lobes of children. As the field of MR imaging has advanced, our understanding on the timing and characteristics of brain maturation has expanded accordingly (Toga et al., 2006).

In light of all these changes occurring in the brain during childhood, pediatric studies of diseases and disorders pose a particular problem in neuroimaging, since it is important to account for the normal maturation of the brain when performing these studies (Giedd and Rapoport, 2010; Marsh et al., 2008; Mills et al., 2016). In the present section we will briefly summarize some of the normal neurodevelopmental changes during childhood and adolescence, as well as the challenges they present for neuroimaging studies.

6.2 First 2 years of life

The first two years of life are marked by stark changes in brain structure and function, with the brain growing to about 70% of the expected adult size in the first year and to about 80% by the end of the second year of life (Tau and Peterson, 2010). At birth, the majority of the production and migration of neurons has already occurred, however, some degree of proliferation and migration of glial progenitors still happens during early postnatal life, with the differentiation and maturation of these cells an ongoing process throughout childhood (Stiles and Jernigan, 2010). The main maturation processes that occur during can be categorized as proliferation and migration, myelination, and regressive events.

Proliferation and migration of neurons after birth occurs almost exclusively on small amounts of neurogenesis in the subventricular zone with migration to the olfactory bulb, and neurogenesis in the hippocampus with migration to the nearby granular layer. These cases of neurogenesis are not exclusive of early life, but rather seem to continue during the whole lifespan. On the other hand, proliferation and migration of glial progenitors is an active process during early childhood, with glial progenitors proliferating in subventricular zone of the forebrain before migrating into WM, cortex, striatum, and hippocampus, finally differentiating into oligodendrocytes and astrocytes (Stiles and Jernigan, 2010).

The differentiation of glial progenitors into oligodendrocytes leads to the process of myelination during early childhood. The oligodendrocytes progenitor cells increase myelin protein expression and start forming membrane wraps around nearby axons while extruding a part of the cytoplasm. This process results in the formation of the multi-layered myelin sheath around axons, which is known to increase axonal conduction velocity.

Due to the human brain development following a strategy of overproduction of neurons, glial cells, neural processes, and synapses, part of brain maturation consists of culling these excesses by what are known as regressive events. During the first two years of life, two types of regressive events happen in the brain, glial cell death and pruning. Glial cell death occurs during the myelination process, with the cellular death of numerous oligodendrocytes signalled

by nearby axons, in order for the number of surviving oligodendrocytes to match the axonal surface area. During this period, there is a marked overabundance of connections in the brain, known as synaptic exuberance. As the brain develops, there is a systematic elimination of the excess connections known as pruning. It is particularly interesting that the exuberance and pruning effects can be observed both at a macroscopic level within brain regions on a timescale of months, as well as at a microscopic level of individual neurons on a timescale of minutes.

In summary, brain development during the first two years of life includes dramatic brain growth primarily driven by the production of glial cells and myelination of axons, rather than neurogenesis. In addition, this developmental period features a fundamental development of GM connections, in particular in sensorimotor and visual cortices (Tau and Peterson, 2010).

6.3 Childhood and Adolescence

After two years of age, the rate of growth of the brain slows down significantly, with the brain growing only from 80% of its expected adult size at two years of age to 90% at five years of age, with cortical GM volume increasing up to 4 or 5 years of age (Tau and Peterson, 2010). During this period, myelination, synaptic formation, and pruning are the main maturation processes. The time-course of synaptic formation and pruning is particularly interesting during this period, with synaptic density peaking first in sensory areas, then association areas, followed by higher cognition areas, such as the prefrontal cortex. The rate of WM volume increase is still high during this period, with myelination still an important driving force. Overall, the relatively slower growth rate during this period can be explained by a decrease in synaptic formation with a simultaneous increase in pruning, thus slowing the overall growth.

After five years of age, cortical GM volume begins to decline, first in dorsal parietal and primary sensorimotor areas between 5-8 years of age, followed by spatial orientation and language areas between 11-13 years of age, and finally higher cognition areas in late adolescence. This decline in GM volume has been corroborated in animal and post-mortem histological data, as well as morphometric MR imaging studies and cortical thickness measurements (Tau and Peterson, 2010; Toga et al., 2006). Furthermore, the myelination process does not stop at 5 years of age, but rather it continues all throughout childhood and adolescence. Due to this process, there is a constant increase in WM volume.

Perhaps the most notable changes occurring in the brain during adolescence are found in the prefrontal cortex. The prefrontal cortex experiences synaptic proliferation at puberty, followed by pruning a reorganization of synaptic connections during late adolescence, leading to a net decrease in synaptic density in the prefrontal cortex by adulthood (Choudhury et al., 2008). It

is also important to note that, due to major hormonal and physiological changes, the peak GM volume in the frontal lobe occurs at around 11 years for girls and 12 years for boys, with the parietal GM volumes peaking around 10 years for girls and 12 years for boys. It is therefore very important to account for sex-based differences in development during puberty and adolescence (Mills et al., 2016).

6.4 Myelination and Contrast Changes

As previously described in subsection 6.2, one of the main changes that occurs during the first 2 years of life is the myelination of WM, playing a critical role in the facilitation of the transmission of nerve impulses travelling through the axons of neurons across the nervous system.

MR imaging studies during early childhood are particularly susceptive to changes in myelination, as shown in 1988 by Barkovich et al. (1988). Particularly, this study showed that differences in contrast due to myelination in T1 and T2-weighted scans have slightly different time-courses. At birth, a T1-weighted scan of the brain will show lower intensities in WM than in GM (the opposite than an adult brain), and as the brain mature there is a reversal in contrast during the first 6-8 months of life. A similar reversal of contrast occurs in T2-weighted images, with GM showing lower intensities than WM in neonates and the reversal occurring after 6 months. Figure 11 shows changes in contrast during the first year of life.

In general, changes in MR imaging due to myelination are observed earlier in T_1-weighted images than in T_2-weighted images. One of the possible explanations for the reversal in contrast and the difference in time-course between modalities was proposed by Barkovich et al. (1988) and later supported by Takeda et al. (1997). In the case of changes in T1-weighted imaging, the proportions of cholesterol and glycolipids that are part of the outer layer of the myelin membrane increase during the first 6-8 months of development, leading to a shortening of the T_1 relaxation. In the case of changes in T2-weighted imaging, the inner layer of myelin becomes hydrophobic during development, decreasing the amount of free water molecules thus affecting the T_2 relaxation.

The general pattern of myelination in the brain has been observed in several MRI studies (Barkovich et al., 1988; Bird et al., 1989; Christophe et al., 1990; Dietrich et al., 1988; Hayakawa et al., 1991), and can be described as follows:

- Myelination of the pons and cerebellar peduncles by birth.
- Myelination of the posterior limb of the internal capsule, the optic radiation and the splenium of the corpus callosum between 1-3 months of age.

- Myelination of the anterior limb of the internal capsule and genu of the corpus callosum around 6 months of age.

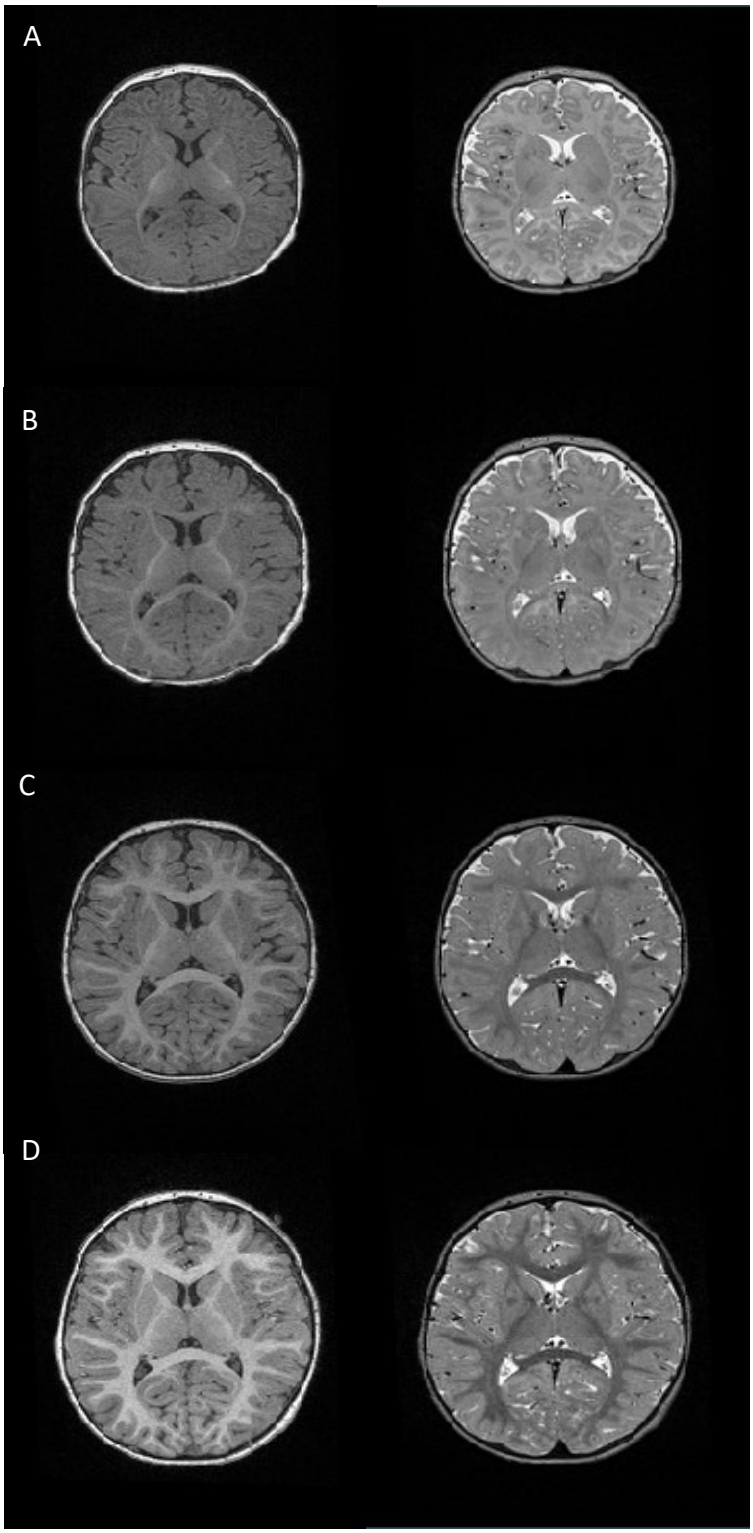

Figure 11. Contrast changes due to myelination in the first 2 years of life. A) 3 months, B) 6 months, C) 12 months, and D) 24 months of age. The left column shows T1-weighted images, while the right column shows T2-weighted images.

These changes in contrast during early childhood have a big impact in the accuracy of neuroimaging tools. In particular, MR images acquired around 6 months of age will show very little contrast between GM and WM, making tissue classification a very complex problem at this age. In recent years several efforts of performing robust, accurate tissue classification and brain segmentation have been done, particularly using atlas-based techniques (Kuklisova-Murgasova et al., 2011; Prastawa et al., 2005; Weisenfeld and Warfield, 2004). These techniques typically separate the common WM label into 2 separate classes, unmyelinated WM and myelinated WM. Methods that rely on accurate tissue classification or where having two distinct classes for WM affect their working, such as VBM, are not well suited for application in morphometric studies during early childhood without special considerations. However, one can easily adapt methods that do not rely on tissue classification, such as TBM, to work within this time period, as long as accurate, age-appropriate templates with the corresponding contrast profile are used.

6.5 Genetics and Neurodevelopment

Due to the prevalence of neurodevelopmental disorders, such as ASD, intellectual disability, and attention deficit hyperactivity disorder, among others, it has become particularly important to understand the role of genetics in neurodevelopment. Normal neurodevelopment can be affected by different types of genetic mutations, including chromosomal rearrangements, copy number variants (CNVs), small indels, and nucleotide substitutions (Cardoso et al., 2019). Most evidence points towards these mutations mainly affecting biological pathways of synaptogenesis, chromatin remodelling, cell proliferation, and cell differentiation (Berryer et al., 2016; Cardoso et al., 2019; Clement et al., 2012).

Unfortunately, understanding the specifics in which genetics and neurodevelopmental disorders are related is a highly complex task, with over 1000 loci potentially involved (Shashi et al., 2014). Furthermore, the heterogeneity of neurodevelopmental disorders, including the existence of syndromic (e.g. Rett syndrome) and non syndromic variants, as well as comorbidity between different neurodevelopmental disorders and with other diseases, complicate these studies (Tărlungeanu and Novarino, 2018). One potential avenue to study the effects of genetics in neurodevelopment is the “genetics first approach”, where the study itself focuses on the effects of a particular mutation (e.g. a CNV in a specific locus) in neurodevelopment, as opposed to focusing on a neurodevelopmental disorder and studying their genetics *post hoc*.

6.6 Morphometry during Early Childhood

The first use of MR images in the study of early childhood focused on analysing the patterns of myelination, rather than growth patterns. As such, many of these studies did not use any particular morphometric techniques, but rather relied in qualitative descriptions of changes in contrast of GM and WM, as well as differences in the timing of observations between T1 and T2-weighted images, to track the progress of myelination in the infant brain (Barkovich et al., 1988; Bird et al., 1989; Christophe et al., 1990; Dietrich et al., 1988; Hayakawa et al., 1991; Martin et al., 1988; McArdle et al., 1987). Perhaps the first attempt at morphometry in early childhood was a study by Barkovich and Kjos (1988), where measurements of thickness and length of the corpus callosum, and reported significant increase in thickness all over, particularly in the splenium between 4-6 months of age.

In 2001, a study by Matsuzawa et al. (2001) set out to investigate the volumetric changes that occur during normal development in early childhood. In their study, they used linear regression on the volumes of GM, WM and CSF obtained using manual segmentation into tissue classes and lobes of 13 children aged 1 month to 2 years. Their results showed that both GM and WM increase during the first 2 years of life, with particularly larger increases in frontal and temporal lobes. In 2008 a similar study was conducted by Knickmeyer et al. (2008) using a larger database of normally developing children (98 children), and automatic tissue classification tools. With a larger number of subjects, they were able to model the volumetric changes of total brain volume, volume of cortical hemispheres, cerebellum, and subcortical and brainstem, in addition to the overall growth trajectories of GM and WM. Some highlights from this study includes the observation of a 240% increase in the size of cerebellum during the first year of life, as well as the observation that, while both GM and WM are increasing, GM has a larger growth rate during the first 2 years of life.

Additional volumetric studies have focused on observing the growth patterns of more specific regions (e.g. deep nuclei, hippocampi, lateral ventricles) by using more advanced brain segmentation techniques (Bompard et al., 2014; Choe et al., 2013; Gilmore et al., 2012). Other morphometric techniques have been rarely used, including DBM (Aljabar et al., 2008) and finite strain (Kim et al., 2016).

6.7 Morphometry during Late Childhood and Adolescence

The characterization of developmental trajectories during childhood and adolescence is an important field of research, not only for the understanding of normal neurodevelopment, but

also as a basis to look for potential abnormalities associated with a variety of disorders and diseases. Early morphometric studies using MR imaging showed that GM volumes in children were considerably larger than in adults, as well as overall estimates of brain growth during childhood (Caviness et al., 1996; Jernigan et al., 1991; Pfefferbaum et al., 1994; Reiss et al., 1996). These early studies were inconsistent in the selection of a "childhood" age range, with some studies covering a large age range (3 months to 30 years) (Pfefferbaum et al., 1994) while others focused on a specific time period (7 to 11 years of age) (Caviness et al., 1996). Moreover, these first studies consisted of cross-sectional MR imaging data that could not look at the growth trajectories of individuals.

In 1999, Giedd et al. (1999) performed landmark brain development study using longitudinal MR imaging of 145 healthy subjects, scanned up to 5 times at two-year intervals, from 4 to 20 years of age. The study used a hybrid tissue classification technique, mixing an intensity-based classification with an atlas-based approach, in order to obtain morphometric volumes of GM and WM for the frontal, parietal, temporal and occipital lobes. Their study showed linear increases in WM volume with nonlinear, regionally specific changes in GM volume. Around the same time, Sowell et al. (1999) used a contrast of average grey matter differences, a precursor of VBM, to explore localized changes between childhood and adolescence, with their findings being consistent with the pattern and distribution of changes found in earlier volumetric studies.

More recently, the interest in the analysis of large, longitudinal data during childhood has increased, leading to the acquisition of large, normal development datasets. In 2006, the NIH MRI study of normal brain development (NIHPD) was created (Evans, 2006), composed of MR imaging, clinical, and behavioral information of normally developing children and adolescents. In particular, the NIHPD cohort includes longitudinal structural MRI acquired at 1.5 T of 392 subjects aged 4 to 22. In 2014, the Philadelphia Neurodevelopmental cohort (PNC) (Satterthwaite et al., 2014) set to acquire longitudinal MR imaging of 1445 normally developing children aged 8 to 23, with the addition of clinical and cognitive phenotypes, as well as genomics.

Several morphometric studies throughout the years have looked into modelling developmental trajectories during childhood, with the most common approach being the use of tissue classification and brain segmentation to explore the volumetric changes in different areas of the brain (Aubert-Broche et al., 2013; Ducharme et al., 2016; Lenroot et al., 2007; Tamnes et al., 2013). Mills et al. (2016) studied the potential inconsistencies in developmental trajectories from tissue classification and brain segmentation due to the comparability of the

datasets, by modelling trajectories across four separate longitudinal samples. Their results suggest good convergence across differently sampled datasets of normal development. A normal development trajectory during childhood and adolescence is shown in Figure 12. This figure is part of the supplementary material presented in Chapter 4 and showcases the application of a linear mixed-effects model that includes age, age^2 and sex as predictors of total brain volume in subjects from the NIHPD database (Evans, 2006).

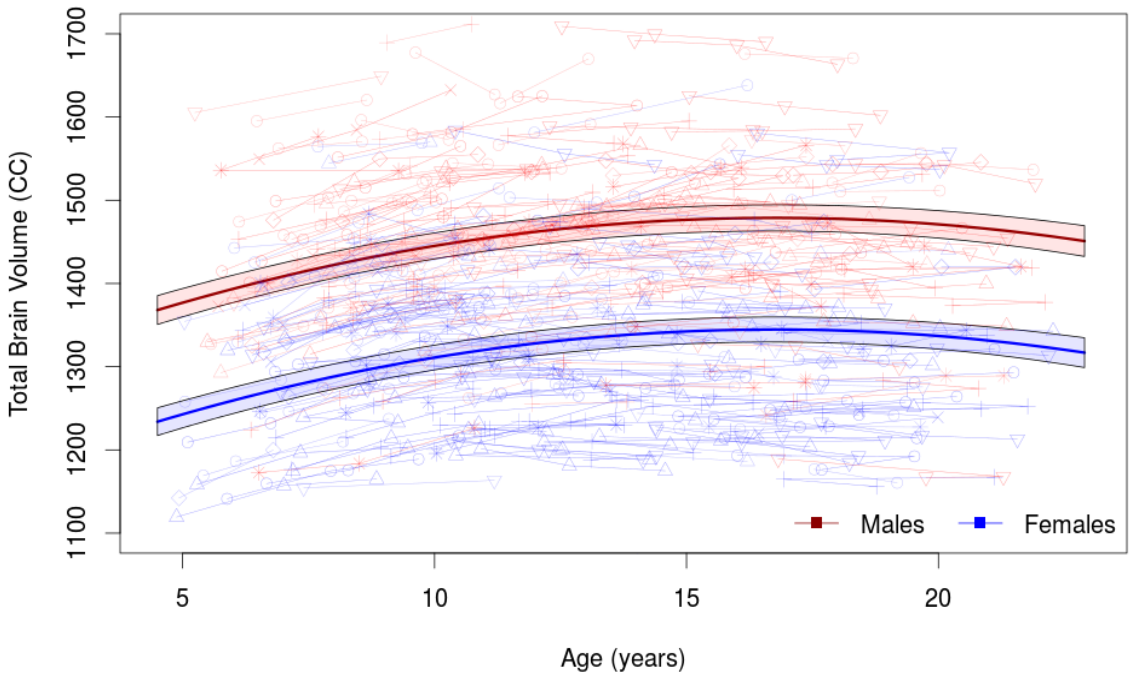

Figure 12. Plot showing an example of normal growth trajectories for males and females during childhood and adolescence for total brain volume. Note how growth reaches a peak and then begins to decline slowly.

Alternative morphometric techniques have not been as common as volumetric methods in the study of normal neurodevelopment. Some of the additional techniques that have been used include tensor mapping (Thompson et al., 2000), TBM (Hua et al., 2009), and cortical thickness (Sowell et al., 2004).

7 Summary of Objectives

The application of MRI tools during childhood presents a series of challenges, as has been described in the present chapter. In order to deal with these complications, the overall objective of this thesis is to describe the development and application of MRI analyses suited for use during childhood. Building on several of the morphometric methods discussed in this chapter, and tailoring many MR image processing tools to children, in Chapter 3 we describe a methodology to analyse longitudinal data from early childhood using TBM and its application to Autism Spectrum Disorder. In Chapter 4, we present a methodology that allows the study of cross-sectional data during childhood and adolescence when the study design lacks the acquisition of enough, well-matched controls. The methodology presented in Chapter 4 can be used both in volumetric studies, as well as voxelwise using TBM, and was applied to the study of 16p11.2 copy number variants. Chapter 5 presents an extension of the methodology presented in Chapter 4, allowing the study of volumetric changes during childhood in multi-site longitudinal studies acquired at either 1.5 T and 3 T. The methodology presented in Chapter 5 can be applied even when a subject is scanned for the first timepoints at 1.5 T and subsequent timepoints are acquired at 3 T, and was applied to the study of pediatric multiple sclerosis.

Chapter 3

A Voxel-wise Assessment of Growth Abnormalities in Infants with Autism Spectrum Disorder

Preface

In this chapter, we present a methodology to apply TBM in a longitudinal database during early childhood (6-24 months of age). Any morphometric technique applied during this age range faces several complications, primarily due to the very fast growth rate that happens overall in the brain during the first 24 months of life, as well as the stark changes in contrast that occur due to myelination in the first 12 months. We propose the use of age-appropriate templates at 3 different timepoints (6, 12 and 24 months) as the target for non-linear registration for scans at the corresponding age as well as using both the T1 and the T2-weighted images simultaneously to perform the registration, therefore taking advantage of the tissue contrast present in each modality and time difference in the occurrence of contrast changes between modalities due to myelination. Furthermore, we use linear mixed-effects to model voxel-wise growth trajectories across the age range.

We applied this method to a study of young children at high risk of ASD. In this study, children with older siblings already diagnosed with ASD were recruited at an early age and were scanned longitudinally throughout their development and assessed at 2 years of age to see if they fit the diagnosis of ASD. ASD is a very heterogeneous neurodevelopmental disorder that has been previously associated with increased head size and overall brain volume in young children, as well as several regional abnormalities in older children and adults, with very little information regarding the neurodevelopment during early childhood, particularly since the ASD is typically diagnosed at an older age (>3y). Our results show significant differences in the growth trajectories of several regions across the brain and present a new insight into the complex neurodevelopmental abnormalities found in ASD.

A Voxel-wise Assessment of Growth Abnormalities in Infants Developing Autism Spectrum Disorder

Alonso Cárdenas-de-la-Parra[1], John D. Lewis[1], Vladimir S. Fonov[1], Kelly N. Botteron[2], Robert C. McKinstry[3], Guido Gerig[4], John R. Pruett Jr.[2], Alan C. Evans[1], and D. Louis Collins[1] for the IBIS Network.

[1] *McConnell Brain Imaging Centre, Montreal Neurological Institute, Montreal, Quebec, Canada.*

[2]*Department of Psychiatry, Washington University School of Medicine, St. Louis, Missouri, USA.*

[3]*Mallinckrodt Institute of Radiology, Washington University, St. Louis, Missouri, USA.*

[4]*Department of Computer Science & Engineering, New York University, New York City, NY, USA.*

Abstract

Autism Spectrum Disorder (ASD) is a complex, heterogeneous developmental disorder typically diagnosed clinically around 4 years of age. The development of biomarkers to help in earlier diagnosis could facilitate earlier intervention and may lead to better outcomes, as well as providing information to help better understand the underlying mechanisms of ASD. In this study, Magnetic Resonance Imaging scans of infants from the Infant Brain Imaging Study (IBIS) at 6, 12 and 24 months of age were included in a morphological analysis, fitting a mixed-effects model to Tensor Based Morphometry (TBM) results to obtain voxel-wise growth trajectories. Subjects were grouped by familial risk and clinical diagnosis at 2 years of age. After correction for multiple comparisons, several regions, including the posterior cingulate gyrus, the cingulum, the fusiform gyrus, and the precentral gyrus, showed a significant effect for the interaction of group and age associated with ASD, either as an increased or a decreased growth rate of the cerebrum. In general, our results showed increase growth rate within white matter with decreased growth rate found mostly in grey matter. These results detail, at the voxel level, abnormalities in brain growth trajectories in ASD, in the first years of life, previously reported in terms of overall brain volume, surface area, or head circumference.

1 Introduction

Autism Spectrum Disorder (ASD) is a complex neurodevelopmental disorder that is typically diagnosed around 4 years of age (Centers for Disease Control and Prevention (CDC), 2014). However, there continues to be no clear understanding of its underlying causes (Buxbaum and Hof, 2013). Early behavioural intervention in children with ASD has been shown to improve their acquisition of language and play skills (Ben-Itzchak and Zachor, 2007; Schreibman et al., 2015; Shire et al., 2017), as well as their overall social behaviour (Dawson et al., 2012, 2010). Thus, our goal is to closely characterize morphological differences of the brain during early neurodevelopment to further our understanding of the underlying mechanisms of ASD that may suggest additional specific interventions. In the future, these may be used as biomarkers that can help in the early diagnosis of ASD allowing for earlier new and established interventions.

ASD is formally characterized by impaired social communication and interaction, as well as repetitive patterns of behavior, and restricted interests and activities. The syndrome encompasses early infantile autism, childhood autism, Kanner's autism, high-functioning autism, atypical autism, childhood disintegrative disorder and Asperger's syndrome (American Psychiatric Association, 2013). This heterogeneity is a challenge in the study of ASD.

Several studies established replicable morphological differences in ASD. Some of the most consistent and prominent findings include larger head circumferences (Bailey et al., 1993; Davidovitch et al., 1996; Elder et al., 2008; Lainhart et al., 1997; Stevenson et al., 1997; Woodhouse et al., 1996) and brain volumes (Carper et al., 2002; Hazlett et al., 2005; Piven et al., 1996, 1995; Redcay and Courchesne, 2005), as well as differences in the growth trajectories of the cerebrum during childhood (Courchesne et al., 2001; Hazlett et al., 2005).

A number of regions have been found to have abnormalities in ASD, including the corpus callosum (Frazier et al., 2012; Hardan et al., 2009, 2000; Manes et al., 1999; Piven et al., 1997; Wolff et al., 2015), the amygdala and hippocampus (Aylward et al., 1999; Barnea-Goraly et al., 2014; Schumann et al., 2009), and the cerebellum (Bauman and Kemper, 1985; Carper and Courchesne, 2000; D'Mello et al., 2015; Stoodley, 2014; Wang et al., 2014). The nature of these abnormalities, however, is sometimes conflicting across different studies. For example, the corpus callosum has been variously reported as reduced in surface area or volume in the anterior region only (Hardan et al., 2000), posterior region only (Piven et al., 1997) or in its whole volume (Boger-Megiddo et al., 2006; Hardan et al., 2009).

These apparently conflicting results may be explained in part by cohort age differences between studies, highlighting the importance of longitudinal developmental studies starting at a very young age. In the case of children between 6 and 24 months of age, a recent study found the corpus callosum to be enlarged (Wolff et al., 2015), in contrast with most studies reporting decreased corpus callosum size in elementary age children and older subjects with ASD (Frazier et al., 2012; Hardan et al., 2009). In addition, several studies have consistently reported an early increase in brain growth rate during childhood (Courchesne et al., 2011; Hazlett et al., 2012b, 2011; Piven et al., 1996; Redcay and Courchesne, 2005), however, there are few studies that have focused on subjects younger than 24 months of age, where early diagnosis may be difficult. Some of the key structural findings that have been reported in children with ASD during early childhood include cortical surface hyperexpansion between 6 and 12 months of age in the middle occipital gyrus (bilaterally), right cuneus, right lingual gyrus, the left inferior temporal gyrus, and right middle frontal gyrus, followed by overall brain overgrowth between 12 and 24 months of age (Hazlett et al., 2017). Additional findings in this age range include abnormal white matter tract development (Wolff et al., 2012), distinct behavioral and cognitive developmental trajectories (IBIS network et al., 2015), and correlation between restrictive and repetitive behavior and alterations in brain functional connectivity (McKinnon et al., 2019).

Longitudinal studies using anatomical magnetic resonance imaging (MRI) can help to understand the structural changes that occur during early childhood (Hazlett et al., 2012b, 2005). In particular, morphometric techniques such as Voxel Based Morphometry (VBM) have been used to look at changes in the volume of white and grey matter in subjects with ASD (Chung et al., 2004; McAlonan et al., 2005). However, VBM may not be the best tool in the analysis of MRI data from early childhood, since it requires the accurate segmentation of grey matter (GM), white matter (WM) and cerebrospinal fluid (CSF) (Ashburner and Friston, 2000), a particularly difficult task due to the evolving myelination process occurring during the first year of life (Barkovich et al., 1988).

As an alternative, Tensor Based Morphometry (TBM), a technique using the deformation fields resulting from a non-linear registration to an appropriate template, can be used to observe morphological changes in individual subjects in a longitudinal study, and compare these changes between groups (Ashburner and Friston, 2004; Lau et al., 2008). Like VBM, one of the advantages of TBM is that there is no restriction to a priori regions of interest, but rather a voxel-by-voxel statistical analysis that yields the location of anatomical differences, including differences within a region, even if there are no evident full-brain or regional size differences (Ashburner and Friston, 2004; Boddaert et al., 2004; Chung et al., 2004). Longitudinal TBM

studies have not been performed to analyze potential neurodevelopmental differences in early childhood (before 2 years of age) in ASD.

In the present study, a longitudinal analysis using TBM in the whole brain was performed on subjects between 6 and 24 months of age, looking both at subjects at high familial risk (defined below) of ASD with a positive diagnosis at 24 months, high-risk with a negative diagnosis, and low-risk, typically developing controls. In order to tackle some of the complications of MRI studies in early childhood (e.g. reduced WM and GM contrast), we propose the use of both T1 and T2-weighted images simultaneously for the optimization of non-linear registration. Contrast changes due to myelination occur at different times in T1 and T2-weighted images (Barkovich et al., 1988), thus providing complimentary information for robust registration. Additionally, we incorporate the use of unbiased, age-appropriate templates as our registration targets. Our findings demonstrate significant differences in the growth trajectories of multiple regions in the brain between the high-risk ASD-positive group and both the high risk ASD-negative and low-risk controls, with some regions showing a faster growth rate and others showing a slower growth rate.

2 Methodology

2.1 Participants

All participants were part of the Infant Brain Imaging Study (IBIS), a collaborative longitudinal study of infants at high and low familial risk of developing ASD based on their family history. It has been shown that siblings of children with ASD are at a higher risk of developing ASD themselves, with a reported risk as high as 18.7% (August et al., 1981; Girault et al., 2020; Ozonoff et al., 2011). Specifically, in this study infants were defined at *high risk* (HR) if they have an older sibling with an ASD diagnosis confirmed by the Social Communication Questionnaire (SCQ) (Rutter et al., 2003b) and the Autism Diagnostic Interview-Revised (ADI-R) (Rutter et al., 2003a). Infants were included in the *low risk ASD-negative* group (LR-) if they have at least one typically developing older sibling confirmed with the SCQ and no first-degree relatives with a developmental disability and also do not qualify for a clinical best estimate diagnosis of ASD at 24 months.

Recruitment, screening and assessment of the participants were performed at each of four sites: University of North Carolina, University of Washington, Children's Hospital of Philadelphia, and Washington University in St. Louis. Participants were excluded from the study if they fulfilled any of the following general criteria: evidence of a specific genetic

condition or syndrome, any significant medical condition potentially affecting neurodevelopment, significant vision or hearing impairments, low weight at birth (<2000 g), birth prior to 36 gestational weeks, significant perinatal adversity, pre-natal exposure to neurotoxins, any contraindication for MRI, predominant home language other than English, adopted children or half siblings, first-degree relative with psychosis, schizophrenia, bipolar disorder, or if they were twins.

All study procedures required the informed, written consent from the parents or legal guardians of all participants, as well as approval by institutional review at each site. All infants enrolled in the study were seen multiple times at 6, 12, and/or 24 months of age for MRI scanning and developmental and behavioural evaluation.

Table 2. Demographic information of participants.

	High-risk ASD-positive	High-risk ASD-negative	Low-risk ASD-negative	p-value
Total Participants	56	285	162	
6 m scans	40	202	137	
12 m scans	35	222	116	
24 m scans	40	203	93	
Participants with 1 time-point	18	53	39	
Participants with 2 time-points	17	122	62	
Participants with 3 time-points	21	110	61	
Age (6 m scan)[1]	6.6 (0.6)	6.7 (0.7)	6.8 (0.7)	0.71
Age (12 m scan)[1]	12.8 (0.5)	12.8 (0.7)	12.9 (0.8)	0.76
Age (24 m scan)[1]	25 (0.7)	25 (0.9)	25.1 (1.1)	0.74
ADOS severity[1]	6.1 (1.8)	1.5 (1.0)	1.3 (0.8)	<0.001
Sex (% male)[1]	85.6	58.3	59.3	<0.001

Using the complete diagnostic assessment at 24 months of age, the HR group was split into *high risk ASD-positive* (HR+) and *high risk ASD-negative* (HR-) subgroups. The HR+ group was defined by familial risk and diagnostic outcome based on clinical best estimate made by experienced, licensed clinicians using the Diagnostic and Statistical Manual of Mental Disorders, 4th Edition, Text Revision (DSM-IV-TR) (American Psychiatric Association and American Psychiatric Association, 2000) checklist and supported by all available behavioural assessment data including the Autism Diagnostic Observation Schedule (ADOS) (Lord et al.,

2000) and the Autism Diagnostic Interview, Revised (ADI-R) (Rutter et al., 2003a). The remaining HR subjects were included into the HR- group. For this study, we compared MRI scans from LR-, HR-, and HR+ infants that passed quality control. These criteria yielded 503 total participants (1,088 total scans) that included 162 LR- (346 scans), 285 HR- (627 scans) and 56 HR+ (115 scans). From these participants, 40% provided data for at least two time points, with 38.2% providing three time points. Demographic data for study participants as detailed in Table 2.

2.2 Image Acquisition

The acquisition of all MRI scans was carried out at the four sites identified above during natural sleep, on identical 3T Siemens TIM Trio scanners with 12-channel head coils using the following protocols: sagittal T1 MPRAGE (repetition time=2400 ms, echo time=3.16 ms, slice thickness=1 mm, field of view=256 mm, 256 x 160 matrix), 3D T2 fast spin echo (repetition time=3200 ms, echo time=499 ms, slice thickness=1 mm, field of view=256 mm, 256 x 160 matrix). Quality assurance was achieved using local Lego phantoms and travelling human phantoms over time to characterize intra- and inter-site reliability (Gouttard et al., 2008). Quality control for each scan included automatic verification of acquisition protocol parameters and visual assessment for potential artifacts due to subject motion, blood flow, or hardware issues.

2.3 Longitudinal Tensor-based Morphometry

2.3.1 Preprocessing

All the scans were corrected for geometric distortion using data collected from the Lego and travelling human phantoms (Fonov et al., 2010). Intensity nonuniformity artifacts were corrected using the nonparametric nonuniform intensity normalization (N3) algorithm (Sled et al., 1998), followed by a histogram-based intensity normalization between 0.0 and 100.0, where the histogram is separated into deciles and the best linear mapping of the histograms is calculated.

2.3.2 Age-appropriate average templates

T1 and T2-weighted unbiased average templates were created for each time-point in the longitudinal analysis (6, 12 and 24 months) according to the methods proposed by Fonov *et al.* (Fonov et al., 2011). All available scans from the IBIS database were used in the creation of the templates, including children from both the high risk and low risk cohorts. As such, each template is made from subjects that are approximately within 1 month of the template age. It

is important to note that while there is a large contrast change over the period from 6 to 24 months, the contrast does not change significantly between 5 and 6 months or between 12 and 13 months for example, making it possible to use these templates as anchors in our registration process.

2.3.3 Registration

Each scan was linearly registered to the corresponding unbiased age-appropriate templates followed by a non-linear registration using the symmetric image normalization (SyN) method (Avants et al., 2008), a symmetric diffeomorphic image registration algorithm. All non-linear registrations were obtained by simultaneously optimizing the mutual information between the T1 and T2-weighted scans and their corresponding unbiased templates.

In order to obtain the inter-template transformations, the 6 and 24 months templates were linearly registered to the 12 months template, followed by a non-linear registration procedure using the SyN method (Avants et al., 2008) and optimizing for T1 and T2-weighted images simultaneously.

Finally, the non-linear deformation grids for each scan's registration to an age-appropriate template were concatenated with the inter-template non-linear transformation, normalized and inverted, effectively yielding a voxel-by-voxel nonlinear mapping from the 12 months template reference space to the native space of each scan. A visual representation of this process is shown in Figure 13. By doing this, the individual differences of each subject to its age-appropriate template are conserved, while ensuring that all subjects at 6 and 24 months of age, respectively, undergo the same transformation from template to template.

2.3.4 Jacobian determinant

The natural logarithm of the Jacobian determinant of the deformation field was computed at every voxel and used as a surrogate of the local volume difference between each subject and the 12 m template. In general, a negative log-Jacobian determinant value represents shrinking from the template to the native space, a value of 0 indicates that there is no volume change in the voxel and a positive value indicates enlargement.

2.3.5 Statistical Analysis

Voxel-by-voxel tests of linear mixed-effects models were performed on the Jacobian determinant maps. These mixed-effects models are used to characterize the local growth trajectory of each voxel. Mixed-effects models are commonly used in longitudinal data analysis since they can deal with missing data while accounting for heterogeneity from different individuals by introducing subject-specific random effects (Cheng et al., 2010).

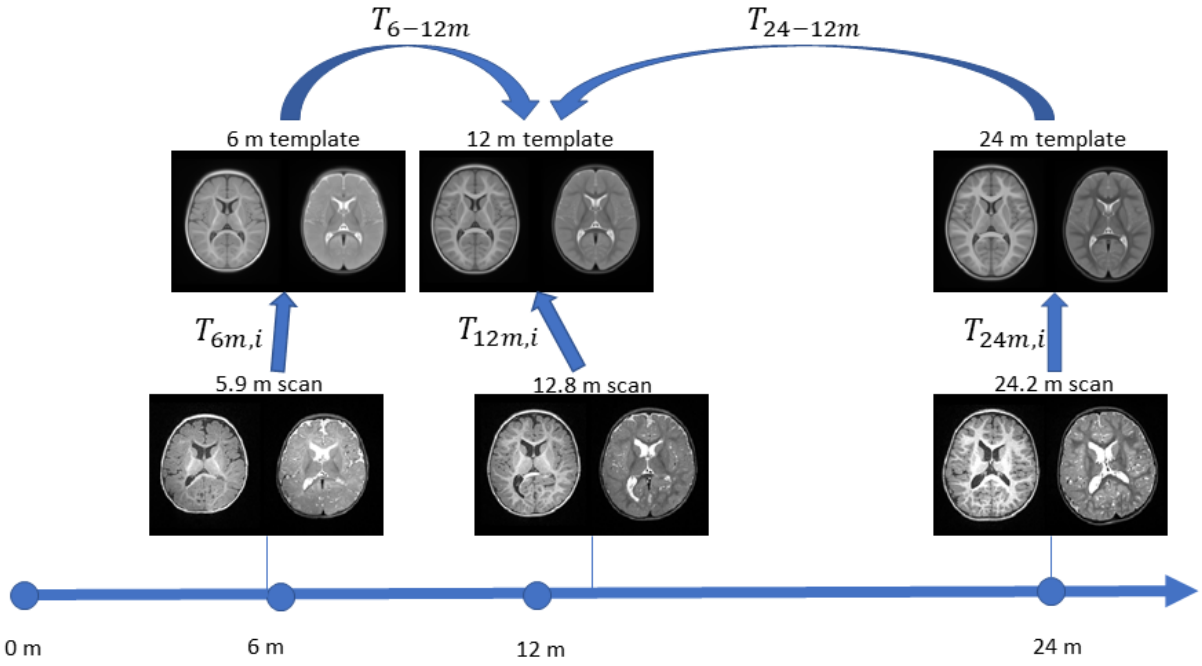

Figure 13. Visual representation of the registration process. For an exemplary 5.9 months old subject the Jacobian determinant would be the result of: $|J| = Concat(T_{6m,i}T_{6-12m})^{-1}$.

Forward selection was used, beginning with the testing of the simplest growth trajectory model and subsequently adding variables that show statistical significance. The fixed effects that were evaluated included the linear, quadratic and cubic age effects (age, age^2, age^3), acquisition site, the effect of sex and group (LR-, HR-, or HR+), as well as any interactions between them (e.g., age*sex). The age in days of each participant was used in the model. For the random effects, both a random intercept and random slope were tested to account for within-subject dependencies, as well as a random intercept to account for potential inter-site differences. The mixed-effects models were compared using voxel-wise log-likelihood ratio tests, and the simpler model was chosen whenever it explained most of the variance. The selected model was applied to all voxels.

The Jacobian determinant maps provide a voxel-wise measure of local relative volume with respect to the 12-month reference space (Ashburner and Friston, 2004). After performing the mixed-effects models testing using the previously mentioned effects, the final statistical model tested in the whole brain included fixed-effects for age (β_1), age^2 (β_2), group (β_3), the interaction between age and group (β_4), and sex (β_5), as well as a random effect for the intercept for each subject (γ_{0i}) and for acquisition site (γ_{0site}). Therefore, the model evaluated for each subject *i* at each voxel was:

$$J_i(x) = \gamma_{0i} + \gamma_{0site} + \beta_0 + \beta_1 * age + \beta_2 * age^2 + \beta_3 * group + \beta_4(group \times age) + \beta_5 * sex + E \quad (16)$$

where β_0 represents the intercept and E is the residual error in the model.

The false discovery rate (FDR) procedure described by Genovese *et al.* (Genovese et al., 2002) was used to control for multiple comparisons with an FDR of 5%. A single t-value threshold was determined for each resulting statistical map by taking into account the estimated degrees of freedom for a given statistical test and an FDR p-value obtained by pooling the uncorrected p-values across all effects and all voxels tested (Lau et al., 2008). All statistical analyses were performed using the R software package (www.r-project.org) in conjunction with the *lme4* (Bates et al., 2015) and *RMINC* (Lerch et al., 2017) libraries.

3 Results

The results of the analysis identified voxels with significant changes in local volume that can be described by the parameters in the model. As such, a statistical map was obtained for each effect in the model, where each statistically significant voxel provides information about the local growth trajectory when the other effects are removed. Of particular interest to this study are the voxels found to be statistically significant for the interaction between age and group, since it signifies a region that is affected differently by age in each group and may be thus associated with a group-specific growth trajectory, indicating an increase or decrease in growth rate in the HR+ group compared to the HR- and LR- groups. The effect of group was not significant at any level at the centered age (6 months).

We used the Neuromorphometics atlas (*Neuromorphometrics Inc.*, 2013) to identify the anatomical regions of groups of voxels showing significantly different growth trajectories. These anatomical regions are summarized in Table 3. Representative slices showing the pairwise HR+ vs LR comparison thresholded t-values with an FDR of 5% of the age by risk group interaction are shown in Figure 14. The largest connected region of increased growth rate associated with the HR+ group includes the splenium of the corpus callosum, WM radiating from the splenium bilaterally, as well as the posterior cingulate gyrus bilaterally. Additional areas of increased growth rate include the cingulum bilaterally, the right parahippocampal gyrus and entorhinal area, and the left temporal pole and cerebellum. Significant regions showing decreased growth rate associated with the HR+ group include the anterior portion of the caudate bilaterally, the left precuneus, middle occipital gyrus and lingual gyrus, and the

right fusiform gyrus, supplementary motor cortex, supramarginal gyrus and subgenual anterior cingulate cortex.

Table 3. Regions with significant differences in growth trajectories between HR+ and LR- groups.

Region	Peak t-value	Beta (at peak)	Cluster Size
Bilateral Posterior Cingulate Gyrus Splenium and Isthmus of the Corpus Callosum Bilateral White Matter	5.3	0.0055	2131
Right Cingulum Right White Matter	4.4	0.0035	1587
Right Fusiform Gyrus Right Inferior Temporal Gyrus	-5.2	-0.0087	1242
Right Supplementary Motor Cortex Right Superior Frontal Gyrus (Medial Segment)	-4.8	-0.0067	964
Left Cingulum Left White Matter	4.3	0.0037	788
Right Supramarginal Gyrus Right Parietal Operculum	-5.0	-0.0123	773
Left Precuneus	-4.4	-0.0099	388
Left Middle Occipital Gyrus Left White Matter	-4.3	-0.0091	312
Left Cerebellum	5.4	0.0067	302
Right Parahippocampal Gyrus Right Entorhinal Area	4.3	0.0033	244
Subgenual Anterior Cingulate Cortex Right Accumbens	-4.7	-0.0042	244
Left Temporal Pole Left Superior Temporal Gyrus	5.4	0.0049	233
Left Posterior Orbital Gyrus Left White Matter	4.3	0.0055	221
Right Precentral Gyrus	4.6	0.0080	173
Right Occipital Fusiform Gyrus	-5.0	-0.0076	151
Left Temporal Pole	5.2	0.0056	147
Left Caudate	-4.4	-0.0042	146
Right Caudate	-4.1	-0.0035	117
Right Precentral Gyrus	4.8	0.0059	115
Right Fusiform Gyrus	4.3	0.0049	95
Left Lingual Gyrus	-4.2	-0.0060	72
Left Precentral Gyrus	5.2	0.0043	68
Right Precentral Gyrus	4.3	0.0062	60
Right Medial Orbital Gyrus	4.2	0.0031	54
Right Middle Frontal Gyrus	4.3	0.0085	50
Right Middle Temporal Gyrus	4.4	0.0047	44
Right Temporal Pole	4.0	0.0038	39
Left Lateral Orbital Gyrus	-4.1	-0.0039	35

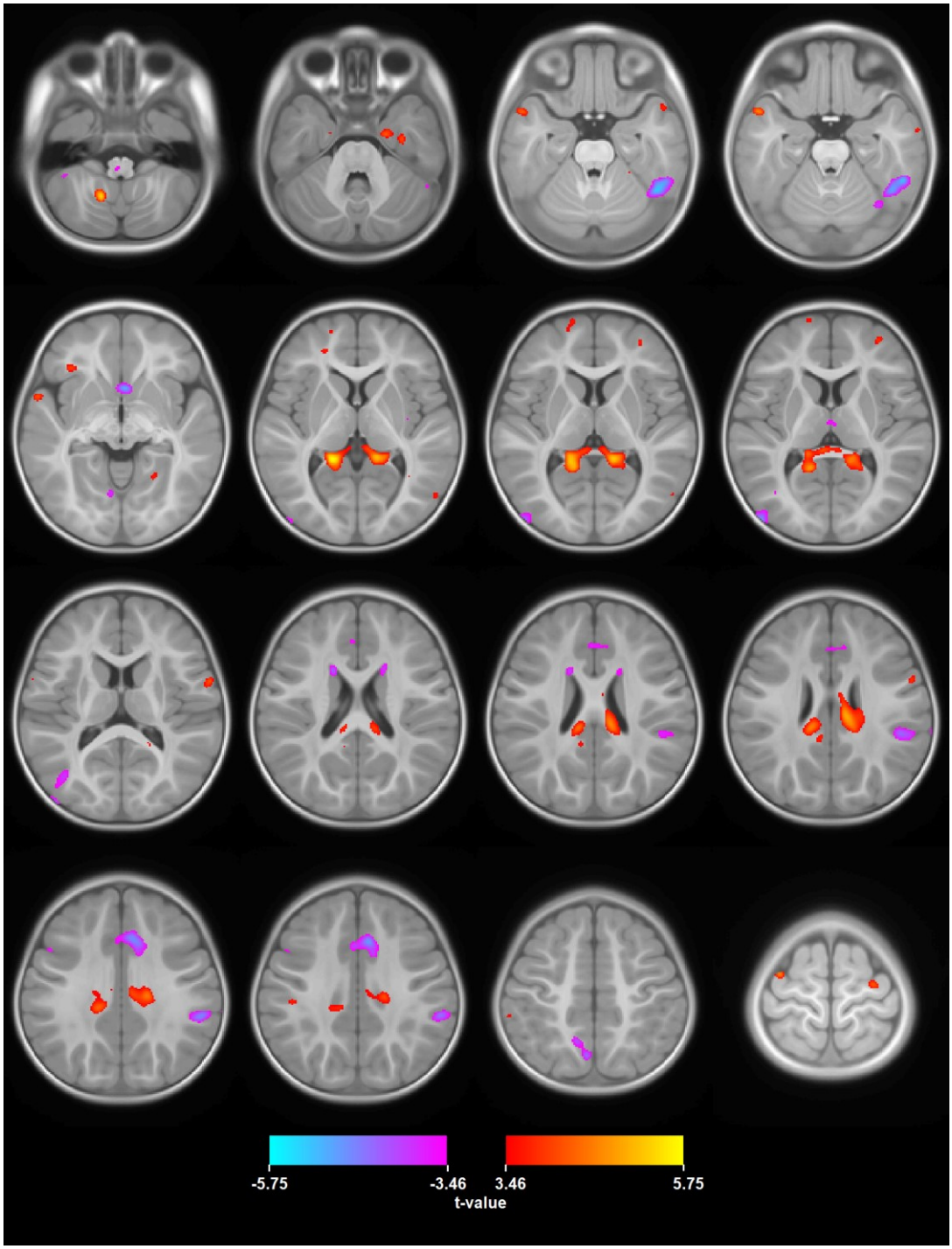

Figure 14. Statistical maps showing regions with significant differences in growth rate given by the age andgroup interaction (HR+ vs LR-). All colored regions are statistically significant for pooled FDR (q=0.05).

To evaluate the magnitude and time-course of these differences, Figure 15 shows exemplar voxel-wise growth trajectories demonstrating distinct increased local growth rate in the HR+ group in 6 different regions distributed across the brain. These regions include the left temporal pole, right posterior cingulate gyrus, left posterior cingulate gyrus, left precentral gyrus, right precentral gyrus and the right cingulum. Additionally, Figure 16 shows trajectories

with decreased local growth rate in the HR+ group in 4 different regions. These regions include the right fusiform gyrus, left anterior tip of the caudate, left precuneus and the right subgenual anterior cingulate cortex.

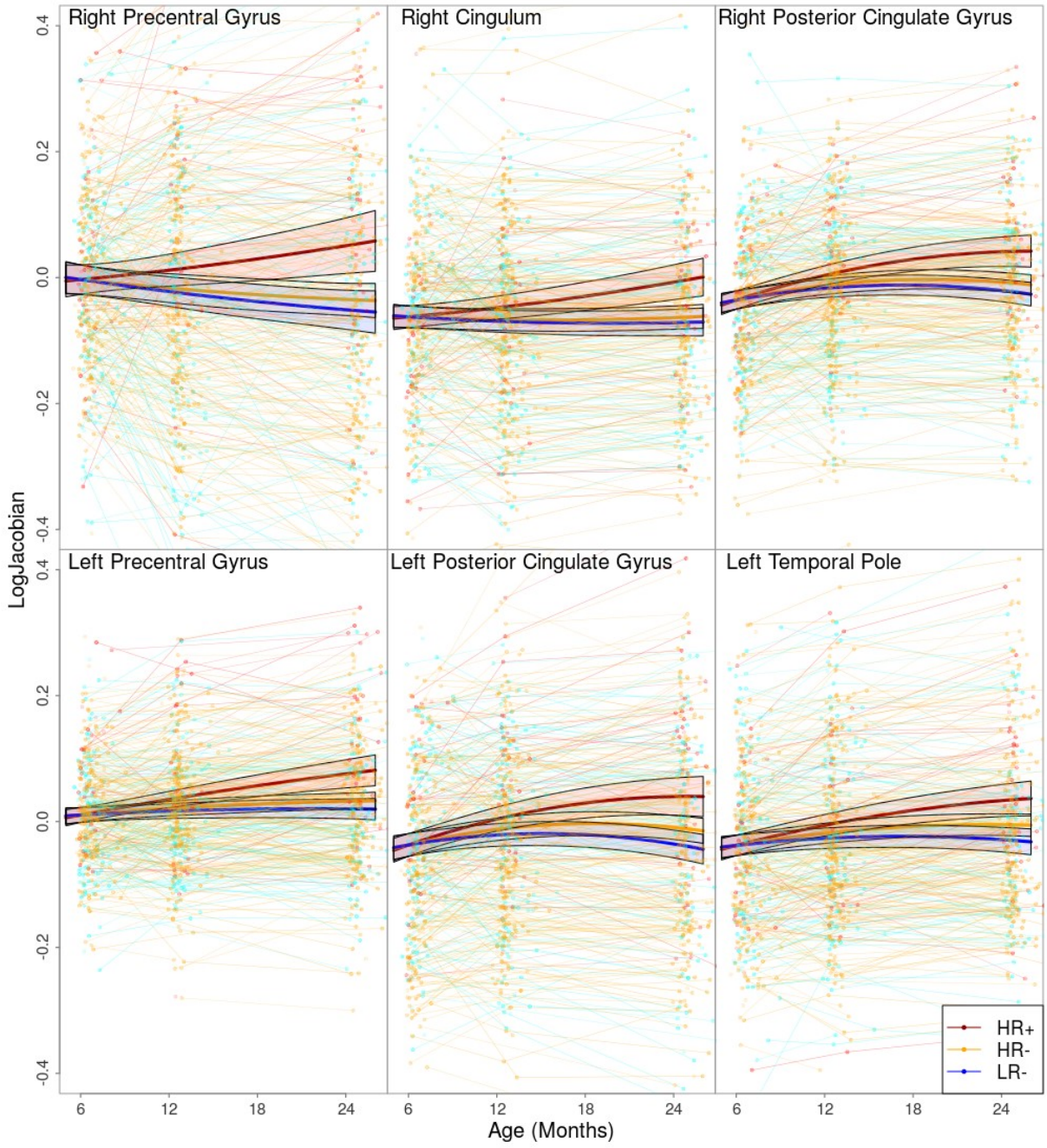

Figure 15. Voxelwise growth trajectories with 95% confidence intervals for selected significant regions showing increased growth rate in the HR+ group when compared to the HR- and LR- groups. Voxels were selected by looking at the peak t-values of both the HR+ vs HR- and HR+ vs LR- comparisons.

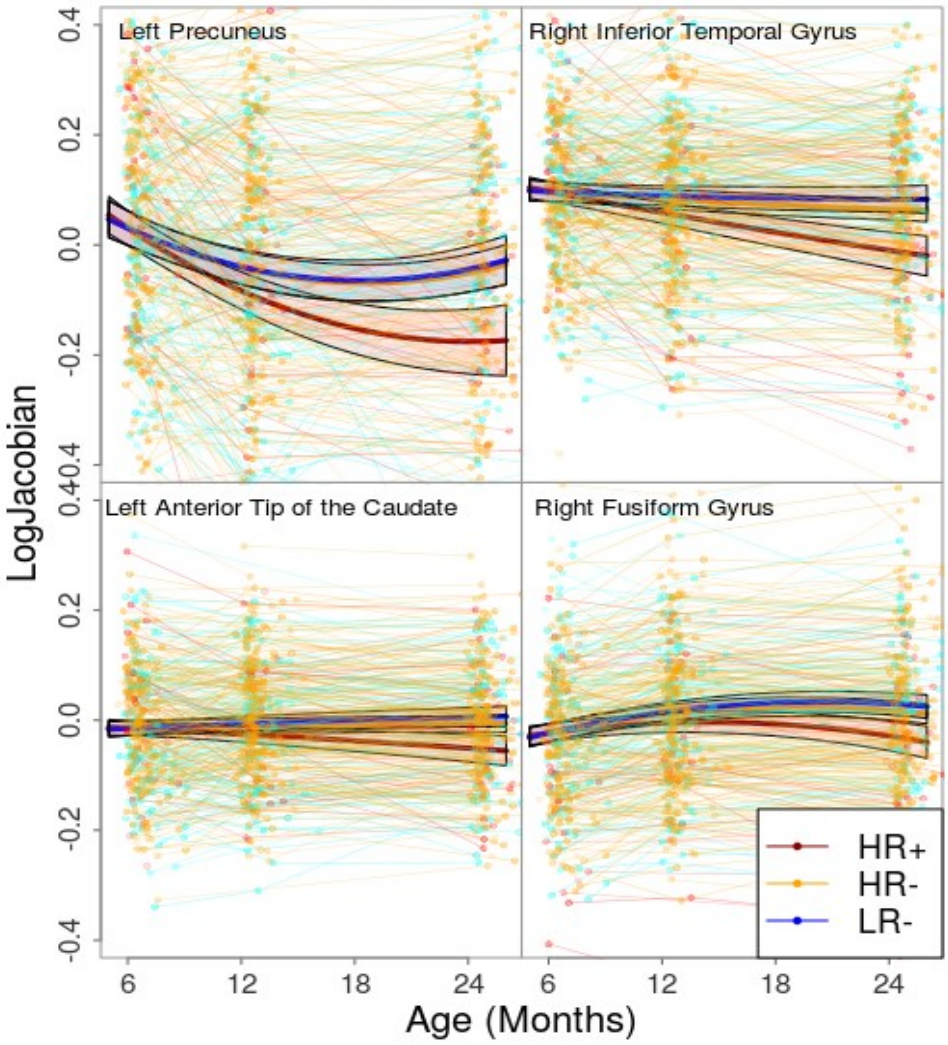

Figure 16. Voxelwise growth trajectories with 95% confidence intervals for selected significant regions showing decreased growth rate in the HR+ group when compared to the HR- and LR- groups. Voxels were selected by looking at the peak t-values of both the HR+ vs HR- and HR+ vs LR- comparisons.

4 Discussion

In this longitudinal study, we found a pattern of significant differences in growth in the HR+ group when compared with the HR- and LR- controls (see Figure 14). Several regions across the brain show abnormal growth patterns in the HR+ group, either as an increased (Figure 15) or a decreased (Figure 16) growth rate. In general, the regions found to have decreased growth rate are found in GM, while regions with increased growth rate are mostly found in WM. Overall, regions found to have increased growth outnumber the regions with decreased growth, this effect could be tied to the well documented general brain overgrowth in children with ASD. Furthermore, the predominance of increased growth rate in WM is consistent with previous studies showing volume increases across WM in ASD (Herbert et al.,

2004). Additionally, the differences between groups found here are dependent on age, with the growth trajectories diverging with aging (see Figures 15 and 16).

Our results are in agreement with previous studies of ASD within the same age range, showing no significant volumetric differences at 6 months of age (Hazlett et al., 2012a), but rather distinct growth trajectories leading to overgrowth that begin to diverge later in life, between 12 and 24 months of age, as shown in total brain volume changes by Hazlett et al. (Hazlett et al., 2017). In their more recent work, Hazlett et al. (Hazlett et al., 2017) developed deep-learning algorithm using cross-sectional features based on surface area information of 6 and12-month old individuals to predict the diagnosis of ASD in individual high-risk children at 24 months with a positive predictive value of 81% and a sensitivity of 88%. Interestingly, 40% of the anatomical regions used in their deep learning framework show significant differences in the longitudinal growth trajectories estimated with the data-driven TBM methodology used here. Some of the more important trajectory differences include the medial portion of the right superior frontal gyrus, the left lingual gyrus, and the left precuneus.

In the case of the regions with increased growth found in the cerebrum, the splenium of the corpus callosum has been related with language production in normally developing children between 6 and 24 months of age (Swanson et al., 2015), and therefore abnormalities in this region might be associated with deficits in communication, one of the core symptoms in ASD. Findings in the corpus callosum are of particular importance when considering that the axons that form the corpus callosum are predominantly involved in long-distance connections, and previous research has shown long-range functional and anatomical underconnectivity (Horwitz et al., 1988; Just et al., 2012; Kana et al., 2009). The posterior cingulate gyrus has been previously implicated in social impairments observed in ASD, particularly the self and other reflection (Chiu et al., 2008; Kennedy and Courchesne, 2008). The cingulum bundle has an important role in the connectivity required for social cognition (Amodio and Frith, 2006) as well as emotional processing (Bush et al., 2000), and has been previously reported to show abnormal WM integrity in ASD as early as 2 to 3 years of age (Weinstein et al., 2011; Xiao et al., 2014). Motor impairments present in ASD have been previously associated with abnormalities in the precentral gyrus, particularly as increases in WM volume in children between 8 and 12 years of age (Mostofsky et al., 2007).

The regions showing a decrease in growth rate are found mainly in GM and are in general smaller in magnitude and size than those showing an increased growth rate. The biggest cluster with decreased growth rate in ASD is found in the right fusiform gyrus and includes a part of the right inferior temporal gyrus. The right fusiform gyrus has been consistently reported to be

involved in face processing tasks (Allison et al., 1994; Puce et al., 1996), and has been found to have increased volume in adolescents and adults with ASD (Rojas et al., 2006; Waiter et al., 2004). Alterations in the right fusiform gyrus have been shown to vary with age in adolescents and adults (Raznahan et al., 2010; Wallace et al., 2010), as such, the decreased growth rate at this early age might be tied to future normalization and overgrowth in later stages. A similar situation occurs with the right inferior temporal gyrus and the left precuneus, where increased volumes have been associated with ASD in adolescents and adults (Liu et al., 2017). The left precuneus and the left lingual gyrus have also been found to have decreased cortical thickness in older subjects with ASD (Pereira et al., 2018). Little is known about potential alterations during early childhood, thus highlighting the importance of looking for longitudinal changes in neurodevelopmental patterns across the different age ranges. In addition, we found a decreased growth rate in the subgenual anterior cingulate cortex. This region is implicated in the inhibition of the amygdala and emotion regulation (McDonald, 1998; Ray and Zald, 2012; Stevens et al., 2011) and is known to play an important role in various mood disorders (Drevets et al., 2008). Furthermore, it has been recently associated with ASD in rat models (Wu et al., 2018) and in older children and adolescents (Velasquez et al., 2017).

We found two potential conflicts of the present results with previous studies. First, a study by Wolff *et al*. (Wolff et al., 2015) examined the length, area and thickness of the corpus callosum in subjects from the IBIS database in the same age range (6-24 m). They reported a significantly greater area and thickness of the normalized corpus callosum in the HR+ subjects at six months, decreasing to a non-significant difference at 24m. Our results show an increased growth rate in the splenium throughout the age range. There are several potential explanations for this apparent discrepancy. First, the metrics analyzed in both studies are different, the shape analysis described in Wolff *et al.* uses explicit shapes and measures thickness, length, and are. Our voxel-based deformations measure local changes which do not really capture "object-level" differences. Second, the normalization procedure is different. In Wolff *et al.*, corpus callosum metrics were normalized for brain volume, sex, site, mother's education and Mullen Early Learning. The TBM method here registers all data to an average 12-month template, and the Jacobian determinant is used to estimate voxel-by-voxel growth on a per-subject basis. The Jacobian values are thus normalized to the size of the average 12-month old brain. Brain volume is accounted for in the TBM registration process, while sex and site are included in our mixed-effects model. Finally, Wolff *et al.* look at group differences in the size of the corpus callosum at 6, 12, and 24 months, while the present study focuses on differences in the growth trajectories, particularly the growth rate as affected by the group and age interaction.

Additionally, we found small regions at the tip of the anterior caudate nuclei to have a decreased growth rate, with no significant difference in the body of the caudate nuclei. The caudate nuclei has been reported to have an increased growth rate and larger overall volumes in older children with ASD (Langen et al., 2014; Qiu et al., 2016). One potential explanation for this discrepancy is that, as the caudate begins to enlarge, the small section adjacent to the ventricular horn is slightly compressed, causing our method to detect a decreased growth rate in a very small portion of the caudate, while in reality the pattern of overgrowth in the caudate volume is increasing but not yet significant.

The limitations of the present study are partially seen by the previously mentioned conflicts. Due to the reliance of TBM on the non-linear registrations, small regions (e.g. the corpus callosum and the anterior tip of the caudate) can be affected by changes in the opposite direction in its neighbouring structures. Furthermore, the contrast between GM and WM in the images changes with age. These changes in contrast affect the quality of the non-linear registration, especially in the data acquired at around 6 months of age, where brain regions undergo contrast reversal, leaving no visible boundary between GM and WM. The registration algorithm might then simply interpolate these regions, with the Jacobian being the result of the choice and scale of interpolation rather than image texture changes. Our methodology is designed to mitigate this problem, mainly with the simultaneous use of T1 and T2-weighted images for registration. The WM and GM contrast due to myelination changes differently in T1 and T2-weighted images and, by leveraging this time-shift between modalities, we provide additional information resulting in more accurate registrations at an early age. However, the myelination process and its effects on T1 and T2-weighted contrast are complex, and some regions may still have no clear boundaries or sufficient information for accurate registration.

In conclusion, these results detail, at voxel level, growth abnormalities previously documented as abnormally increased head circumference and brain volume. These voxel level measures of growth abnormality indicate that the abnormal patterns of growth are more complex than has been inferred from the global patterns, with regions showing growth abnormalities in either direction. Further, many of these regions are involved in social information processing, emotion and language, all of which are known to be impaired in ASD. These results thus more tightly couple the brain overgrowth seen in ASD to the behavioural phenotype. This may help uncover the underlying etiology and lead to more specific, targeted interventions.

Acknowledgements

The Infant Brain Imaging Study (IBIS) Network clinical sites are located at the University of North Carolina (J. Piven, IBIS Network primary investigator; H.C. Hazlett, C. Chappell); the University of Washington (S.R. Dager, A.M. Estes, D. Shaw); Washington University (K.N. Botteron, R.C. McKinstry, J. Constantino, J. Pruett); Children's Hospital of Philadelphia (R.T. Schultz, S .J. Paterson); the University of Alberta (L. Zwaigenbaum); and the University of Minnesota (J.T. Elison, J.J. Wolff). The data coordinating center is at the Montreal Neurological Institute (A.C. Evans, D.L. Collins, V.S. Fonov, P. Kostopoulos, S. Das). The image processing core is at New York University (G. Gerig) and the University of North Carolina (M. Styner). The statistical analysis core is at the University of North Carolina (H. Gu). This work was supported by an NIH Autism Center of Excellence grant (NIH and NICHD HD055741), a Brain Canada, a grant from the Azrieli Foundation grant (BC_Azrieli_MIRI_3388) and the Fondation Marcelle et Jean Coutu.

References

Allison, T., Ginter, H., McCarthy, G., Nobre, A.C., Puce, A., Luby, M., Spencer, D.D., 1994. Face recognition in human extrastriate cortex. Journal of Neurophysiology 71, 821–825. https://doi.org/10.1152/jn.1994.71.2.821

American Psychiatric Association (Ed.), 2013. Diagnostic and statistical manual of mental disorders: DSM-5, 5th ed. ed. American Psychiatric Association, Washington, D.C.

American Psychiatric Association, American Psychiatric Association (Eds.), 2000. Diagnostic and statistical manual of mental disorders: DSM-IV-TR, 4th ed., text revision. ed. American Psychiatric Association, Washington, DC.

Amodio, D.M., Frith, C.D., 2006. Meeting of minds: the medial frontal cortex and social cognition. Nat. Rev. Neurosci. 7, 268–277. https://doi.org/10.1038/nrn1884

Ashburner, J., Friston, K.J., 2004. Morphometry, in: Frackowiak, R.S.J. (Ed.), Human Brain Function. Elsevier Academic Press, Amsterdam ; Boston.

Ashburner, J., Friston, K.J., 2000. Voxel-Based Morphometry—The Methods. NeuroImage 11, 805–821. https://doi.org/10.1006/nimg.2000.0582

August, G.J., Stewart, M.A., Tsai, L., 1981. The incidence of cognitive disabilities in the siblings of autistic children. Br J Psychiatry 138, 416–422.

Avants, B., Epstein, C., Grossman, M., Gee, J., 2008. Symmetric diffeomorphic image registration with cross-correlation: Evaluating automated labeling of elderly and neurodegenerative brain. Medical Image Analysis 12, 26–41. https://doi.org/10.1016/j.media.2007.06.004

Aylward, E.H., Minshew, N.J., Goldstein, G., Honeycutt, N.A., Augustine, A.M., Yates, K.O., Barta, P.E., Pearlson, G.D., 1999. MRI volumes of amygdala and hippocampus in non-mentally retarded autistic adolescents and adults. Neurology 53, 2145–2150.

Bailey, A., Luthert, P., Bolton, P., Le Couteur, A., Rutter, M., Harding, B., 1993. Autism and megalencephaly. Lancet 341, 1225–1226.

Barkovich, A.J., Kjos, B.O., Jackson, D.E., Norman, D., 1988. Normal maturation of the neonatal and infant brain: MR imaging at 1.5 T. Radiology 166, 173–180. https://doi.org/10.1148/radiology.166.1.3336675

Barnea-Goraly, N., Frazier, T.W., Piacenza, L., Minshew, N.J., Keshavan, M.S., Reiss, A.L., Hardan, A.Y., 2014. A preliminary longitudinal volumetric MRI study of amygdala and hippocampal volumes in autism. Prog. Neuropsychopharmacol. Biol. Psychiatry 48, 124–128. https://doi.org/10.1016/j.pnpbp.2013.09.010

Bates, D., Mächler, M., Bolker, B., Walker, S., 2015. Fitting Linear Mixed-Effects Models Using lme4. J. Stat. Soft. 67. https://doi.org/10.18637/jss.v067.i01

Bauman, M., Kemper, T.L., 1985. Histoanatomic observations of the brain in early infantile autism. Neurology 35, 866–874.

Ben-Itzchak, E., Zachor, D.A., 2007. The effects of intellectual functioning and autism severity on outcome of early behavioral intervention for children with autism. Res Dev Disabil 28, 287–303. https://doi.org/10.1016/j.ridd.2006.03.002

Boddaert, N., Chabane, N., Gervais, H., Good, C.D., Bourgeois, M., Plumet, M.-H., Barthélémy, C., Mouren, M.-C., Artiges, E., Samson, Y., Brunelle, F., Frackowiak, R.S.J., Zilbovicius, M., 2004. Superior temporal sulcus anatomical abnormalities in childhood autism: a voxel-based morphometry MRI study. Neuroimage 23, 364–369. https://doi.org/10.1016/j.neuroimage.2004.06.016

Boger-Megiddo, I., Shaw, D.W.W., Friedman, S.D., Sparks, B.F., Artru, A.A., Giedd, J.N., Dawson, G., Dager, S.R., 2006. Corpus callosum morphometrics in young children with autism spectrum disorder. J Autism Dev Disord 36, 733–739. https://doi.org/10.1007/s10803-006-0121-2

Bush, null, Luu, null, Posner, null, 2000. Cognitive and emotional influences in anterior cingulate cortex. Trends Cogn. Sci. (Regul. Ed.) 4, 215–222. https://doi.org/10.1016/s1364-6613(00)01483-2

Buxbaum, J.D., Hof, P.R. (Eds.), 2013. The neuroscience of autism spectrum disorders, First edition. ed. Elsevier/AP, Boston.

Carper, R.A., Courchesne, E., 2000. Inverse correlation between frontal lobe and cerebellum sizes in children with autism. Brain 123 (Pt 4), 836–844.

Carper, R.A., Moses, P., Tigue, Z.D., Courchesne, E., 2002. Cerebral lobes in autism: early hyperplasia and abnormal age effects. Neuroimage 16, 1038–1051.

Centers for Disease Control and Prevention (CDC), 2014. Prevalence of autism spectrum disorder among children aged 8 years - autism and developmental disabilities monitoring network, 11 sites, United States, 2010. MMWR Surveill Summ 63, 1–21.

Cheng, J., Edwards, L.J., Maldonado-Molina, M.M., Komro, K.A., Muller, K.E., 2010. Real longitudinal data analysis for real people: building a good enough mixed model. Stat Med 29, 504–520. https://doi.org/10.1002/sim.3775

Chiu, P.H., Kayali, M.A., Kishida, K.T., Tomlin, D., Klinger, L.G., Klinger, M.R., Montague, P.R., 2008. Self responses along cingulate cortex reveal quantitative neural phenotype for high-functioning autism. Neuron 57, 463–473. https://doi.org/10.1016/j.neuron.2007.12.020

Chung, M.K., Dalton, K.M., Alexander, A.L., Davidson, R.J., 2004. Less white matter concentration in autism: 2D voxel-based morphometry. Neuroimage 23, 242–251. https://doi.org/10.1016/j.neuroimage.2004.04.037

Courchesne, E., Campbell, K., Solso, S., 2011. Brain growth across the life span in autism: age-specific changes in anatomical pathology. Brain Res. 1380, 138–145. https://doi.org/10.1016/j.brainres.2010.09.101

Courchesne, E., Karns, C.M., Davis, H.R., Ziccardi, R., Carper, R.A., Tigue, Z.D., Chisum, H.J., Moses, P., Pierce, K., Lord, C., Lincoln, A.J., Pizzo, S., Schreibman, L., Haas,

R.H., Akshoomoff, N.A., Courchesne, R.Y., 2001. Unusual brain growth patterns in early life in patients with autistic disorder: an MRI study. Neurology 57, 245–254.
Davidovitch, M., Patterson, B., Gartside, P., 1996. Head circumference measurements in children with autism. J. Child Neurol. 11, 389–393.
Dawson, G., Jones, E.J.H., Merkle, K., Venema, K., Lowy, R., Faja, S., Kamara, D., Murias, M., Greenson, J., Winter, J., Smith, M., Rogers, S.J., Webb, S.J., 2012. Early behavioral intervention is associated with normalized brain activity in young children with autism. J Am Acad Child Adolesc Psychiatry 51, 1150–1159. https://doi.org/10.1016/j.jaac.2012.08.018
Dawson, G., Rogers, S., Munson, J., Smith, M., Winter, J., Greenson, J., Donaldson, A., Varley, J., 2010. Randomized, controlled trial of an intervention for toddlers with autism: the Early Start Denver Model. Pediatrics 125, e17-23. https://doi.org/10.1542/peds.2009-0958
D'Mello, A.M., Crocetti, D., Mostofsky, S.H., Stoodley, C.J., 2015. Cerebellar gray matter and lobular volumes correlate with core autism symptoms. Neuroimage Clin 7, 631–639. https://doi.org/10.1016/j.nicl.2015.02.007
Drevets, W.C., Savitz, J., Trimble, M., 2008. The Subgenual Anterior Cingulate Cortex in Mood Disorders. CNS spectr. 13, 663–681. https://doi.org/10.1017/S1092852900013754
Elder, L.M., Dawson, G., Toth, K., Fein, D., Munson, J., 2008. Head circumference as an early predictor of autism symptoms in younger siblings of children with autism spectrum disorder. J Autism Dev Disord 38, 1104–1111. https://doi.org/10.1007/s10803-007-0495-9
Fonov, V., Evans, A.C., Botteron, K., Almli, C.R., McKinstry, R.C., Collins, D.L., Brain Development Cooperative Group, 2011. Unbiased average age-appropriate atlases for pediatric studies. Neuroimage 54, 313–327. https://doi.org/10.1016/j.neuroimage.2010.07.033
Fonov, V.S., Janke, A., Caramanos, Z., Arnold, D.L., Narayanan, S., Pike, G.B., Collins, D.L., 2010. Improved Precision in the Measurement of Longitudinal Global and Regional Volumetric Changes via a Novel MRI Gradient Distortion Characterization and Correction Technique, in: Liao, H., Edwards, P.J. "Eddie," Pan, X., Fan, Y., Yang, G.-Z. (Eds.), Medical Imaging and Augmented Reality: 5th International Workshop, MIAR 2010, Beijing, China, September 19-20, 2010. Proceedings. Springer Berlin Heidelberg, Berlin, Heidelberg, pp. 324–333.
Frazier, T.W., Keshavan, M.S., Minshew, N.J., Hardan, A.Y., 2012. A two-year longitudinal MRI study of the corpus callosum in autism. J Autism Dev Disord 42, 2312–2322. https://doi.org/10.1007/s10803-012-1478-z
Genovese, C.R., Lazar, N.A., Nichols, T., 2002. Thresholding of statistical maps in functional neuroimaging using the false discovery rate. Neuroimage 15, 870–878. https://doi.org/10.1006/nimg.2001.1037
Girault, J.B., Swanson, M.R., Meera, S.S., Grzadzinski, R.L., Shen, M.D., Burrows, C.A., Wolff, J.J., Pandey, J., John, T.S., Estes, A., Zwaigenbaum, L., Botteron, K.N., Hazlett, H.C., Dager, S.R., Schultz, R.T., Constantino, J.N., Piven, J., for the IBIS Network, 2020. Quantitative trait variation in ASD probands and toddler sibling outcomes at 24 months. J Neurodevelop Disord 12, 5. https://doi.org/10.1186/s11689-020-9308-7
Gouttard, S., Styner, M., Prastawa, M., Piven, J., Gerig, G., 2008. Assessment of reliability of multi-site neuroimaging via traveling phantom study. Med Image Comput Comput Assist Interv 11, 263–270.

Hardan, A.Y., Minshew, N.J., Keshavan, M.S., 2000. Corpus callosum size in autism. Neurology 55, 1033–1036.
Hardan, A.Y., Pabalan, M., Gupta, N., Bansal, R., Melhem, N.M., Fedorov, S., Keshavan, M.S., Minshew, N.J., 2009. Corpus callosum volume in children with autism. Psychiatry Res 174, 57–61. https://doi.org/10.1016/j.pscychresns.2009.03.005
Hazlett, H.C., Gu, H., McKinstry, R.C., Shaw, D.W.W., Botteron, K.N., Dager, S.R., Styner, M., Vachet, C., Gerig, G., Paterson, S.J., Schultz, R.T., Estes, A.M., Evans, A.C., Piven, J., IBIS Network, 2012a. Brain volume findings in 6-month-old infants at high familial risk for autism. Am J Psychiatry 169, 601–608. https://doi.org/10.1176/appi.ajp.2012.11091425
Hazlett, H.C., Poe, M., Gerig, G., Smith, R.G., Provenzale, J., Ross, A., Gilmore, J., Piven, J., 2005. Magnetic resonance imaging and head circumference study of brain size in autism: birth through age 2 years. Arch. Gen. Psychiatry 62, 1366–1376. https://doi.org/10.1001/archpsyc.62.12.1366
Hazlett, H.C., Poe, M.D., Gerig, G., Styner, M., Chappell, C., Smith, R.G., Vachet, C., Piven, J., 2011. Early brain overgrowth in autism associated with an increase in cortical surface area before age 2 years. Arch. Gen. Psychiatry 68, 467–476. https://doi.org/10.1001/archgenpsychiatry.2011.39
Hazlett, H.C., Poe, M.D., Lightbody, A.A., Styner, M., MacFall, J.R., Reiss, A.L., Piven, J., 2012b. Trajectories of early brain volume development in fragile X syndrome and autism. J Am Acad Child Adolesc Psychiatry 51, 921–933. https://doi.org/10.1016/j.jaac.2012.07.003
Hazlett, Heather Cody, Gu, H., Munsell, B.C., Kim, S.H., Styner, Martin, Wolff, Jason J., Elison, Jed T., Swanson, M.R., Zhu, H., Botteron, Kelly N., Collins, D. Louis, Constantino, John N., Dager, Stephen R., Estes, Annette M., Evans, Alan C., Fonov, Vladimir S., Gerig, Guido, Kostopoulos, Penelope, McKinstry, Robert C., Pandey, J., Paterson, Sarah, Pruett, J.R., Schultz, Robert T., Shaw, Dennis W., Zwaigenbaum, Lonnie, Piven, Joseph, Piven, J., Hazlett, H. C., Chappell, C., Dager, S. R., Estes, A. M., Shaw, D. W., Botteron, K. N., McKinstry, R. C., Constantino, J. N., Pruett Jr, J.R., Schultz, R. T., Paterson, S., Zwaigenbaum, L., Elison, J. T., Wolff, J. J., Evans, A. C., Collins, D. L., Pike, G.B., Fonov, V. S., Kostopoulos, P., Das, S., Gerig, G., Styner, M., Gu, C.H., 2017. Early brain development in infants at high risk for autism spectrum disorder. Nature 542, 348–351. https://doi.org/10.1038/nature21369
Herbert, M.R., Ziegler, D.A., Makris, N., Filipek, P.A., Kemper, T.L., Normandin, J.J., Sanders, H.A., Kennedy, D.N., Caviness, V.S., 2004. Localization of white matter volume increase in autism and developmental language disorder. Annals of Neurology 55, 530–540. https://doi.org/10.1002/ana.20032
Horwitz, B., Rumsey, J.M., Grady, C.L., Rapoport, S.I., 1988. The cerebral metabolic landscape in autism. Intercorrelations of regional glucose utilization. Arch. Neurol. 45, 749–755.
IBIS network, Estes, A., Zwaigenbaum, L., Gu, H., St. John, T., Paterson, S., Elison, J.T., Hazlett, H., Botteron, K., Dager, S.R., Schultz, R.T., Kostopoulos, P., Evans, A., Dawson, G., Eliason, J., Alvarez, S., Piven, J., 2015. Behavioral, cognitive, and adaptive development in infants with autism spectrum disorder in the first 2 years of life. J Neurodevelop Disord 7, 24. https://doi.org/10.1186/s11689-015-9117-6
Just, M.A., Keller, T.A., Malave, V.L., Kana, R.K., Varma, S., 2012. Autism as a neural systems disorder: a theory of frontal-posterior underconnectivity. Neurosci Biobehav Rev 36, 1292–1313. https://doi.org/10.1016/j.neubiorev.2012.02.007
Kana, R.K., Keller, T.A., Cherkassky, V.L., Minshew, N.J., Just, M.A., 2009. Atypical frontal-posterior synchronization of Theory of Mind regions in autism during mental

state attribution. Soc Neurosci 4, 135–152. https://doi.org/10.1080/17470910802198510
Kennedy, D.P., Courchesne, E., 2008. Functional abnormalities of the default network during self- and other-reflection in autism. Social Cognitive and Affective Neuroscience 3, 177–190. https://doi.org/10.1093/scan/nsn011
Lainhart, J.E., Piven, J., Wzorek, M., Landa, R., Santangelo, S.L., Coon, H., Folstein, S.E., 1997. Macrocephaly in children and adults with autism. J Am Acad Child Adolesc Psychiatry 36, 282–290. https://doi.org/10.1097/00004583-199702000-00019
Langen, M., Bos, D., Noordermeer, S.D.S., Nederveen, H., van Engeland, H., Durston, S., 2014. Changes in the Development of Striatum Are Involved in Repetitive Behavior in Autism. Biological Psychiatry 76, 405–411. https://doi.org/10.1016/j.biopsych.2013.08.013
Lau, J.C., Lerch, J.P., Sled, J.G., Henkelman, R.M., Evans, A.C., Bedell, B.J., 2008. Longitudinal neuroanatomical changes determined by deformation-based morphometry in a mouse model of Alzheimer's disease. Neuroimage 42, 19–27. https://doi.org/10.1016/j.neuroimage.2008.04.252
Lerch, J., Hammill, C., van Eede, M., Cassel, D., 2017. RMINC: Statistical Tools for Medical Imaging NetCDF (MINC) Files.
Liu, J., Yao, L., Zhang, W., Xiao, Y., Liu, L., Gao, X., Shah, C., Li, S., Tao, B., Gong, Q., Lui, S., 2017. Gray matter abnormalities in pediatric autism spectrum disorder: a meta-analysis with signed differential mapping. Eur Child Adolesc Psychiatry 26, 933–945. https://doi.org/10.1007/s00787-017-0964-4
Lord, C., Rutter, M., Dilavore, P.C., Risi, S., 2000. Autism Diagnostic Observation Schedule. Western Psychological Services, Los Angeles, CA.
Manes, F., Piven, J., Vrancic, D., Nanclares, V., Plebst, C., Starkstein, S.E., 1999. An MRI study of the corpus callosum and cerebellum in mentally retarded autistic individuals. J Neuropsychiatry Clin Neurosci 11, 470–474.
McAlonan, G.M., Cheung, V., Cheung, C., Suckling, J., Lam, G.Y., Tai, K.S., Yip, L., Murphy, D.G.M., Chua, S.E., 2005. Mapping the brain in autism. A voxel-based MRI study of volumetric differences and intercorrelations in autism. Brain 128, 268–276. https://doi.org/10.1093/brain/awh332
McDonald, A.J., 1998. Cortical pathways to the mammalian amygdala. Progress in Neurobiology 55, 257–332. https://doi.org/10.1016/S0301-0082(98)00003-3
McKinnon, C.J., Eggebrecht, A.T., Todorov, A., Wolff, J.J., Elison, J.T., Adams, C.M., Snyder, A.Z., Estes, A.M., Zwaigenbaum, L., Botteron, K.N., McKinstry, R.C., Marrus, N., Evans, A., Hazlett, H.C., Dager, S.R., Paterson, S.J., Pandey, J., Schultz, R.T., Styner, M.A., Gerig, G., Schlaggar, B.L., Petersen, S.E., Piven, J., Pruett, J.R., 2019. Restricted and Repetitive Behavior and Brain Functional Connectivity in Infants at Risk for Developing Autism Spectrum Disorder. Biological Psychiatry: Cognitive Neuroscience and Neuroimaging 4, 50–61. https://doi.org/10.1016/j.bpsc.2018.09.008
Mostofsky, S.H., Burgess, M.P., Gidley Larson, J.C., 2007. Increased motor cortex white matter volume predicts motor impairment in autism. Brain 130, 2117–2122. https://doi.org/10.1093/brain/awm129
Ozonoff, S., Young, G.S., Carter, A., Messinger, D., Yirmiya, N., Zwaigenbaum, L., Bryson, S., Carver, L.J., Constantino, J.N., Dobkins, K., Hutman, T., Iverson, J.M., Landa, R., Rogers, S.J., Sigman, M., Stone, W.L., 2011. Recurrence Risk for Autism Spectrum Disorders: A Baby Siblings Research Consortium Study. PEDIATRICS peds.2010-2825. https://doi.org/10.1542/peds.2010-2825
Pereira, A.M., Campos, B.M., Coan, A.C., Pegoraro, L.F., de Rezende, T.J.R., Obeso, I., Dalgalarrondo, P., da Costa, J.C., Dreher, J.-C., Cendes, F., 2018. Differences in

Cortical Structure and Functional MRI Connectivity in High Functioning Autism. Front. Neurol. 9, 539. https://doi.org/10.3389/fneur.2018.00539
Piven, J., Arndt, S., Bailey, J., Andreasen, N., 1996. Regional Brain Enlargement in Autism: A Magnetic Resonance Imaging Study. Journal of the American Academy of Child & Adolescent Psychiatry 35, 530–536. https://doi.org/10.1097/00004583-199604000-00020
Piven, J., Arndt, S., Bailey, J., Havercamp, S., Andreasen, N.C., Palmer, P., 1995. An MRI study of brain size in autism. Am J Psychiatry 152, 1145–1149.
Piven, J., Bailey, J., Ranson, B.J., Arndt, S., 1997. An MRI study of the corpus callosum in autism. Am J Psychiatry 154, 1051–1056. https://doi.org/10.1176/ajp.154.8.1051
Puce, A., Allison, T., Asgari, M., Gore, J.C., McCarthy, G., 1996. Differential Sensitivity of Human Visual Cortex to Faces, Letterstrings, and Textures: A Functional Magnetic Resonance Imaging Study. J. Neurosci. 16, 5205–5215. https://doi.org/10.1523/JNEUROSCI.16-16-05205.1996
Qiu, T., Chang, C., Li, Y., Qian, L., Xiao, C.Y., Xiao, T., Xiao, X., Xiao, Y.H., Chu, K.K., Lewis, M.H., Ke, X., 2016. Two years changes in the development of caudate nucleus are involved in restricted repetitive behaviors in 2–5-year-old children with autism spectrum disorder. Developmental Cognitive Neuroscience 19, 137–143. https://doi.org/10.1016/j.dcn.2016.02.010
Ray, R.D., Zald, D.H., 2012. Anatomical insights into the interaction of emotion and cognition in the prefrontal cortex. Neuroscience & Biobehavioral Reviews 36, 479–501. https://doi.org/10.1016/j.neubiorev.2011.08.005
Raznahan, A., Toro, R., Daly, E., Robertson, D., Murphy, C., Deeley, Q., Bolton, P.F., Paus, T., Murphy, D.G.M., 2010. Cortical Anatomy in Autism Spectrum Disorder: An In Vivo MRI Study on the Effect of Age. Cerebral Cortex 20, 1332–1340. https://doi.org/10.1093/cercor/bhp198
Redcay, E., Courchesne, E., 2005. When is the brain enlarged in autism? A meta-analysis of all brain size reports. Biol. Psychiatry 58, 1–9. https://doi.org/10.1016/j.biopsych.2005.03.026
Rojas, D.C., Peterson, E., Winterrowd, E., Reite, M.L., Rogers, S.J., Tregellas, J.R., 2006. Regional gray matter volumetric changes in autism associated with social and repetitive behavior symptoms. BMC Psychiatry 6, 56. https://doi.org/10.1186/1471-244X-6-56
Rutter, M., Bailey, A., Lord, C., 2003a. Autism Diagnostic Interview, Revised. Western Psychological Services, Los Angeles, CA.
Rutter, M., Bailey, A., Lord, C., Berument, S., 2003b. Social Communication Questionnaire. Western Psychological Services, Los Angeles, CA.
Schreibman, L., Dawson, G., Stahmer, A.C., Landa, R., Rogers, S.J., McGee, G.G., Kasari, C., Ingersoll, B., Kaiser, A.P., Bruinsma, Y., McNerney, E., Wetherby, A., Halladay, A., 2015. Naturalistic Developmental Behavioral Interventions: Empirically Validated Treatments for Autism Spectrum Disorder. J Autism Dev Disord 45, 2411–2428. https://doi.org/10.1007/s10803-015-2407-8
Schumann, C.M., Barnes, C.C., Lord, C., Courchesne, E., 2009. Amygdala enlargement in toddlers with autism related to severity of social and communication impairments. Biol. Psychiatry 66, 942–949. https://doi.org/10.1016/j.biopsych.2009.07.007
Shire, S.Y., Chang, Y.-C., Shih, W., Bracaglia, S., Kodjoe, M., Kasari, C., 2017. Hybrid implementation model of community-partnered early intervention for toddlers with autism: a randomized trial. J Child Psychol Psychiatr 58, 612–622. https://doi.org/10.1111/jcpp.12672

Sled, J.G., Zijdenbos, A.P., Evans, A.C., 1998. A nonparametric method for automatic correction of intensity nonuniformity in MRI data. IEEE Trans Med Imaging 17, 87–97. https://doi.org/10.1109/42.668698

Stevens, F.L., Hurley, R.A., Taber, K.H., 2011. Anterior cingulate cortex: unique role in cognition and emotion. J Neuropsychiatry Clin Neurosci 23, 121–125. https://doi.org/10.1176/jnp.23.2.jnp121

Stevenson, R.E., Schroer, R.J., Skinner, C., Fender, D., Simensen, R.J., 1997. Autism and macrocephaly. Lancet 349, 1744–1745. https://doi.org/10.1016/S0140-6736(05)62956-X

Stoodley, C.J., 2014. Distinct regions of the cerebellum show gray matter decreases in autism, ADHD, and developmental dyslexia. Frontiers in Systems Neuroscience 8. https://doi.org/10.3389/fnsys.2014.00092

Swanson, M.R., Wolff, J.J., Elison, J.T., Gu, H., Hazlett, H.C., Botteron, K., Styner, M., Paterson, S., Gerig, G., Constantino, J., Dager, S., Estes, A., Vachet, C., Piven, J., IBIS Network, 2015. Splenium development and early spoken language in human infants. Dev Sci. https://doi.org/10.1111/desc.12360

Velasquez, F., Wiggins, J.L., Mattson, W.I., Martin, D.M., Lord, C., Monk, C.S., 2017. The influence of 5-HTTLPR transporter genotype on amygdala-subgenual anterior cingulate cortex connectivity in autism spectrum disorder. Dev Cogn Neurosci 24, 12–20. https://doi.org/10.1016/j.dcn.2016.12.002

Waiter, G.D., Williams, J.H.G., Murray, A.D., Gilchrist, A., Perrett, D.I., Whiten, A., 2004. A voxel-based investigation of brain structure in male adolescents with autistic spectrum disorder. NeuroImage 22, 619–625. https://doi.org/10.1016/j.neuroimage.2004.02.029

Wallace, G.L., Dankner, N., Kenworthy, L., Giedd, J.N., Martin, A., 2010. Age-related temporal and parietal cortical thinning in autism spectrum disorders. Brain 133, 3745–3754. https://doi.org/10.1093/brain/awq279

Wang, S.S.-H., Kloth, A.D., Badura, A., 2014. The cerebellum, sensitive periods, and autism. Neuron 83, 518–532. https://doi.org/10.1016/j.neuron.2014.07.016

Weinstein, M., Ben-Sira, L., Levy, Y., Zachor, D.A., Itzhak, E.B., Artzi, M., Tarrasch, R., Eksteine, P.M., Hendler, T., Bashat, D.B., 2011. Abnormal white matter integrity in young children with autism. Hum. Brain Mapp. 32, 534–543. https://doi.org/10.1002/hbm.21042

Wolff, J.J., Gerig, G., Lewis, J.D., Soda, T., Styner, M.A., Vachet, C., Botteron, K.N., Elison, J.T., Dager, S.R., Estes, A.M., Hazlett, H.C., Schultz, R.T., Zwaigenbaum, L., Piven, J., IBIS Network, 2015. Altered corpus callosum morphology associated with autism over the first 2 years of life. Brain 138, 2046–2058. https://doi.org/10.1093/brain/awv118

Wolff, J.J., Gu, H., Gerig, G., Elison, J.T., Styner, M., Gouttard, S., Botteron, K.N., Dager, S.R., Dawson, G., Estes, A.M., Evans, A.C., Hazlett, H.C., Kostopoulos, P., McKinstry, R.C., Paterson, S.J., Schultz, R.T., Zwaigenbaum, L., Piven, J., IBIS Network, 2012. Differences in white matter fiber tract development present from 6 to 24 months in infants with autism. Am J Psychiatry 169, 589–600. https://doi.org/10.1176/appi.ajp.2011.11091447

Woodhouse, W., Bailey, A., Rutter, M., Bolton, P., Baird, G., Le Couteur, A., 1996. Head circumference in autism and other pervasive developmental disorders. J Child Psychol Psychiatry 37, 665–671.

Wu, H.-F., Chen, Y.-J., Chu, M.-C., Hsu, Y.-T., Lu, T.-Y., Chen, I.-T., Chen, P., Lin, H.-C., 2018. Deep Brain Stimulation Modified Autism-Like Deficits via the Serotonin System in a Valproic Acid-Induced Rat Model. IJMS 19, 2840. https://doi.org/10.3390/ijms19092840

Xiao, Z., Qiu, T., Ke, X., Xiao, X., Xiao, T., Liang, F., Zou, B., Huang, H., Fang, H., Chu, K., Zhang, J., Liu, Y., 2014. Autism Spectrum Disorder as Early Neurodevelopmental Disorder: Evidence from the Brain Imaging Abnormalities in 2–3 Years Old Toddlers. J Autism Dev Disord 44, 1633–1640. https://doi.org/10.1007/s10803-014-2033-x

Chapter 4
Developmental Trajectories of Neuroanatomical Alterations Associated with the 16p11.2 Copy Number Variations

Preface

In this chapter, we present a normalization technique that allows the study of morphometric differences across childhood and adolescence (4 to 22 years of age). Pediatric neuroimaging studies typically struggle to recruit a large number of normally developing controls, sufficient to properly model the underlying normal neurodevelopmental processes. We propose the use of a normative database (the NIHPD database (Evans, 2006)) to model the normal growth trajectories of brain volumes as well as in a voxel-wise fashion using TBM. We applied this method to a study of 16p11.2 copy number variants, a genetic disorder associated with several neurodevelopmental disorders, including autism spectrum disorder (ASD). 16p11.2 copy number variants can be present as a deletion or a duplication, and typically present opposing phenotypes.

Our results show that brain volume abnormalities are already present at 4 years of age in both deletion and duplication groups and seem to remain stable throughout childhood and adolescence.

Note to the reader: To facilitate reading, all supplementary figures and tables referenced in the present Chapter can be found in the Supplementary Material section at the end of this Chapter.

This work has been published as:
Cárdenas-de-la-Parra, A., Martin-Brevet, S., Moreau, C., Rodriguez-Herreros, B., Fonov, V.S., Maillard, A.M., Zürcher, N.R., Hadjikhani, N., Beckmann, J.S., Reymond, A., Draganski, B., 16p11.2 European Consortium, Jacquemont, S., Collins, D.L., 2019. Developmental trajectories of neuroanatomical alterations associated with the 16p11.2 Copy Number Variations. NeuroImage 203, 116155.
https://doi.org/10.1016/j.neuroimage.2019.116155

Developmental trajectories of neuroanatomical alterations associated with the 16p11.2 Copy Number Variations

Alonso Cárdenas-de-la-Parra[1]*, Sandra Martin-Brevet[2,3]*, Clara Moreau[4], Borja Rodriguez-Herreros[2,4], Vladimir S. Fonov[1], Anne M. Maillard[2,5], Nicole R. Zürcher[6], 16p11.2 European Consortium, Nouchine Hadjikhani[6,7], Jacques S. Beckmann[2], Alexandre Reymond[8], Bogdan Draganski[3,9], Sébastien Jacquemont[2,4]**, D. Louis Collins[1]**

* shared 1st authorship

** shared senior authorship

The 16p11.2 European Consortium collaborators are listed at the end of this article.

[1] Department of Biological and Biomedical Engineering, Montreal Neurological Institute, Montreal, Quebec, Canada.

[2] Service of Medical Genetics, Centre Hospitalier Universitaire Vaudois and University of Lausanne, Lausanne, Switzerland

[3] LREN, Département des neurosciences cliniques, Centre Hospitalier Universitaire Vaudois and University of Lausanne, Lausanne, Switzerland

[4] CHU Sainte-Justine Research Center, Université de Montréal, Montréal, QC, Canada

[5] Centre Cantonal Autisme, Centre Hospitalier Universitaire Vaudois and University of Lausanne, Lausanne, Switzerland

[6] Athinoula A. Martinos Center for Biomedical Imaging, Department of Radiology, Massachusetts General Hospital, Harvard Medical School, Boston, MA, USA

[7] Gillberg Neuropsychiatry Centre, Göteborg, Sweden

[8] Center for Integrative Genomics, University of Lausanne, Lausanne, Switzerland

[9] Department of Neurology, Max Planck Institute for Human Cognitive and Brain Sciences, Leipzig, Germany

NeuroImage 203, 116155

Abstract

Most of human genome is present in two copies (maternal and paternal). However, segments of the genome can be deleted or duplicated, and many of these genomic variations (known as Copy Number Variants) are associated with psychiatric disorders. 16p11.2 copy number variants (breakpoint 4-5) confer high risk for neurodevelopmental disorders and are associated with structural brain alterations of large effect-size. Methods used in previous studies were unable to investigate the onset of these alterations and whether they evolve with age. In this study, we aim at characterizing age-related effects of 16p11.2 copy number variants by analyzing a group with a broad age range including younger individuals. A large normative developmental dataset was used to accurately adjust for effects of age. We normalized volumes of segmented brain regions as well as volumes of each voxel defined by tensor-based morphometry. Results show that the total intracranial volumes, the global gray and white matter volumes are respectively higher and lower in deletion and duplication carriers compared to control subjects at 4.5 years of age. These differences remain stable through childhood, adolescence and adulthood until 23 years of age (range: 0.5 to 1.0 Z-score). Voxel-based results are consistent with previous findings in 16p11.2 copy number variant carriers, including increased volume in the calcarine cortex and insula in deletions, compared to controls, with an inverse effect in duplication carriers (1.0 Z-score). All large effect-size voxel-based differences are present at 4.5 years and seem to remain stable until the age of 23. Our results highlight the stability of a neuroimaging endophenotype over 2 decades during which neurodevelopmental symptoms evolve at a rapid pace.

Keywords: 16p11.2 Copy number variants; Neurodevelopmental disorders; Genetics; Imaging; Brain development; Normative growth trajectories

1 Introduction

Most of human genome is present in two copies (a maternal and paternal copy). However, large segments of the genome can be deleted or duplicated and are therefore present in one or three copies respectively. While these genomic variations (known as Copy Number Variants, CNVs) can often be harmless, many have also been associated with neurodevelopmental and psychiatric disorders. The ~600kb 16p11.2 CNVs (chromosome 16, locus 11.2, breakpoints (BP) 4–5, 29.6-30.2 Mb-Hg19) are strongly associated with neurodevelopmental disorders (Weiss et al., 2008). Deletion and duplication carriers have a 10-fold increased risk of developing autism spectrum disorders (ASD) (Moreno-De-Luca et al., 2013), and duplication (but not deletion) carriers a 10-fold increased risk for schizophrenia (Marshall et al., 2017). Genetic variants associated with psychiatric disorders offer unique opportunity to study the effects of the same molecular mechanisms on brain structure and behavior across different neurodevelopmental periods.

Deletion and duplications at the 16p11.2 locus have "mirror" effects on head circumference, increasing and decreasing respectively with differences becoming apparent before two years of age (D'Angelo et al., 2016). At the macroscopic level, total gray and white matter volumes correlate negatively with the number of genomic copies (Maillard et al., 2015; Qureshi et al., 2014), with increased volume in deletion and volume loss in duplication carriers when compared to non-carriers. Previous studies in deletion carriers report regional structural differences in the insula, calcarine cortex and superior, middle, transverse temporal gyri, which are independent of head size alterations. Duplication carriers show differences in the insula, caudate and hippocampus (Martin-Brevet et al., 2018). These findings are observed independently of sex and ascertainment (ie. the presence or absence of a psychiatric diagnosis). Alterations are present in adolescents as well as in adults. In the absence of proper normative data we have been unable to accurately adjust for age effects. It is unknown when these alterations appear during brain development or whether they are modified across childhood and adolescence.

Given that genes included in the 16p11.2 interval are expressed throughout early brain development (Lin et al., 2015), we hypothesized that the established pattern of brain alterations associated with 16p11.2 CNVs might appear during early childhood. We aimed to characterize brain growth in 16p11.2 CNVs carriers by comparing global and regional developmental trajectories to those of healthy children. Considering the fact that most of the brain measures

do not show linear changes across childhood and adolescence (Giedd et al., 1999), we assume that it is very difficult, if not impossible, to properly correct for age based on small control groups. Instead, large normative developmental datasets are required to infer these trajectories. We (Aubert-Broche et al., 2013) have previously developed a longitudinal image processing pipeline and Z-scoring method to adjust for age- and sex effects on brain growth trajectories using the NIH MRI study of normal brain development (NIHPD) (Evans and Brain Development Cooperative Group, 2006). This normalizing method extended to whole-brain voxel-level data, where all Jacobian determinants of a deformation field were used as a surrogate metric of relative local tissue volume. This approach has been successful in the study of pediatric-onset multiple sclerosis (Aubert-Broche et al., 2014). In the present study, we use similar methods to Z-score a cross-sectional 16p11.2 dataset (56 deletion carriers, 19 duplication carriers, 105 control individuals, including data on 8 individuals not analyzed in previous studies) to identify global and voxel-based differences between groups.

2 Material and methods

2.1 Participants

2.1.1 16p11.2 CNVs cohort

Cross-sectional data was acquired in 2 different cohorts (the European -EU 16p11.2 consortium and the Simons VIP -SVIP study in North America) of 180 individuals (Martin-Brevet et al., 2018; The Simons VIP Consortium, 2012). In order to be able to normalize with NIHPD data, we only included participants between 4.5 to 23 years of age. This included 56 16p11.2 BP4-5 deletion carriers (DEL) from American (n=42) and European (=14) cohorts; 19 duplication carriers (DUP) from American (n=15) and European (n=4) cohorts); and 105 controls (CTRL), from American (n=75) and European cohorts (n=30). Four controls, 3 duplication and 1 deletion carriers were not included in our previous publication (Martin-Brevet et al., 2018). CNV carriers were either probands referred for genetic testing or relatives of probands. The controls were recruited among non-carriers first-degree relatives of CNV carriers (n=34) or volunteers from the general population who did not have a relative with a neurodevelopmental disorder (n=71). The study was approved by the institutional review boards of each consortium, and signed informed consents were obtained from the participants or their legal representatives. Demographics, age distribution and neuropsychiatric diagnoses are detailed in Table 4, Supplementary Figure 2, Supplementary Table 1. Because our analysis

covers a broad age range, there is increased risk of systematic age-dependent motion artefacts. We performed a thorough visual quality control check looking for evidence of motion artefacts.

Table 4. Population characteristics of the 16p11.2 dataset

	DEL	CTRL	DUP
N	56	105	19
Age (years)			
Mean (SD)	11.26 (3.62)[1]	14.15 (4.24)	12.29 (4.87)
range (min-max)	6.33-22.33	4.67-22.92	5-20.33
Sex (M/F)	29/27	67/38	13/6
Scan parameter (Multi/Single echo acquisition)	38/18	76/29	12/7
NVIQ Mean (SD)	87 (14)[2]	108 (12)	77 (19)[2]
Ancestry			
African-American	0	12	0
Asian	1	1	0
White	50	35	15
Mixed and Other	4	8	2

[1] *Deletion carriers significantly younger than control individuals (t = -4.5272, p= 1.347e-05)*

[2] *Mean NVIQ is significantly lower in deletion and duplication carriers than control individuals (respectively t = -9.3194, p=1.0126e-14; t = -6.6931, p=4.18997e-06)*

DEL, deletion carriers; CTRL, control individuals; DUP, duplication carriers; N, sample size; SD, standard deviation; M, male; F, female; NVIQ, non-verbal intelligent quotient. Ancestry is unknown for 3 CNV carriers and 49 controls.

2.1.2 General population – NIHPD cohort

As normative reference data for brain growth, we used the multi-site longitudinal data from Objective 1 (i.e. initial time-point for enrolment from 4.5 and 18.5 years) of the publicly available NIHPD project (Evans and Brain Development Cooperative Group, 2006). The normative model (Aubert-Broche et al., 2011) used data from 339 children (179 females and 160 males), scanned longitudinally at 2 or 3 time points, with approximately 24 months between scans and mean age at first scan of 11.0 years, for a total of 874 scans. Only subjects that passed quality control were included. Supplementary Figure 1 shows the age distribution of the data for the NIHPD cohort.

2.2 MRI protocol

The MRI data from the 16p11.2 individuals included T1-weighted (T1w) anatomical images acquired at 7 sites using different 3T scanners: Philips Achieva, Siemens Prisma Syngo and Siemens Tim Trio. The MRI protocol included a whole-brain, 3D T1w magnetization prepared rapid gradient echo sequence (MPRAGE) with 1-mm-thick sagittal slices. Three sites used multi-echo sequences for 126 participants (38 DEL, 12 DUP, 76 CTRL with 5 familial and 71 unrelated CTRL), and 4 sites used single-echo sequences for 54 participants (18 DEL, 7 DUP and 29 familial CTRL). Details of the scanners and image acquisition sequences can be found in Supplementary Table 2. Extensive analyses on the potential effect of these scanning sites and protocols were performed in a previous study showing that none of the regions associated with the 16p11.2 deletion or duplication could be attributed to artifacts introduced by the multisite analyses (Martin-Brevet et al., 2018).

Scans of the NIHPD controls were obtained at 6 study centers with 1.5 Tesla MRI scanners from Philips, General Electric or Siemens Medical Systems. The MRI protocol included a whole-brain, 3D T1w RF-spoiled gradient echo sequence (1-mm-thick sagittal partitions, TR 22–25 msec, TE 10–11 msec, excitation pulse angle 30°, Field Of View 160–180 mm). Details on acquisition and participants were previously published (Evans and Brain Development Cooperative Group, 2006).

2.3 Image processing

The longitudinal automatic image processing pipeline, developed for NIHPD analysis (Aubert-Broche et al., 2013), was adapted to the scans from the 16p11.2 dataset as described below. The preprocessing steps applied to the native T1w images were (1) denoising, (2) intensity inhomogeneity correction using the N3 algorithm (Sled et al., 1998), and (3) intensity normalization by histogram matching to the ICBM152 template (Fonov et al., 2011). A hierarchical 9-parameter linear registration based on an intensity cross-correlation similarity measure was performed between the T1w images and the ICBM152 template to align the images with the stereotaxic population template (Collins et al., 1994). Brain extraction was achieved using the Brain Extraction based on nonlocal Segmentation Technique (BEaST) (Eskildsen et al., 2012), a multi-resolution, nonlocal patch-based segmentation technique. Subsequently, images were non-linearly registered using the Automated Nonlinear Image Matching and Anatomical Labelling (ANIMAL) algorithm (Collins et al., 1995), a hierarchical, multi-scale registration algorithm. Whole-brain, individual lobes, thalamus, putamen, caudate,

globus pallidus and ventricular volumes were calculated, with the right and left volumes combined for analysis.

To investigate brain alterations beyond *a priori* specified anatomical regions of interest, we used Tensor Based Morphometry (TBM), which enables a whole-brain voxel-by-voxel statistical analysis while accounting for brain size. TBM uses the deformation fields resulting from a non-linear registration to an appropriate template to analyze group differences and quantify changes in morphology (Frackowiak, 2004; Lau et al., 2008). The non-linear deformation grids for each scan's registration to the ICBM152 template were inverted, effectively yielding a voxel-by-voxel nonlinear mapping from the ICBM152 template reference space to the space of each linearly registered scan. A 3D Gaussian filter with FWHM of 10 mm was applied to the resulting inverted deformation grids. The Jacobian determinant of the deformation field was computed for every voxel, log-transformed and used as a surrogate of the local volume difference between each subject and the ICBM152 template. In general, a log-transformed Jacobian determinant value less than 0 represents shrinking from the template to the native space, a value of 0 indicates that there is no volume change in the voxel and a value of more than 0 indicates enlargement with respect to the template. When Jacobian determinant measures are applied to normative datasets such as the NIHPD study (Aubert-Broche et al., 2011; Frackowiak, 2004), it enables the estimation of voxel-wise trajectories of brain development.

2.4 Data analyses

2.4.1 Z-scoring for the main effect of age and gender for global and voxel-based volumes

To compute Z-scores that normalize for the effect of growth and sex in a pediatric population, we modeled the effect of those 2 variables in the NIHPD normative dataset. Mixed-effect models were used since it is appropriate to estimate growth in longitudinal studies that take repeated measures from the same individuals over time. It accounts for the within-participant correlation and for varying numbers of measurements for each participant.

As we previously described (Aubert-Broche et al., 2013), individual profiles suggest modeling brain growth as a quadratic function over time: we included both linear and quadratic effects of age in the fixed effects structure. Age was not divided into bins, but was considered as a continuous variable and was centered at 13 years - the mean age of NIHPD cohort. Linear effect of sex was also included in the fixed terms (Aubert-Broche et al., 2013).

The mixed-effects model that best fits the normative data is:

$$Vol_i = \beta_0 + \gamma_0 + (\beta_1 + \gamma_1)(Age_i - 13) + \beta_2(Age_i - 13)^2 + \beta_3 Sex_i + \varepsilon_i \qquad (17)$$

where

• Vol_i is the value of the response variable (global brain volume or voxel) for subject *i,*

• Age_i, $Age^2_{i,}$ Sex_i are the fixed and random effect explanatory variables for subject *i*,

• $\beta_{0,}$ γ_0 are the intercept for the fixed and random terms,

• $\beta_{1,}$ $\beta_{2,}$ β_3 are the fixed effects coefficients and are identical for all subjects,

• γ_1 is a random effect coefficient,

• ε_i is the error in subject *i*. The errors for subject *i* are assumed to have mean zero and constant independent variance.

Using the mean and the estimated standard deviation of the model we were able to compute Z-scores for the global volumes of the brain as well as for each voxel independently, for the 16p11.2 and control participants using the following formula: $z=(x-\bar{x})/s$. x is the sample value (i.e. the volume or Jacobian of an individual subject), $\bar{x}$ is the estimated mean from the Mixed Effects model of the NIHPD cohort, and s is an estimate of the standard deviation, calculated from the variance-covariance matrix of the fixed effects along with the residual variance of the random effects. Supplementary Figure 3 shows the resulting Mixed-Effects fit on Total Brain Volume for the NIHPD population.

2.4.2 Correcting for scanning protocol between NIHPD normative data and 16p11.2 case-control data

After normalization of the 16p11.2 controls, we observed that certain regions required small additional corrections attributed to differences in scanning parameters between the NIHPD and the 16p11.2 data (e.g. 1.5 T vs 3T scans). We estimated a linear model that included Age and Intercept (i.e. bias and slope) for the Z-scored segmented volumes and the voxel-wise log-transformed Jacobian determinants of the 16p11.2 control data. The parameters of this linear model were used to adjust the 16p11.2 control dataset in order to obtain a mean Z-score of 0 for all ages. Supplementary Figure 4 shows a linear fit of the controls before and after normalization. The same adjustment was applied to the CNV carrier groups. This correction shows that there is a simple linear effect of the scanning protocol. This linear effect is the same between the NIHPD and 16p11.2 control data as well as between the NIHPD and 16p11.2 CNV carrier data. The intercepts and the slopes were, respectively -0.68 / -0.04 for the total brain

volume; -0.11 / -0.1 for the gray matter volume (GM); 0.42 / 0.05 for the white matter volume (WM) and -0.32 / -0.02 for the lateral ventricle (LV). Regarding voxel-based mean Z-scores, 16p11.2 CTRL also show deviations from the baseline of NIHPD controls, in particular in the left putamen and the medial frontal cortex (Z-scores between -0.88 and 1.09) (Supplementary Figure 5.A).

2.4.3 Analyzing the age-related effects of deletions and duplications on brain structure

We used a linear model introducing genetic status as a covariate to investigate the effect of the DEL and DUP on normalized segmented regional and voxel-level adjusted Z-scores volumes. The following interaction terms were tested : age*sex and age*group.

We extracted the p-values from the linear models. Results for the 4 global volumes are Bonferroni corrected for 8 simultaneous comparisons (4 × DEL vs CTRL and 4 × DUP vs CTRL). Results for the voxel-wise analysis are adjusted using Benjamini-Hochberg False Discovery Rate – FDR correction ($q<0.05$) (Benjamini and Hochberg, 1995). Regions with significant differences were anatomically labeled using the neuromorphometric atlas (http://www.neuromorphometrics.com).

All analyses were conducted using R 3.4.0 (The R Project for Statistical Computing; http://www.R-project.org/). The mixed-effect models were built using the *nlme* package.

3 Results

Data was analyzed for 56 DEL, 19 DUP, 105 familial and unrelated CTRL with ages ranging from 4.5 to 23 years. The clinical phenotype description of the participants is provided in Table 4.

3.1 Developmental trajectory of total intracranial, global gray and white matter volumes for deletion and duplication carriers

16p11.2 carriers present an inverse gene dosage effect for most of the global metrics. Deletion carriers have higher volume than controls for total brain (mean Z-score=1.165, p-value<0.0001), gray (mean Z-score=0.414, p-value=0.00433) and white matter volumes (mean Z-score=0.693, p-value<0.0001) (Figure 17). Duplication carriers show the opposite effect, with lower total brain (mean Z-score=-1.17, p-value=0.0001), gray (mean Z-score=-0.631, p-value=0.00272) and white matter volume (mean Z-score=-0.53, p-value=0.0018) compared to

controls. Duplication carriers have larger lateral ventricles, with mean Z-score of 1.629 (p-value<0.0001).

We do not observe any interaction between the effects of genetic groups and age nor between sex and age. These global brain differences are unchanged across the full age range in our dataset (Figure 17).

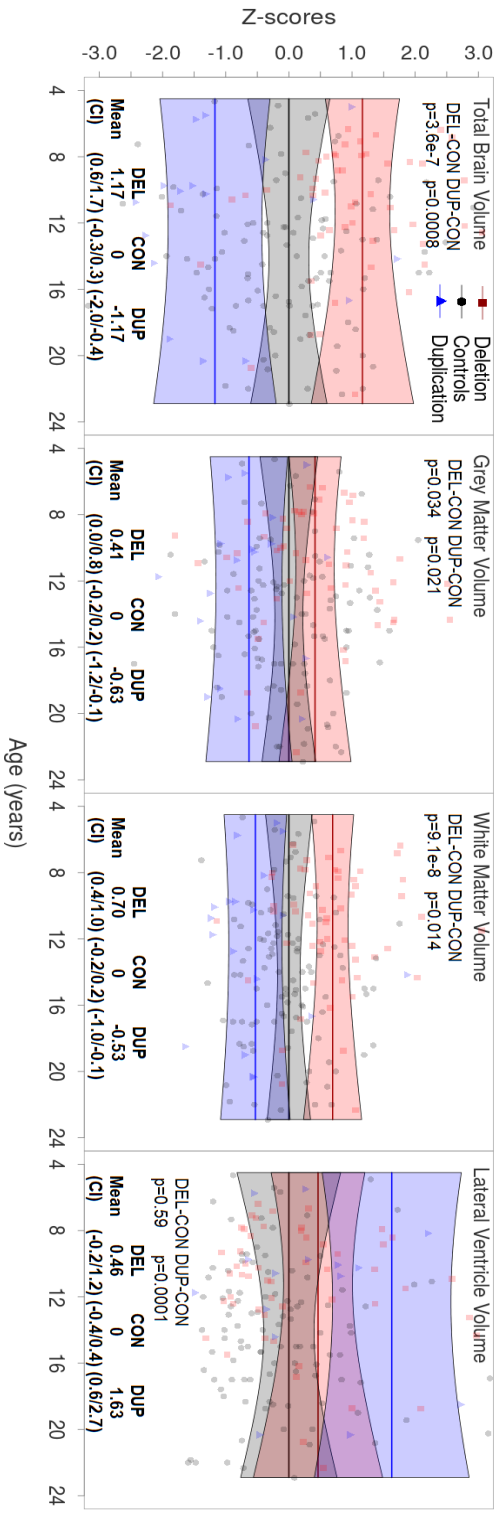

Figure 17.- Developmental trajectory of global brain metrics. Trajectory of the global brain metrics for the 3 genetic groups show an inverse gene dosage effect, the differences between groups are already present at 4.5 years and identical through the development until 23 years of age. Raw values of each metrics are corrected for age and protocol (i.e. single echo vs multi echo scans) through a linear model, then values from control individuals are centered to 0 for visualization purposes. For each of the genetic groups, fitted lines represent the predicted mean computed per age range of 2.4 months, polygons represent the confidence interval at each age, the points are normalized subject-level data-points. Mean (minimum/maximum of the confidence interval) are presented in the table. P-values are corrected with Bonferroni correction for 8 simultaneous comparisons (p<0.05). DEL: deletion carriers; CTRL: control individuals; DUP: duplication carriers.

3.2 Developmental trajectory of regional voxel-based differences

The TBM analysis identifies several brain regions associated with an inverse gene dosage effect: Deletion carriers have significantly higher Jacobian determinants than controls, whereas duplication have significantly lower values (i.e. DEL>CTRL>DUP) in the following regions: bilateral calcarine cortex, insula, left transverse temporal gyrus, planum temporale and parietal operculum. Reciprocal inverse gene dosage effects are also present in the frontal and occipital white matter (Supplemental Table 2, Figure 18).

Differences predominantly or specifically associated with DEL include increased Jacobian determinants values in the cuneus, anterior cingulate, posterior orbital and inferior frontal gyri. Regions predominantly decreased in DEL compared to controls include the bilateral cerebellum, middle cingulate gyrus, pallidum, putamen, precentral and post-central gyri, fusiform gyrus, middle and inferior temporal gyri, supplementary motor cortex, gyrus rectus, left accumbens area and angular gyrus. The only region predominantly or specifically associated with DUP is the occipital fusiform gyrus with a decrease in volume compared to controls as well as the lateral ventricles that are increased in DUP. Additional regions with smaller significant clusters are described in Supplemental Table 2.

We did not identify any effect of age for any of the clusters described above. Figure 19 shows this complete lack of age-related effects for the top 8 regional differences with the largest effect sizes. Whatever the age, the DEL have volume Z-scores of 0.7 and 1 for the anterior insula and the calcarine cortex respectively, and the DUP have volume Z-scores of -0.9 and -1.2 on the same structures. DEL have volume Z-scores of 0.9 and 0.7 for the posterior orbital and anterior cingulate gyri respectively; they have the most negative volume Z-scores: -1.6 and -1.1 for the cerebellar hemispheres and the fusiform gyrus. DUP have also high volume Z-scores for the lateral ventricle and inferior temporal gyrus, 1.6 and 0.9 respectively.

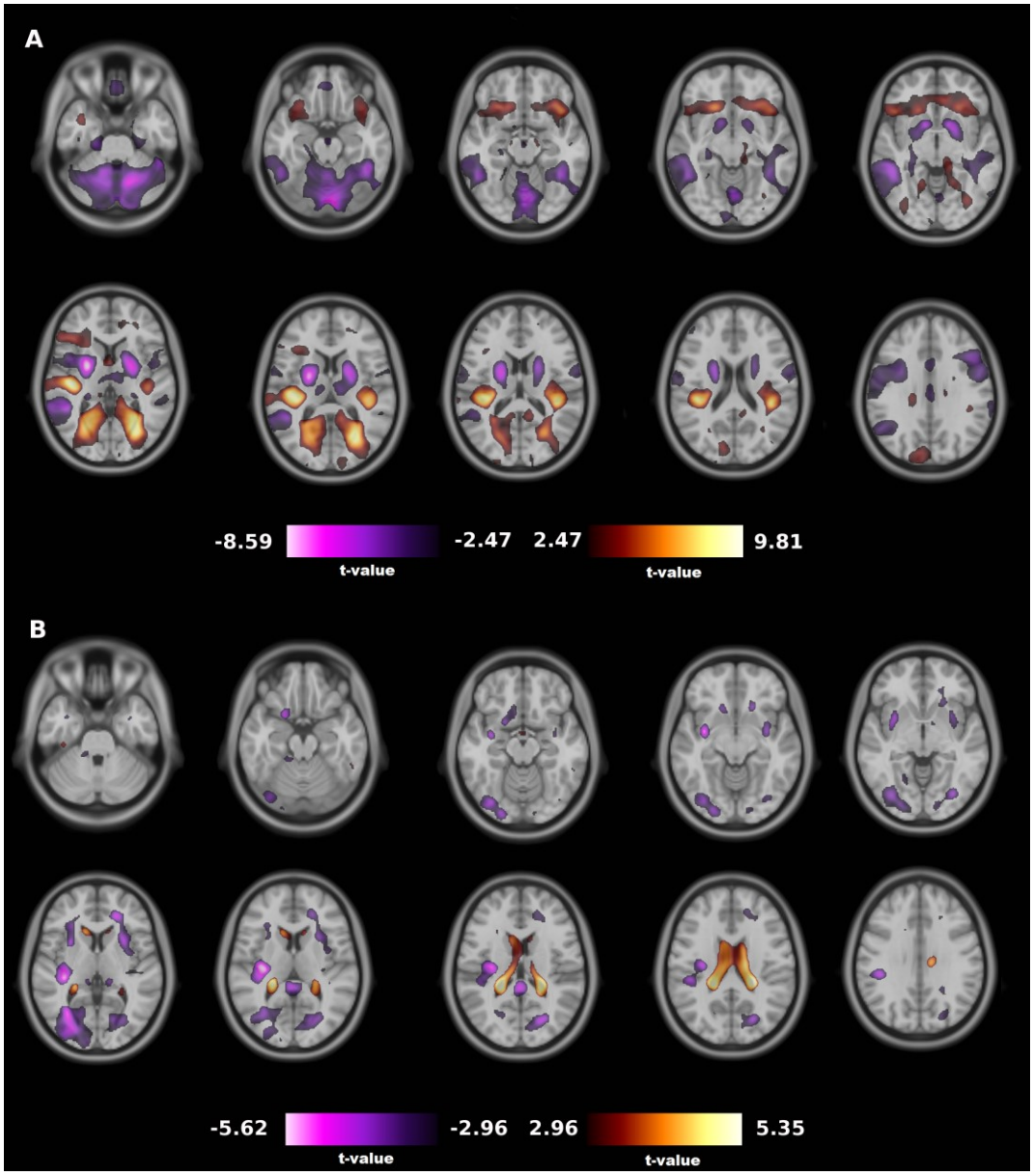

Figure 18. Effect of genetic status on brain structures for voxel-based analyses. Significant differences on Jacobian determinants highlight the inverse gene dosage effect at the regional voxel-based level on volumes between DEL>CTRL>DUP, as well as some specific volume differences between DEL>CTRL, CTRL>DUP and DEL<CTRL. A. DEL versus CTRL, B. DUP versus CTRL. Only regions with a FDR correction (q<0.05) are presented. Negative t-values represent, respectively, the contrasts DEL<CTRL and DUP<CTRL, positive t-values represent the contrasts DEL>CTRL and DUP>CTRL. DEL: deletion carriers; CTRL: control individuals; DUP: duplication carriers

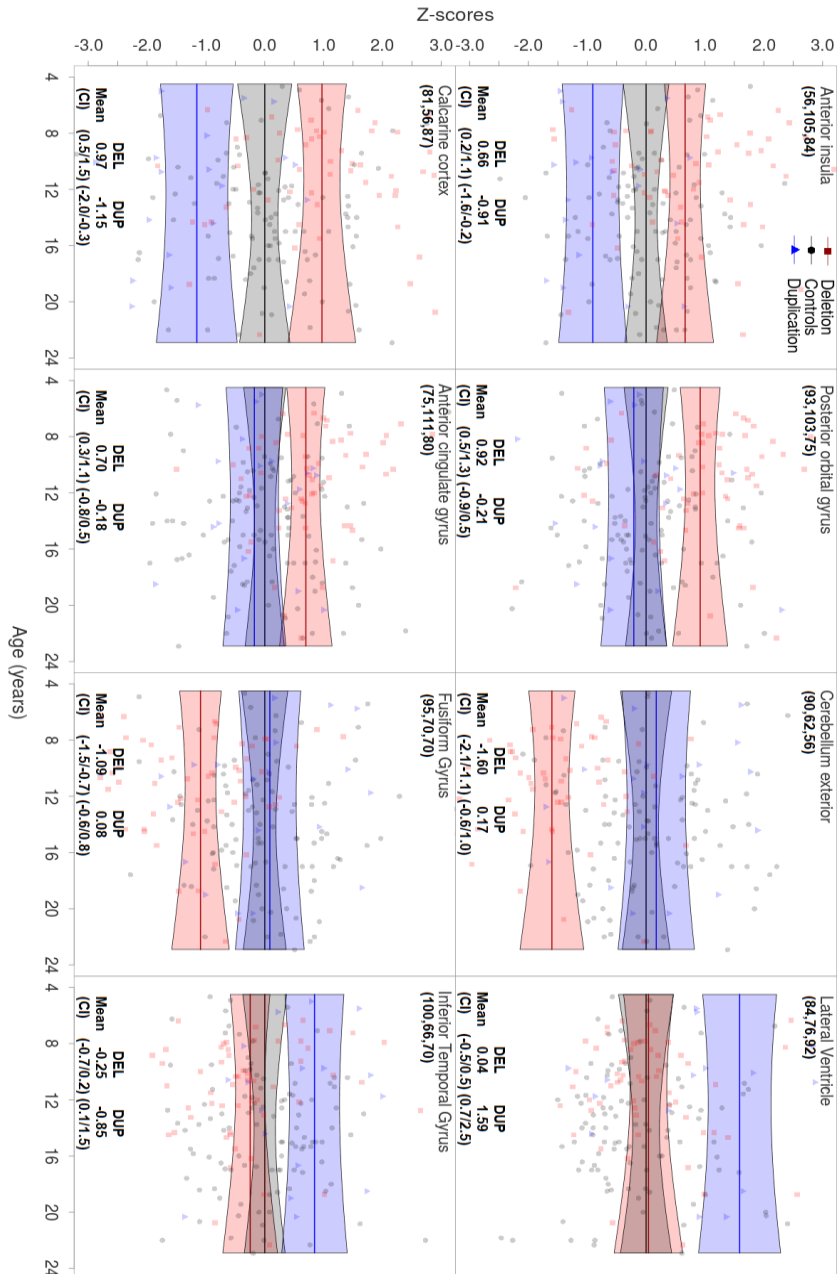

Figure 19. Developmental trajectory from typical voxel showing a difference between genetic groups. Trajectory of the Jacobian determinants of 8 representative voxels from regions with significant differences between genetic groups. All of them are from the right hemisphere. Anterior insula and calcarine cortex have some voxels with significantly higher values in deletion and lower values in duplication than control individuals. Posterior orbital gyrus and anterior cingulate gyrus have significantly higher values in deletion carriers compared to controls; on the contrary cerebellum exterior and fusiform gyrus have significantly lower values in deletion carriers than controls. Lateral ventricle and inferior temporal gyrus have significantly higher values in duplication carriers than controls. All these differences are already present at 4.5 years and identical through the development until 23 years of age. Raw values of each voxel are corrected for age and number of echo (i.e. single echo vs multi echo scans) through a linear model, then values from control individuals are centered to 0 for visualization purposes. For each of the genetic groups, fitted lines represent the predicted mean computed per age range of 2.4 months, polygons represent the confidence interval at each age, the points are normalized subject-level data-points. Mean (minimum/maximum of the confidence interval) are presented in the table. DEL: deletion carriers; DUP: duplication carriers. P-values are corrected with an FDR correction, q<0.05.

4 Discussion

The main goal of this study is to identify the onset and potential changes through childhood, adolescence, and adulthood of brain differences associated with 16p11.2 CNVs. Our study provides a thorough investigation of the age-related effects of 16p11.2 deletions and duplications on brain anatomy between the ages of 4.5 and 23 years. We do not observe any age-related effects on global and voxel-based volumes in deletions or duplication carriers. These results are in favor of early onset of brain changes that remain stable across childhood, adolescence and early adulthood. Differences related to 16p11.2 CNV carriers are already present at 5 years of age.

Our method allows us to compute normalized values for neuroanatomical regions as well as for each individual voxel despite the fact that the normative data was acquired on a different scanner. Our results corroborate global and voxel-based effects described in our previous study: insula is affected in both CNVs in a mirror fashion, while calcarine cortex, temporal and precentral gyri are altered in deletion carriers.

4.1 Continuous model of normative developmental trajectory

The major contribution of our paper is the use of a model to normalize the non-linear effect of age during typical brain development (Giedd et al., 1999). This allows us to reliably study a sample of mutation carriers and controls spanning a broad age range. Papers studying neuroimaging alterations associated with neurodevelopmental disorders have mostly used narrow age bins because the study-specific control groups were too small (less than 100 individuals) to reliably model the effect of age. We show that despite the fact that the NIHPD data has been collected with a 1.5T magnet, the model for the effect of age during typical brain development is robust and applies to data acquired on a 3T after a linear adjustment. However, integrating large normative datasets to correct for complex covariates such as age still requires an additional control group scanned with the same protocol as done here, to be able to match a particular study to the norm.

4.2 Developmental trajectories in neurodevelopmental disorders and genetic risk factors

Recently, a large cross-sectional neuroimaging study in idiopathic ASD (van Rooij et al., 2018) identified differences in subcortical volumes that are stable across the entire age range

of the study from 2 to 64 years of age. The study also highlighted differences in cortical thickness between the ASD and control groups. The strongest group differences were observed during childhood and adolescence, with normalized or even reversed thickness results in adulthood. However, in the absence of longitudinal data, it is unknown whether the same mechanisms were underlying ASD symptoms in participants from these different age groups. Indeed, ASD diagnostic boundaries have changed tremendously during the past decade. In contrast, the interpretation of cross-sectional studies is easier in genetically defined groups since the inclusion criteria (presence of a specific mutation) does not vary across time, clinical sites or age of the participants.

Longitudinal studies in idiopathic ASD showed that subcortical alterations and increased total and regional cortical surface area present at 2 years of age remain stable at the age of 4 years (Hazlett et al., 2011). An increase in growth rate of cortical surface area occurs between 6 and 12 months of age and remains stable between 12 and 24 months of age in high-risk infants who are later diagnosed with ASD compared to low-risk children (Hazlett et al., 2017). The longitudinal investigation of network efficiencies also showed that alterations in connectivity of the superior and middle temporal gyrus as well as the insula are present at 6 and 12 months of age (Lewis et al., 2017).

Few developmental studies in carriers of large genetic risk factors for ASD or intellectual disability have been conducted. In Fragile X syndrome, larger brain volumes are stable between 2 and 5 years of age (Hazlett et al., 2012b). Similar to observations in ASD, neuroimaging studies of 22q11.2 deletion carriers suggest that alterations in subcortical and surface area are stable from 5 to 65 years while a few cortical thickness measures show age-related differences (Sun et al., 2018). They are the greatest during preadolescence and seem to disappear during adulthood, although much larger studies are required to confirm this observation (Schaer et al., 2009).

The main limitations of the present study stem from the technical differences in acquisition, which include the aforementioned 1.5 T and 3 T fields used in the NIHPD and 16p11.2 datasets respectively. In addition, the 16p11.2 is a multi-center database, further increasing the variability in the scans. These acquisition differences can affect the quality of the non-linear registrations from which the Jacobians are calculated.

The broad age range could have introduced systematic age-dependent motion artefacts leading to spurious findings. This is however unlikely due to the absence of any age-related findings in our analysis and the thorough quality check performed on the dataset.

Our power to observe age-related differences was constrained by sample size. We estimate that the smallest detectable change with power=0.80, and alpha=0.05 in the duplication carriers for whole brain is 0.16 Z-score per year, for grey matter 0.10/year and 0.09/year for white matter. For deletions, we could detect 0.12 Z-score per year for whole brain, 0.09/year for grey matter and 0.07/year for white matter. There is also uncertainty for the lower age range of our study. A larger sample of younger participants is required to further investigate the presence of these findings at 4 years of age.

Results may not generalize to 16p11.2 CNV carriers with extreme obesity or severe ASD symptoms that were unable to complete the scanning session. Nevertheless, our cohort is highly representative of the Intelligence quotient and psychiatric symptoms observed in our broader sample of 16p11.2 CNV carriers (D'Angelo et al., 2016).

Future directions to refine the normalization procedure, include normative data acquired with 3T longitudinal scans and investigations of other methods such as splines instead of linear mixed models (Mills et al., 2016).

5 Conclusion

Investigating individuals who carry the same genetic mutation is a powerful strategy to study alterations of brain growth trajectories associated with molecular mechanisms underlying neurodevelopmental disorders. Thanks to a continuous voxel-wise model of normative developmental trajectory, we show that 16p11.2 CNV carriers have brain alterations present already at 4.5 years, with comparable effect size from 5 to 20 years of age. The brain differences are reminiscent of MRI studies in several 16p11.2 deletion mice models which have identified alterations in the insula and striatum at 7 days, equivalent to a prenatal period in humans (Portmann et al., 2014). Data in neonates and toddlers will be required to advance our understanding on the onset of these alterations.

Acknowledgments

The NIHPD cohort: Data from the Pediatric MRI Data Repository, Objective 1, was created by the NIH MRI Study of Normal Brain Development. This is a multi-site, longitudinal study of typically developing children conducted by the Brain Development Cooperative Group and supported by the National Institute of Child Health and Human Development, the National Institute on Drug Abuse, the National Institute of Mental Health, and the National Institute of

Neurological Disorders and Stroke (Contract #s N01-HD02-3343, N01-MH9-0002, and N01-NS-9-2314, -2315, -2316, -2317, -2319 and -2320). A listing of the participating sites and a complete listing of the study investigators can be found at http://www.bic.mni.mcgill.ca/nihpd/info/participating_centers.html.

This manuscript reflects the views of the authors and may not reflect the opinions or views of the NIH.

The Simons VIP Consortium: We are grateful to all of the families at the participating Simons Variation in Individuals Project (VIP) sites, as well as the Simons VIP Consortium. We appreciate obtaining access to imaging and phenotypic data on SFARI Base. Approved researchers can obtain the Simons VIP population dataset described in this study by applying at https://base.sfari.org. The 16p11.2 European Consortium: We are grateful to all families who participated in the 16p11.2 European Consortium.

SJ is supported by a Bursary Professor fellowship of the Swiss National Science Foundation (SNSF), a Canada Research Chair in neurodevelopmental disorders and a chair from the Jeanne et Jean Louis Levesque Foundation.

This research was enabled by a MIRI Brain Canada grant (SJ), an IVADO fund (SJ) (Institut de Valorisation des Données), Calcul Quebec (http://www.calculquebec.ca) and Compute Canada (http://www.computecanada.ca).

LC is supported by the Canadian Institutes of Health Research (MOP-111169) and MIRI Brain Canada grant (3388). AC is supported by the Fonds de Recherche Nature et technologies du Québec (PBEEE program).

This work was supported by SNSF grants 31003A_160203 and 31003A_182632 and the Horizon2020 Twinning project ePerMed 692145 to AR.

BD is supported by the Swiss National Science Foundation (NCCR Synapsy, project grant Nr 32003B_159780 and 33CS30-148401) and the Leenaards Foundation. LREN is very grateful to the Roger De Spoelberch and Partridge Foundations for their generous financial support.

Members of the European 16p11.2 Consortium include the following: Addor Marie-Claude, Service de génétique médicale, Centre Hospitalier Universitaire Vaudois, Lausanne University, Switzerland ; Andrieux Joris, Institut de Génétique Médicale, CHRU de Lille, Hopital Jeanne de Flandre, France; Arveiler Benoît, Service de génétique médicale, CHU de Bordeaux-GH Pellegrin, France; Baujat Geneviève, Service de Génétique Médicale, CHU Paris - Hôpital Necker-Enfants Malades, France; Sloan-Béna Frédérique, Service de médecine

génétique, Hôpitaux Universitaires de Genève - HUG, Switzerland; Belfiore Marco, Service de génétique médicale, Centre Hospitalier Universitaire Vaudois, Lausanne University, Switzerland; Bonneau Dominique, Service de génétique médicale, CHU d'Angers, France; Bouquillon Sonia, Institut de Génétique Médicale, Hopital Jeanne de Flandre, Lille, France; Boute Odile, Hôpital Jeanne de Flandre, CHRU de Lille, Lille, France; Brusco Alfredo, Genetica Medica, Dipartimento di Scienze Mediche, Università di Torino, Italy; Busa Tiffany, Département de génétique médicale, CHU de Marseille, Hôpital de la Timone, France; Caberg Jean-Hubert, Centre de génétique humaine, CHU de Liège, Belgique; Campion Dominique, Service de psychiatrie, Centre hospitalier de Rouvray, Sotteville lès Rouen, France; Colombert Vanessa, Service de génétique médicale, Centre Hospitalier Bretagne Atlantique CH Chubert-Vannes, France; Cordier Marie-Pierre, Service de génétique clinique, CHU de Lyon, Hospices Civils de Lyon, France; David Albert, Service de Génétique Médicale, CHU de Nantes, Hôtel Dieu, France; Debray François-Guillaume, Service de Génétique Humaine, CHU Sart Tilman - Liège, Belgique; Delrue Marie-Ange, Service de génétique médicale, CHU de Bordeaux, Hôpital Pellegrin, France; Doco-Fenzy Martine, Service de Génétique et Biologie de la Reproduction, CHU de Reims, Hôpital Maison Blanche, France; Dunkhase-Heinl Ulrike, Department of Pediatrics, Aabenraa Hospital, Sonderjylland, Denmark; Edery Patrick, Service de génétique clinique, CHU de Lyon, Hospices Civils de Lyon, France; Fagerberg Christina, Department of Clinical Genetics, Odense University hospital, Denmark; Faivre Laurence, Centre de génétique, Hôpital d'Enfants, CHU Dijon Bourgogne - Hôpital François Mitterrand, France; Forzano Francesca, Ambulatorio di Genetica Medica, Ospedali Galliera di Genova, Italy and Clinical Genetics Department, 7th Floor Borough Wing, Guy's Hospital, Guy's & St Thomas' NHS Foundation Trust, Great Maze Pond, London SE1 9RT, UK; Genevieve David, Département de Génétique Médicale, Maladies Rares et Médecine Personnalisée, service de génétique clinique, Université Montpellier, Unité Inserm U1183, CHU Montpellier, Montpellier, France; Gérard Marion, Service de Génétique, CHU de Caen, Hôpital Clémenceau, France; Giachino Daniela, Genetica Medica, Dipartimento di Scienze Cliniche e Biologiche, Università di Torino, Italy; Guichet Agnès, Service de génétique, CHU d'Angers, France; Guillin Olivier, Service de psychiatrie, Centre hospitalier du Rouvray, Sotteville lès Rouen, France; Héron Delphine, Service de Génétique clinique, CHU Paris-GH La Pitié Salpêtrière-Charles Foix - Hôpital Pitié-Salpêtrière, France; Isidor Bertrand, Service de Génétique Médicale, CHU de Nantes, Hôtel Dieu, France; Jacquette Aurélia, Service de Génétique clinique, CHU Paris-GH La Pitié Salpêtrière-Charles Foix - Hôpital Pitié-

Salpêtrière, France; Jaillard Sylvie, Service de Génétique Moléculaire et Génomique – Pôle biologie, CHU de Rennes, Hôpital Pontchaillou, France; Journel Hubert, Service de génétique médicale, Centre Hospitalier Bretagne Atlantique CH Chubert- Vannes, France; Keren Boris, Centre de Génétique Moléculaire et Chromosomique, CHU Paris-GH La Pitié Salpêtrière-Charles Foix - Hôpital Pitié-Salpêtrière, France; Lacombe Didier, Service de génétique médicale, CHU de Bordeaux-GH Pellegrin, France; Lebon Sébastien, Pediatric Neurology Unit, Department of Pediatrics, Lausanne University Hospital, Lausanne, Switzerland; Le Caignec Cédric, Service de Génétique Médicale - Institut de Biologie, CHU de Nantes, France; Lemaître Marie-Pierre, Service de Neuropédiatrie, Centre Hospitalier Régional Universitaire de Lille, France; Lespinasse James, Service génétique médicale et oncogénétique, Hotel Dieu, Chambéry, France; Mathieu-Dramart Michèle, Service de Génétique Clinique, CHU Amiens Picardie, France; Mercier Sandra, Service de Génétique Médicale, CHU de Nantes, Hôtel Dieu, France; Mignot Cyril, Service de Génétique clinique, CHU Paris-GH La Pitié Salpêtrière-Charles Foix - Hôpital Pitié-Salpêtrière, France; Missirian Chantal, Département de génétique médicale, CHU de Marseille, Hôpital de la Timone, France; Petit Florence, Service de génétique clinique Guy Fontaine, Hôpital Jeanne de Flandre, CHRU de Lille, France; Pilekær Sørensen Kristina, Department of Clinical Genetics, Odense University Hospital, Denmark; Pinson Lucile, Département de Génétique Médicale, Maladies Rares et Médecine Personnalisée, service de génétique clinique, Université Montpellier, Unité Inserm U1183, CHU Montpellier, Montpellier, France; Plessis Ghislaine, Service de Génétique, CHU de Caen, Hôpital Clémenceau, France; Prieur Fabienne, Service de génétique clinique, CHU de Saint-Etienne - Hôpital Nord, France; Rooryck-Thambo Caroline, Laboratoire de génétique moléculaire, CHU de Bordeaux-GH Pellegrin, France; Rossi Massimiliano, Service de génétique clinique, CHU de Lyon, Hospices Civils de Lyon, France; Sanlaville Damien, Laboratoire de Cytogénétique Constitutionnelle, CHU de Lyon, Hospices Civils de Lyon, France ; Schlott Kristiansen Britta, Department of Clinical Genetics, Odense University Hospital, Denmark; Schluth-Bolard Caroline, Laboratoire de Cytogénétique Constitutionnelle, CHU de Lyon, Hospices Civils de Lyon, France; Till Marianne, Service de génétique clinique, CHU de Lyon, Hospices Civils de Lyon, France; Van Haelst Mieke, Department of Genetics, University Medical Center Utrecht, Holland; Van Maldergem Lionel, Centre de Génétique humaine, CHRU de Besançon - Hôpital Saint-Jacques, France.

Conflict of interest

The authors report no biomedical financial interests or potential conflicts of interest.

References

Aubert-Broche, B., Fonov, V., Ghassemi, R., Narayanan, S., Arnold, D.L., Banwell, B., Sled, J.G., Collins, D.L., 2011. Regional brain atrophy in children with multiple sclerosis. NeuroImage 58, 409–415. https://doi.org/10.1016/j.neuroimage.2011.03.025

Aubert-Broche, B., Fonov, V., Narayanan, S., Arnold, D.L., Araujo, D., Fetco, D., Till, C., Sled, J.G., Banwell, B., Collins, D.L., On behalf of the Canadian Pediatric Demyelinating Disease Network, 2014. Onset of multiple sclerosis before adulthood leads to failure of age-expected brain growth. Neurology 83, 2140–2146. https://doi.org/10.1212/WNL.0000000000001045

Aubert-Broche, B., Fonov, V.S., García-Lorenzo, D., Mouiha, A., Guizard, N., Coupé, P., Eskildsen, S.F., Collins, D.L., 2013. A new method for structural volume analysis of longitudinal brain MRI data and its application in studying the growth trajectories of anatomical brain structures in childhood. NeuroImage 82, 393–402. https://doi.org/10.1016/j.neuroimage.2013.05.065

Benjamini, Y., Hochberg, Y., 1995. Controlling the False Discovery Rate: A Practical and Powerful Approach to Multiple Testing. J. R. Stat. Soc., Methodological 57, 289–300. https://doi.org/10.2307/2346101

Collins, D.L., Holmes, C.J., Peters, T.M., Evans, A.C., 1995. Automatic 3-D model-based neuroanatomical segmentation. Hum. Brain Mapp. 3, 190–208. https://doi.org/10.1002/hbm.460030304

Collins, D.L., Neelin, P., Peters, T.M., Evans, A.C., 1994. Automatic 3D intersubject registration of MR volumetric data in standardized Talairach space. J. Comput. Assist. Tomogr. 18, 192–205.

D'Angelo, D., Lebon, S., Chen, Q., Martin-Brevet, S., Snyder, L.G., Hippolyte, L., Hanson, E., Maillard, A.M., Faucett, W.A., Macé, A., Pain, A., Bernier, R., Chawner, S.J.R.A., David, A., Andrieux, J., Aylward, E., Baujat, G., Caldeira, I., Conus, P., Ferrari, C., Forzano, F., Gérard, M., Goin-Kochel, R.P., Grant, E., Hunter, J.V., Isidor, B., Jacquette, A., Jønch, A.E., Keren, B., Lacombe, D., Le Caignec, C., Martin, C.L., Männik, K., Metspalu, A., Mignot, C., Mukherjee, P., Owen, M.J., Passeggeri, M., Rooryck-Thambo, C., Rosenfeld, J.A., Spence, S.J., Steinman, K.J., Tjernagel, J., Van Haelst, M., Shen, Y., Draganski, B., Sherr, E.H., Ledbetter, D.H., van den Bree, M.B.M., Beckmann, J.S., Spiro, J.E., Reymond, A., Jacquemont, S., Chung, W.K., for the Cardiff University Experiences of Children With Copy Number Variants (ECHO) Study, the 16p11.2 European Consortium, and the Simons Variation in Individuals Project (VIP) Consortium, 2016. Defining the Effect of the 16p11.2 Duplication on Cognition, Behavior, and Medical Comorbidities. JAMA Psychiatry 73, 20. https://doi.org/10.1001/jamapsychiatry.2015.2123

Eskildsen, S.F., Coupé, P., Fonov, V., Manjón, J.V., Leung, K.K., Guizard, N., Wassef, S.N., Østergaard, L.R., Collins, D.L., 2012. BEaST: Brain extraction based on nonlocal segmentation technique. NeuroImage 59, 2362–2373. https://doi.org/10.1016/j.neuroimage.2011.09.012

Evans, A.C., Brain Development Cooperative Group, 2006. The NIH MRI study of normal brain development. NeuroImage 30, 184–202. https://doi.org/10.1016/j.neuroimage.2005.09.068

Fonov, V., Evans, A.C., Botteron, K., Almli, C.R., McKinstry, R.C., Collins, D.L., Brain Development Cooperative Group, 2011. Unbiased average age-appropriate atlases for pediatric studies. NeuroImage 54, 313–327. https://doi.org/10.1016/j.neuroimage.2010.07.033

Frackowiak, R.S.J. (Ed.), 2004. Human brain function, 2nd ed. ed. Elsevier Academic Press, Amsterdam ; Boston.

Giedd, J.N., Blumenthal, J., Jeffries, N.O., Castellanos, F.X., Liu, H., Zijdenbos, A., Paus, T., Evans, A.C., Rapoport, J.L., 1999. Brain development during childhood and adolescence: a longitudinal MRI study. Nat. Neurosci. 2, 861–863. https://doi.org/10.1038/13158

Hazlett, H.C., Poe, M.D., Gerig, G., Styner, M., Chappell, C., Smith, R.G., Vachet, C., Piven, J., 2011. Early brain overgrowth in autism associated with an increase in cortical surface area before age 2 years. Arch. Gen. Psychiatry 68, 467–476. https://doi.org/10.1001/archgenpsychiatry.2011.39

Hazlett, H.C., Poe, M.D., Lightbody, A.A., Styner, M., MacFall, J.R., Reiss, A.L., Piven, J., 2012. Trajectories of early brain volume development in fragile X syndrome and autism. J. Am. Acad. Child Adolesc. Psychiatry 51, 921–933. https://doi.org/10.1016/j.jaac.2012.07.003

Hazlett, Heather Cody, Gu, H., Munsell, B.C., Kim, S.H., Styner, Martin, Wolff, Jason J., Elison, Jed T., Swanson, M.R., Zhu, H., Botteron, Kelly N., Collins, D. Louis, Constantino, John N., Dager, Stephen R., Estes, Annette M., Evans, Alan C., Fonov, Vladimir S., Gerig, Guido, Kostopoulos, Penelope, McKinstry, Robert C., Pandey, J., Paterson, Sarah, Pruett, J.R., Schultz, Robert T., Shaw, Dennis W., Zwaigenbaum, Lonnie, Piven, Joseph, Piven, J., Hazlett, H. C., Chappell, C., Dager, S. R., Estes, A. M., Shaw, D. W., Botteron, K. N., McKinstry, R. C., Constantino, J. N., Pruett Jr, J.R., Schultz, R. T., Paterson, S., Zwaigenbaum, L., Elison, J. T., Wolff, J. J., Evans, A. C., Collins, D. L., Pike, G.B., Fonov, V. S., Kostopoulos, P., Das, S., Gerig, G., Styner, M., Gu, C.H., 2017. Early brain development in infants at high risk for autism spectrum disorder. Nature 542, 348–351. https://doi.org/10.1038/nature21369

Lau, J.C., Lerch, J.P., Sled, J.G., Henkelman, R.M., Evans, A.C., Bedell, B.J., 2008. Longitudinal neuroanatomical changes determined by deformation-based morphometry in a mouse model of Alzheimer's disease. NeuroImage 42, 19–27. https://doi.org/10.1016/j.neuroimage.2008.04.252

Lewis, J.D., Evans, Alan C., Pruett, John R., Botteron, Kelly N., McKinstry, Robert C., Zwaigenbaum, Lonnie, Estes, Annette M., Collins, D. Louis, Kostopoulos, Penelope, Gerig, Guido, Dager, Stephen R., Paterson, Sarah, Schultz, Robert T., Styner, Martin A., Hazlett, Heather C., Piven, Joseph, Piven, J., Hazlett, H.C., Chappell, C., Dager, S.R., Estes, A.M., Shaw, D., Botteron, K.N., McKinstry, R.C., Constantino, J., Pruett, J.R., Schultz, R.T., Paterson, S., Zwaigenbaum, L., Elison, J.T., Evans, A.C., Collins, D.L., Pike, G.B., Fonov, V., Kostopoulos, P., Das, S., Gerig, G., Styner, M.A., Gu, H., 2017. The Emergence of Network Inefficiencies in Infants With Autism Spectrum Disorder. Biol. Psychiatry 82, 176–185. https://doi.org/10.1016/j.biopsych.2017.03.006

Lin, G.N., Corominas, R., Lemmens, I., Yang, X., Tavernier, J., Hill, D.E., Vidal, M., Sebat, J., Iakoucheva, L.M., 2015. Spatiotemporal 16p11.2 Protein Network Implicates Cortical Late Mid-Fetal Brain Development and KCTD13-Cul3-RhoA Pathway in

Psychiatric Diseases. Neuron 85, 742–754. https://doi.org/10.1016/j.neuron.2015.01.010

Maillard, A.M., Ruef, A., Pizzagalli, F., Migliavacca, E., Hippolyte, L., Adaszewski, S., Dukart, J., Ferrari, C., Conus, P., Männik, K., Zazhytska, M., Siffredi, V., Maeder, P., Kutalik, Z., Kherif, F., Hadjikhani, N., Beckmann, J.S., Reymond, A., Draganski, B., Jacquemont, S., 16p11.2 European Consortium, 2015. The 16p11.2 locus modulates brain structures common to autism, schizophrenia and obesity. Mol. Psychiatry 20, 140–147. https://doi.org/10.1038/mp.2014.145

Marshall, C.R., Howrigan, D.P., Psychosis Endophenotypes International Consortium, CNV and Schizophrenia Working Groups of the Psychiatric Genomics Consortium, Merico, D., Thiruvahindrapuram, B., Wu, W., Greer, D.S., Antaki, D., Shetty, A., Holmans, P.A., Pinto, D., Gujral, M., Brandler, W.M., Malhotra, D., Wang, Z., Fajarado, K.V.F., Maile, M.S., Ripke, S., Agartz, I., Albus, M., Alexander, M., Amin, F., Atkins, J., Bacanu, S.A., Belliveau, R.A., Bergen, S.E., Bertalan, M., Bevilacqua, E., Bigdeli, T.B., Black, D.W., Bruggeman, R., Buccola, N.G., Buckner, R.L., Bulik-Sullivan, B., Byerley, W., Cahn, W., Cai, G., Cairns, M.J., Campion, D., Cantor, R.M., Carr, V.J., Carrera, N., Catts, S.V., Chambert, K.D., Cheng, W., Cloninger, C.R., Cohen, D., Cormican, P., Craddock, N., Crespo-Facorro, B., Crowley, J.J., Curtis, D., Davidson, M., Davis, K.L., Degenhardt, F., Del Favero, J., DeLisi, L.E., Dikeos, D., Dinan, T., Djurovic, S., Donohoe, G., Drapeau, E., Duan, J., Dudbridge, F., Eichhammer, P., Eriksson, J., Escott-Price, V., Essioux, L., Fanous, A.H., Farh, K.-H., Farrell, M.S., Frank, J., Franke, L., Freedman, R., Freimer, N.B., Friedman, J.I., Forstner, A.J., Fromer, M., Genovese, G., Georgieva, L., Gershon, E.S., Giegling, I., Giusti-Rodríguez, P., Godard, S., Goldstein, J.I., Gratten, J., de Haan, L., Hamshere, M.L., Hansen, M., Hansen, T., Haroutunian, V., Hartmann, A.M., Henskens, F.A., Herms, S., Hirschhorn, J.N., Hoffmann, P., Hofman, A., Huang, H., Ikeda, M., Joa, I., Kähler, A.K., Kahn, R.S., Kalaydjieva, L., Karjalainen, J., Kavanagh, D., Keller, M.C., Kelly, B.J., Kennedy, J.L., Kim, Y., Knowles, J.A., Konte, B., Laurent, C., Lee, P., Lee, S.H., Legge, S.E., Lerer, B., Levy, D.L., Liang, K.-Y., Lieberman, J., Lönnqvist, J., Loughland, C.M., Magnusson, P.K.E., Maher, B.S., Maier, W., Mallet, J., Mattheisen, M., Mattingsdal, M., McCarley, R.W., McDonald, C., McIntosh, A.M., Meier, S., Meijer, C.J., Melle, I., Mesholam-Gately, R.I., Metspalu, A., Michie, P.T., Milani, L., Milanova, V., Mokrab, Y., Morris, D.W., Müller-Myhsok, B., Murphy, K.C., Murray, R.M., Myin-Germeys, I., Nenadic, I., Nertney, D.A., Nestadt, G., Nicodemus, K.K., Nisenbaum, L., Nordin, A., O'Callaghan, E., O'Dushlaine, C., Oh, S.-Y., Olincy, A., Olsen, L., O'Neill, F.A., Van Os, J., Pantelis, C., Papadimitriou, G.N., Parkhomenko, E., Pato, M.T., Paunio, T., Perkins, D.O., Pers, T.H., Pietiläinen, O., Pimm, J., Pocklington, A.J., Powell, J., Price, A., Pulver, A.E., Purcell, S.M., Quested, D., Rasmussen, H.B., Reichenberg, A., Reimers, M.A., Richards, A.L., Roffman, J.L., Roussos, P., Ruderfer, D.M., Salomaa, V., Sanders, A.R., Savitz, A., Schall, U., Schulze, T.G., Schwab, S.G., Scolnick, E.M., Scott, R.J., Seidman, L.J., Shi, J., Silverman, J.M., Smoller, J.W., Söderman, E., Spencer, C.C.A., Stahl, E.A., Strengman, E., Strohmaier, J., Stroup, T.S., Suvisaari, J., Svrakic, D.M., Szatkiewicz, J.P., Thirumalai, S., Tooney, P.A., Veijola, J., Visscher, P.M., Waddington, J., Walsh, D., Webb, B.T., Weiser, M., Wildenauer, D.B., Williams, N.M., Williams, S., Witt, S.H., Wolen, A.R., Wormley, B.K., Wray, N.R., Wu, J.Q., Zai, C.C., Adolfsson, R., Andreassen, O.A., Blackwood, D.H.R., Bramon, E., Buxbaum, J.D., Cichon, S., Collier, D.A., Corvin, A., Daly, M.J., Darvasi, A., Domenici, E., Esko, T., Gejman, P.V., Gill, M., Gurling, H., Hultman,

C.M., Iwata, N., Jablensky, A.V., Jönsson, E.G., Kendler, K.S., Kirov, G., Knight, J., Levinson, D.F., Li, Q.S., McCarroll, S.A., McQuillin, A., Moran, J.L., Mowry, B.J., Nöthen, M.M., Ophoff, R.A., Owen, M.J., Palotie, A., Pato, C.N., Petryshen, T.L., Posthuma, D., Rietschel, M., Riley, B.P., Rujescu, D., Sklar, P., St Clair, D., Walters, J.T.R., Werge, T., Sullivan, P.F., O'Donovan, M.C., Scherer, S.W., Neale, B.M., Sebat, J., 2017. Contribution of copy number variants to schizophrenia from a genome-wide study of 41,321 subjects. Nat. Genet. 49, 27–35. https://doi.org/10.1038/ng.3725

Martin-Brevet, S., Rodríguez-Herreros, B., Nielsen, J.A., Moreau, C., Modenato, C., Maillard, A.M., Pain, A., Richetin, S., Jønch, A.E., Qureshi, A.Y., Zürcher, N.R., Conus, P., Chung, W.K., Sherr, E.H., Spiro, J.E., Kherif, F., Beckmann, J.S., Hadjikhani, N., Reymond, A., Buckner, R.L., Draganski, B., Jacquemont, S., Addor, M.-C., Andrieux, J., Arveiler, B., Baujat, G., Sloan-Béna, F., Belfiore, M., Bonneau, D., Bouquillon, S., Boute, O., Brusco, A., Busa, T., Caberg, J.-H., Campion, D., Colombert, V., Cordier, M.-P., David, A., Debray, F.-G., Delrue, M.-A., Doco-Fenzy, M., Dunkhase-Heinl, U., Edery, P., Fagerberg, C., Faivre, L., Forzano, F., Genevieve, D., Gérard, M., Giachino, D., Guichet, A., Guillin, O., Héron, D., Isidor, B., Jacquette, A., Jaillard, S., Journel, H., Keren, B., Lacombe, D., Lebon, S., Le Caignec, C., Lemaître, M.-P., Lespinasse, J., Mathieu-Dramart, M., Mercier, S., Mignot, C., Missirian, C., Petit, F., Pilekær Sørensen, K., Pinson, L., Plessis, G., Prieur, F., Rooryck-Thambo, C., Rossi, M., Sanlaville, D., Schlott Kristiansen, B., Schluth-Bolard, C., Till, M., Van Haelst, M., Van Maldergem, L., Alupay, H., Aaronson, B., Ackerman, S., Ankenman, K., Anwar, A., Atwell, C., Bowe, A., Beaudet, A.L., Benedetti, M., Berg, J., Berman, J., Berry, L.N., Bibb, A.L., Blaskey, L., Brennan, J., Brewton, C.M., Buckner, R., Bukshpun, P., Burko, J., Cali, P., Cerban, B., Chang, Y., Cheong, M., Chow, V., Chu, Z., Chudnovskaya, D., Cornew, L., Dale, C., Dell, J., Dempsey, A.G., Deschamps, T., Earl, R., Edgar, J., Elgin, J., Olson, J.E., Evans, Y.L., Findlay, A., Fischbach, G.D., Fisk, C., Fregeau, B., Gaetz, B., Gaetz, L., Garza, S., Gerdts, J., Glenn, O., Gobuty, S.E., Golembski, R., Greenup, M., Heiken, K., Hines, K., Hinkley, L., Jackson, F.I., Jenkins, J., Jeremy, R.J., Johnson, K., Kanne, S.M., Kessler, S., Khan, S.Y., Ku, M., Kuschner, E., Laakman, A.L., Lam, P., Lasala, M.W., Lee, H., LaGuerre, K., Levy, S., Cavanagh, A.L., Llorens, A.V., Campe, K.L., Luks, T.L., Marco, E.J., Martin, S., Martin, A.J., Marzano, G., Masson, C., McGovern, K.E., McNally Keehn, R., Miller, D.T., Miller, F.K., Moss, T.J., Murray, R., Nagarajan, S.S., Nowell, K.P., Owen, J., Paal, A.M., Packer, A., Page, P.Z., Paul, B.M., Peters, A., Peterson, D., Poduri, A., Pojman, N.J., Porche, K., Proud, M.B., Qasmieh, S., Ramocki, M.B., Reilly, B., Roberts, T.P.L., Shaw, D., Sinha, T., Smith-Packard, B., Gallagher, A.S., Swarnakar, V., Thieu, T., Triantafallou, C., Vaughan, R., Wakahiro, M., Wallace, A., Ward, T., Wenegrat, J., Wolken, A., 2018. Quantifying the Effects of 16p11.2 Copy Number Variants on Brain Structure: A Multisite Genetic-First Study. Biol. Psychiatry 84, 253–264. https://doi.org/10.1016/j.biopsych.2018.02.1176

Mills, K.L., Goddings, A.-L., Herting, M.M., Meuwese, R., Blakemore, S.-J., Crone, E.A., Dahl, R.E., Güroğlu, B., Raznahan, A., Sowell, E.R., Tamnes, C.K., 2016. Structural brain development between childhood and adulthood: Convergence across four longitudinal samples. NeuroImage 141, 273–281. https://doi.org/10.1016/j.neuroimage.2016.07.044

Moreno-De-Luca, D., Sanders, S.J., Willsey, A.J., Mulle, J.G., Lowe, J.K., Geschwind, D.H., State, M.W., Martin, C.L., Ledbetter, D.H., 2013. Using large clinical data sets to

infer pathogenicity for rare copy number variants in autism cohorts. Mol. Psychiatry 18, 1090–1095. https://doi.org/10.1038/mp.2012.138

Portmann, T., Yang, M., Mao, R., Panagiotakos, G., Ellegood, J., Dolen, G., Bader, P.L., Grueter, B.A., Goold, C., Fisher, E., Clifford, K., Rengarajan, P., Kalikhman, D., Loureiro, D., Saw, N.L., Zhengqui, Z., Miller, M.A., Lerch, J.P., Henkelman, R.M., Shamloo, M., Malenka, R.C., Crawley, J.N., Dolmetsch, R.E., 2014. Behavioral Abnormalities and Circuit Defects in the Basal Ganglia of a Mouse Model of 16p11.2 Deletion Syndrome. Cell Rep. 7, 1077–1092. https://doi.org/10.1016/j.celrep.2014.03.036

Qureshi, A.Y., Mueller, S., Snyder, A.Z., Mukherjee, P., Berman, J.I., Roberts, T.P.L., Nagarajan, S.S., Spiro, J.E., Chung, W.K., Sherr, E.H., Buckner, R.L., Simons VIP Consortium, 2014. Opposing brain differences in 16p11.2 deletion and duplication carriers. J. Neurosci. Off. J. Soc. Neurosci. 34, 11199–11211. https://doi.org/10.1523/JNEUROSCI.1366-14.2014

Schaer, M., Debbané, M., Bach Cuadra, M., Ottet, M.-C., Glaser, B., Thiran, J.-P., Eliez, S., 2009. Deviant trajectories of cortical maturation in 22q11.2 deletion syndrome (22q11DS): A cross-sectional and longitudinal study. Schizophr. Res. 115, 182–190. https://doi.org/10.1016/j.schres.2009.09.016

Sled, J.G., Zijdenbos, A.P., Evans, A.C., 1998. A nonparametric method for automatic correction of intensity nonuniformity in MRI data. IEEE Trans. Med. Imaging 17, 87–97. https://doi.org/10.1109/42.668698

Sun, D., Ching, C.R.K., Lin, A., Forsyth, J.K., Kushan, L., Vajdi, A., Jalbrzikowski, M., Hansen, L., Villalon-Reina, J.E., Qu, X., Jonas, R.K., van Amelsvoort, T., Bakker, G., Kates, W.R., Antshel, K.M., Fremont, W., Campbell, L.E., McCabe, K.L., Daly, E., Gudbrandsen, M., Murphy, C.M., Murphy, D., Craig, M., Vorstman, J., Fiksinski, A., Koops, S., Ruparel, K., Roalf, D.R., Gur, R.E., Schmitt, J.E., Simon, T.J., Goodrich-Hunsaker, N.J., Durdle, C.A., Bassett, A.S., Chow, E.W.C., Butcher, N.J., Vila-Rodriguez, F., Doherty, J., Cunningham, A., van den Bree, M.B.M., Linden, D.E.J., Moss, H., Owen, M.J., Murphy, K.C., McDonald-McGinn, D.M., Emanuel, B., van Erp, T.G.M., Turner, J.A., Thompson, P.M., Bearden, C.E., 2018. Large-scale mapping of cortical alterations in 22q11.2 deletion syndrome: Convergence with idiopathic psychosis and effects of deletion size. Mol. Psychiatry. https://doi.org/10.1038/s41380-018-0078-5

The Simons VIP Consortium, 2012. Simons Variation in Individuals Project (Simons VIP): A Genetics-First Approach to Studying Autism Spectrum and Related Neurodevelopmental Disorders. Neuron 73, 1063–1067. https://doi.org/10.1016/j.neuron.2012.02.014

van Rooij, D., Anagnostou, E., Arango, C., Auzias, G., Behrmann, M., Busatto, G.F., Calderoni, S., Daly, E., Deruelle, C., Di Martino, A., Dinstein, I., Duran, F.L.S., Durston, S., Ecker, C., Fair, D., Fedor, J., Fitzgerald, J., Freitag, C.M., Gallagher, L., Gori, I., Haar, S., Hoekstra, L., Jahanshad, N., Jalbrzikowski, M., Janssen, J., Lerch, J., Luna, B., Martinho, M.M., McGrath, J., Muratori, F., Murphy, C.M., Murphy, D.G.M., O'Hearn, K., Oranje, B., Parellada, M., Retico, A., Rosa, P., Rubia, K., Shook, D., Taylor, M., Thompson, P.M., Tosetti, M., Wallace, G.L., Zhou, F., Buitelaar, J.K., 2018. Cortical and Subcortical Brain Morphometry Differences Between Patients With Autism Spectrum Disorder and Healthy Individuals Across the Lifespan: Results From the ENIGMA ASD Working Group. Am. J. Psychiatry 175, 359–369. https://doi.org/10.1176/appi.ajp.2017.17010100

Weiss, L.A., Shen, Y., Korn, J.M., Arking, D.E., Miller, D.T., Fossdal, R., Saemundsen, E., Stefansson, H., Ferreira, M.A.R., Green, T., Platt, O.S., Ruderfer, D.M., Walsh, C.A., Altshuler, D., Chakravarti, A., Tanzi, R.E., Stefansson, K., Santangelo, S.L., Gusella, J.F., Sklar, P., Wu, B.-L., Daly, M.J., 2008. Association between Microdeletion and Microduplication at 16p11.2 and Autism. N. Engl. J. Med. 358, 667–675. https://doi.org/10.1056/NEJMoa075974

6 Supplementary Material

Supplementary Table 1. Neuropsychiatric diagnoses. From the Diagnostic and Statistical Manual of Mental Disorders, DSM-5 (American Psychiatric Association, 2013). A total of 53 of 56 deletion carriers (95%) had at least one psychiatric diagnosis: 11 had one diagnosis and 42 had several diagnoses; 15 of 19 duplication carriers (79%) had at least one psychiatric diagnosis: 1 had one diagnosis and 14 had several diagnoses; 12 of 34 familial control subjects (35%) had at least one psychiatric diagnosis: 7 had one diagnosis and 5 had two diagnoses. In both cohorts, unrelated control subjects without psychiatric diagnosis were recruited.

	DEL	**Familial CTRL**	**DUP**
N	56	34	19
Attention-deficit/hyperactivity disorder	12	6	5
Intellectual Disabiliy	5	-	2
Langage and communication disorders	14	2	2
Phonological disorder	41	1	-
Learning disorders	12	1	4
Autistic Spectrum Disorder	9	1	3
Developmental coordination disorder	16	-	5
Enuresis and encopresis disorders	17	1	2
Oppositional-defiant-disorder / Disruptive-behavior and other conduct disorders	5	-	2
Mood disorder	1	-	1
Anxiety Disorders – social phobia	6	4	6
Stereotypic Movement disorder	1	-	-
Tic disorder	2	1	1
Borderline Intellectual Functioning	8	-	5
Other disorders (stuttering, trichotillomania, sexual-abuse-of-child)	2	-	1

Supplementary Table 2. Image acquisition parameters for the 16p11.2 dataset. EU European cohort, SVIP Simons VIP cohort, ME-MPRAGE Multi-Echo Magnetization Prepared RApid Gradient Echo, MPRAGE Magnetization Prepared RApid Gradient Echo, TR Repetition Time, TE Echo Time.

Cohort	Scanner	Echo sequences	TR	TE	Flip angle	Field Of View
EU	Magnetom TIM Trio (1 site)	ME-MPRAGE	2530 ms	TE1: 1.64 ms TE2: 3.5 ms TE3: 5.36 ms TE4 : 7.22 ms	7°	256
EU	Magnetom Prisma Syngo (1 site)	MPRAGE	2000 ms	2.39 ms	9°	256
SVIP	Magnetom TIM Trio (2 sites)	ME-MPRAGE	2530 ms	1.64 ms	7°	256
SVIP	Philips Achieva (2 sites)	MPRAGE	2300 ms	3 ms	9°	256
SVIP	Magnetom TIM Trio (1 site)	MPRAGE	2300 ms	2.98 ms	9°	256

Supplementary Table 3. Coordinates of brain regions with significant differences between genetic groups in Jacobian determinant analyses. "Overlap" refers to the percentage of significant voxels within each brain region. When some brain regions have more than one cluster that overlaps with them, we reported the bigger one. Only regions with a False Discovery Rate FDR correction (q<0.05) and with cluster size >30 voxels are presented. (1) The developmental trajectory of a typical voxel for each of these regions is shown in Figure 19.

A. Deletion > Control	Side	Size (voxels)	Overlap (%)	Z	Y	X	t-score
CLUSTER 1							
Posterior orbital gyrus (1)	Right	200	62	-14	21	40	5.58
	Left	190	61	-17	23	-31	4.52
Inferior frontal gyrus orbital part	Left	73	49	-8	25	-45	4.39
	Right	64	42	-9	23	41	5.04
Frontal operculum	Left	95	41	-1	27	-43	5.35
Inferior frontal gyrus triangular part	Left	150	35	1	29	-53	4.90
Anterior cingulate gyrus (1)	Right	212	33	-4	37	5	4.44
	Left	142	21	-1	41	-10	3.57
Anterior insula (1)	Left	156	28	3	25	-33	3.88
	Right	148	27	-5	28	29	4.47
Temporal pole	Left	93	8	-26	9	-37	4.80
	Right	61	5	-22	9	39	3.72
CLUSTER 2							
Transverse temporal gyrus	Right	87	60	14	-29	43	7.77
Parietal operculum		174	59	16	-33	41	8.27
Posterior insula		87	31	15	-25	33	5.92
Planum temporale		44	23	13	-33	41	8.17
Posterior cingulate gyrus		134	22	5	-53	21	6.76
Middle occipital gyrus		133	21	6	-81	36	4.76
Calcarine cortex (1)		96	17	7	-68	25	8.75
Lingual gyrus		164	14	3	-58	25	7.94
Ventral DC		92	14	-14	-15	15	3.40
Cuneus		69	11	13	-98	11	5.04
Occipital pole		31	9	11	-103	14	2.82
Central operculum		33	7	14	-19	43	3.88
Precuneus		116	6	7	-60	25	8.16
Lateral ventricle		75	6	6	-54	29	7.58
Inferior occipital gyrus		47	6	4	-83	33	4.07
Thalamus proper		41	3	1	-35	13	4.03

Supplementary Table 3 (continued)

CLUSTER 3							
Calcarine cortex	Left	260	45	5	-67	-25	7.44
Superior occipital gyrus		194	43	30	-88	-12	4.15
Cuneus		241	35	13	-63	-15	4.48
Lingual gyrus		183	15	3	-57	-19	7.04
Posterior cingulate gyrus		95	15	5	-51	-17	6.13
Lateral ventricle		115	9	8	-53	-28	6.25
Inferior occipital gyrus		68	9	3	-83	-33	4.36
Precuneus		140	8	7	-58	-20	6.97
Middle occipital gyrus		30	5	6	-84	-31	3.71
Thalamus proper		35	3	4	-33	-11	3.80
CLUSTER 4							
Transverse temporal gyrus	Left	130	94	7	-21	-41	9.82
Planum temporale		128	59	14	-33	-38	8.11
Parietal operculum		162	59	18	-31	-38	8.35
Posterior insula		99	35	8	-21	-35	7.74
Superior temporal gyrus		124	13	9	-27	-71	4.19
B. Deletion < Control	Side	Size (voxels)	Overlap (%)	Z	Y	X	t-score
CLUSTER 1							
Pallidum	Right	190	95	4	-1	23	-7.12
	Left	182	89	5	-3	-24	-8.07
Middle cingulate gyrus	Right	543	81	42	9	1	-5.12
	Left	426	61	39	12	-3	-5.30
Putamen	Right	480	77	5	-1	23	-7.20
	Left	454	73	7	-3	-25	-8.60
Accumbens area	Left	34	77	-7	11	-11	-6.04
Cerebellum exterior (1)	Right	6247	70	-53	-61	35	-8.37
	Left	6113	69	-54	-59	-33	-6.89
Precentral gyrus	Left	924	56	61	-13	-30	-5.06
	Right	556	33	27	-1	55	-4.36
Fusiform gyrus (1)	Right	589	54	-26	-45	44	-6.34
	Left	224	20	-21	-50	-47	-4.43
Middle temporal gyrus	Left	1139	51	5	-45	-49	-6.05
	Right	243	12	-5	-29	50	-3.72
Angular gyrus	Left	801	51	47	-65	-50	-5.20

Supplementary Table 3 (continued).

Inferior temporal gyrus	Left	715	40	-17	-51	-51	-5.41
	Right	465	25	-19	-43	47	-5.41
Supplementary motor	Left	258	36	45	11	-3	-4.50
cortex	Right	208	28	45	9	5	-4.20
Postcentral gyrus	Left	434	32	31	-7	-57	-4.03
	Right	167	12	21	-4	57	-3.70
Caudate	Right	116	31	13	10	17	-5.36
	Left	77	21	-5	13	-11	-5.52
Parahippocampal gyrus	Left	90	30	-29	-21	-23	-4.82
	Right	75	27	-30	-20	27	-3.66
Thalamus proper	Right	325	27	9	-15	9	-4.56
Hippocampus	Left	121	25	-2	-37	-27	-4.20
	Right	62	12	-7	-33	33	-3.41
Central operculum	Left	121	24	3	7	-43	-4.90
	Right	106	23	5	-1	47	-3.69
Anterior insula	Left	134	24	4	5	-41	-4.90
	Right	37	7	1	1	45	-3.65
Inferior frontal gyrus							
opercular part	Right	98	22	29	17	51	-4.61
Superior temporal gyrus	Left	186	20	10	-43	-51	-5.18
	Right	176	20	-5	-25	49	-3.92
Lingual gyrus	Right	237	20	-17	-90	7	-4.99
	Left	208	17	-15	-90	-3	-4.35
Precentral gyrus medial							
segment	Right	64	18	49	-21	3	-3.58
Brain stem		387	14	-47	-41	-11	-5.78
Temporal pole	Right	136	11	-34	15	23	-3.62
Supramarginal gyrus	Left	146	11	50	-51	-47	-3.27
Middle frontal gyrus	Right	240	8	31	20	49	-5.23
	Left	227	8	31	7	-35	-4.36
Ventral DC	Left	31	5	-9	-25	-25	-3.77
Superior frontal gyrus	Left	84	4	59	-11	-27	-4.47
CLUSTER 2							
Gyrus rectus	Left	182	55	-25	45	-5	-4.68
	Right	149	47	-25	43	1	-4.25
Medial orbital gyrus	Left	102	17	-26	43	-9	-4.36
CLUSTER 3							
Temporal pole	Left	232	19	-37	19	-25	-4.34

Supplementary Table 3 (continued).

CLUSTER 4							
Supramarginal gyrus	Right	137	12	27	-32	70	-3.97
CLUSTER 5							
Superior parietal lobule	Left	153	10	66	-63	-13	-3.71
CLUSTER 6							
Superior parietal lobule	Right	69	5	60	-68	15	-3.22
CLUSTER 7							
Superior frontal gyrus medial segment	Right	41	4	39	49	2	-2.99
C. Duplication > Control	Side	Size (voxels)	Overlap (%)	Z	Y	X	t-score
CLUSTER 1							
Lateral ventricule (1)	Left	1038	77	14	-37	-23	5.29
	Right	875	67	19	-33	23	5.36
Caudate	Right	66	18	24	-13	17	4.92
	Left	66	18	9	19	-13	3.98
Thalamus Proper	Left	100	8	17	-23	-14	4.43
	Right	70	6	19	-17	15	4.56
CLUSTER 2							
Inferior temporal gyrus (1)	Right	91	5	-24	-53	53	3.56
CLUSTER 3							
Posterior cingulate gyrus	Left	70	11	35	-35	-5	3.76
CLUSTER 4							
Fusiform gyrus	Left	41	4	-29	-27	-39	3.67
D. Duplication < Control	Side	Size (voxels)	Overlap (%)	Z	Y	X	t-score
CLUSTER 1							
Occipital fusiform gyrus	Left	267	60	-13	-91	-25	-4.45
	Right	46	12	-7	-78	31	-4.05
Calcarine cortex (1)	Left	260	45	5	-67	-17	-3.93
	Right	171	30	9	-73	17	-3.94
Inferior occipital gyrus	Left	300	38	2	-85	-29	-4.79
Occipital pole	Left	45	13	3	-101	-11	-3.45
Superior occipital gyrus	Right	58	12	27	-78	28	-3.66
Middle occipital gyurs	Left	62	10	5	-85	-29	-4.72
Cuneus	Right	52	8	19	-71	20	-3.73

Supplementary Table 3 (continued).

Lingual gyrus	Right	65	5	-7	-90	15	-3.48
	Left	43	3	-2	-65	-17	-3.77
Cerebellum exterior	Left	219	2	-21	-81	-37	-3.84
CLUSTER 2							
	Right						
Anterior insula (1)		187	34	6	15	32	-4.4
Putamen		123	20	3	9	29	-4.34
CLUSTER 3							
Parietal operculum	Left	147	53	25	-33	-45	-4.69
Posterior insula		139	49	8	-19	-35	-5.63
Transverse temporal gyrus		67	49	9	-23	-37	-5.36
Planum temporale		49	23	23	-35	-49	-4.21
Central operculum		37	7	21	-15	-37	-4.1
CLUSTER 4							
Anterior insula	Left	96	17	3	27	-29	-4.08
Putamen		105	17	1	9	-29	-4.65
CLUSTER 5							
Thalamus Proper	Right	88	7	3	-30	15	-4.05
Posterior cingulate gyrus	Left	43	7	15	-43	0	-4.37
CLUSTER 6							
Medial orbital gyrus	Left	54	9	-19	11	-19	-4.62

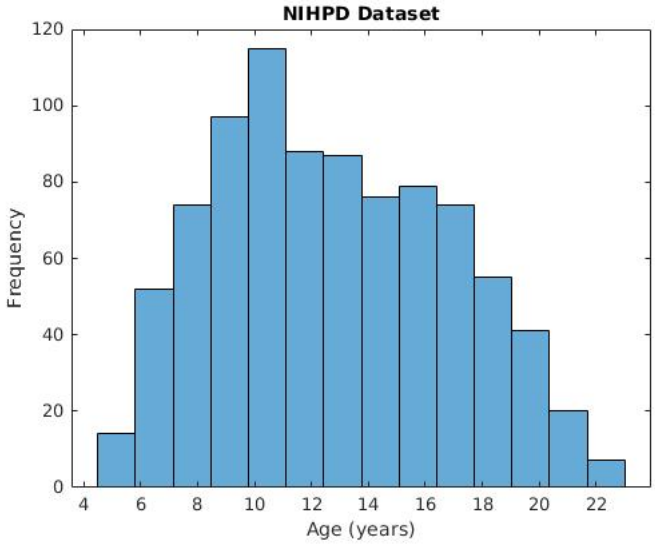

Supplementary Figure 1. Age distribution of the NIHPD cohort.

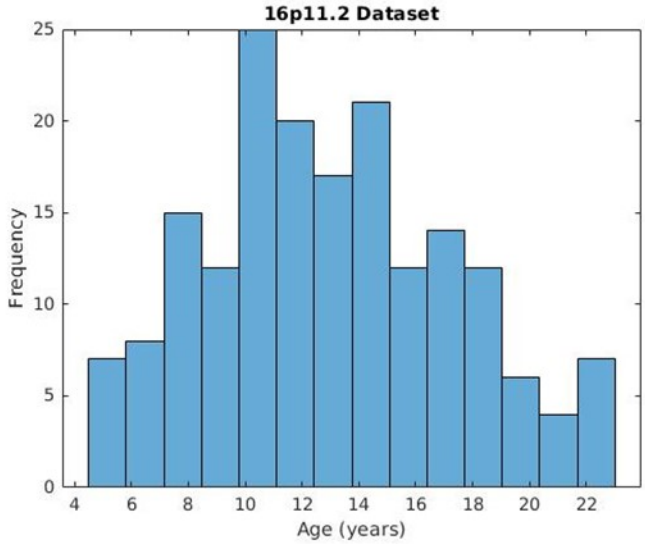

Supplementary Figure 2. Age distribution of the 16p11.2 cohort.

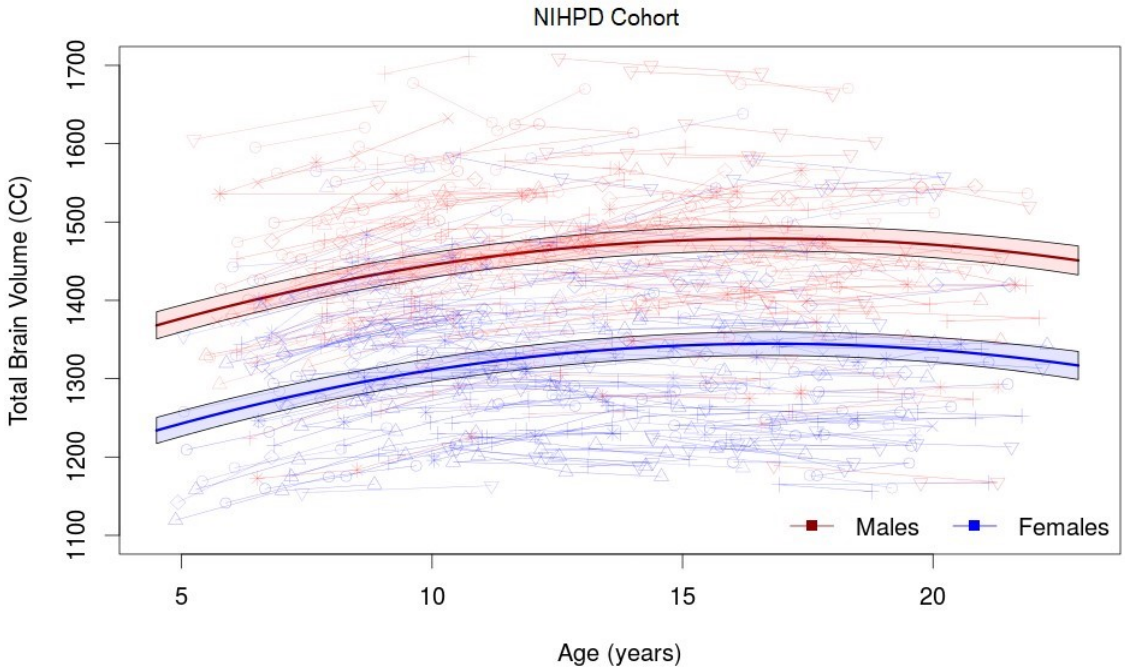

Supplementary Figure 3. Mixed Effects fit of Total Brain Volume for NIHPD controls. Males are shown in red and females in blue. Individual data points are shown, with each acquisition site represented by a different marker.

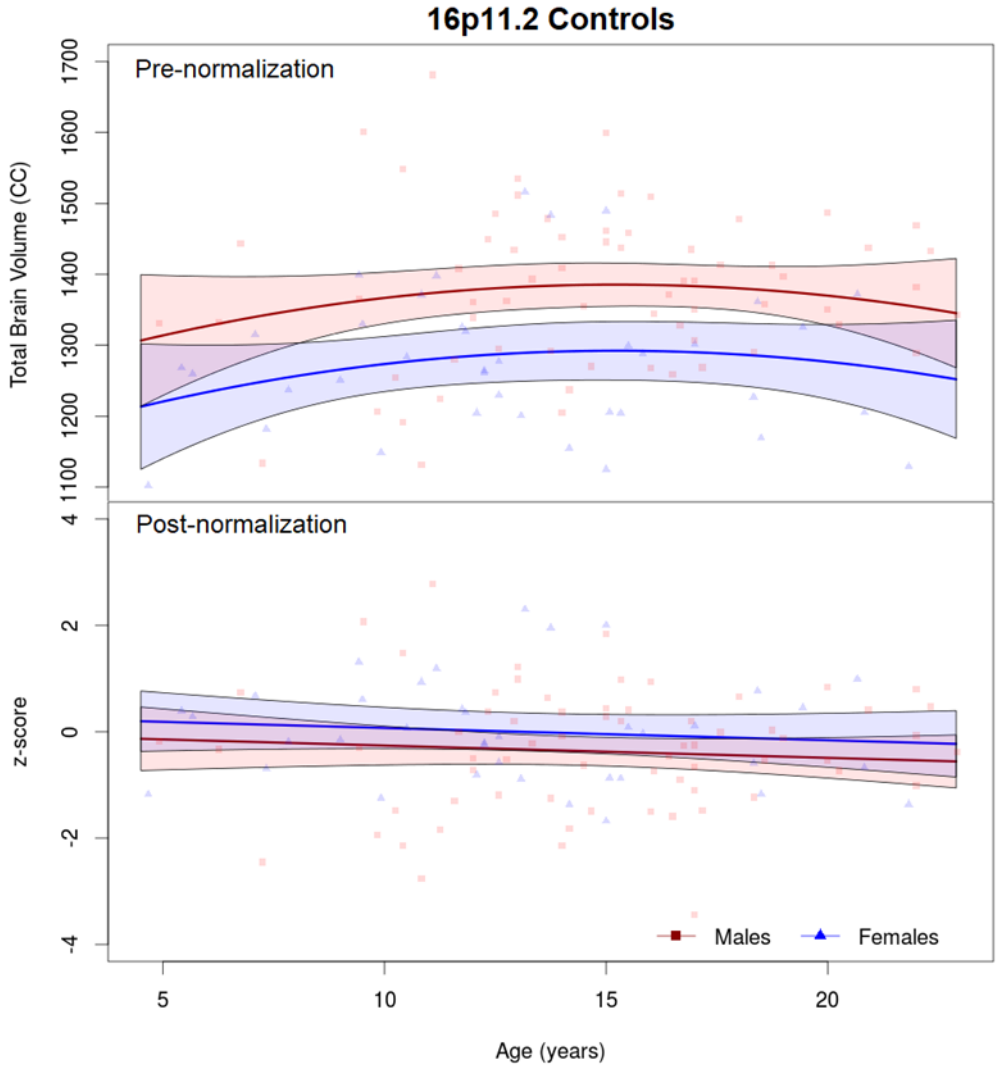

Supplementary Figure 4. Normalization procedure on 16p11.2 controls. The top plot shows a simple linear model (age+sex) fit to the original data. The bottom plot shows the results after normalization, where neither sex nor age terms are significantly different than 0. Males are shown in red and females are shown in blue.

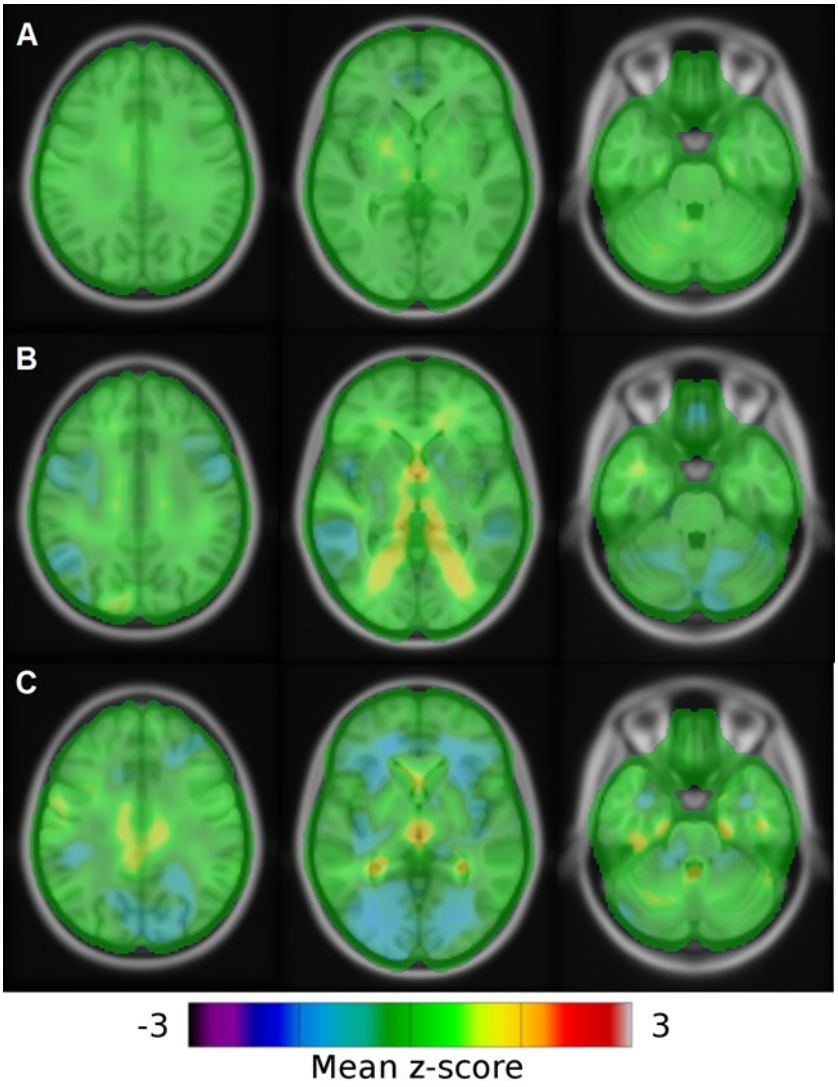

Supplementary Figure 5. Mean Z-scores voxel-based per genetic group. Results of the mean Z-scores per genetic groups, on the Jacobian determinants voxel-by-voxel. A. Mean Z-scores for the CTRL; B. Mean Z-scores for the DEL; C. Mean Z-scores for the DUP. 16p11.2 CTRL show similar profile than the baseline of NIHPD controls, with only some deviations in the left putamen and the medial frontal cortex, whereas DEL and DUP show extensive clusters different from NIHPD controls. DEL, deletion carriers; CTRL, control individuals; DUP, duplication carriers.

Supplementary References

American Psychiatric Association (Ed.), 2013. Diagnostic and statistical manual of mental disorders: DSM-5, 5th ed. ed. American Psychiatric Association, Washington, D.C

Chapter 5

Methodology for Normalization of Serial 1.5 and 3 Tesla Magnetic Resonance Imaging Scans and its Application in Pediatric Multiple Sclerosis

Preface

In this chapter, we extend the previous work to design and validate a normalization technique for more complex, longitudinal, multi-center studies, where data can be acquired at 1.5 or 3 T. Furthermore, an individual subject may have their first scans acquired at 1.5 T and subsequent scans at 3 T. During longitudinal studies that span a wide age-range, it is common that scanners within a site are updated and even upgraded or replaced (e.g. from a 1.5 to a 3 T scanner). Such equipment changes can confound the analysis of longitudinal data – what detected changes are due to the scanner change, and what changes are due to the biology? We propose the use of an optimized longitudinal pipeline based on previous work by Aubert-Broche et al. (2013). Our novel contribution is to account for MRI acquisition at 1.5 or 3 T during pre-processing, while still preserving the longitudinal connection between the scans of individual subjects. In addition, we extend the previous normalization technique by incorporating a second normative database (the Philadelphia Neurodevelopmental cohort (Satterthwaite et al., 2014)) acquired at 3 T, to complement the NIHPD database acquired at 1.5 T. By doing this, we attempt to account for field intensity differences within our normal growth trajectory modelling. We applied this technique to a longitudinal, multi-site, study of pediatric onset multiple sclerosis (MS).

Our results show a lack of age expected growth associated with pediatric onset MS in the overall brain volume, thalamus, putamen, and globus pallidus.

This work has been submitted to NeuroImage: Clinical as: Cárdenas-de-la-Parra, A., Fonov, V.S., Yeh, E.A., Bar-Or, A, Marrie, R.A., Arnold, D.L., O'Mahony, J., Banwell, B., Collins, D.L (2020). Methodology for Normalization of Serial 1.5 and 3 Tesla Magnetic Resonance Imaging Scans and its Application in Pediatric Multiple Sclerosis. NICL-S-20-00557

Methodology for Normalization of Serial 1.5 and 3 Tesla Magnetic Resonance Imaging Scans and its Application in Pediatric Multiple Sclerosis.

Alonso Cárdenas-de-la-Parra[1], Vladimir S. Fonov[1], E. Ann Yeh[2], Amit Bar-Or[3], Ruth Ann Marrie[4], Douglas L. Arnold[1], Julia O'Mahony[2], Brenda Banwell[5], and D. Louis Collins[1] on behalf of the Canadian Pediatric Demyelinating Disease Network.

[1] *McConnell Brain Imaging Centre, Montreal Neurological Institute, Montreal, Quebec, Canada.*

[2] *Department of Pediatrics, Division of Neurology, University of Toronto, Hospital for Sick Children, SickKids Research Institute, Toronto, Ontario, Canada*

[3] *Department of Neurology, Perelman School of Medicine, University of Pennsylvania, Philadelphia, Pennsylvania, United States of America*

[4] *Departments of Internal Medicine and Community Health Sciences, Max Rady College of Medicine, Rady Faculty of Health Sciences, University of Manitoba, Winnipeg, Manitoba, Canada*

[5] *Department of Pediatrics, Division of Child Neurology, The Children's Hospital of Philadelphia, Philadelphia, Pennsylvania, United States of America.*

Abstract

Pediatric neuroimaging studies need to carefully account for normal neurodevelopment, which includes ongoing changes in size, shape, and maturation of the brain, which occurs differentially in males and females. With increasing availability of stronger field magnets and retirement of 1.5 T scanners, several established pediatric neuroimaging cohorts face the challenge of harmonization of archived data with new images acquired at 3 T. We propose a morphometric normalization technique that uses two large longitudinal normative databases, one acquired at 1.5 T and the other at 3.0 T, to establish growth trajectories for the volume of the brain and several brain regions in typically-developing boys and girls. Our methodology effectively accounts for changes due to age, sex, and acquisition field strength. To determine whether our technique was applicable in the context of a pediatric disorder known to negatively impact normative brain growth, we analyzed serial 1.5 and 3 T MRI scans of children and youth with relapsing CNS demyelination and regional control participants, obtained as part of the Canadian Pediatric Demyelinating Disease Study (CPDDS). We confirm a lack of age-expected growth and subsequent whole brain and deep gray matter atrophy in pediatric MS patients and in those with relapsing CNS demyelination associated with antibodies against myelin oligodendrocyte glycoprotein (relapsing aMOG disease). Furthermore, using the proposed normalization technique, we were able to observe that deviations from age-expected brain growth trajectories increase with disease duration, and differences in thalamic and putamen volume are already present at disease onset. We suggest that our methodology will be of value in the context of longitudinal cohorts and multi-site, pediatric studies.

Keywords: MRI Harmonization; Pediatric Onset Multiple Sclerosis; Pediatric MOG disease; Imaging; Brain Development; Normative Growth Trajectories

1 Introduction

Current trends in neuroimaging studies are leading towards the use of large cohorts to analyze potential differences in the brain caused by a variety of diseases. To collect these large cohorts, it is common to resort to multi-site data acquisition, where certain MRI parameters are standardized to attempt to mitigate inter-site variability (Clark et al., 2006; van Haren et al., 2003), or to pool data from separate, independent studies that have already occurred. This can lead to higher number of participants to study, but with a possible increase in the variability in the scans due to different acquisition sequence or scanner field strength (Biberacher et al., 2016; Schnack et al., 2010).

Additionally, it is in the interest of many studies to have long follow-up on patients to better understand the longitudinal implications of a particular disease. When these studies span multiple years, it is common that even within a single site, the scanner used will undergo updates, upgrades, or even be replaced by a newer higher Tesla model (Han et al., 2006). In addition, it can also be complicated to obtain a control group of healthy participants with sufficient participants acquired longitudinally throughout the complete duration of the study at a single site. This longitudinal control group is required for proper statistical comparisons with the patient group, as well as to account for any changes or upgrades done to the scanner during the study.

Furthermore, pediatric studies present a unique challenge, since during the course of normal neurodevelopment the brain is growing and undergoing various changes (Mills et al., 2016). As such, it is important to account for the normal developmental trajectory of growth in the brain when considering potential differences due to disease in childhood.

To address some of these challenges, we propose a normalization procedure for brain volumes that can be used to analyze longitudinal, multi-site, 1.5 T or 3.0 T data, during childhood. To explore the functionality of our method, we analyzed a longitudinal dataset of pediatric participants with relapsing central nervous system (CNS) demyelination, specifically multiple sclerosis (MS) and relapsing anti-myelin oligodendrocyte glycoprotein (MOG) demyelination, conditions known to negatively impact brain growth and volume over time in childhood. Atrophy in adults with MS has been widely reported both for Grey Matter (GM) and White Matter (WM) (Ghione et al., 2019) with the thalamus, putamen, caudate and globus pallidus particularly affected (Chard and Miller, 2009). We have shown abnormal brain growth trajectories during childhood, leading to failure of age-expected growth in overall brain

volume, reduced maximal brain volumes, relatively greater loss in thalamic volume, and atrophy of the brain by adolescence in pediatric-onset MS as well (Aubert-Broche et al., 2014).

2 Materials and methods

2.1 Participants

2.1.1 Typically Developing Controls—NIHPD cohort

We used the multi-site longitudinal data from Objective 1 of the publicly available NIH study of normal brain development (NIHPD) (Evans, 2006) as one of two normative datasets. We accessed MRI data from 402 children (207 females and 195 males), scanned at 1, 2 or 3 time points, with approximately 24 months between scans, for a total of 910 scans (age at scan 4.5 to 22.3 years).

Scans of the NIHPD controls were obtained at six study centres with 1.5 T MRI scanners from Philips, General Electric or Siemens Medical Systems. The MRI protocol included a whole-brain, 3D T1w RF-spoiled gradient echo sequence (1-mm-thick sagittal partitions, TR=22–25 msec, TE=10–11 msec, excitation pulse angle 30°, Field of View =160–180 mm). Details on acquisition and participants were previously published (Evans, 2006).

2.1.2 Typically Developing Controls—Philadelphia Neurodevelopmental cohort

In addition to the NIHPD cohort, we included data from the Philadelphia Neurodevelopmental cohort (Satterthwaite et al., 2014) as normative data acquired at 3 T. We accessed data from 410 children (196 females and 214 males), scanned at 1 or 2 time points with an average separation between scans of 18 months, for a total of 529 scans (age at scan 8.2 to 22.5 years). MRI acquisition occurred at a single study centre using a 3.0 T Siemens TIM Trio and included a whole-brain, 3D T1w MPRAGE sequence (TR= 1810 msec, TE=3.51 msec, flip angle=9°, Field of View=180/240 mm). Details on acquisition and participants were previously published (Satterthwaite et al., 2014).

2.1.3 Canadian Pediatric Demyelinating Disease Study (CPDDS)

The Canadian Pediatric Demyelinating Disease Study (CPDDS) is a longitudinal incident cohort study (2004-present) of children with acute CNS demyelination evaluated at onset, 3, 6, and 12 months and then annually with comprehensive clinical data, research and clinical brain MRI, and biological specimen analysis (Banwell et al., 2011). We analyzed MRI scans from 211 participants (486 research scans) selected from the three largest CPDDS sites. We restricted our analyses to research scans obtained from the three largest sites to ensure a

reasonable number (n>25, spread across the age range) of typically-developing youth imaged on their local scanner. Table 5 delineates the MRI acquisition protocols. Each site provided MRI scans from two participant groups: (i) typically-developing healthy local study controls (total controls, n=135) from whom a single MRI scan was acquired at 1.5 or 3 T; and (ii) serial MRI scans of participants enrolled prior to age 17 years 11 months with relapsing remitting MS (as per 2017 McDonald diagnostic criteria for MS (Thompson et al., 2018) or relapsing aMOG disease (total n=73; 348 scans; n=65 MS and 8 relapsing non-MS). Demographic features of the 211 participants are shown in Table 6.

Table 5. Description of the different sites from the CPDDS cohort, including scanner model and sequence parameters.

Site	Scanner	Field strength (T)	Sequence	TE (ms)	TR (ms)	Flip Angle (deg)	FOV (mm)
The Hospital for Sick Children	GE Signa Excite	1.5	T1w RF-spoiled gradient recalled echo	8	22	30	250
	GE Signa HDxt	1.5	T1w RF-spoiled gradient recalled echo	8	22	30	250
	Siemens TIM Trio	3.0	T1w MPRAGE	3.51	1810	9	256
	Siemens Prisma Fit	3.0	T1w MPRAGE	3.51	1910	9	256
Children's Hospital of Philadelphia	Siemens Verio	3.0	T1w MPRAGE	2.87	1900	9	256
Alberta Children's Hospital	Siemens Avanto	1.5	T1w FLASH	8	22	30	250

Table 6. Demographic description of the different datasets, grouped as normative, local controls, and Relapsing Demyelinating (RD). NIHPD= NIH study of normal brain development, PNC=Philadelphia Neurodevelopmental Cohort, HSC= Hospital for Sick Children, CHP= Children's Hospital of Philadelphia, CAL= Alberta Children's Hospital.

Dataset	Group	Participants			No. Scans	Age range (years)
		Total	Males	Females		
NIHPD	Normative	402	195	207	910	4.9-22.3
PNC	Normative	411	214	197	529	8.2-22.5
HSC	1.5 T Controls	45	16	29	45	6.2-17.3
	1.5 T RD	17	6	11	93	7.3-22.3
	3.0 T Controls	40	14	26	40	8.2-22
	3.0 T RD	20	7	13	58	13.6-21.4
	1.5 + 3 T RD	16	3	13	144	5.9-22.4
CHP	3.0 T Controls	27	12	15	27	5.7-17.6
	3.0 T RD	17	1	16	40	7.3-19.8
CAL	1.5 T Controls	26	17	9	26	8.0-16.0
	1.5 T RD	3	2	1	13	11.1-16.32

2.2 Image Processing

The longitudinal automatic image processing pipeline, developed for NIHPD analysis (Aubert-Broche et al., 2013), was adapted to the scans from the CPDDS dataset as described below. The preprocessing steps applied to the native T1w images were (1) denoising; (2) intensity inhomogeneity correction using the N4 algorithm (Tustison et al., 2010b); and (3) intensity normalization by histogram matching to the ICBM152 template used in our previous work in pediatric MS (Fonov et al., 2011). Revised BestLinReg, a 5-stage hierarchical linear registration technique based on a normalized mutual information similarity measure, was performed between the T1w images and the ICBM152 template to align the images with the

stereotaxic population template using a full 9-parameter transformation (Dadar et al., 2018). Brain extraction was achieved using the Brain Extraction based on nonlocal Segmentation Technique (BEaST), a multi-resolution, nonlocal patch-based segmentation technique (Eskildsen et al., 2012). Subsequently, images were non-linearly registered using the symmetric image normalization (SyN) method (Avants et al., 2008), a symmetric diffeomorphic image registration algorithm. For participants with MS or aMOG disease, T2 lesions were masked to avoid matching healthy tissue to lesions. These T2w lesion masks were obtained using an automated multispectral Bayesian classifier designed specifically for the segmentation of MS and aMOG disease patients (Francis, 2004) followed by a manual label correction. Volumes for whole brain, thalamus, putamen, caudate, and globus pallidus were calculated, with the right and left volumes combined for analysis. In the case of thalamus, putamen, caudate, and globus pallidus, the volumes used for analysis were normalized by the whole brain volume.

2.3 Data analyses

2.3.1 Z-scoring for age, gender, and field strength effects.

To compute Z-scores that normalize for the effect of growth and sex in a pediatric population, as well as possible differences due to field strength, we modelled the effect of those variables in our normative dataset. We chose to use mixed-effects modelling since it allows estimation of growth in longitudinal studies with repeated measures from the same individuals over time, while accounting for the within-participant correlation and varying numbers of measurements for each participant.

As we previously described (Aubert-Broche et al., 2013), individual profiles suggest modelling brain growth as a quadratic function over time: we included both linear and quadratic effects of age in the fixed effects structure. Age was considered as a continuous variable and was centred at 14 years—the mean age of our normative cohort. (Note the mean age of the CPDDS cohort was 15 years.) The fixed terms also included the effect of sex, interaction of sex and age, as well as acquisition field strength.

The mixed-effects model that best fits the normative data is:

$$Vol_i = \beta_0 + \gamma_0 + (\beta_1 + \gamma_1)Age_i + \beta_2 Age_i^2 + \beta_3 Sex_i + \beta_4 (Sex_i \times Age_i) + \beta_5 Field_i + \varepsilon_i \quad (18)$$

where

• Vol_i is the value of the response variable (volume) for subject *i,*

• Age_i, Age^2_i, Sex_i, $Field_i$ are the fixed and random effect explanatory variables for subject *i*,

• (Sex_i * Age_i) is the fixed effect of the interaction of sex and age for subject *i*,

• β_0, γ_0 are the intercept for the fixed and random terms,

• β_1, β_2, β_3 are the fixed effects coefficients and are identical for all participants,

• γ_1 is a random effect coefficient,

• ε_i is the error in subject *i*. The errors for subject *i* are assumed to have mean zero and constant independent variance.

To estimate the standard deviation of the model, we extracted the variance-covariance matrix of the fixed effects along with the residual variance of the random effects. Using the mean and the estimated standard deviation of the model, we computed z-scores for the five different brain volumes for the MS and aMOG disease participants and the local study controls.

2.3.2 Correcting for scanning protocol between normative data and CPDDS local control data

To correct for differences in scanning parameters between our normative dataset and the three CPDDS acquisition sites, we estimated a simple bias term for the z-scored segmented volumes of the typically developing local controls scanned as part of the CPDDS. If this bias was found to be significantly different than 0 ($p < 0.05$), it was used to adjust both the typically developing local controls and the corresponding MS and aMOG disease group of that particular site.

2.3.3 Analyzing the normalization of local control data

To validate the functionality of our normalization technique, we analyzed the z-scores of the local study controls belonging to each study acquisition site for the total brain and different brain region estimated volumes. We used linear regression to look for any significant intercept (i.e. mean z-score different than 0.0) and slope (i.e. changes in z-score with age) across the age range. This was done both individually for each control site, as well as taking all controls as a single group. Additionally, we used the one-sample Kolmogorov-Smirnov test to verify that the z-scores of the local study controls approximate a standard normal distribution ($\mu=0$, $\sigma=1$), for each of the volumes of interest.

2.3.4 Analyzing the effect of field strength on the normalization

We further explored the performance of our normalization procedure between field strengths by analyzing patients (n=16) with initial time points acquired at 1.5 T *and* subsequent

time points acquired at 3 T (note: typically developing control participants enrolled at different sites did not have serial scans obtained at both field strengths, as these individuals were not followed over as long a time period). We tested if the change in field strength caused a step and/or slope change by performing interrupted time series regressions for estimated volumes of total brain and regional brain structures.

2.3.5 Analyzing the trajectories of MS and aMOG disease participants.

We tested if the trajectories of relapsing-remitting MS and aMOG disease participants were different from the normative data (i.e., differed from z-score=0.0, across the age range) using a simple linear mixed-effects model that included age as a predictor for total brain volume and the selected brain regions. We performed an additional analysis using an additional linear mixed-effects model that included disease duration (i.e., time since onset, in years) as a predictor. The use of mixed-effects models helps us deal with the longitudinal aspect of the data, as well as handling missing data (i.e., not all participants have the same number of time points). We applied a Bonferroni correction to account for multiple comparisons. All analyses were conducted using MATLAB 2018b (The MathWorks Inc., 2018).

3 Results

3.1 Normalization of Typically Developing Control Data

We found no significant deviation from a mean of zero, nor any slope, across the age range of the study, both when fitting a linear model to the controls of each site individually, as well as when taking all the controls as a single group ($p>>0.05$ in all cases). The results of the Kolmogorov-Smirnov tests show that the z-scores of local study controls approximate a standard normal distribution, thus supporting that the normalization procedure is working correctly on the typically developing controls across all sites (Figure 20).

3.2 Normalization for different field strengths

The results of the interrupted time series regressions showed no significant step or slope change for any of the volumes ($p>>0.05$ in all cases) when subjects transition from 1.5 to 3 T scans. These results support the functionality of the normalization technique in accounting for acquisition field changes. Figure 21 shows the behaviour of the z-scored structure volumes at 1.5 and 3 T for overall brain volume.

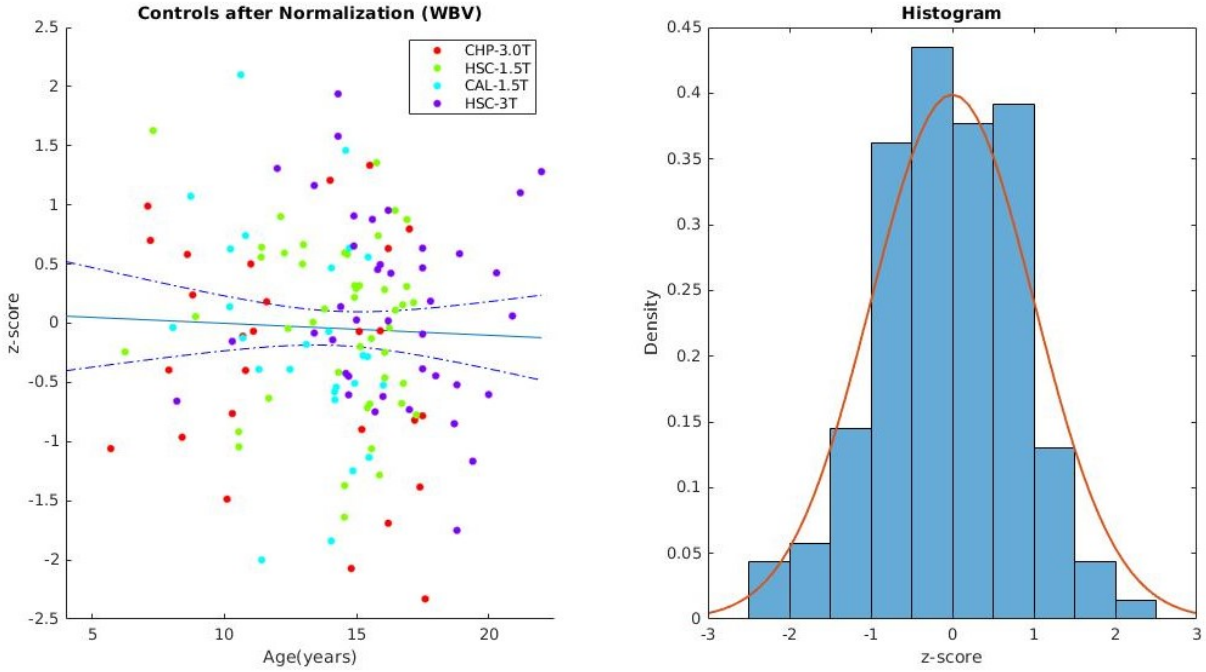

Figure 20. On the right: Plot showing the z-scores of the whole brain volume of normal controls from the different CPDDS sites and the corresponding linear model fit (neither the slope nor the intercept are significant). On the left a histogram showing that the z-scores of controls after normalization approximate a normal distribution with mean of 0 and standard deviation of 1. HSC= Hospital for Sick Children, CHP= Children's Hospital of Philadelphia, CAL= Alberta Children's Hospital

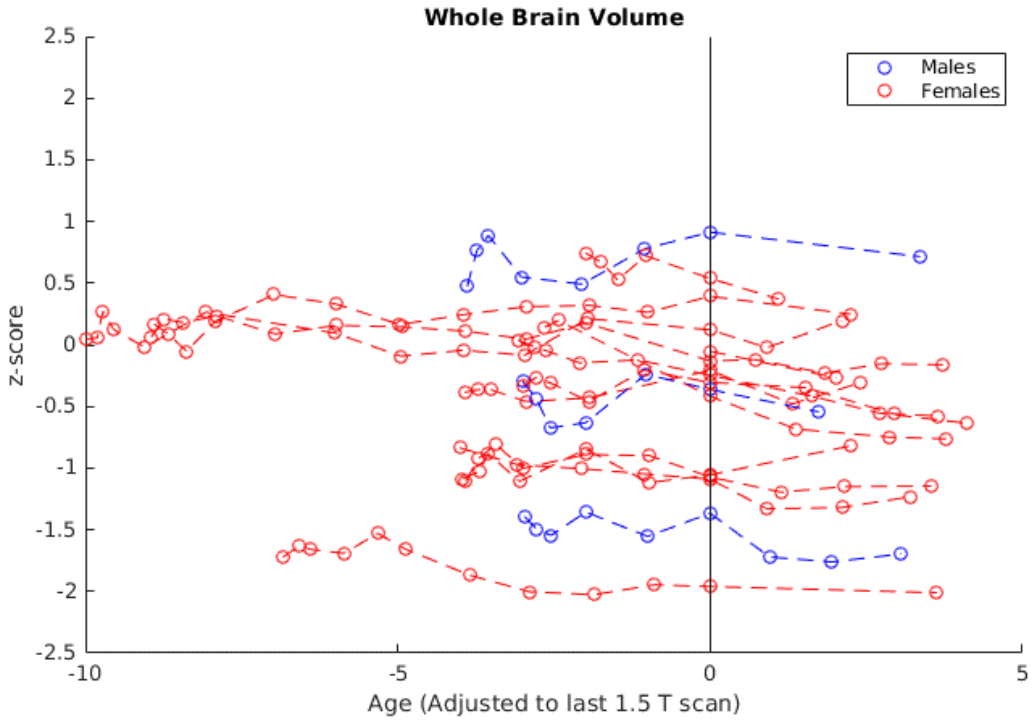

Figure 21. Plot showing the z-scores of whole brain volume of participants with scans at both 1.5 and 3.0 T. Scans obtained at 1.5 T appear to the left while scans obtained at 3.0 appear to the right of the vertical line (Adjusted age=0).

3.3 Failure to reach age-expected growth in pediatric relapsing-remitting MS and aMOG participants

Given the relatively small number of relapsing aMOG disease patients, we first analyzed all 73 relapsing MS and aMOG disease patients as a group (relapsing demyelination). After z-scoring, a clear difference in the expected growth of the relapsing demyelination group was seen for overall brain volume, normalized thalamus, normalized putamen, and normalized globus pallidus in Figure 22. There was a downward slope ($p<<0.001$ in all cases) in total brain volume, normalized (to brain volume) thalamic, putamen, and globus pallidus volumes found in the relapsing demyelination group, signifying that they are straying further away from age-expected growth (z-score of 0) as they age. The plots show that these deep grey structures have additional atrophy over and above that expected for age, sex and brain size.

Furthermore, the difference in expected growth of the relapsing demyelination group is more evident when we consider disease duration, as opposed to age, as the predictor in our model. Figure 23 shows a deviation from expected growth as disease duration increases in the relapsing demyelination group as a downward slope ($p<<0.001$ in all cases) in total brain volume, normalized (to brain volume) thalamic, putamen, and globus pallidus volumes. Additionally, this analysis shows that the normalized (to brain volume) thalamic, and putamen volumes were already lower than expected ($p<<0.001$ in all cases) at disease onset.

As is apparent in Figures 22 and 23, some relapsing demyelination patients demonstrated particularly dramatic deviation from age-expected thalamic (7 patients) and putamen volume (1 patient who also had thalamic volume loss: all indicated by filled black circles in Figures 22 and 23). Data from these participants was carefully verified for imaging or processing artifacts, with no errors found. The clinical and MRI features of these patients are compared to the rest of the relapsing demyelination group in Table 7. We repeated our analysis, excluding these 7 participants, and found that the downward slope in the relapsing demyelination group was still significant (data not shown). Of interest, while there was no difference in age, duration of disease, duration of follow-up, or disability as measured by EDSS, patients with the greatest reduction in deep gray volumes had significantly larger T2 lesion volumes (see Table 7), suggesting a potential relationship between high inflammatory disease burden and loss of brain tissue.

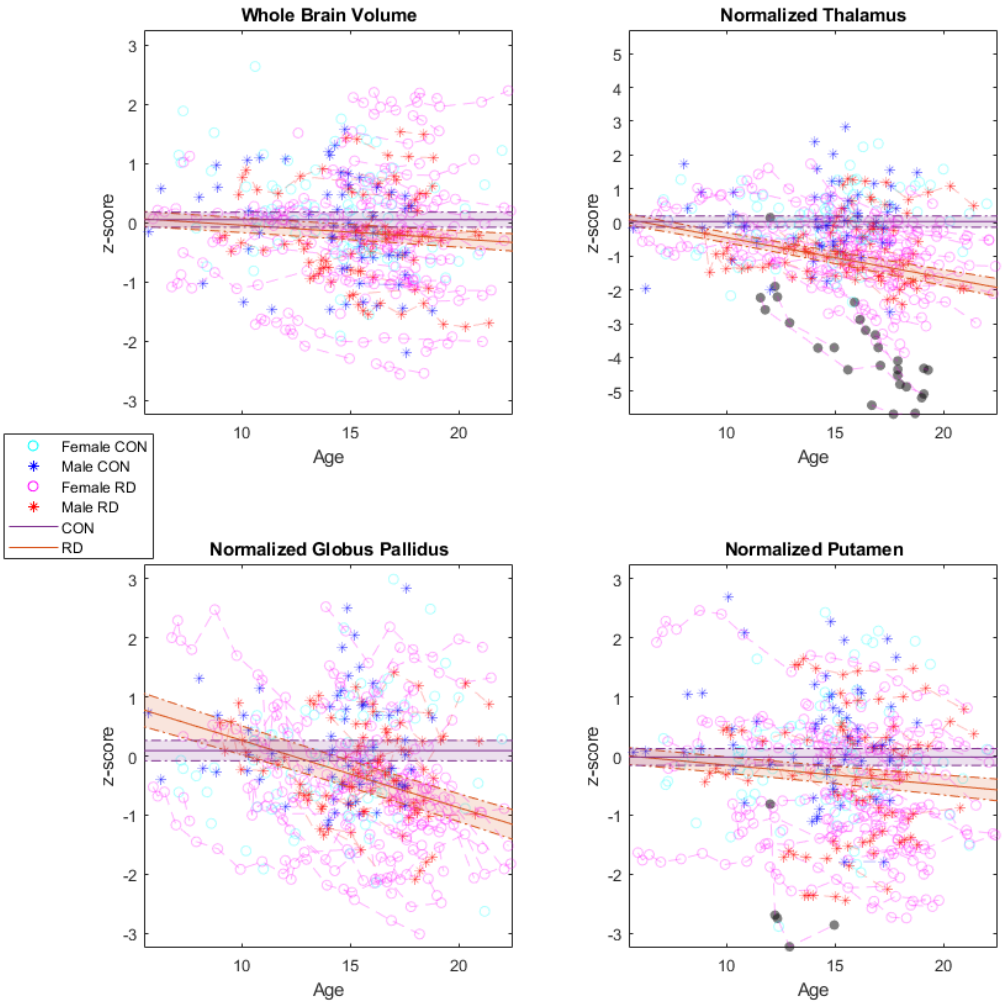

Figure 22. Plots showing the lack of age-expected growth in whole brain volume, thalamus, globus pallidus, and putamen for the Relapsing Demyelination (RD) group. Thalamus, globus pallidus and putamen have been normalized by whole brain volume before obtaining the corresponding z-scores. Participants marked with filled black circles were considered extreme, individually checked, and excluded from a secondary analysis to ensure they were not driving the fit. All significance testing was corrected for multiple comparisons using Bonferroni correction.

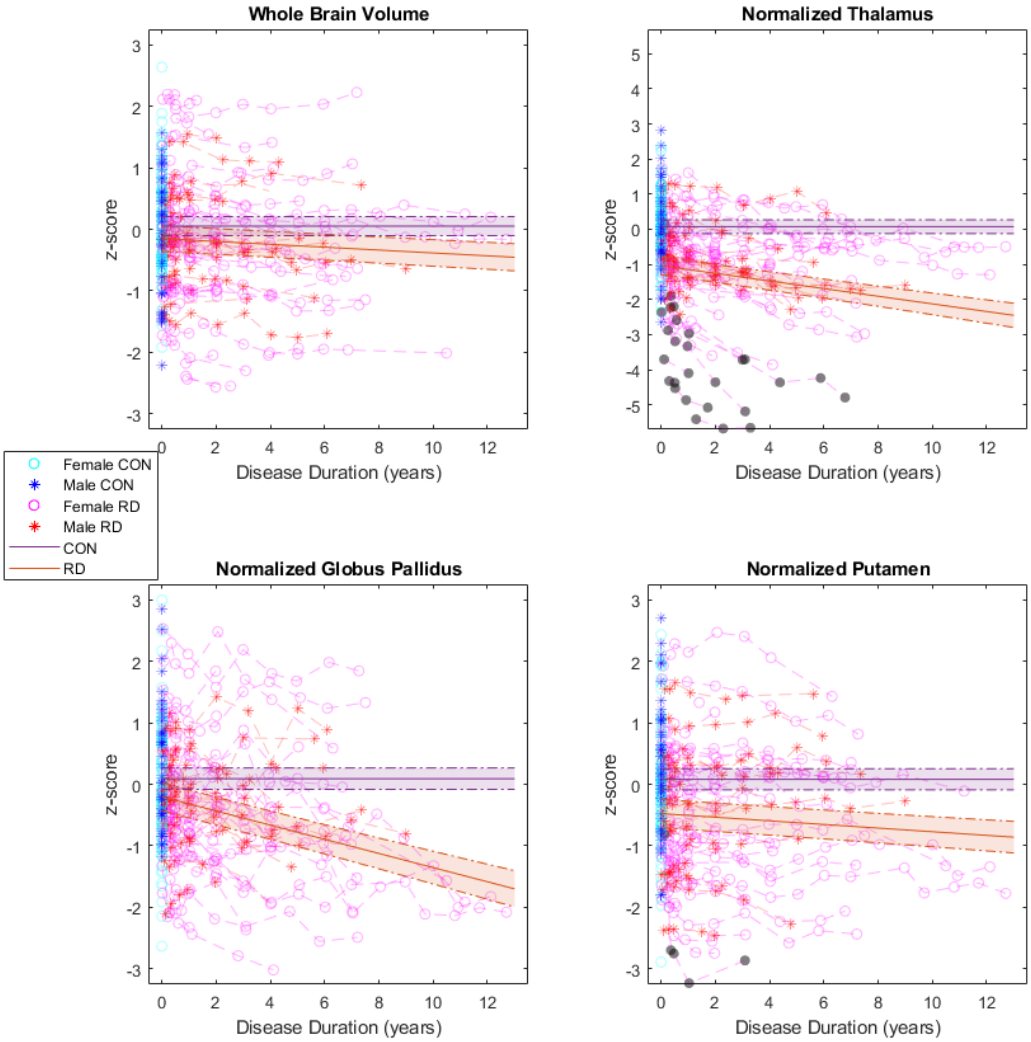

Figure 23. Plots showing the decline in age-expected growth as disease duration increases in whole brain volume, thalamus, globus pallidus, and putamen for the Relapsing Demyelination (RD) group. Thalamus, globus pallidus and putamen have been normalized by whole brain volume before obtaining the corresponding z-scores. Participants marked with filled black circles were considered extreme, individually checked, and excluded from a secondary analysis to ensure they were not driving the fit. All significance testing was corrected for multiple comparisons using Bonferroni correction.

Table 7. Demographic and lesion volume comparisons for MS, Relapsing Non-MS, and Outlier participants.

		All Participants (n=73)	All MS (N=65)	MS Non-Outliers (n=58)	MS Outliers (n=7)	Relapsing Non-MS (n=8)	p-value[1]
Female n (%)		54	48	41	7	6	0.10
Age at Onset (median, IQR)		14.9 (13.0 – 16.1)	15.2 (13.8 – 16.3)	15.1 (13.8 – 16.2)	15.9 (11.9 – 17.4)	9.4 (7.0 – 10.4)	0.38
EDSS at time of Last Scan (median, IQR)		3 (2 – 4)	3 (2 – 4)	3 (2 – 4)	3 (2 – 4)	2.4 (2 – 3.5)	0.97
First Research MRI Acquired within 30 days of onset n (%)		21 (29%)	16 (25%)	15 (26%)	1 (14%)	5 (63%)	-
T2 Total Lesion Volume Within 30 days of onset	(median, IQR)	2.9 (1.0 – 9.5)	3.4 (1.3 – 9.1)	2.9 (1.1 – 8.6)	13.5	0.4 (0.04 – 16.6)	0.16[2]
	(mean, SD)	7.2 (10.1)	5.6 (4.8)	5.0 (4.5)	13.5	12.3 (19.4)	
First Research MRI Acquired within 60 days of onset n (%)		36 (49%)	29 (45%)	26 (45%)	3 (43%)	7 (88%)	-
T2 Total Lesion Volume With 60 days of onset	(median, IQR)	4.4 (1.2 – 12.8)	5.0 (2.3 – 12.0)	4.4 (1.5 – 8.6)	14.6 (13.5 – 32.5)	0.4 (0 – 16.6)	0.03
	(mean, SD)	8.5 (11.0)	8.4 (9.6)	7.0 (8.6)	20.2 (10.6)	9.1 (16.8)	
First Research MRI Acquired within 90 days of onset n (%)		41 (56%)	33 (69%)	30 (52%)	3 (43%)	8 (100%)	-
T2 Total Lesion Volume Within 90 days of onset	(median, IQR)	3.9 (1.1 – 9.5)	4.8 (1.3 – 9.5)	3.9 (1.2 – 7.7)	14.5 (13.5 – 32.5)	0.2 (0.02 – 9.5)	0.02
	(mean, SD)	7.7 (10.6)	7.6 (9.2)	6.4 (8.2)	20.2 (10.6)	8.0 (15.9)	
T2 Volume Acquired at Most Recent MRI[3] n (%)		71 (97%)	63 (97%)	56 (97%)	7 (100%)	8 (100%)	-
T2 Total Lesion Volume at Most Recent MRI	(median, IQR)	3.8 (1.3 – 11.0)	4.2 (1.9 – 12.1)	3.7 (1.6 – 7.0)	15.0 (13.3 – 16.0)	0.09 (0.04 – 0.6)	<0.001
	(mean, SD)	6.4 (7.2)	7.1 (7.3)	6.2 (7.1)	15.0 (2.4)	0.7 (1.3)	

[1]We prioritized comparison of lesion volume as a contributing factor to brain volumes over time within the MS population (MS non-outliers were compared to MS outliers). Relapsing non-MS patients were not evaluated as these individuals have a distinct disease; future studies evaluating relapsing MOG demyelination require a larger cohort.

[2]We are underpowered for this comparison.

[3] Every participant provided a most recent MRI. Time (median [IQR]) from first event to most recent MRI by group was: all participants 2.3 (1.1 – 5.6) years; all MS participants 2.0 (1.0 – 4.8) years; MS non-outliers 2.0 (1.0 – 5.0) years; MS outliers 3.1 (1.2 – 4.2) years and; relapsing non-MS 8.1 (5.2 – 11.3) years.

4 Discussion

We demonstrate a normalization method for brain volumetrics capable of using serial data obtained from different sites and different magnet strengths. Our methods will enhance pooling of data in the study of neurological diseases during childhood, particularly in the case of collaborative studies and those that have data acquired over many years. Furthermore, we confirm our previous longitudinal results showing that pediatric-onset MS leads to failure of age-expected brain growth, and that deep grey matter structures are even more impacted than the brain as a whole (Aubert-Broche et al., 2014). While the previous studies could not detect such a loss for normalized caudate, putamen or globus pallidus volume, our new normalization technique enabled the addition of data from 3.0 T scans, which then yielded sufficient power to detect a statistically significant loss of age-expected growth for the putamen and globus pallidus.

Additionally, our normalization technique allows us to analyze the trajectory of changes in brain volumes associated with disease duration. We clearly observe in Figure 23 that the difference in brain volumes between the relapsing demyelination group and typical development increase with disease duration. Furthermore, a difference in thalamic and putamen volume was already present at disease onset- implicating a negative impact on brain integrity occurring even in the pre-symptomatic phase prior to initial attack. Interestingly, retrospective modeling in adult MS cohorts, suggests that putamenal atrophy might already be present even years before incident MS attack (Krämer et al., 2015).

Early and progressive thalamic atrophy has been consistently reported in adult-onset MS and associated with worsening physical disability as measured by higher EDSS scores over time. The onset of MS as well as aMOG disease during childhood, however, is not characterized by early neurological disability (Armangue et al., 2020; Waldman et al., 2014), as also evidenced in our present cohort. As such, correlations between brain volumetrics and EDSS are not demonstrable during childhood or adolescence. Of concern is the impact of progressive brain volume loss on future disability in early or mid-adulthood. We, and others, have demonstrated a strong relationship between reduced thalamic volume and reduced cognitive function in pediatric MS (De Meo et al., 2019; Till et al., 2011) and our ongoing work will evaluate relationships between brain volume trajectories and cognitive performance over time.

We also observed a possible association between very high T2 lesion volumes and particularly prominent loss of deep gray volumes. While this preliminary observation in only seven participants requires further validation in larger cohorts, it suggests that highly inflammatory disease may also drive more aggressive neurodegeneration. In adults, a recent study by Pontillo et al. (Pontillo et al., 2019) found global T2 lesion volume to be a main determinant of atrophy in deep grey volumes in patients with relapsing-remitting MS, while a morphometric study by Al-Radaideh et al. (Al-Radaideh et al., 2019) found a weak, yet significant, inverse correlation between T2 lesion volume and volumes of the putamen ($r = -0.408$), globus pallidus ($r = -0.410$) and thalamus ($r = -0.407$) in relapsing-remitting MS.

Limitations of our work include the relatively small size of our relapsing demyelination cohort, an inherent challenge given the rarity of these diseases in children. To best define our methodology, we selected only research scans that passed a rigorous quality assurance process, analyzed scans from only three sites that had scanned patients and regional controls, and ensured that each site contributed a reasonable number (typically more than 25, sufficient to uniformly cover the age range) of scans for analysis. At baseline, and at the serial imaging timepoints, we did not analyze clinically acquired scans, nor did we include research scans that failed quality control. As such, our method may not generalize equally well to cohort studies wherein scans are acquired with more variability in sequence parameters between sites or between serial scans, or when quality assurance processes permit greater variability in acquisitions.

Our work has immediate relevance. Serial MRI data from pediatric cohorts, typically-developing and in the context of neurological disease, are limited. Our methods enable analyses of invaluable longitudinal cohort data, and permit retention of 1.5 T scan data as new 3 T MRI acquisition invariably occurs.

Acknowledgments

The authors are particularly grateful to the participating children and their families of the Canadian Pediatric Demyelinating Disease Study, the NIHPD Study, and the Philadelphia Neurodevelopmental Cohort for their cooperation and commitment to our research. The Canadian Pediatric Demyelinating Disease Study is supported by the Canadian Multiple Sclerosis Scientific Research Foundation, the Multiple Sclerosis Society of Canada, and the Canadian Institutes of Health. We wish to acknowledge the members of the Canadian Pediatric

Demyelinating Disease Network, especially Rozie Arnaoutelis at the McConnell Brain Imaging Centre (Montreal, QC, Canada).

Conflict of interest

The authors report no biomedical financial interests or potential conflicts of interest.

References

Al-Radaideh, A., Athamneh, I., Alabadi, H., Hbahbih, M., 2019. Cortical and Subcortical Morphometric and Iron Changes in Relapsing-Remitting Multiple Sclerosis and Their Association with White Matter T2 Lesion Load: A 3-Tesla Magnetic Resonance Imaging Study. Clin. Neuroradiol. 29, 51–64. https://doi.org/10.1007/s00062-017-0654-0

Armangue, T., Olivé-Cirera, G., Martínez-Hernandez, E., Sepulveda, M., Ruiz-Garcia, R., Muñoz-Batista, M., Ariño, H., González-Álvarez, V., Felipe-Rucián, A., Jesús Martínez-González, M., Cantarín-Extremera, V., Concepción Miranda-Herrero, M., Monge-Galindo, L., Tomás-Vila, M., Miravet, E., Málaga, I., Arrambide, G., Auger, C., Tintoré, M., Montalban, X., Vanderver, A., Graus, F., Saiz, A., Dalmau, J., Alcantud, A., Aguilera-Albesa, S., Alvarez Demanuel, D., Alvarez Molinero, M., Aquino Fariña, L., Arrabal, L., Arriola-Pereda, G., Aznar-Laín, G., Benavides-Medina, M., Bermejo, T., Blanco-Lago, R., Caballero, E., Calvo, R., Camacho Salas, A., Conejo-Moreno, D., Delgadillo-Chilavert, V., Elosegi-Castellanos, A., Esteban Canto, V., Fernández-Ramos, J., Garcia-Puig, M., García-Ribes, A., Gómez-Martín, H., Gonzalez-Barrios, D., González-Gutiérrez-Solana, L., Jimena-Garcia, S., Jiménez-Legido, M., Juliá-Palacios, N., López-Laso, E., Martí-Carrera, I., Martínez González, M., Martín-Viota, L., Mattozi, S., Maqueda-Castellote, E., Mendibe, M.D.M., Mora-Ramírez, M.D., Muñoz-Cabello, B., Navarro-Morón, J., Nunes-Cabrera, T., Orellana, G., Pujol-Soler, B., Querol, L., Ramírez, A., Rodriguez-Lucenilla, M.I., Ruiz, C., Soto-Insuga, V., Toledo Bravo de Laguna, L., Turon-Viñas, E., Vázquez-López, M., Villar-Vera, C., 2020. Associations of paediatric demyelinating and encephalitic syndromes with myelin oligodendrocyte glycoprotein antibodies: a multicentre observational study. Lancet Neurol. 19, 234–246. https://doi.org/10.1016/S1474-4422(19)30488-0

Aubert-Broche, B., Fonov, V., Narayanan, S., Arnold, D.L., Araujo, D., Fetco, D., Till, C., Sled, J.G., Banwell, B., Collins, D.L., On behalf of the Canadian Pediatric Demyelinating Disease Network, 2014. Onset of multiple sclerosis before adulthood leads to failure of age-expected brain growth. Neurology 83, 2140–2146. https://doi.org/10.1212/WNL.0000000000001045

Aubert-Broche, B., Fonov, V.S., García-Lorenzo, D., Mouiha, A., Guizard, N., Coupé, P., Eskildsen, S.F., Collins, D.L., 2013. A new method for structural volume analysis of longitudinal brain MRI data and its application in studying the growth trajectories of anatomical brain structures in childhood. NeuroImage 82, 393–402. https://doi.org/10.1016/j.neuroimage.2013.05.065

Avants, B., Epstein, C., Grossman, M., Gee, J., 2008. Symmetric diffeomorphic image registration with cross-correlation: Evaluating automated labeling of elderly and neurodegenerative brain. Med. Image Anal. 12, 26–41. https://doi.org/10.1016/j.media.2007.06.004

Banwell, B., Bar-Or, A., Arnold, D.L., Sadovnick, D., Narayanan, S., McGowan, M., O'Mahony, J., Magalhaes, S., Hanwell, H., Vieth, R., Tellier, R., Vincent, T., Disanto, G., Ebers, G., Wambera, K., Connolly, M.B., Yager, J., Mah, J.K., Booth, F., Sebire, G., Callen, D., Meaney, B., Dilenge, M.-E., Lortie, A., Pohl, D., Doja, A., Venketaswaran, S., Levin, S., MacDonald, E.A., Meek, D., Wood, E., Lowry, N., Buckley, D., Yim, C., Awuku, M., Cooper, P., Grand'Maison, F., Baird, J.B., Bhan, V., Marrie, R.A., 2011. Clinical, environmental, and genetic determinants of multiple sclerosis in children with acute demyelination: a prospective national cohort study. Lancet Neurol. 10, 436–445. https://doi.org/10.1016/S1474-4422(11)70045-X

Biberacher, V., Schmidt, P., Keshavan, A., Boucard, C.C., Righart, R., Sämann, P., Preibisch, C., Fröbel, D., Aly, L., Hemmer, B., Zimmer, C., Henry, R.G., Mühlau, M., 2016. Intra- and interscanner variability of magnetic resonance imaging based volumetry in multiple sclerosis. NeuroImage 142, 188–197. https://doi.org/10.1016/j.neuroimage.2016.07.035

Chard, D., Miller, D., 2009. Grey matter pathology in clinically early multiple sclerosis: Evidence from magnetic resonance imaging. J. Neurol. Sci. 282, 5–11. https://doi.org/10.1016/j.jns.2009.01.012

Clark, K.A., Woods, R.P., Rottenberg, D.A., Toga, A.W., Mazziotta, J.C., 2006. Impact of acquisition protocols and processing streams on tissue segmentation of T1 weighted MR images. NeuroImage 29, 185–202. https://doi.org/10.1016/j.neuroimage.2005.07.035

Dadar, M., Fonov, V.S., Collins, D.L., 2018. A comparison of publicly available linear MRI stereotaxic registration techniques. NeuroImage 174, 191–200. https://doi.org/10.1016/j.neuroimage.2018.03.025

De Meo, E., Meani, A., Moiola, L., Ghezzi, A., Veggiotti, P., Filippi, M., Rocca, M.A., 2019. Dynamic gray matter volume changes in pediatric multiple sclerosis: A 3.5 year MRI study. Neurology 92, e1709–e1723. https://doi.org/10.1212/WNL.0000000000007267

Eskildsen, S.F., Coupé, P., Fonov, V., Manjón, J.V., Leung, K.K., Guizard, N., Wassef, S.N., Østergaard, L.R., Collins, D.L., 2012. BEaST: Brain extraction based on nonlocal segmentation technique. NeuroImage 59, 2362–2373. https://doi.org/10.1016/j.neuroimage.2011.09.012

Evans, A.C., 2006. The NIH MRI study of normal brain development. NeuroImage 30, 184–202. https://doi.org/10.1016/j.neuroimage.2005.09.068

Fonov, V., Evans, A.C., Botteron, K., Almli, C.R., McKinstry, R.C., Collins, D.L., Brain Development Cooperative Group, 2011. Unbiased average age-appropriate atlases for pediatric studies. NeuroImage 54, 313–327. https://doi.org/10.1016/j.neuroimage.2010.07.033

Francis, S.J., 2004. Automatic lesion identification in MRI of multiple sclerosis patients. McGill University.

Ghione, E., Bergsland, N., Dwyer, M.G., Hagemeier, J., Jakimovski, D., Paunkoski, I., Ramasamy, D.P., Carl, E., Hojnacki, D., Kolb, C., Weinstock-Guttman, B., Zivadinov, R., 2019. Aging and Brain Atrophy in Multiple Sclerosis. J. Neuroimaging. https://doi.org/10.1111/jon.12625

Han, X., Jovicich, J., Salat, D., van der Kouwe, A., Quinn, B., Czanner, S., Busa, E., Pacheco, J., Albert, M., Killiany, R., Maguire, P., Rosas, D., Makris, N., Dale, A.,

Dickerson, B., Fischl, B., 2006. Reliability of MRI-derived measurements of human cerebral cortical thickness: The effects of field strength, scanner upgrade and manufacturer. NeuroImage 32, 180–194. https://doi.org/10.1016/j.neuroimage.2006.02.051

Krämer, J., Meuth, S., Tenberge, J.-G., Schiffler, P., Wiendl, H., Deppe, M., 2015. Early and Degressive Putamen Atrophy in Multiple Sclerosis. Int. J. Mol. Sci. 16, 23195–23209. https://doi.org/10.3390/ijms161023195

Mills, K.L., Goddings, A.-L., Herting, M.M., Meuwese, R., Blakemore, S.-J., Crone, E.A., Dahl, R.E., Güroğlu, B., Raznahan, A., Sowell, E.R., Tamnes, C.K., 2016. Structural brain development between childhood and adulthood: Convergence across four longitudinal samples. NeuroImage 141, 273–281. https://doi.org/10.1016/j.neuroimage.2016.07.044

Pontillo, G., Cocozza, S., Lanzillo, R., Russo, C., Stasi, M.D., Paolella, C., Vola, E.A., Criscuolo, C., Borrelli, P., Palma, G., Tedeschi, E., Morra, V.B., Elefante, A., Brunetti, A., 2019. Determinants of Deep Gray Matter Atrophy in Multiple Sclerosis: A Multimodal MRI Study. Am. J. Neuroradiol. 40, 99–106. https://doi.org/10.3174/ajnr.A5915

Satterthwaite, T.D., Elliott, M.A., Ruparel, K., Loughead, J., Prabhakaran, K., Calkins, M.E., Hopson, R., Jackson, C., Keefe, J., Riley, M., Mentch, F.D., Sleiman, P., Verma, R., Davatzikos, C., Hakonarson, H., Gur, R.C., Gur, R.E., 2014. Neuroimaging of the Philadelphia neurodevelopmental cohort. NeuroImage 86, 544–553. https://doi.org/10.1016/j.neuroimage.2013.07.064

Schnack, H.G., van Haren, N.E.M., Brouwer, R.M., van Baal, G.C.M., Picchioni, M., Weisbrod, M., Sauer, H., Cannon, T.D., Huttunen, M., Lepage, C., Collins, D.L., Evans, A., Murray, R.M., Kahn, R.S., Hulshoff Pol, H.E., 2010. Mapping reliability in multicenter MRI: Voxel-based morphometry and cortical thickness. Hum. Brain Mapp. 31, 1967–1982. https://doi.org/10.1002/hbm.20991

The MathWorks Inc., 2018. MATLAB. The MathWorks Inc., Natick, Massachusetts.

Thompson, A.J., Banwell, B.L., Barkhof, F., Carroll, W.M., Coetzee, T., Comi, G., Correale, J., Fazekas, F., Filippi, M., Freedman, M.S., Fujihara, K., Galetta, S.L., Hartung, H.P., Kappos, L., Lublin, F.D., Marrie, R.A., Miller, A.E., Miller, D.H., Montalban, X., Mowry, E.M., Sorensen, P.S., Tintoré, M., Traboulsee, A.L., Trojano, M., Uitdehaag, B.M.J., Vukusic, S., Waubant, E., Weinshenker, B.G., Reingold, S.C., Cohen, J.A., 2018. Diagnosis of multiple sclerosis: 2017 revisions of the McDonald criteria. Lancet Neurol. 17, 162–173. https://doi.org/10.1016/S1474-4422(17)30470-2

Till, C., Ghassemi, R., Aubert-Broche, B., Kerbrat, A., Collins, D.L., Narayanan, S., Arnold, D.L., Desrocher, M., Sled, J.G., Banwell, B.L., 2011. MRI correlates of cognitive impairment in childhood-onset multiple sclerosis. Neuropsychology 25, 319–332. https://doi.org/10.1037/a0022051

Tustison, N.J., Avants, B.B., Cook, P.A., Yuanjie Zheng, Egan, A., Yushkevich, P.A., Gee, J.C., 2010. N4ITK: Improved N3 Bias Correction. IEEE Trans. Med. Imaging 29, 1310–1320. https://doi.org/10.1109/TMI.2010.2046908

van Haren, N.E.M., Cahn, W., Hulshoff Pol, H.E., Schnack, H.G., Caspers, E., Lemstra, A., Sitskoorn, M.M., Wiersma, D., van den Bosch, R.J., Dingemans, P.M., Schene, A.H., Kahn, R.S., 2003. Brain volumes as predictor of outcome in recent-onset schizophrenia: a multi-center MRI study. Schizophr. Res. 64, 41–52. https://doi.org/10.1016/s0920-9964(03)00018-5

Waldman, A., Ghezzi, A., Bar-Or, A., Mikaeloff, Y., Tardieu, M., Banwell, B., 2014. Multiple sclerosis in children: an update on clinical diagnosis, therapeutic strategies, and research. Lancet Neurol. 13, 936–948. https://doi.org/10.1016/S1474-4422(14)70093-6

Chapter 6

Discussion, Future Work and Conclusion

In this chapter, we provide a summary of the rationale and main findings of Chapters 3, 4 and 5, as well as additional discussion regarding their contributions, strengths and limitations. Furthermore, we discuss prospective future work that can be built upon these contributions and provide an overall conclusion to the present work.

1 Discussion

The main goal of this thesis is the development and application of morphometric image analysis techniques for pediatric studies. The principal challenge in this task stems from the wealth of changes that occur in the brain during the different stages of normal neurodevelopment, for it is of the outmost importance to be able to disentangle these normal changes from any potential abnormalities associated with a given disease or disorder. In addition to the unique challenges of pediatric studies, the techniques presented are also required to address challenges inherent to any image analysis study, including the use of different scanners and protocols, having data acquired at various sites, and having sufficient, high quality control data to perform comparisons.

One of the most important factors to consider when applying image processing tools in studies of neurodevelopment is that each individual study presents its own complications, and as such any methods used need to be tuned for the specific data and analysis at hand. One of the main factors behind this comes down to the selection of an age range for the study, since the rate of changes, as well as the type of changes, vary significantly between the different stages of neurodevelopment. In terms of volume, the first years of age are characterized by very rapid growth, while later stages are characterized by slower growth that reaches a plateau and begins a very slow decline. In the case of myelination, strong changes in contrast in MRI can be seen during the first 12 months of life due to rapid and widespread myelination, while in later years myelination happens at a much slower rate and is confined to specific regions. We can easily observe this in Figure 24 by comparing what happens in the brain during the early stages of childhood (0-27 months of age) and later childhood and adolescence (3.5-18.5 years of age). As such, the requirements for a study that includes early childhood are quite

different from those centred in later childhood and adolescence, and thus the methods used need to be adapted differently in each case.

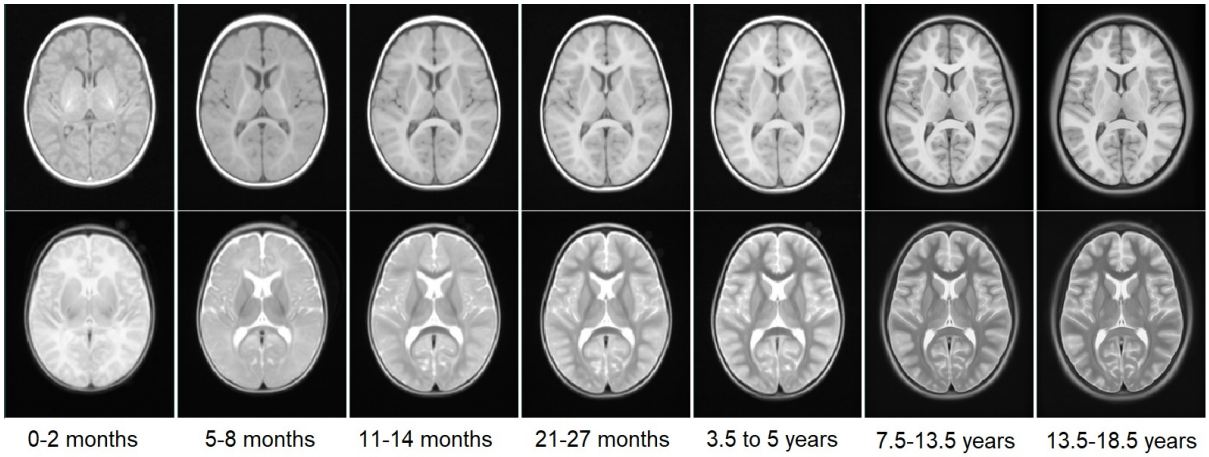

Figure 24. Average templates at different stages of neurodevelopment. The top row shows T1-weighted images, while the bottom row shows T2-weighted images.

The proposed technique in Chapter 3 focuses on dealing with the application of voxel-wise morphometric techniques, specifically TBM, during early childhood (6 months to 2 years of age). The main issues that our proposed technique tackles are the stark changes in contrast that happen during the first 8 months of life, where the T1 and T2 weighted signals from WM and GM reverse in intensity contrast, as well as the drastic change in overall head and brain size throughout the first 2 years of life. In order to improve the non-linear registration, in particular for scans acquired at around 6 months of age where the WM and GM contrast is very small, we use the information of both the T1 and T2-weighted scans simultaneously to optimize the registration. The use of both scans proves to be useful mainly because the changes in contrast due to myelination have different timelines in T1 and T2-weighted scans (Barkovich et al., 1988), and therefore provide complementary data for the registration algorithm. Furthermore, we chose to use three different age-appropriate templates (6, 12 and 24 months of age) as our registration targets, so that the non-linear transformation required for an individual scan was minimized and was performed to a template with the most similar WM and GM contrast. During quality control, the resulting non-linear registrations were found to be accurate and robust.

The application of this method to the Infant Brain Imaging Study (IBIS) of children at high risk of autism spectrum disorder (ASD) was of particular interest since this database included a large number of normally neurodeveloping controls (n=162) scanned longitudinally, thus providing enough information to model normal growth trajectories at the voxel level, while

accounting for changes due to age and sex during early childhood. Furthermore, this database includes 2 additional cohorts, one of children at high risk of autism diagnosed as neurotypical (HR-) and one of children at high risk of autism diagnosed with ASD (HR+). When comparing the 3 groups, it was found that the HR+ had significant differences in local growth trajectories when compared to controls, while the HR- were found to have similar growth trajectories to normal controls. In the few regions where the HR- group was found to be trending or only slightly (but statistically significantly) different from controls, the direction of the differences was the same as the ones found in the HR+ group and lay in between controls and the HR+ group. This leads to the speculation that the factors that play a role in the development of ASD are present in the HR- group but not sufficient to lead to ASD, as is the case for the HR+ group.

The importance of studying ASD at such an early age is highlighted by the well-known increase in head circumference and brain size found retrospectively in children diagnosed with ASD (Bailey et al., 1993; Davidovitch et al., 1996; Elder et al., 2008; Redcay and Courchesne, 2005; Woodhouse et al., 1996) coupled to studies showing abnormal morphology in older children and adults (Amaral et al., 2008; Barnea-Goraly et al., 2014; Hardan et al., 2000). Our results show that the growth trajectories of several regions in the brain are different in the HR+ group and may be the origin of volume abnormalities found in older children. Additionally, our results support the idea that ASD is strongly age-dependent, demonstrating different structural abnormalities at different stages of development (Carper et al., 2002; Courchesne et al., 2011), while providing one of the first insights into the nature of such abnormalities found in ASD during early childhood.

While the study conducted in Chapter 3 included enough normally developing controls with longitudinal information to model the normal growth trajectories, this is rarely the case in pediatric studies, where neurotypical controls are hard to come by and it is particularly difficult to obtain longitudinal data. This issue was part of the rationale for developing the normalization technique presented in Chapter 4. There, we propose the use of a large database of normally developing children (NIHPD) (Evans, 2006) to estimate normal growth trajectories for volumes of interest (e.g. whole brain volume, putamen, thalamus, among others) as well as at the voxel level using TBM. We can now use these models to normalize data from a pediatric study and obtain z-scores that give us information about how much a subject deviates from the expected volume (or Jacobian determinant in the case of TBM) given the subject's age and sex. This procedure has two main advantages, the first being that the dataset of interest requires fewer normal controls and does not require controls to be longitudinally acquired, as long as

they are spread evenly across the age-range, and the second being that any abnormality can be easily interpreted as a deviation from age-expected growth.

We applied this normalization technique to a study of 16p11.2 copy number variants (Martin-Brevet et al., 2018; The Simons VIP Consortium, 2012), with the goal of understanding the location, direction (i.e. increase or decrease), and time-course of potential brain abnormalities in the duplication and deletion cohorts with an age range from 4.5 to 23 years. It is important to note that the normalization procedure works as intended. We can observe this in the supplementary material of Chapter 4, where the control cohort of the 16p11.2 study is shown to have a mean z-score of 0.0 as expected across the age range after normalization, with neither a significant slope nor sex differences, while the data before normalization behaves as a quadratic function with a growth plateau around 17 years of age and a significant difference between males and females. Additionally, the voxel-wise z-scores of the 16p11.2 control cohort follow a standard Gaussian distribution ($\mu=0$, $\sigma=1$). Therefore, the normal controls from the 16p11.2 study were not found to be significantly different from the NIHPD dataset.

When we look at the duplication and deletion cohorts, we can see 2 different types of abnormalities: gene dose dependent abnormalities (i.e. the behaviour is mirrored in duplications and deletions) and abnormalities specific to either the duplication or the deletion cohort. These 2 types of abnormalities highlight the importance of performing "genetics first" (i.e. understanding genetic differences before looking at disorders) studies, particularly in the case of the 16p11.2 copy number variants, since these variants are specifically associated with several neurodevelopmental disorders, including ASD. Thus, knowing which areas of the brain present mirror alterations versus which areas are specific to a cohort can potentially help in understanding phenotypical traits specifically associated with either duplication or deletion, and could also potentially be tied to specific neurodevelopmental disorders.

In terms of our methodology, it is important to note that the results found using regional volumes and using voxel-wise analysis are in agreement. The clearest example of this can be seen in the lateral ventricles, where the volumetric and the voxel-wise analyses clearly show an increase in ventricular volume in duplication carriers. Furthermore, our results indicate that these brain abnormalities are already present at 4-6 years of age and remain stable throughout childhood and adolescence, making the study of early neurodevelopment, and perhaps even during gestation, necessary to truly understand the origin and time-course of these abnormalities.

The normalization procedure proposed in Chapter 4 was later expanded in Chapter 5 with the objective of making it more generalizable, thus allowing it to be applied to more complex datasets, particularly datasets that include data acquired at MRI field strengths of 1.5 and 3 T. The rationale is that in longitudinal pediatric studies, a multi-site approach enables larger data collection but inserts the potential for scanner differences, and when acquiring longitudinal data within a large age range, updates to scanners, and even upgrades (i.e. from a 1.5 T to a 3 T scanner) are possible. Therefore, a normalization technique that can account for these possibilities has a wider range of applications.

Some of the changes implemented include modifying some of the preprocessing steps, like improved bias field correction and integrating more robust non-linear registration methods. In addition to the changes in preprocessing, the normalization technique was enriched by adding an additional normative dataset acquired at 3T, the Philadelphia Neurodevelopmental Cohort (Satterthwaite et al., 2014). As such, our normative modeling is now more complex, since it includes 2 longitudinal datasets, one acquired at 1.5 T and one at 3 T, and a field strength effect is introduced to the mixed-effects model.

This normalization technique was applied to a longitudinal, multi-site study of pediatric onset multiple sclerosis from the Canadian Pediatric Demyelinating Disease Study (Verhey et al., 2011), with data acquired at 1.5 and 3 T, and a neurotypical cohort acquired at each site. This study presented a great opportunity to test the normalization technique, since it includes longitudinal data of subjects acquired exclusively at 1.5 T, exclusively at 3 T, and some subjects with initial timepoints acquired at 1.5 T and subsequent timepoints acquired at 3 T. The normalization technique was evaluated in 5 volumes of interest: whole brain volume, putamen, thalamus, globus pallidus, and caudate. The first important results come from looking at the normalization of the neurotypical cohort from each site of the pediatric MS study, where we can see two different validations of the normalization process. First, when testing using a linear model, the z-scores of the local controls do not have a significant intercept nor a significant slope, both when each site is considered independently as well as when all of the local controls are considered as a single group, so the controls have a mean z-score of 0.0 that is stable across the age range, as expected. Second, we looked at the distribution of the resulting z-score of the local controls and found that they follow a standard Gaussian distribution ($\mu=0$, $\sigma=1$). Therefore, the growth trajectories of the local controls from the Canadian Pediatric Demyelinating Disease Study are not significantly different from our normative datasets.

An additional test was performed to observe the effect of a subject transitioning from being scanned at 1.5 T at the start of the study to being scanned at 3 T later in the study. Unfortunately, we did not have neurotypical local controls that had been scanned longitudinally at both 1.5 and 3 T, so we looked at this effect in subjects diagnosed with MS that were longitudinally scanned first at 1.5 T and then at 3 T. By using interrupted time series regressions, we did not find significant step or slope changes due to the change in field strength. This result is of particular importance, since it supports the conclusions that the normalization technique is properly accounting for changes due to field strength, and that the overall trend and behaviour of an individual subject can be studied using this procedure.

The results obtained by applying this normalization technique to the MS cohort provide important insight into the development of this disease during childhood and adolescence. By looking at the behaviour of z-scores with age, we observe a lack of age-expected growth in the MS patients in terms of whole brain volume, with even larger differences found in thalamus, putamen and globus pallidus. Differences in whole brain volume and thalamus had already been reported in pediatric onset MS (Aubert-Broche et al., 2014) using a subset of the MS cohort used in Chapter 5 (i.e., using data from only one site, with fewer subjects and fewer timepoints). It is of note that using a larger, multi-site cohort shows a similar pattern of lack of age-expected growth, as well as extending the differences to the putamen and globus pallidus. Furthermore, by looking at changes in z-score related to disease duration, the differences are larger and indicate that at the moment of diagnosis, some atrophy is already present, particularly in the thalamus. This can be important evidence of disease presence even before enough symptoms for diagnosis are developed, improving our current understanding of the time course of MS in the pediatric population.

Beyond the clinical implications found for ASD, 16p11.2 copy number variants, and pediatric onset MS, it is important to note that the techniques described in Chapters 3, 4, and 5 can be applied to a wide array of pediatric imaging studies. These techniques were designed with the idea of accounting for the normal neurodevelopment to better isolate the potential abnormalities associated with a disease or disorder. The results of applying the normalization techniques to local neurotypical controls in Chapters 4 and 5 are especially important in showing that (local) normal controls behave as expected and that age and sex related changes occurring throughout childhood are properly accounted for.

2 Limitations

The main methodological limitations of the techniques described in Chapters 3, 4, and 5 stem from the accuracy of the main image processing tools used. In particular, the accuracy of non-linear registration heavily affects the overall performance and reliability of these techniques, since several key steps depend on high-quality nonlinear registration. Among these key steps we have the creation of age-appropriate templates in Chapter 3, the creation of longitudinal templates for each subject in Chapters 4 and 5, the use of atlas priors for the segmentation of deep nuclei in Chapters 4 and 5, and the use of Tensor Based Morphometry in Chapters 3 and 4. Due to the importance of nonlinear registration, we implemented a very thorough quality control process to evaluate the resulting transformations, as well as performing a round of tests to find the optimal parameters. Additionally, in Chapter 3 we used both T1 and T2 weighted images to curb the contrast problems found at an early age.

In Chapter 3, the study of ASD at such an early age presents a series of challenges and limitations from a clinical perspective. One important thing to note is the definition of the High Risk negative (HR-) and the High Risk positive (HR+) groups. In both cases, the subjects were at a high risk of ASD due to having a sibling diagnosed with ASD, and the split was based on the best-estimate diagnosis of ASD at 2 years of age. While this diagnosis is the most commonly used predictor of ASD outcome, with an estimated diagnostic agreement at 2 and 9 years of age of 67% (Lord et al., 2006), it is still highly likely that some of the subjects from the HR- group will later be diagnosed with ASD, while subjects from the HR+ group might have their diagnosis reversed. Furthermore, ASD is a complex disorder that affects individuals differently, with some experiencing larger problems in specific domains. This heterogeneity in ASD is difficult to analyze at such an early age, where it is quite a challenge to measure how different skill domains are affected.

In the study of 16p11.2 copy number variants presented in Chapter 4, one big limitation came from the data available. Only cross-sectional scans were acquired, and only a few younger children (between 4 and 6 years) with either duplications or deletions were included in the study. This essentially eliminated the possibility of observing within-subject longitudinal changes throughout childhood, while also limiting our power to detect differences at an early age and age-related differences.

The pediatric onset MS study from Chapter 5 also presented a limitation due to the availability of data. In this case, the subjects diagnosed with MS had longitudinal data, while

the local normal controls from each site had only cross-sectional scans. This lack of longitudinal local neurotypical controls reduces our ability to correct for site specific differences during the normalization procedure. While this correction can be done with cross-sectional controls, it would be more robust if it is performed with longitudinal data.

3 Future Work

From a methodological perspective, there are many improvements that can be made to the techniques presented in Chapters 3, 4, and 5. One area of opportunity can be found in developing a normalization technique similar to the work from Chapters 4 and 5 for early childhood. While the normal controls from the IBIS database used in Chapter 3 could be used as a normative database, a better normative cohort would ideally include scans at a younger age (e.g. 3 months), before the WM/GM contrast reversal. The inclusion of scans at a younger age would enable a better mapping of the normal neurodevelopment and could help in the processing of data at 6 months, which is the most complicated age to analyze due to the lack of contrast between tissue types. Furthermore, data from before the contrast reversal could prove useful in developing a longitudinal tissue classification algorithm, designed to work during early childhood.

In terms of the normalization technique for childhood and adolescence, we should be able to use the multi-field approach (i.e. using data acquired at 1.5 and 3 T) presented in Chapter 5 at the voxel level, similar to what was shown in Chapter 4. In reality, this process is quite advanced and shows promise, however further evaluation of its performance is needed. Additionally, adopting newer, better tissue classification algorithms, and adapting them to our longitudinal framework could also provide further improvement in the overall performance of these normalization analyses. Finally, these normalization techniques can be constantly improved with the addition of more normative data, as long as these databases evenly cover the age-range and provide longitudinal data.

For the ASD study, it would be interesting to obtain the clinical outcomes of the high-risk group when they turn 9 or 10 years old, and use these outcomes, as well as any quantitative measures of impairment for the different domains (e.g. social, emotional, repetitive behaviour), in a more complex analysis of the abnormalities found at this early age.

In the case of 16p11.2 copy number variants, our results showed that abnormalities were already present at around 4-6 years of age and seem to remain stable during childhood and adolescence. This opens two interesting avenues of study. The first one being the study of these

copy number variants during early childhood, and perhaps even *in utero*, to better understand the moment in neurodevelopment that the deviation from neurotypical occurs. The second avenue of study would be to look into subgroups within the 16p11.2 duplications and deletions, by looking at the diagnosis of associated diseases and disorders. By studying these subgroups, we could potentially isolate abnormalities that are specifically associated with a particular disease or disorder.

As for the pediatric onset MS study, the application of the normalization technique at the voxel level could lead to interesting insights, particularly in the thalamus, where perhaps the lack of age-expected growth may have a spatial pattern involving some structures more than others. This would have interesting anatomical-functional-behavioral implications.

Finally, while the techniques presented in Chapters 3, 4, and 5 were each applied to a unique pediatric study, they can be used in many potential pediatric imaging studies for wide range of neurodevelopmental disorders as well as psychiatric diseases. In particular, the normalization for childhood and adolescence can be used in any pediatric study within the age range of 6 to 22 years, the study can be multi-site and be acquired cross-sectionally or longitudinally, at 1.5 T, 3 T or both, and only requires to have enough local controls that cover the whole age range to validate the normalization procedure before analyzing to specific study group.

4 Conclusion

In the past few years, brain image processing tools have advanced at a rapid pace, allowing us to investigate potential changes in the brain associated with diseases and disorders with better accuracy. However, many of these novel tools were developed and validated using an adult population, thus the need to tailor and adjust these tools for use in pediatric studies, where modelling and understanding the normal neurodevelopment becomes an additional challenge to overcome. In this thesis we propose some morphometric techniques tuned for their application to pediatric data, with the main objective of properly accounting for the normal changes that occur due to neurodevelopment so that we can have a better understanding of the potential abnormalities associated with a disease or disorder.

By using the proposed techniques, we were able to observe changes in growth trajectories in children at high risk of ASD, to identify local brain volume differences in 16p11.2 copy number variants, and to observe the lack of age-expected growth in pediatric onset MS. These techniques provide an opportunity to better understand the time course and specific alterations

of a disease during childhood and have the potential to be used in the investigation of a vast number of neurodevelopmental disorders.

In conclusion, these morphometric tools are a stepping-stone in the ever-evolving field of pediatric brain imaging, with many further improvements possible, and have been shown to be useful in the study of various diseases. Furthermore, by applying these techniques we can obtain valuable information that can potentially lead to improved understanding of the etiology of a disorder, the development of biomarkers for clinical trials, and new diagnostic aids.

References

Ahmed, M.N., Yamany, S.M., Mohamed, N., Farag, A.A., Moriarty, T., 2002. A modified fuzzy c-means algorithm for bias field estimation and segmentation of MRI data. IEEE Trans. Med. Imaging 21, 193–199. https://doi.org/10.1109/42.996338

Albert Huang, A., Abugharbieh, R., Tam, R., 2009. A Hybrid Geometric–Statistical Deformable Model for Automated 3-D Segmentation in Brain MRI. IEEE Trans. Biomed. Eng. 56, 1838–1848. https://doi.org/10.1109/TBME.2009.2017509

Aljabar, P., Bhatia, K.K., Murgasova, M., Hajnal, J.V., Boardman, J.P., Srinivasan, L., Rutherford, M.A., Dyet, L.E., Edwards, A.D., Rueckert, D., 2008. Assessment of brain growth in early childhood using deformation-based morphometry. Neuroimage 39, 348–358. https://doi.org/10.1016/j.neuroimage.2007.07.067

Allison, T., Ginter, H., McCarthy, G., Nobre, A.C., Puce, A., Luby, M., Spencer, D.D., 1994. Face recognition in human extrastriate cortex. Journal of Neurophysiology 71, 821–825. https://doi.org/10.1152/jn.1994.71.2.821

Al-Radaideh, A., Athamneh, I., Alabadi, H., Hbahbih, M., 2019. Cortical and Subcortical Morphometric and Iron Changes in Relapsing-Remitting Multiple Sclerosis and Their Association with White Matter T2 Lesion Load: A 3-Tesla Magnetic Resonance Imaging Study. Clin Neuroradiol 29, 51–64. https://doi.org/10.1007/s00062-017-0654-0

Amaral, D.G., Schumann, C.M., Nordahl, C.W., 2008. Neuroanatomy of autism. Trends Neurosci. 31, 137–145. https://doi.org/10.1016/j.tins.2007.12.005

American Psychiatric Association, American Psychiatric Association (Eds.), 2000. Diagnostic and statistical manual of mental disorders: DSM-IV-TR, 4th ed., text revision. ed. American Psychiatric Association, Washington, DC.

Amodio, D.M., Frith, C.D., 2006. Meeting of minds: the medial frontal cortex and social cognition. Nat. Rev. Neurosci. 7, 268–277. https://doi.org/10.1038/nrn1884

Armangue, T., Olivé-Cirera, G., Martínez-Hernandez, E., Sepulveda, M., Ruiz-Garcia, R., Muñoz-Batista, M., Ariño, H., González-Álvarez, V., Felipe-Rucián, A., Jesús Martínez-González, M., Cantarín-Extremera, V., Concepción Miranda-Herrero, M., Monge-Galindo, L., Tomás-Vila, M., Miravet, E., Málaga, I., Arrambide, G., Auger, C., Tintoré, M., Montalban, X., Vanderver, A., Graus, F., Saiz, A., Dalmau, J., Alcantud, A., Aguilera-Albesa, S., Alvarez Demanuel, D., Alvarez Molinero, M., Aquino Fariña, L., Arrabal, L., Arriola-Pereda, G., Aznar-Laín, G., Benavides-Medina, M., Bermejo, T., Blanco-Lago, R., Caballero, E., Calvo, R., Camacho Salas, A., Conejo-Moreno, D., Delgadillo-Chilavert, V., Elosegi-Castellanos, A., Esteban Canto, V., Fernández-Ramos, J., Garcia-Puig, M., García-Ribes, A., Gómez-Martín, H., Gonzalez-Barrios, D., González-Gutiérrez-Solana, L., Jimena-Garcia, S., Jiménez-Legido, M., Juliá-Palacios, N., López-Laso, E., Martí-Carrera, I., Martínez González, M., Martín-Viota, L., Mattozi, S., Maqueda-Castellote, E., Mendibe, M.D.M., Mora-Ramírez, M.D., Muñoz-Cabello, B., Navarro-Morón, J., Nunes-Cabrera, T., Orellana, G., Pujol-Soler, B., Querol, L., Ramírez, A., Rodriguez-Lucenilla, M.I., Ruiz, C., Soto-Insuga, V., Toledo Bravo de Laguna, L., Turon-Viñas, E., Vázquez-López, M., Villar-Vera, C., 2020. Associations of paediatric demyelinating and encephalitic syndromes with myelin oligodendrocyte glycoprotein antibodies: a multicentre observational study. The Lancet Neurology 19, 234–246. https://doi.org/10.1016/S1474-4422(19)30488-0

Artaechevarria, X., Munoz-Barrutia, A., Ortiz-de-Solorzano, C., 2009. Combination Strategies in Multi-Atlas Image Segmentation: Application to Brain MR Data. IEEE Trans. Med. Imaging 28, 1266–1277. https://doi.org/10.1109/TMI.2009.2014372
Ashburner, J., Friston, K.J., 2005. Unified segmentation. NeuroImage 26, 839–851. https://doi.org/10.1016/j.neuroimage.2005.02.018
Ashburner, J., Friston, K.J., 2004. Morphometry, in: Frackowiak, R.S.J. (Ed.), Human Brain Function. Elsevier Academic Press, Amsterdam ; Boston.
Ashburner, J., Friston, K.J., 2000. Voxel-Based Morphometry—The Methods. NeuroImage 11, 805–821. https://doi.org/10.1006/nimg.2000.0582
Aubert-Broche, B., Fonov, V., Ghassemi, R., Narayanan, S., Arnold, D.L., Banwell, B., Sled, J.G., Collins, D.L., 2011. Regional brain atrophy in children with multiple sclerosis. NeuroImage 58, 409–415. https://doi.org/10.1016/j.neuroimage.2011.03.025
Aubert-Broche, B., Fonov, V., Narayanan, S., Arnold, D.L., Araujo, D., Fetco, D., Till, C., Sled, J.G., Banwell, B., Collins, D.L., On behalf of the Canadian Pediatric Demyelinating Disease Network, 2014. Onset of multiple sclerosis before adulthood leads to failure of age-expected brain growth. Neurology 83, 2140–2146. https://doi.org/10.1212/WNL.0000000000001045
Aubert-Broche, B., Fonov, V.S., García-Lorenzo, D., Mouiha, A., Guizard, N., Coupé, P., Eskildsen, S.F., Collins, D.L., 2013. A new method for structural volume analysis of longitudinal brain MRI data and its application in studying the growth trajectories of anatomical brain structures in childhood. NeuroImage 82, 393–402. https://doi.org/10.1016/j.neuroimage.2013.05.065
August, G.J., Stewart, M.A., Tsai, L., 1981. The incidence of cognitive disabilities in the siblings of autistic children. Br J Psychiatry 138, 416–422.
Avants, B., Epstein, C., Grossman, M., Gee, J., 2008. Symmetric diffeomorphic image registration with cross-correlation: Evaluating automated labeling of elderly and neurodegenerative brain. Medical Image Analysis 12, 26–41. https://doi.org/10.1016/j.media.2007.06.004
Avants, B.B., Tustison, N.J., Song, G., Cook, P.A., Klein, A., Gee, J.C., 2011. A reproducible evaluation of ANTs similarity metric performance in brain image registration. NeuroImage 54, 2033–2044. https://doi.org/10.1016/j.neuroimage.2010.09.025
Bailey, A., Luthert, P., Bolton, P., Le Couteur, A., Rutter, M., Harding, B., 1993. Autism and megalencephaly. Lancet 341, 1225–1226.
Bajcsy, R., 2003. Digital Anatomy Atlas and Its Registration to MRI, fMRI, PET: The Past Presents a Future, in: Gee, J.C., Maintz, J.B.A., Vannier, M.W. (Eds.), Biomedical Image Registration, Lecture Notes in Computer Science. Springer Berlin Heidelberg, Berlin, Heidelberg, pp. 201–211. https://doi.org/10.1007/978-3-540-39701-4_21
Banwell, B., Bar-Or, A., Arnold, D.L., Sadovnick, D., Narayanan, S., McGowan, M., O'Mahony, J., Magalhaes, S., Hanwell, H., Vieth, R., Tellier, R., Vincent, T., Disanto, G., Ebers, G., Wambera, K., Connolly, M.B., Yager, J., Mah, J.K., Booth, F., Sebire, G., Callen, D., Meaney, B., Dilenge, M.-E., Lortie, A., Pohl, D., Doja, A., Venketaswaran, S., Levin, S., MacDonald, E.A., Meek, D., Wood, E., Lowry, N., Buckley, D., Yim, C., Awuku, M., Cooper, P., Grand'Maison, F., Baird, J.B., Bhan, V., Marrie, R.A., 2011. Clinical, environmental, and genetic determinants of multiple sclerosis in children with acute demyelination: a prospective national cohort study. The Lancet Neurology 10, 436–445. https://doi.org/10.1016/S1474-4422(11)70045-X
Barkovich, A.J., Kjos, B.O., 1988. Normal postnatal development of the corpus callosum as demonstrated by MR imaging. AJNR Am J Neuroradiol 9, 487–491.

Barkovich, A.J., Kjos, B.O., Jackson, D.E., Norman, D., 1988. Normal maturation of the neonatal and infant brain: MR imaging at 1.5 T. Radiology 166, 173–180. https://doi.org/10.1148/radiology.166.1.3336675

Barnea-Goraly, N., Frazier, T.W., Piacenza, L., Minshew, N.J., Keshavan, M.S., Reiss, A.L., Hardan, A.Y., 2014. A preliminary longitudinal volumetric MRI study of amygdala and hippocampal volumes in autism. Prog. Neuropsychopharmacol. Biol. Psychiatry 48, 124–128. https://doi.org/10.1016/j.pnpbp.2013.09.010

Bates, D., Mächler, M., Bolker, B., Walker, S., 2015. Fitting Linear Mixed-Effects Models Using lme4. J. Stat. Soft. 67. https://doi.org/10.18637/jss.v067.i01

Benjamini, Y., Hochberg, Y., 1995. Controlling the False Discovery Rate: A Practical and Powerful Approach to Multiple Testing. Journal of the Royal Statistical Society, Methodological 57, 289–300. https://doi.org/10.2307/2346101

Benjamini, Y., Yekutieli, D., 2001. The Control of the False Discovery Rate in Multiple Testing Under Dependency. The Annals of Statistics 29, 1165–1188. https://doi.org/10.1214/aos/1013699998

Bernal-Rusiel, J.L., Greve, D.N., Reuter, M., Fischl, B., Sabuncu, M.R., Alzheimer's Disease Neuroimaging Initiative, 2013. Statistical analysis of longitudinal neuroimage data with Linear Mixed Effects models. Neuroimage 66, 249–260. https://doi.org/10.1016/j.neuroimage.2012.10.065

Berryer, M.H., Chattopadhyaya, B., Xing, P., Riebe, I., Bosoi, C., Sanon, N., Antoine-Bertrand, J., Lévesque, M., Avoli, M., Hamdan, F.F., Carmant, L., Lamarche-Vane, N., Lacaille, J.-C., Michaud, J.L., Di Cristo, G., 2016. Decrease of SYNGAP1 in GABAergic cells impairs inhibitory synapse connectivity, synaptic inhibition and cognitive function. Nat Commun 7, 13340. https://doi.org/10.1038/ncomms13340

Biberacher, V., Schmidt, P., Keshavan, A., Boucard, C.C., Righart, R., Sämann, P., Preibisch, C., Fröbel, D., Aly, L., Hemmer, B., Zimmer, C., Henry, R.G., Mühlau, M., 2016. Intra- and interscanner variability of magnetic resonance imaging based volumetry in multiple sclerosis. NeuroImage 142, 188–197. https://doi.org/10.1016/j.neuroimage.2016.07.035

Bird, C.R., Hedberg, M., Drayer, B.P., Keller, P.J., Flom, R.A., Hodak, J.A., 1989. MR assessment of myelination in infants and children: usefulness of marker sites. AJNR Am J Neuroradiol 10, 731–740.

Bompard, L., Xu, S., Styner, M., Paniagua, B., Ahn, M., Yuan, Y., Jewells, V., Gao, W., Shen, D., Zhu, H., Lin, W., 2014. Multivariate Longitudinal Shape Analysis of Human Lateral Ventricles during the First Twenty-Four Months of Life. PLoS ONE 9, e108306. https://doi.org/10.1371/journal.pone.0108306

Bonferroni, C.E., 1936. Teoria Statistica Delle Classi e Calcolo Delle Probabilità. Pubblicazioni del R. Istituto superiore di scienze economiche e commerciali di Firenze. https://doi.org/10.4135/9781412961288.n455

Brodmann, K., 1909. Vergleichende Lokalisationslehre der Großhirnrinde : in ihren Prinzipien dargestellt auf Grund des Zellenbaues. Johann Ambrosius Barth, Leipzig.

Bush, null, Luu, null, Posner, null, 2000. Cognitive and emotional influences in anterior cingulate cortex. Trends Cogn. Sci. (Regul. Ed.) 4, 215–222. https://doi.org/10.1016/s1364-6613(00)01483-2

Cabezas, M., Oliver, A., Lladó, X., Freixenet, J., Bach Cuadra, M., 2011. A review of atlas-based segmentation for magnetic resonance brain images. Computer Methods and Programs in Biomedicine 104, e158–e177. https://doi.org/10.1016/j.cmpb.2011.07.015

Cardoso, A.R., Lopes-Marques, M., Silva, R.M., Serrano, C., Amorim, A., Prata, M.J., Azevedo, L., 2019. Essential genetic findings in neurodevelopmental disorders. Hum Genomics 13, 31. https://doi.org/10.1186/s40246-019-0216-4

Carper, R.A., Moses, P., Tigue, Z.D., Courchesne, E., 2002. Cerebral lobes in autism: early hyperplasia and abnormal age effects. Neuroimage 16, 1038–1051.

Caviness, V.S., Kennedy, D.N., Richelme, C., Rademacher, J., Filipek, P.A., 1996. The Human Brain Age 7–11 Years: A Volumetric Analysis Based on Magnetic Resonance Images. Cereb Cortex 6, 726–736. https://doi.org/10.1093/cercor/6.5.726

Chard, D., Miller, D., 2009. Grey matter pathology in clinically early multiple sclerosis: Evidence from magnetic resonance imaging. Journal of the Neurological Sciences 282, 5–11. https://doi.org/10.1016/j.jns.2009.01.012

Chen, S., Zhang, D., 2004. Robust Image Segmentation Using FCM With Spatial Constraints Based on New Kernel-Induced Distance Measure. IEEE Trans. Syst., Man, Cybern. B 34, 1907–1916. https://doi.org/10.1109/TSMCB.2004.831165

Cheng, J., Edwards, L.J., Maldonado-Molina, M.M., Komro, K.A., Muller, K.E., 2010. Real longitudinal data analysis for real people: building a good enough mixed model. Stat Med 29, 504–520. https://doi.org/10.1002/sim.3775

Chiu, P.H., Kayali, M.A., Kishida, K.T., Tomlin, D., Klinger, L.G., Klinger, M.R., Montague, P.R., 2008. Self responses along cingulate cortex reveal quantitative neural phenotype for high-functioning autism. Neuron 57, 463–473. https://doi.org/10.1016/j.neuron.2007.12.020

Choe, M. -s., Ortiz-Mantilla, S., Makris, N., Gregas, M., Bacic, J., Haehn, D., Kennedy, D., Pienaar, R., Caviness, V.S., Benasich, A.A., Grant, P.E., 2013. Regional Infant Brain Development: An MRI-Based Morphometric Analysis in 3 to 13 Month Olds. Cerebral Cortex 23, 2100–2117. https://doi.org/10.1093/cercor/bhs197

Choudhury, S., Charman, T., Blakemore, S.-J., 2008. Development of the Teenage Brain. Mind, Brain, and Education 2, 142–147. https://doi.org/10.1111/j.1751-228X.2008.00045.x

Christensen, G.E., Rabbitt, R.D., Miller, M.I., 1994. 3D brain mapping using a deformable neuroanatomy. Phys. Med. Biol. 39, 609–618. https://doi.org/10.1088/0031-9155/39/3/022

Christophe, C., Muller, M.F., Bal�riaux, D., Kahn, A., Pardou, A., Perlmutter, N., Szliwowski, H., Segebarth, C., 1990. Mapping of normal brain maturation in infants on phase-sensitive inversion-recovery MR images. Neuroradiology 32, 173–178. https://doi.org/10.1007/BF00589106

Chunming Li, Rui Huang, Zhaohua Ding, Gatenby, J.C., Metaxas, D.N., Gore, J.C., 2011. A Level Set Method for Image Segmentation in the Presence of Intensity Inhomogeneities With Application to MRI. IEEE Trans. on Image Process. 20, 2007–2016. https://doi.org/10.1109/TIP.2011.2146190

Clark, K.A., Woods, R.P., Rottenberg, D.A., Toga, A.W., Mazziotta, J.C., 2006. Impact of acquisition protocols and processing streams on tissue segmentation of T1 weighted MR images. Neuroimage 29, 185–202. https://doi.org/10.1016/j.neuroimage.2005.07.035

Clement, J.P., Aceti, M., Creson, T.K., Ozkan, E.D., Shi, Y., Reish, N.J., Almonte, A.G., Miller, B.H., Wiltgen, B.J., Miller, C.A., Xu, X., Rumbaugh, G., 2012. Pathogenic SYNGAP1 Mutations Impair Cognitive Development by Disrupting Maturation of Dendritic Spine Synapses. Cell 151, 709–723. https://doi.org/10.1016/j.cell.2012.08.045

Cocosco, C.A., Zijdenbos, A.P., Evans, A.C., 2003. A fully automatic and robust brain MRI tissue classification method. Med Image Anal 7, 513–527. https://doi.org/10.1016/s1361-8415(03)00037-9

Collins, D.L., Holmes, C.J., Peters, T.M., Evans, A.C., 1995. Automatic 3-D model-based neuroanatomical segmentation. Human Brain Mapping 3, 190–208. https://doi.org/10.1002/hbm.460030304

Collins, D.L., Neelin, P., Peters, T.M., Evans, A.C., 1994. Automatic 3D intersubject registration of MR volumetric data in standardized Talairach space. J Comput Assist Tomogr 18, 192–205.

Condon, B., Grant, R., Hadley, D., Lawrence, A., 1988. Brain and intracranial cavity volumes: *in vivo* determination by MRI. Acta Neurologica Scandinavica 78, 387–393. https://doi.org/10.1111/j.1600-0404.1988.tb03674.x

Condon, B.R., Patterson, J., Wyper, D., Hadley, D.M., Teasdale, G., Grant, R., Jenkins, A., Macpherson, P., Rowan, J., 1986. A Quantitative Index of Ventricular and Extraventricular Intracranial CSF Volumes Using MR Imaging: Journal of Computer Assisted Tomography 10, 784–792. https://doi.org/10.1097/00004728-198609000-00015

Coupé, P., Manjón, J.V., Fonov, V., Pruessner, J., Robles, M., Collins, D.L., 2011. Patch-based segmentation using expert priors: Application to hippocampus and ventricle segmentation. NeuroImage 54, 940–954. https://doi.org/10.1016/j.neuroimage.2010.09.018

Coupe, P., Yger, P., Prima, S., Hellier, P., Kervrann, C., Barillot, C., 2008. An Optimized Blockwise Nonlocal Means Denoising Filter for 3-D Magnetic Resonance Images. IEEE Trans. Med. Imaging 27, 425–441. https://doi.org/10.1109/TMI.2007.906087

Courchesne, E., Campbell, K., Solso, S., 2011. Brain growth across the life span in autism: age-specific changes in anatomical pathology. Brain Res. 1380, 138–145. https://doi.org/10.1016/j.brainres.2010.09.101

Cover, T., Hart, P., 1967. Nearest neighbor pattern classification. IEEE Trans. Inform. Theory 13, 21–27. https://doi.org/10.1109/TIT.1967.1053964

Dadar, M., Fonov, V.S., Collins, D.L., 2018. A comparison of publicly available linear MRI stereotaxic registration techniques. NeuroImage 174, 191–200. https://doi.org/10.1016/j.neuroimage.2018.03.025

D'Angelo, D., Lebon, S., Chen, Q., Martin-Brevet, S., Snyder, L.G., Hippolyte, L., Hanson, E., Maillard, A.M., Faucett, W.A., Macé, A., Pain, A., Bernier, R., Chawner, S.J.R.A., David, A., Andrieux, J., Aylward, E., Baujat, G., Caldeira, I., Conus, P., Ferrari, C., Forzano, F., Gérard, M., Goin-Kochel, R.P., Grant, E., Hunter, J.V., Isidor, B., Jacquette, A., Jønch, A.E., Keren, B., Lacombe, D., Le Caignec, C., Martin, C.L., Männik, K., Metspalu, A., Mignot, C., Mukherjee, P., Owen, M.J., Passeggeri, M., Rooryck-Thambo, C., Rosenfeld, J.A., Spence, S.J., Steinman, K.J., Tjernagel, J., Van Haelst, M., Shen, Y., Draganski, B., Sherr, E.H., Ledbetter, D.H., van den Bree, M.B.M., Beckmann, J.S., Spiro, J.E., Reymond, A., Jacquemont, S., Chung, W.K., for the Cardiff University Experiences of Children With Copy Number Variants (ECHO) Study, the 16p11.2 European Consortium, and the Simons Variation in Individuals Project (VIP) Consortium, 2016. Defining the Effect of the 16p11.2 Duplication on Cognition, Behavior, and Medical Comorbidities. JAMA Psychiatry 73, 20. https://doi.org/10.1001/jamapsychiatry.2015.2123

Davidovitch, M., Patterson, B., Gartside, P., 1996. Head circumference measurements in children with autism. J. Child Neurol. 11, 389–393.

De Meo, E., Meani, A., Moiola, L., Ghezzi, A., Veggiotti, P., Filippi, M., Rocca, M.A., 2019. Dynamic gray matter volume changes in pediatric multiple sclerosis: A 3.5 year MRI study. Neurology 92, e1709–e1723. https://doi.org/10.1212/WNL.0000000000007267

del Fresno, M., Vénere, M., Clausse, A., 2009. A combined region growing and deformable model method for extraction of closed surfaces in 3D CT and MRI scans. Computerized Medical Imaging and Graphics 33, 369–376. https://doi.org/10.1016/j.compmedimag.2009.03.002

Despotović, I., Goossens, B., Philips, W., 2015. MRI Segmentation of the Human Brain: Challenges, Methods, and Applications. Computational and Mathematical Methods in Medicine 2015, 1–23. https://doi.org/10.1155/2015/450341

Dietrich, R.B., Bradley, W.G., Zaragoza, E.J., Otto, R.J., Taira, R.K., Wilson, G.H., Kangarloo, H., 1988. MR evaluation of early myelination patterns in normal and developmentally delayed infants. AJR Am J Roentgenol 150, 889–896. https://doi.org/10.2214/ajr.150.4.889

Drevets, W.C., Savitz, J., Trimble, M., 2008. The Subgenual Anterior Cingulate Cortex in Mood Disorders. CNS spectr. 13, 663–681. https://doi.org/10.1017/S1092852900013754

Ducharme, S., Albaugh, M.D., Nguyen, T.-V., Hudziak, J.J., Mateos-Pérez, J.M., Labbe, A., Evans, A.C., Karama, S., 2016. Trajectories of cortical thickness maturation in normal brain development — The importance of quality control procedures. NeuroImage 125, 267–279. https://doi.org/10.1016/j.neuroimage.2015.10.010

Elder, L.M., Dawson, G., Toth, K., Fein, D., Munson, J., 2008. Head circumference as an early predictor of autism symptoms in younger siblings of children with autism spectrum disorder. J Autism Dev Disord 38, 1104–1111. https://doi.org/10.1007/s10803-007-0495-9

Erturk, M.A., Bottomley, P.A., El-Sharkawy, A.-M.M., 2013. Denoising MRI using spectral subtraction. IEEE Trans Biomed Eng 60, 1556–1562. https://doi.org/10.1109/TBME.2013.2239293

Eskildsen, S.F., Coupé, P., Fonov, V., Manjón, J.V., Leung, K.K., Guizard, N., Wassef, S.N., Østergaard, L.R., Collins, D.L., 2012. BEaST: Brain extraction based on nonlocal segmentation technique. NeuroImage 59, 2362–2373. https://doi.org/10.1016/j.neuroimage.2011.09.012

Evans, A.C., 2006. The NIH MRI study of normal brain development. NeuroImage 30, 184–202. https://doi.org/10.1016/j.neuroimage.2005.09.068

Evans, A.C., Brain Development Cooperative Group, 2006. The NIH MRI study of normal brain development. Neuroimage 30, 184–202. https://doi.org/10.1016/j.neuroimage.2005.09.068

Fischl, B., Salat, D.H., Busa, E., Albert, M., Dieterich, M., Haselgrove, C., van der Kouwe, A., Killiany, R., Kennedy, D., Klaveness, S., Montillo, A., Makris, N., Rosen, B., Dale, A.M., 2002. Whole brain segmentation: automated labeling of neuroanatomical structures in the human brain. Neuron 33, 341–355. https://doi.org/10.1016/s0896-6273(02)00569-x

Fonov, V., Evans, A.C., Botteron, K., Almli, C.R., McKinstry, R.C., Collins, D.L., Brain Development Cooperative Group, 2011. Unbiased average age-appropriate atlases for pediatric studies. Neuroimage 54, 313–327. https://doi.org/10.1016/j.neuroimage.2010.07.033

Fonov, V.S., Janke, A., Caramanos, Z., Arnold, D.L., Narayanan, S., Pike, G.B., Collins, D.L., 2010. Improved Precision in the Measurement of Longitudinal Global and Regional Volumetric Changes via a Novel MRI Gradient Distortion Characterization

and Correction Technique, in: Liao, H., Edwards, P.J. “Eddie,” Pan, X., Fan, Y., Yang, G.-Z. (Eds.), Medical Imaging and Augmented Reality: 5th International Workshop, MIAR 2010, Beijing, China, September 19-20, 2010. Proceedings. Springer Berlin Heidelberg, Berlin, Heidelberg, pp. 324–333.
Fox, P.T., Perlmutter, J.S., Raichle, M.E., 1985. A Stereotactic Method of Anatomical Localization for Positron Emission Tomography: Journal of Computer Assisted Tomography 9, 141–153. https://doi.org/10.1097/00004728-198501000-00025
Frackowiak, R.S.J. (Ed.), 2004. Human brain function, 2nd ed. ed. Elsevier Academic Press, Amsterdam ; Boston.
Francis, S.J., 2004. Automatic lesion identification in MRI of multiple sclerosis patients. McGill University.
Fransson, P., 2005. Spontaneous low-frequency BOLD signal fluctuations: an fMRI investigation of the resting-state default mode of brain function hypothesis. Hum Brain Mapp 26, 15–29. https://doi.org/10.1002/hbm.20113
Gee, J.C., Reivich, M., Bajcsy, R., 1993. Elastically Deforming 3D Atlas to Match Anatomical Brain Images: Journal of Computer Assisted Tomography 17, 225–236. https://doi.org/10.1097/00004728-199303000-00011
Genovese, C.R., Lazar, N.A., Nichols, T., 2002. Thresholding of statistical maps in functional neuroimaging using the false discovery rate. Neuroimage 15, 870–878. https://doi.org/10.1006/nimg.2001.1037
Gerig, G., Kubler, O., Kikinis, R., Jolesz, F.A., 1992. Nonlinear anisotropic filtering of MRI data. IEEE Trans. Med. Imaging 11, 221–232. https://doi.org/10.1109/42.141646
Ghione, E., Bergsland, N., Dwyer, M.G., Hagemeier, J., Jakimovski, D., Paunkoski, I., Ramasamy, D.P., Carl, E., Hojnacki, D., Kolb, C., Weinstock-Guttman, B., Zivadinov, R., 2019. Aging and Brain Atrophy in Multiple Sclerosis. Journal of Neuroimaging. https://doi.org/10.1111/jon.12625
Giedd, J.N., Blumenthal, J., Jeffries, N.O., Castellanos, F.X., Liu, H., Zijdenbos, A., Paus, T., Evans, A.C., Rapoport, J.L., 1999. Brain development during childhood and adolescence: a longitudinal MRI study. Nat Neurosci 2, 861–863. https://doi.org/10.1038/13158
Giedd, J.N., Rapoport, J.L., 2010. Structural MRI of Pediatric Brain Development: What Have We Learned and Where Are We Going? Neuron 67, 728–734. https://doi.org/10.1016/j.neuron.2010.08.040
Gilmore, J.H., Shi, F., Woolson, S.L., Knickmeyer, R.C., Short, S.J., Lin, W., Zhu, H., Hamer, R.M., Styner, M., Shen, D., 2012. Longitudinal Development of Cortical and Subcortical Gray Matter from Birth to 2 Years. Cerebral Cortex 22, 2478–2485. https://doi.org/10.1093/cercor/bhr327
Girault, J.B., Swanson, M.R., Meera, S.S., Grzadzinski, R.L., Shen, M.D., Burrows, C.A., Wolff, J.J., Pandey, J., John, T.S., Estes, A., Zwaigenbaum, L., Botteron, K.N., Hazlett, H.C., Dager, S.R., Schultz, R.T., Constantino, J.N., Piven, J., for the IBIS Network, 2020. Quantitative trait variation in ASD probands and toddler sibling outcomes at 24 months. J Neurodevelop Disord 12, 5. https://doi.org/10.1186/s11689-020-9308-7
Good, C.D., Johnsrude, I.S., Ashburner, J., Henson, R.N.A., Friston, K.J., Frackowiak, R.S.J., 2001. A Voxel-Based Morphometric Study of Ageing in 465 Normal Adult Human Brains. NeuroImage 14, 21–36. https://doi.org/10.1006/nimg.2001.0786
Gouttard, S., Styner, M., Prastawa, M., Piven, J., Gerig, G., 2008. Assessment of reliability of multi-site neuroimaging via traveling phantom study. Med Image Comput Comput Assist Interv 11, 263–270.

Gudbjartsson, H., Patz, S., 1995. The Rician distribution of noisy MRI data. Magn Reson Med 34, 910–914. https://doi.org/10.1002/mrm.1910340618
Habib, A.F., Alruzouq, R.I., 2004. Line-based modified iterated Hough transform for automatic registration of multi-source imagery. Photogrammetric Record 19, 5–21. https://doi.org/10.1111/j.0031-868X.2003.00254.x
Han, X., Jovicich, J., Salat, D., van der Kouwe, A., Quinn, B., Czanner, S., Busa, E., Pacheco, J., Albert, M., Killiany, R., Maguire, P., Rosas, D., Makris, N., Dale, A., Dickerson, B., Fischl, B., 2006. Reliability of MRI-derived measurements of human cerebral cortical thickness: The effects of field strength, scanner upgrade and manufacturer. NeuroImage 32, 180–194. https://doi.org/10.1016/j.neuroimage.2006.02.051
Hanson, A.R., Riseman, E.M. (Eds.), 1978. Computer vision systems: papers from the Workshop on Computer Vision Systems, held at the University of Massachusetts, Amherst, Massachusetts, June 1-3, 1977. Presented at the Workshop on Computer Vision Systems, University of Massachusetts, Academic Press, New York.
Hardan, A.Y., Minshew, N.J., Keshavan, M.S., 2000. Corpus callosum size in autism. Neurology 55, 1033–1036.
Haug, H., 1986. History of neuromorphometry. Journal of Neuroscience Methods 18, 1–17. https://doi.org/10.1016/0165-0270(86)90110-X
Hayakawa, K., Konishi, Y., Kuriyama, M., Konishi, K., Matsuda, T., 1991. Normal brain maturation in MRI. Eur J Radiol 12, 208–215. https://doi.org/10.1016/0720-048x(91)90074-6
Hazlett, H.C., Gu, H., McKinstry, R.C., Shaw, D.W.W., Botteron, K.N., Dager, S.R., Styner, M., Vachet, C., Gerig, G., Paterson, S.J., Schultz, R.T., Estes, A.M., Evans, A.C., Piven, J., IBIS Network, 2012a. Brain volume findings in 6-month-old infants at high familial risk for autism. Am J Psychiatry 169, 601–608. https://doi.org/10.1176/appi.ajp.2012.11091425
Hazlett, H.C., Poe, M.D., Gerig, G., Styner, M., Chappell, C., Smith, R.G., Vachet, C., Piven, J., 2011. Early brain overgrowth in autism associated with an increase in cortical surface area before age 2 years. Arch. Gen. Psychiatry 68, 467–476. https://doi.org/10.1001/archgenpsychiatry.2011.39
Hazlett, H.C., Poe, M.D., Lightbody, A.A., Styner, M., MacFall, J.R., Reiss, A.L., Piven, J., 2012b. Trajectories of early brain volume development in fragile X syndrome and autism. J Am Acad Child Adolesc Psychiatry 51, 921–933. https://doi.org/10.1016/j.jaac.2012.07.003
Hazlett, Heather Cody, Gu, H., Munsell, B.C., Kim, S.H., Styner, Martin, Wolff, Jason J., Elison, Jed T., Swanson, M.R., Zhu, H., Botteron, Kelly N., Collins, D. Louis, Constantino, John N., Dager, Stephen R., Estes, Annette M., Evans, Alan C., Fonov, Vladimir S., Gerig, Guido, Kostopoulos, Penelope, McKinstry, Robert C., Pandey, J., Paterson, Sarah, Pruett, J.R., Schultz, Robert T., Shaw, Dennis W., Zwaigenbaum, Lonnie, Piven, Joseph, Piven, J., Hazlett, H. C., Chappell, C., Dager, S. R., Estes, A. M., Shaw, D. W., Botteron, K. N., McKinstry, R. C., Constantino, J. N., Pruett Jr, J.R., Schultz, R. T., Paterson, S., Zwaigenbaum, L., Elison, J. T., Wolff, J. J., Evans, A. C., Collins, D. L., Pike, G.B., Fonov, V. S., Kostopoulos, P., Das, S., Gerig, G., Styner, M., Gu, C.H., 2017. Early brain development in infants at high risk for autism spectrum disorder. Nature 542, 348–351. https://doi.org/10.1038/nature21369
Healy, D.M., Weaver, J.B., 1992. Two applications of wavelet transforms in magnetic resonance imaging. IEEE Trans. Inform. Theory 38, 840–860. https://doi.org/10.1109/18.119740

Heckemann, R.A., Hajnal, J.V., Aljabar, P., Rueckert, D., Hammers, A., 2006. Automatic anatomical brain MRI segmentation combining label propagation and decision fusion. NeuroImage 33, 115–126. https://doi.org/10.1016/j.neuroimage.2006.05.061
Hellier, P., 2003. Consistent intensity correction of MR images, in: Proceedings 2003 International Conference on Image Processing (Cat. No.03CH37429). Presented at the International Conference on Image Processing, IEEE, Barcelona, Spain, p. I-1109–12. https://doi.org/10.1109/ICIP.2003.1247161
Hellman, M.E., 1970. The Nearest Neighbor Classification Rule with a Reject Option. IEEE Trans. Syst. Sci. Cyber. 6, 179–185. https://doi.org/10.1109/TSSC.1970.300339
Herbert, M.R., Ziegler, D.A., Makris, N., Filipek, P.A., Kemper, T.L., Normandin, J.J., Sanders, H.A., Kennedy, D.N., Caviness, V.S., 2004. Localization of white matter volume increase in autism and developmental language disorder. Annals of Neurology 55, 530–540. https://doi.org/10.1002/ana.20032
Holland, B.S., Copenhaver, M.D., 1987. An Improved Sequentially Rejective Bonferroni Test Procedure. Biometrics 43, 417. https://doi.org/10.2307/2531823
Holm, S., 1979. A Simple Sequentially Rejective Multiple Test Procedure. Scandinavian Journal of Statistics 6, 65–70.
Hong, J., Hashizume, M., 2010. An effective point-based registration tool for surgical navigation. Surg Endosc 24, 944–948. https://doi.org/10.1007/s00464-009-0568-2
Hongzhi Wang, Suh, J.W., Das, S.R., Pluta, J.B., Craige, C., Yushkevich, P.A., 2013. Multi-Atlas Segmentation with Joint Label Fusion. IEEE Trans. Pattern Anal. Mach. Intell. 35, 611–623. https://doi.org/10.1109/TPAMI.2012.143
Horwitz, B., Rumsey, J.M., Grady, C.L., Rapoport, S.I., 1988. The cerebral metabolic landscape in autism. Intercorrelations of regional glucose utilization. Arch. Neurol. 45, 749–755.
Hua, X., Leow, A.D., Levitt, J.G., Caplan, R., Thompson, P.M., Toga, A.W., 2009. Detecting brain growth patterns in normal children using tensor-based morphometry. Hum Brain Mapp 30, 209–219. https://doi.org/10.1002/hbm.20498
Huttenlocher, P.R., 1979. Synaptic density in human frontal cortex — Developmental changes and effects of aging. Brain Research 163, 195–205. https://doi.org/10.1016/0006-8993(79)90349-4
Jager, F., Hornegger, J., 2009. Nonrigid Registration of Joint Histograms for Intensity Standardization in Magnetic Resonance Imaging. IEEE Trans. Med. Imaging 28, 137–150. https://doi.org/10.1109/TMI.2008.2004429
Jenkinson, M., Bannister, P., Brady, M., Smith, S., 2002. Improved optimization for the robust and accurate linear registration and motion correction of brain images. Neuroimage 17, 825–841. https://doi.org/10.1016/s1053-8119(02)91132-8
Jernigan, T.L., Tallal, P., 1990. Late childhood changes in brain morphology observable with MRI. Dev Med Child Neurol 32, 379–385. https://doi.org/10.1111/j.1469-8749.1990.tb16956.x
Jernigan, T.L., Trauner, D.A., Hesselink, J.R., Tallal, P.A., 1991. Maturation of human cerebrum observed in vivo during adolescence. Brain 114, 2037–2049. https://doi.org/10.1093/brain/114.5.2037
Just, M.A., Keller, T.A., Malave, V.L., Kana, R.K., Varma, S., 2012. Autism as a neural systems disorder: a theory of frontal-posterior underconnectivity. Neurosci Biobehav Rev 36, 1292–1313. https://doi.org/10.1016/j.neubiorev.2012.02.007
Kana, R.K., Keller, T.A., Cherkassky, V.L., Minshew, N.J., Just, M.A., 2009. Atypical frontal-posterior synchronization of Theory of Mind regions in autism during mental

state attribution. Soc Neurosci 4, 135–152. https://doi.org/10.1080/17470910802198510
Kass, M., Witkin, A., Terzopoulos, D., 1988. Snakes: Active contour models. Int J Comput Vision 1, 321–331. https://doi.org/10.1007/BF00133570
Kennedy, D.P., Courchesne, E., 2008. Functional abnormalities of the default network during self- and other-reflection in autism. Social Cognitive and Affective Neuroscience 3, 177–190. https://doi.org/10.1093/scan/nsn011
Kim, J.C., Wang, L., Shen, D., Lin, W., 2016. Biomechanical Analysis of Normal Brain Development during the First Year of Life Using Finite Strain Theory. Sci Rep 6, 37666. https://doi.org/10.1038/srep37666
Knickmeyer, R.C., Gouttard, S., Kang, C., Evans, D., Wilber, K., Smith, J.K., Hamer, R.M., Lin, W., Gerig, G., Gilmore, J.H., 2008. A structural MRI study of human brain development from birth to 2 years. J. Neurosci. 28, 12176–12182. https://doi.org/10.1523/JNEUROSCI.3479-08.2008
Krämer, J., Meuth, S., Tenberge, J.-G., Schiffler, P., Wiendl, H., Deppe, M., 2015. Early and Degressive Putamen Atrophy in Multiple Sclerosis. IJMS 16, 23195–23209. https://doi.org/10.3390/ijms161023195
Kuklisova-Murgasova, M., Aljabar, P., Srinivasan, L., Counsell, S.J., Doria, V., Serag, A., Gousias, I.S., Boardman, J.P., Rutherford, M.A., Edwards, A.D., Hajnal, J.V., Rueckert, D., 2011. A dynamic 4D probabilistic atlas of the developing brain. NeuroImage 54, 2750–2763. https://doi.org/10.1016/j.neuroimage.2010.10.019
Laird, N.M., Ware, J.H., 1982. Random-effects models for longitudinal data. Biometrics 38, 963–974.
Langen, M., Bos, D., Noordermeer, S.D.S., Nederveen, H., van Engeland, H., Durston, S., 2014. Changes in the Development of Striatum Are Involved in Repetitive Behavior in Autism. Biological Psychiatry 76, 405–411. https://doi.org/10.1016/j.biopsych.2013.08.013
Lau, J.C., Lerch, J.P., Sled, J.G., Henkelman, R.M., Evans, A.C., Bedell, B.J., 2008. Longitudinal neuroanatomical changes determined by deformation-based morphometry in a mouse model of Alzheimer's disease. Neuroimage 42, 19–27. https://doi.org/10.1016/j.neuroimage.2008.04.252
Lenroot, R.K., Gogtay, N., Greenstein, D.K., Wells, E.M., Wallace, G.L., Clasen, L.S., Blumenthal, J.D., Lerch, J., Zijdenbos, A.P., Evans, A.C., Thompson, P.M., Giedd, J.N., 2007. Sexual dimorphism of brain developmental trajectories during childhood and adolescence. NeuroImage 36, 1065–1073. https://doi.org/10.1016/j.neuroimage.2007.03.053
Lepore, N., Brun, C., Chou, Y.Y., Chiang, M.C., Dutton, R.A., Hayashi, K.M., Luders, E., Lopez, O.L., Aizenstein, H.J., Toga, A.W., Becker, J.T., Thompson, P.M., 2008. Generalized tensor-based morphometry of HIV/AIDS using multivariate statistics on deformation tensors. IEEE Trans Med Imaging 27, 129–141. https://doi.org/10.1109/TMI.2007.906091
Lerch, J., Hammill, C., van Eede, M., Cassel, D., 2017. RMINC: Statistical Tools for Medical Imaging NetCDF (MINC) Files.
Lewis, J.D., Evans, Alan C., Pruett, John R., Botteron, Kelly N., McKinstry, Robert C., Zwaigenbaum, Lonnie, Estes, Annette M., Collins, D. Louis, Kostopoulos, Penelope, Gerig, Guido, Dager, Stephen R., Paterson, Sarah, Schultz, Robert T., Styner, Martin A., Hazlett, Heather C., Piven, Joseph, Piven, J., Hazlett, H.C., Chappell, C., Dager, S.R., Estes, A.M., Shaw, D., Botteron, K.N., McKinstry, R.C., Constantino, J., Pruett, J.R., Schultz, R.T., Paterson, S., Zwaigenbaum, L., Elison, J.T., Evans, A.C., Collins,

D.L., Pike, G.B., Fonov, V., Kostopoulos, P., Das, S., Gerig, G., Styner, M.A., Gu, H., 2017. The Emergence of Network Inefficiencies in Infants With Autism Spectrum Disorder. Biological Psychiatry 82, 176–185. https://doi.org/10.1016/j.biopsych.2017.03.006

Liang, Z., Macfall, J.R., Harrington, D.P., 1994. Parameter estimation and tissue segmentation from multispectral MR images. IEEE Trans Med Imaging 13, 441–449. https://doi.org/10.1109/42.310875

Lim, K.O., Pfefferbaum, A., 1989. Segmentation of MR brain images into cerebrospinal fluid spaces, white and gray matter. J Comput Assist Tomogr 13, 588–593. https://doi.org/10.1097/00004728-198907000-00006

Lin, G.N., Corominas, R., Lemmens, I., Yang, X., Tavernier, J., Hill, D.E., Vidal, M., Sebat, J., Iakoucheva, L.M., 2015. Spatiotemporal 16p11.2 Protein Network Implicates Cortical Late Mid-Fetal Brain Development and KCTD13-Cul3-RhoA Pathway in Psychiatric Diseases. Neuron 85, 742–754. https://doi.org/10.1016/j.neuron.2015.01.010

Liu, J., Yao, L., Zhang, W., Xiao, Y., Liu, L., Gao, X., Shah, C., Li, S., Tao, B., Gong, Q., Lui, S., 2017. Gray matter abnormalities in pediatric autism spectrum disorder: a meta-analysis with signed differential mapping. Eur Child Adolesc Psychiatry 26, 933–945. https://doi.org/10.1007/s00787-017-0964-4

Lord, C., Risi, S., DiLavore, P.S., Shulman, C., Thurm, A., Pickles, A., 2006. Autism From 2 to 9 Years of Age. Arch Gen Psychiatry 63, 694. https://doi.org/10.1001/archpsyc.63.6.694

Lord, C., Rutter, M., Dilavore, P.C., Risi, S., 2000. Autism Diagnostic Observation Schedule. Western Psychological Services, Los Angeles, CA.

Lutkenhoff, E.S., Rosenberg, M., Chiang, J., Zhang, K., Pickard, J.D., Owen, A.M., Monti, M.M., 2014. Optimized Brain Extraction for Pathological Brains (optiBET). PLoS ONE 9, e115551. https://doi.org/10.1371/journal.pone.0115551

Maillard, A.M., Ruef, A., Pizzagalli, F., Migliavacca, E., Hippolyte, L., Adaszewski, S., Dukart, J., Ferrari, C., Conus, P., Männik, K., Zazhytska, M., Siffredi, V., Maeder, P., Kutalik, Z., Kherif, F., Hadjikhani, N., Beckmann, J.S., Reymond, A., Draganski, B., Jacquemont, S., 16p11.2 European Consortium, 2015. The 16p11.2 locus modulates brain structures common to autism, schizophrenia and obesity. Mol. Psychiatry 20, 140–147. https://doi.org/10.1038/mp.2014.145

Manjon, J., Carbonellcaballero, J., Lull, J., Garciamarti, G., Martibonmati, L., Robles, M., 2008. MRI denoising using Non-Local Means. Medical Image Analysis 12, 514–523. https://doi.org/10.1016/j.media.2008.02.004

Manjón, J.V., Coupé, P., 2016. volBrain: An Online MRI Brain Volumetry System. Front. Neuroinform. 10. https://doi.org/10.3389/fninf.2016.00030

Marsh, R., Gerber, A.J., Peterson, B.S., 2008. Neuroimaging Studies of Normal Brain Development and Their Relevance for Understanding Childhood Neuropsychiatric Disorders. Journal of the American Academy of Child & Adolescent Psychiatry 47, 1233–1251. https://doi.org/10.1097/CHI.0b013e318185e703

Marshall, C.R., Howrigan, D.P., Psychosis Endophenotypes International Consortium, CNV and Schizophrenia Working Groups of the Psychiatric Genomics Consortium, Merico, D., Thiruvahindrapuram, B., Wu, W., Greer, D.S., Antaki, D., Shetty, A., Holmans, P.A., Pinto, D., Gujral, M., Brandler, W.M., Malhotra, D., Wang, Z., Fajarado, K.V.F., Maile, M.S., Ripke, S., Agartz, I., Albus, M., Alexander, M., Amin, F., Atkins, J., Bacanu, S.A., Belliveau, R.A., Bergen, S.E., Bertalan, M., Bevilacqua, E., Bigdeli, T.B., Black, D.W., Bruggeman, R., Buccola, N.G., Buckner, R.L., Bulik-

Sullivan, B., Byerley, W., Cahn, W., Cai, G., Cairns, M.J., Campion, D., Cantor, R.M., Carr, V.J., Carrera, N., Catts, S.V., Chambert, K.D., Cheng, W., Cloninger, C.R., Cohen, D., Cormican, P., Craddock, N., Crespo-Facorro, B., Crowley, J.J., Curtis, D., Davidson, M., Davis, K.L., Degenhardt, F., Del Favero, J., DeLisi, L.E., Dikeos, D., Dinan, T., Djurovic, S., Donohoe, G., Drapeau, E., Duan, J., Dudbridge, F., Eichhammer, P., Eriksson, J., Escott-Price, V., Essioux, L., Fanous, A.H., Farh, K.-H., Farrell, M.S., Frank, J., Franke, L., Freedman, R., Freimer, N.B., Friedman, J.I., Forstner, A.J., Fromer, M., Genovese, G., Georgieva, L., Gershon, E.S., Giegling, I., Giusti-Rodríguez, P., Godard, S., Goldstein, J.I., Gratten, J., de Haan, L., Hamshere, M.L., Hansen, M., Hansen, T., Haroutunian, V., Hartmann, A.M., Henskens, F.A., Herms, S., Hirschhorn, J.N., Hoffmann, P., Hofman, A., Huang, H., Ikeda, M., Joa, I., Kähler, A.K., Kahn, R.S., Kalaydjieva, L., Karjalainen, J., Kavanagh, D., Keller, M.C., Kelly, B.J., Kennedy, J.L., Kim, Y., Knowles, J.A., Konte, B., Laurent, C., Lee, P., Lee, S.H., Legge, S.E., Lerer, B., Levy, D.L., Liang, K.-Y., Lieberman, J., Lönnqvist, J., Loughland, C.M., Magnusson, P.K.E., Maher, B.S., Maier, W., Mallet, J., Mattheisen, M., Mattingsdal, M., McCarley, R.W., McDonald, C., McIntosh, A.M., Meier, S., Meijer, C.J., Melle, I., Mesholam-Gately, R.I., Metspalu, A., Michie, P.T., Milani, L., Milanova, V., Mokrab, Y., Morris, D.W., Müller-Myhsok, B., Murphy, K.C., Murray, R.M., Myin-Germeys, I., Nenadic, I., Nertney, D.A., Nestadt, G., Nicodemus, K.K., Nisenbaum, L., Nordin, A., O'Callaghan, E., O'Dushlaine, C., Oh, S.-Y., Olincy, A., Olsen, L., O'Neill, F.A., Van Os, J., Pantelis, C., Papadimitriou, G.N., Parkhomenko, E., Pato, M.T., Paunio, T., Perkins, D.O., Pers, T.H., Pietiläinen, O., Pimm, J., Pocklington, A.J., Powell, J., Price, A., Pulver, A.E., Purcell, S.M., Quested, D., Rasmussen, H.B., Reichenberg, A., Reimers, M.A., Richards, A.L., Roffman, J.L., Roussos, P., Ruderfer, D.M., Salomaa, V., Sanders, A.R., Savitz, A., Schall, U., Schulze, T.G., Schwab, S.G., Scolnick, E.M., Scott, R.J., Seidman, L.J., Shi, J., Silverman, J.M., Smoller, J.W., Söderman, E., Spencer, C.C.A., Stahl, E.A., Strengman, E., Strohmaier, J., Stroup, T.S., Suvisaari, J., Svrakic, D.M., Szatkiewicz, J.P., Thirumalai, S., Tooney, P.A., Veijola, J., Visscher, P.M., Waddington, J., Walsh, D., Webb, B.T., Weiser, M., Wildenauer, D.B., Williams, N.M., Williams, S., Witt, S.H., Wolen, A.R., Wormley, B.K., Wray, N.R., Wu, J.Q., Zai, C.C., Adolfsson, R., Andreassen, O.A., Blackwood, D.H.R., Bramon, E., Buxbaum, J.D., Cichon, S., Collier, D.A., Corvin, A., Daly, M.J., Darvasi, A., Domenici, E., Esko, T., Gejman, P.V., Gill, M., Gurling, H., Hultman, C.M., Iwata, N., Jablensky, A.V., Jönsson, E.G., Kendler, K.S., Kirov, G., Knight, J., Levinson, D.F., Li, Q.S., McCarroll, S.A., McQuillin, A., Moran, J.L., Mowry, B.J., Nöthen, M.M., Ophoff, R.A., Owen, M.J., Palotie, A., Pato, C.N., Petryshen, T.L., Posthuma, D., Rietschel, M., Riley, B.P., Rujescu, D., Sklar, P., St Clair, D., Walters, J.T.R., Werge, T., Sullivan, P.F., O'Donovan, M.C., Scherer, S.W., Neale, B.M., Sebat, J., 2017. Contribution of copy number variants to schizophrenia from a genome-wide study of 41,321 subjects. Nat Genet 49, 27–35. https://doi.org/10.1038/ng.3725

Martin, E., Kikinis, R., Zuerrer, M., Boesch, C., Briner, J., Kewitz, G., Kaelin, P., 1988. Developmental stages of human brain: an MR study. J Comput Assist Tomogr 12, 917–922. https://doi.org/10.1097/00004728-198811000-00002

Martin-Brevet, S., Rodríguez-Herreros, B., Nielsen, J.A., Moreau, C., Modenato, C., Maillard, A.M., Pain, A., Richetin, S., Jønch, A.E., Qureshi, A.Y., Zürcher, N.R., Conus, P., Chung, W.K., Sherr, E.H., Spiro, J.E., Kherif, F., Beckmann, J.S., Hadjikhani, N., Reymond, A., Buckner, R.L., Draganski, B., Jacquemont, S., Addor,

M.-C., Andrieux, J., Arveiler, B., Baujat, G., Sloan-Béna, F., Belfiore, M., Bonneau, D., Bouquillon, S., Boute, O., Brusco, A., Busa, T., Caberg, J.-H., Campion, D., Colombert, V., Cordier, M.-P., David, A., Debray, F.-G., Delrue, M.-A., Doco-Fenzy, M., Dunkhase-Heinl, U., Edery, P., Fagerberg, C., Faivre, L., Forzano, F., Genevieve, D., Gérard, M., Giachino, D., Guichet, A., Guillin, O., Héron, D., Isidor, B., Jacquette, A., Jaillard, S., Journel, H., Keren, B., Lacombe, D., Lebon, S., Le Caignec, C., Lemaître, M.-P., Lespinasse, J., Mathieu-Dramart, M., Mercier, S., Mignot, C., Missirian, C., Petit, F., Pilekær Sørensen, K., Pinson, L., Plessis, G., Prieur, F., Rooryck-Thambo, C., Rossi, M., Sanlaville, D., Schlott Kristiansen, B., Schluth-Bolard, C., Till, M., Van Haelst, M., Van Maldergem, L., Alupay, H., Aaronson, B., Ackerman, S., Ankenman, K., Anwar, A., Atwell, C., Bowe, A., Beaudet, A.L., Benedetti, M., Berg, J., Berman, J., Berry, L.N., Bibb, A.L., Blaskey, L., Brennan, J., Brewton, C.M., Buckner, R., Bukshpun, P., Burko, J., Cali, P., Cerban, B., Chang, Y., Cheong, M., Chow, V., Chu, Z., Chudnovskaya, D., Cornew, L., Dale, C., Dell, J., Dempsey, A.G., Deschamps, T., Earl, R., Edgar, J., Elgin, J., Olson, J.E., Evans, Y.L., Findlay, A., Fischbach, G.D., Fisk, C., Fregeau, B., Gaetz, B., Gaetz, L., Garza, S., Gerdts, J., Glenn, O., Gobuty, S.E., Golembski, R., Greenup, M., Heiken, K., Hines, K., Hinkley, L., Jackson, F.I., Jenkins, J., Jeremy, R.J., Johnson, K., Kanne, S.M., Kessler, S., Khan, S.Y., Ku, M., Kuschner, E., Laakman, A.L., Lam, P., Lasala, M.W., Lee, H., LaGuerre, K., Levy, S., Cavanagh, A.L., Llorens, A.V., Campe, K.L., Luks, T.L., Marco, E.J., Martin, S., Martin, A.J., Marzano, G., Masson, C., McGovern, K.E., McNally Keehn, R., Miller, D.T., Miller, F.K., Moss, T.J., Murray, R., Nagarajan, S.S., Nowell, K.P., Owen, J., Paal, A.M., Packer, A., Page, P.Z., Paul, B.M., Peters, A., Peterson, D., Poduri, A., Pojman, N.J., Porche, K., Proud, M.B., Qasmieh, S., Ramocki, M.B., Reilly, B., Roberts, T.P.L., Shaw, D., Sinha, T., Smith-Packard, B., Gallagher, A.S., Swarnakar, V., Thieu, T., Triantafallou, C., Vaughan, R., Wakahiro, M., Wallace, A., Ward, T., Wenegrat, J., Wolken, A., 2018. Quantifying the Effects of 16p11.2 Copy Number Variants on Brain Structure: A Multisite Genetic-First Study. Biological Psychiatry 84, 253–264. https://doi.org/10.1016/j.biopsych.2018.02.1176

Matsuzawa, J., 2001. Age-related Volumetric Changes of Brain Gray and White Matter in Healthy Infants and Children. Cerebral Cortex 11, 335–342. https://doi.org/10.1093/cercor/11.4.335

Maurer, C.R., Maciunas, R.J., Fitzpatrick, J.M., 1998. Registration of head CT images to physical space using a weighted combination of points and surfaces [image-guided surgery]. IEEE Trans. Med. Imaging 17, 753–761. https://doi.org/10.1109/42.736031

McArdle, C.B., Richardson, C.J., Nicholas, D.A., Mirfakhraee, M., Hayden, C.K., Amparo, E.G., 1987. Developmental features of the neonatal brain: MR imaging. Part I. Gray-white matter differentiation and myelination. Radiology 162, 223–229. https://doi.org/10.1148/radiology.162.1.3786767

McCullagh, P., Nelder, J.A., 1989. Generalized Linear Models. Springer US, Boston, MA. https://doi.org/10.1007/978-1-4899-3242-6

McDonald, A.J., 1998. Cortical pathways to the mammalian amygdala. Progress in Neurobiology 55, 257–332. https://doi.org/10.1016/S0301-0082(98)00003-3

Mesejo, P., Valsecchi, A., Marrakchi-Kacem, L., Cagnoni, S., Damas, S., 2015. Biomedical image segmentation using geometric deformable models and metaheuristics. Computerized Medical Imaging and Graphics 43, 167–178. https://doi.org/10.1016/j.compmedimag.2013.12.005

Mills, K.L., Goddings, A.-L., Herting, M.M., Meuwese, R., Blakemore, S.-J., Crone, E.A., Dahl, R.E., Güroğlu, B., Raznahan, A., Sowell, E.R., Tamnes, C.K., 2016. Structural brain development between childhood and adulthood: Convergence across four longitudinal samples. NeuroImage 141, 273–281. https://doi.org/10.1016/j.neuroimage.2016.07.044

Moreno-De-Luca, D., Sanders, S.J., Willsey, A.J., Mulle, J.G., Lowe, J.K., Geschwind, D.H., State, M.W., Martin, C.L., Ledbetter, D.H., 2013. Using large clinical data sets to infer pathogenicity for rare copy number variants in autism cohorts. Mol Psychiatry 18, 1090–1095. https://doi.org/10.1038/mp.2012.138

Mostofsky, S.H., Burgess, M.P., Gidley Larson, J.C., 2007. Increased motor cortex white matter volume predicts motor impairment in autism. Brain 130, 2117–2122. https://doi.org/10.1093/brain/awm129

Nelder, J.A., Wedderburn, R.W.M., 1972. Generalized Linear Models. Journal of the Royal Statistical Society. Series A (General) 135, 370. https://doi.org/10.2307/2344614

Neuromorphometrics Inc., 2013. . Neuromorphometrics Inc., Somerville, MA, USA.

Novosad, P., Collins, D.L., Alzheimer's Disease Neuroimaging Initiative, 2018. An efficient and accurate method for robust inter-dataset brain extraction and comparisons with 9 other methods. Hum Brain Mapp 39, 4241–4257. https://doi.org/10.1002/hbm.24243

Nyúl, L.G., Udupa, J.K., 1999. On standardizing the MR image intensity scale. Magn Reson Med 42, 1072–1081.

Nyul, L.G., Udupa, J.K., Xuan Zhang, 2000. New variants of a method of MRI scale standardization. IEEE Transactions on Medical Imaging 19, 143–150. https://doi.org/10.1109/42.836373

Ozonoff, S., Young, G.S., Carter, A., Messinger, D., Yirmiya, N., Zwaigenbaum, L., Bryson, S., Carver, L.J., Constantino, J.N., Dobkins, K., Hutman, T., Iverson, J.M., Landa, R., Rogers, S.J., Sigman, M., Stone, W.L., 2011. Recurrence Risk for Autism Spectrum Disorders: A Baby Siblings Research Consortium Study. PEDIATRICS peds.2010-2825. https://doi.org/10.1542/peds.2010-2825

Pelizzari, C.A., Chen, G.T., Spelbring, D.R., Weichselbaum, R.R., Chen, C.T., 1989. Accurate three-dimensional registration of CT, PET, and/or MR images of the brain. J Comput Assist Tomogr 13, 20–26.

Pereira, A.M., Campos, B.M., Coan, A.C., Pegoraro, L.F., de Rezende, T.J.R., Obeso, I., Dalgalarrondo, P., da Costa, J.C., Dreher, J.-C., Cendes, F., 2018. Differences in Cortical Structure and Functional MRI Connectivity in High Functioning Autism. Front. Neurol. 9, 539. https://doi.org/10.3389/fneur.2018.00539

Pfefferbaum, A., Mathalon, D.H., Sullivan, E.V., Rawles, J.M., Zipursky, R.B., Lim, K.O., 1994. A Quantitative Magnetic Resonance Imaging Study of Changes in Brain Morphology From Infancy to Late Adulthood. Archives of Neurology 51, 874–887. https://doi.org/10.1001/archneur.1994.00540210046012

Pontillo, G., Cocozza, S., Lanzillo, R., Russo, C., Stasi, M.D., Paolella, C., Vola, E.A., Criscuolo, C., Borrelli, P., Palma, G., Tedeschi, E., Morra, V.B., Elefante, A., Brunetti, A., 2019. Determinants of Deep Gray Matter Atrophy in Multiple Sclerosis: A Multimodal MRI Study. AJNR Am J Neuroradiol 40, 99–106. https://doi.org/10.3174/ajnr.A5915

Portmann, T., Yang, M., Mao, R., Panagiotakos, G., Ellegood, J., Dolen, G., Bader, P.L., Grueter, B.A., Goold, C., Fisher, E., Clifford, K., Rengarajan, P., Kalikhman, D., Loureiro, D., Saw, N.L., Zhengqui, Z., Miller, M.A., Lerch, J.P., Henkelman, R.M., Shamloo, M., Malenka, R.C., Crawley, J.N., Dolmetsch, R.E., 2014. Behavioral Abnormalities and Circuit Defects in the Basal Ganglia of a Mouse Model of 16p11.2

Deletion Syndrome. Cell Reports 7, 1077–1092. https://doi.org/10.1016/j.celrep.2014.03.036
Prastawa, M., Gilmore, J.H., Lin, W., Gerig, G., 2005. Automatic segmentation of MR images of the developing newborn brain. Med Image Anal 9, 457–466. https://doi.org/10.1016/j.media.2005.05.007
Puce, A., Allison, T., Asgari, M., Gore, J.C., McCarthy, G., 1996. Differential Sensitivity of Human Visual Cortex to Faces, Letterstrings, and Textures: A Functional Magnetic Resonance Imaging Study. J. Neurosci. 16, 5205–5215. https://doi.org/10.1523/JNEUROSCI.16-16-05205.1996
Qiu, T., Chang, C., Li, Y., Qian, L., Xiao, C.Y., Xiao, T., Xiao, X., Xiao, Y.H., Chu, K.K., Lewis, M.H., Ke, X., 2016. Two years changes in the development of caudate nucleus are involved in restricted repetitive behaviors in 2–5-year-old children with autism spectrum disorder. Developmental Cognitive Neuroscience 19, 137–143. https://doi.org/10.1016/j.dcn.2016.02.010
Qureshi, A.Y., Mueller, S., Snyder, A.Z., Mukherjee, P., Berman, J.I., Roberts, T.P.L., Nagarajan, S.S., Spiro, J.E., Chung, W.K., Sherr, E.H., Buckner, R.L., Simons VIP Consortium, 2014. Opposing brain differences in 16p11.2 deletion and duplication carriers. J. Neurosci. 34, 11199–11211. https://doi.org/10.1523/JNEUROSCI.1366-14.2014
Rajagopalan, V., Schwartzman, A., Hua, X., Leow, A., Thompson, P., Lepore, N., 2015. Multivariate analysis of eigenvalues and eigenvectors in tensor based morphometry, in: Romero, E., Lepore, N. (Eds.), . p. 928707. https://doi.org/10.1117/12.2073737
Ray, R.D., Zald, D.H., 2012. Anatomical insights into the interaction of emotion and cognition in the prefrontal cortex. Neuroscience & Biobehavioral Reviews 36, 479–501. https://doi.org/10.1016/j.neubiorev.2011.08.005
Raznahan, A., Toro, R., Daly, E., Robertson, D., Murphy, C., Deeley, Q., Bolton, P.F., Paus, T., Murphy, D.G.M., 2010. Cortical Anatomy in Autism Spectrum Disorder: An In Vivo MRI Study on the Effect of Age. Cerebral Cortex 20, 1332–1340. https://doi.org/10.1093/cercor/bhp198
Redcay, E., Courchesne, E., 2005. When is the brain enlarged in autism? A meta-analysis of all brain size reports. Biol. Psychiatry 58, 1–9. https://doi.org/10.1016/j.biopsych.2005.03.026
Reiss, A.L., Abrams, M.T., Singer, H.S., Ross, J.L., Denckla, M.B., 1996. Brain development, gender and IQ in children: A volumetric imaging study. Brain 119, 1763–1774. https://doi.org/10.1093/brain/119.5.1763
Robitaille, N., Mouiha, A., Crépeault, B., Valdivia, F., Duchesne, S., The Alzheimer's Disease Neuroimaging Initiative, 2012. Tissue-Based MRI Intensity Standardization: Application to Multicentric Datasets. International Journal of Biomedical Imaging 2012, 1–11. https://doi.org/10.1155/2012/347120
Rojas, D.C., Peterson, E., Winterrowd, E., Reite, M.L., Rogers, S.J., Tregellas, J.R., 2006. Regional gray matter volumetric changes in autism associated with social and repetitive behavior symptoms. BMC Psychiatry 6, 56. https://doi.org/10.1186/1471-244X-6-56
Rousseau, F., Habas, P.A., Studholme, C., 2011. A Supervised Patch-Based Approach for Human Brain Labeling. IEEE Trans. Med. Imaging 30, 1852–1862. https://doi.org/10.1109/TMI.2011.2156806
Rutter, M., Bailey, A., Lord, C., 2003a. Autism Diagnostic Interview, Revised. Western Psychological Services, Los Angeles, CA.

Rutter, M., Bailey, A., Lord, C., Berument, S., 2003b. Social Communication Questionnaire. Western Psychological Services, Los Angeles, CA.
Samsonov, A.A., Johnson, C.R., 2004. Noise-adaptive nonlinear diffusion filtering of MR images with spatially varying noise levels. Magn. Reson. Med. 52, 798–806. https://doi.org/10.1002/mrm.20207
Satterthwaite, T.D., Elliott, M.A., Ruparel, K., Loughead, J., Prabhakaran, K., Calkins, M.E., Hopson, R., Jackson, C., Keefe, J., Riley, M., Mentch, F.D., Sleiman, P., Verma, R., Davatzikos, C., Hakonarson, H., Gur, R.C., Gur, R.E., 2014. Neuroimaging of the Philadelphia neurodevelopmental cohort. Neuroimage 86, 544–553. https://doi.org/10.1016/j.neuroimage.2013.07.064
Schaer, M., Debbané, M., Bach Cuadra, M., Ottet, M.-C., Glaser, B., Thiran, J.-P., Eliez, S., 2009. Deviant trajectories of cortical maturation in 22q11.2 deletion syndrome (22q11DS): A cross-sectional and longitudinal study. Schizophrenia Research 115, 182–190. https://doi.org/10.1016/j.schres.2009.09.016
Schnack, H.G., van Haren, N.E.M., Brouwer, R.M., van Baal, G.C.M., Picchioni, M., Weisbrod, M., Sauer, H., Cannon, T.D., Huttunen, M., Lepage, C., Collins, D.L., Evans, A., Murray, R.M., Kahn, R.S., Hulshoff Pol, H.E., 2010. Mapping reliability in multicenter MRI: Voxel-based morphometry and cortical thickness. Hum. Brain Mapp. 31, 1967–1982. https://doi.org/10.1002/hbm.20991
Ségonne, F., Dale, A.M., Busa, E., Glessner, M., Salat, D., Hahn, H.K., Fischl, B., 2004. A hybrid approach to the skull stripping problem in MRI. Neuroimage 22, 1060–1075. https://doi.org/10.1016/j.neuroimage.2004.03.032
Shashi, V., McConkie-Rosell, A., Rosell, B., Schoch, K., Vellore, K., McDonald, M., Jiang, Y.-H., Xie, P., Need, A., Goldstein, D.B., 2014. The utility of the traditional medical genetics diagnostic evaluation in the context of next-generation sequencing for undiagnosed genetic disorders. Genet Med 16, 176–182. https://doi.org/10.1038/gim.2013.99
Shaw, P., Greenstein, D., Lerch, J., Clasen, L., Lenroot, R., Gogtay, N., Evans, A., Rapoport, J., Giedd, J., 2006. Intellectual ability and cortical development in children and adolescents. Nature 440, 676–679. https://doi.org/10.1038/nature04513
Sled, J.G., Zijdenbos, A.P., Evans, A.C., 1998. A nonparametric method for automatic correction of intensity nonuniformity in MRI data. IEEE Trans Med Imaging 17, 87–97. https://doi.org/10.1109/42.668698
Smith, S.M., 2002. Fast robust automated brain extraction. Hum Brain Mapp 17, 143–155. https://doi.org/10.1002/hbm.10062
Sowell, E.R., Thompson, P.M., Holmes, C.J., Batth, R., Jernigan, T.L., Toga, A.W., 1999. Localizing Age-Related Changes in Brain Structure between Childhood and Adolescence Using Statistical Parametric Mapping. NeuroImage 9, 587–597. https://doi.org/10.1006/nimg.1999.0436
Sowell, E.R., Thompson, P.M., Leonard, C.M., Welcome, S.E., Kan, E., Toga, A.W., 2004. Longitudinal mapping of cortical thickness and brain growth in normal children. J. Neurosci. 24, 8223–8231. https://doi.org/10.1523/JNEUROSCI.1798-04.2004
Stevens, F.L., Hurley, R.A., Taber, K.H., 2011. Anterior cingulate cortex: unique role in cognition and emotion. J Neuropsychiatry Clin Neurosci 23, 121–125. https://doi.org/10.1176/jnp.23.2.jnp121
Stiles, J., Jernigan, T.L., 2010. The Basics of Brain Development. Neuropsychol Rev 20, 327–348. https://doi.org/10.1007/s11065-010-9148-4
Sun, D., Ching, C.R.K., Lin, A., Forsyth, J.K., Kushan, L., Vajdi, A., Jalbrzikowski, M., Hansen, L., Villalon-Reina, J.E., Qu, X., Jonas, R.K., van Amelsvoort, T., Bakker, G.,

Kates, W.R., Antshel, K.M., Fremont, W., Campbell, L.E., McCabe, K.L., Daly, E., Gudbrandsen, M., Murphy, C.M., Murphy, D., Craig, M., Vorstman, J., Fiksinski, A., Koops, S., Ruparel, K., Roalf, D.R., Gur, R.E., Schmitt, J.E., Simon, T.J., Goodrich-Hunsaker, N.J., Durdle, C.A., Bassett, A.S., Chow, E.W.C., Butcher, N.J., Vila-Rodriguez, F., Doherty, J., Cunningham, A., van den Bree, M.B.M., Linden, D.E.J., Moss, H., Owen, M.J., Murphy, K.C., McDonald-McGinn, D.M., Emanuel, B., van Erp, T.G.M., Turner, J.A., Thompson, P.M., Bearden, C.E., 2018. Large-scale mapping of cortical alterations in 22q11.2 deletion syndrome: Convergence with idiopathic psychosis and effects of deletion size. Mol Psychiatry. https://doi.org/10.1038/s41380-018-0078-5

Swanson, M.R., Wolff, J.J., Elison, J.T., Gu, H., Hazlett, H.C., Botteron, K., Styner, M., Paterson, S., Gerig, G., Constantino, J., Dager, S., Estes, A., Vachet, C., Piven, J., IBIS Network, 2015. Splenium development and early spoken language in human infants. Dev Sci. https://doi.org/10.1111/desc.12360

Takeda, K., Nomura, Y., Sakuma, H., Tagami, T., Okuda, Y., Nakagawa, T., 1997. MR assessment of normal brain development in neonates and infants: comparative study of T1- and diffusion-weighted images. J Comput Assist Tomogr 21, 1–7.

Talairach, J., Szikla, G., Tournoux, P., Prosalentis, A., Bordas-Ferrier, M., Covello, L., Iacob, M., Mempel, E., 1967. Atlas d'anatomie stereotaxique du telencephale. Masson, Paris.

Talairach, J., Tournoux, P., 1988. Co-planar stereotaxic atlas of the human brain: 3-dimensional proportional system: an approach to cerebral imaging. Georg Thieme, Stuttgart ; New York.

Tamnes, C.K., Walhovd, K.B., Dale, A.M., Østby, Y., Grydeland, H., Richardson, G., Westlye, L.T., Roddey, J.C., Hagler, D.J., Due-Tønnessen, P., Holland, D., Fjell, A.M., 2013. Brain development and aging: Overlapping and unique patterns of change. NeuroImage 68, 63–74. https://doi.org/10.1016/j.neuroimage.2012.11.039

Tărlungeanu, D.C., Novarino, G., 2018. Genomics in neurodevelopmental disorders: an avenue to personalized medicine. Exp Mol Med 50, 100. https://doi.org/10.1038/s12276-018-0129-7

Tau, G.Z., Peterson, B.S., 2010. Normal Development of Brain Circuits. Neuropsychopharmacology 35, 147–168. https://doi.org/10.1038/npp.2009.115

The MathWorks Inc., 2018. MATLAB. The MathWorks Inc., Natick, Massachusetts.

The Simons VIP Consortium, 2012. Simons Variation in Individuals Project (Simons VIP): A Genetics-First Approach to Studying Autism Spectrum and Related Neurodevelopmental Disorders. Neuron 73, 1063–1067. https://doi.org/10.1016/j.neuron.2012.02.014

Thompson, A.J., Banwell, B.L., Barkhof, F., Carroll, W.M., Coetzee, T., Comi, G., Correale, J., Fazekas, F., Filippi, M., Freedman, M.S., Fujihara, K., Galetta, S.L., Hartung, H.P., Kappos, L., Lublin, F.D., Marrie, R.A., Miller, A.E., Miller, D.H., Montalban, X., Mowry, E.M., Sorensen, P.S., Tintoré, M., Traboulsee, A.L., Trojano, M., Uitdehaag, B.M.J., Vukusic, S., Waubant, E., Weinshenker, B.G., Reingold, S.C., Cohen, J.A., 2018. Diagnosis of multiple sclerosis: 2017 revisions of the McDonald criteria. The Lancet Neurology 17, 162–173. https://doi.org/10.1016/S1474-4422(17)30470-2

Thompson, P.M., Giedd, J.N., Woods, R.P., MacDonald, D., Evans, A.C., Toga, A.W., 2000. Growth patterns in the developing brain detected by using continuum mechanical tensor maps. Nature 404, 190–193. https://doi.org/10.1038/35004593

Till, C., Ghassemi, R., Aubert-Broche, B., Kerbrat, A., Collins, D.L., Narayanan, S., Arnold, D.L., Desrocher, M., Sled, J.G., Banwell, B.L., 2011. MRI correlates of cognitive

impairment in childhood-onset multiple sclerosis. Neuropsychology 25, 319–332. https://doi.org/10.1037/a0022051
Toga, A.W., Thompson, P.M., Sowell, E.R., 2006. Mapping brain maturation. Trends Neurosci. 29, 148–159. https://doi.org/10.1016/j.tins.2006.01.007
Tustison, N.J., Avants, B.B., Cook, P.A., Yuanjie Zheng, Egan, A., Yushkevich, P.A., Gee, J.C., 2010a. N4ITK: Improved N3 Bias Correction. IEEE Transactions on Medical Imaging 29, 1310–1320. https://doi.org/10.1109/TMI.2010.2046908
Tustison, N.J., Avants, B.B., Cook, P.A., Yuanjie Zheng, Egan, A., Yushkevich, P.A., Gee, J.C., 2010b. N4ITK: Improved N3 Bias Correction. IEEE Transactions on Medical Imaging 29, 1310–1320. https://doi.org/10.1109/TMI.2010.2046908
van Haren, N.E.M., Cahn, W., Hulshoff Pol, H.E., Schnack, H.G., Caspers, E., Lemstra, A., Sitskoorn, M.M., Wiersma, D., van den Bosch, R.J., Dingemans, P.M., Schene, A.H., Kahn, R.S., 2003. Brain volumes as predictor of outcome in recent-onset schizophrenia: a multi-center MRI study. Schizophr. Res. 64, 41–52. https://doi.org/10.1016/s0920-9964(03)00018-5
Van Leemput, K., Maes, F., Vandermeulen, D., Suetens, P., 1999. Automated model-based tissue classification of MR images of the brain. IEEE Trans Med Imaging 18, 897–908. https://doi.org/10.1109/42.811270
van Rooij, D., Anagnostou, E., Arango, C., Auzias, G., Behrmann, M., Busatto, G.F., Calderoni, S., Daly, E., Deruelle, C., Di Martino, A., Dinstein, I., Duran, F.L.S., Durston, S., Ecker, C., Fair, D., Fedor, J., Fitzgerald, J., Freitag, C.M., Gallagher, L., Gori, I., Haar, S., Hoekstra, L., Jahanshad, N., Jalbrzikowski, M., Janssen, J., Lerch, J., Luna, B., Martinho, M.M., McGrath, J., Muratori, F., Murphy, C.M., Murphy, D.G.M., O'Hearn, K., Oranje, B., Parellada, M., Retico, A., Rosa, P., Rubia, K., Shook, D., Taylor, M., Thompson, P.M., Tosetti, M., Wallace, G.L., Zhou, F., Buitelaar, J.K., 2018. Cortical and Subcortical Brain Morphometry Differences Between Patients With Autism Spectrum Disorder and Healthy Individuals Across the Lifespan: Results From the ENIGMA ASD Working Group. AJP 175, 359–369. https://doi.org/10.1176/appi.ajp.2017.17010100
Velasquez, F., Wiggins, J.L., Mattson, W.I., Martin, D.M., Lord, C., Monk, C.S., 2017. The influence of 5-HTTLPR transporter genotype on amygdala-subgenual anterior cingulate cortex connectivity in autism spectrum disorder. Dev Cogn Neurosci 24, 12–20. https://doi.org/10.1016/j.dcn.2016.12.002
Verhey, L.H., Branson, H.M., Shroff, M.M., Callen, D.J., Sled, J.G., Narayanan, S., Sadovnick, A.D., Bar-Or, A., Arnold, D.L., Marrie, R.A., Banwell, B., 2011. MRI parameters for prediction of multiple sclerosis diagnosis in children with acute CNS demyelination: a prospective national cohort study. The Lancet Neurology 10, 1065–1073. https://doi.org/10.1016/S1474-4422(11)70250-2
Waiter, G.D., Williams, J.H.G., Murray, A.D., Gilchrist, A., Perrett, D.I., Whiten, A., 2004. A voxel-based investigation of brain structure in male adolescents with autistic spectrum disorder. NeuroImage 22, 619–625. https://doi.org/10.1016/j.neuroimage.2004.02.029
Waldman, A., Ghezzi, A., Bar-Or, A., Mikaeloff, Y., Tardieu, M., Banwell, B., 2014. Multiple sclerosis in children: an update on clinical diagnosis, therapeutic strategies, and research. The Lancet Neurology 13, 936–948. https://doi.org/10.1016/S1474-4422(14)70093-6
Wallace, G.L., Dankner, N., Kenworthy, L., Giedd, J.N., Martin, A., 2010. Age-related temporal and parietal cortical thinning in autism spectrum disorders. Brain 133, 3745–3754. https://doi.org/10.1093/brain/awq279

Wang, L., Lai, H.M., Barker, G.J., Miller, D.H., Tofts, P.S., 1998. Correction for variations in MRI scanner sensitivity in brain studies with histogram matching. Magn Reson Med 39, 322–327. https://doi.org/10.1002/mrm.1910390222

Warfield, S.K., Kaus, M., Jolesz, F.A., Kikinis, R., 2000. Adaptive, template moderated, spatially varying statistical classification. Medical Image Analysis 4, 43–55. https://doi.org/10.1016/S1361-8415(00)00003-7

Weinstein, M., Ben-Sira, L., Levy, Y., Zachor, D.A., Itzhak, E.B., Artzi, M., Tarrasch, R., Eksteine, P.M., Hendler, T., Bashat, D.B., 2011. Abnormal white matter integrity in young children with autism. Hum. Brain Mapp. 32, 534–543. https://doi.org/10.1002/hbm.21042

Weisenfeld, N.I., Warfield, S.K., 2004. Normalization of joint image-intensity statistics in MRI using the kullback-leibler divergence, in: 2004 2nd IEEE International Symposium on Biomedical Imaging: Macro to Nano (IEEE Cat No. 04EX821). Presented at the 2004 2nd IEEE International Symposium on Biomedical Imaging: Macro to Nano, IEEE, Arlington, VA, USA, pp. 101–104. https://doi.org/10.1109/ISBI.2004.1398484

Weiss, L.A., Shen, Y., Korn, J.M., Arking, D.E., Miller, D.T., Fossdal, R., Saemundsen, E., Stefansson, H., Ferreira, M.A.R., Green, T., Platt, O.S., Ruderfer, D.M., Walsh, C.A., Altshuler, D., Chakravarti, A., Tanzi, R.E., Stefansson, K., Santangelo, S.L., Gusella, J.F., Sklar, P., Wu, B.-L., Daly, M.J., 2008. Association between Microdeletion and Microduplication at 16p11.2 and Autism. New England Journal of Medicine 358, 667–675. https://doi.org/10.1056/NEJMoa075974

Wilke, M., Schmithorst, V.J., Holland, S.K., 2002. Assessment of spatial normalization of whole-brain magnetic resonance images in children. Human Brain Mapping 17, 48–60. https://doi.org/10.1002/hbm.10053

Wolff, J.J., Gerig, G., Lewis, J.D., Soda, T., Styner, M.A., Vachet, C., Botteron, K.N., Elison, J.T., Dager, S.R., Estes, A.M., Hazlett, H.C., Schultz, R.T., Zwaigenbaum, L., Piven, J., IBIS Network, 2015. Altered corpus callosum morphology associated with autism over the first 2 years of life. Brain 138, 2046–2058. https://doi.org/10.1093/brain/awv118

Woodhouse, W., Bailey, A., Rutter, M., Bolton, P., Baird, G., Le Couteur, A., 1996. Head circumference in autism and other pervasive developmental disorders. J Child Psychol Psychiatry 37, 665–671.

Worsley, K.J., Andermann, M., Koulis, T., MacDonald, D., Evans, A.C., 1999. Detecting changes in nonisotropic images. Hum Brain Mapp 8, 98–101.

Worsley, K.J., Marrett, S., Neelin, P., Vandal, A.C., Friston, K.J., Evans, A.C., 1996. A unified statistical approach for determining significant signals in images of cerebral activation. Hum Brain Mapp 4, 58–73. https://doi.org/10.1002/(SICI)1097-0193(1996)4:1<58::AID-HBM4>3.0.CO;2-O

Wright, I.C., McGuire, P.K., Poline, J.-B., Travere, J.M., Murray, R.M., Frith, C.D., Frackowiak, R.S.J., Friston, K.J., 1995. A Voxel-Based Method for the Statistical Analysis of Gray and White Matter Density Applied to Schizophrenia. NeuroImage 2, 244–252. https://doi.org/10.1006/nimg.1995.1032

Wu, H.-F., Chen, Y.-J., Chu, M.-C., Hsu, Y.-T., Lu, T.-Y., Chen, I.-T., Chen, P., Lin, H.-C., 2018. Deep Brain Stimulation Modified Autism-Like Deficits via the Serotonin System in a Valproic Acid-Induced Rat Model. IJMS 19, 2840. https://doi.org/10.3390/ijms19092840

Xiao, Z., Qiu, T., Ke, X., Xiao, X., Xiao, T., Liang, F., Zou, B., Huang, H., Fang, H., Chu, K., Zhang, J., Liu, Y., 2014. Autism Spectrum Disorder as Early Neurodevelopmental

Disorder: Evidence from the Brain Imaging Abnormalities in 2–3 Years Old Toddlers. J Autism Dev Disord 44, 1633–1640. https://doi.org/10.1007/s10803-014-2033-x
Yakovlev, P.A., Lecours, I.R., 1967. The myelogenetic cycles of regional maturation of the brain, in: Minkowski, A. (Ed.), Regional Development of the Brain in Early Life. Blackwel Scientific, Oxford, U.K., pp. 3–70.
Yang, X., Fei, B., 2011. A wavelet multiscale denoising algorithm for magnetic resonance (MR) images. Meas. Sci. Technol. 22, 025803. https://doi.org/10.1088/0957-0233/22/2/025803
Young, I.R., Hall, A.S., Pallis, C.A., Bydder, G.M., Legg, N.J., Steiner, R.E., 1981. NUCLEAR MAGNETIC RESONANCE IMAGING OF THE BRAIN IN MULTIPLE SCLEROSIS. The Lancet 318, 1063–1066. https://doi.org/10.1016/S0140-6736(81)91273-3
Zhang, Y., Brady, M., Smith, S., 2001. Segmentation of brain MR images through a hidden Markov random field model and the expectation-maximization algorithm. IEEE Trans Med Imaging 20, 45–57. https://doi.org/10.1109/42.906424
Zucker, S.W., 1976. Region growing: Childhood and adolescence. Computer Graphics and Image Processing 5, 382–399. https://doi.org/10.1016/S0146-664X(76)80014-7